The Characterization of the Yield Surface for Fine-Grained Sediments

by

Anthony Joseph Hanley

B.E. in Civil and Environmental Engineering, National University of Ireland-Galway, 2015

Submitted to the Department of Civil and Environmental Engineering

in partial fulfillment of the requirements for the degree of

Master of Science

in

Civil & Environmental Engineering - Geosystems Engineering

Tufts University

August 2017

Signature of Author………………………………………………………………………………

Department of Civil and Environmental Engineering

July 21st, 2014

Certified by…………………………………………………………………………………

John T. Germaine

Research Professor Tufts University

Thesis Supervisor

Accepted by ………………………………………………………………………………..

The Characterization of the Yield Surface for Fine-Grained Sediments

by

Anthony Joseph Hanley

Submitted to the Department of Civil and Environmental Engineering on

July 21st, 2014 in in partial fulfillment of the requirements for the degree of

Master of Science in Civil & Environmental Engineering - Geosystems Engineering

ABSTRACT

The yield surface is a contour in stress space that separates a material as behaving elastically from plastically. The yield surface is fundamental to most mathematical soil models which are used as the basis for many modern day finite element software packages. Most model formulations prescribe the yield surface as an elliptical shape symmetrical about the consolidation axis, however, these models are based on very limited data. MIT model formulations are typically calibrated using three undrained effective stress paths: normally consolidated undrained compression, normally consolidated undrained extension and overconsolidated undrained compression. This research adopted the use of the Strain Energy Method to characterize the shape of the yield surface for Resedimented Gulf of Mexico Eugene Island (RGoM-EI) and intact Boston Blue Clay (BBC). Specimens were first K_0 consolidated to 1MPa to set the yield surface. They were then unloaded to along a prescribed $K_{0,\ OCR}$ path to an OCR of 2. Once unloaded, drained triaxial tests were carried out to probe in different directions. The strain energy adsorbed by each specimen travelling along its individual path was plotted and used to characterize the yield stress.

The interpreted yield surface was compared to model formulations; such as MIT-E3 and MCC. It was found that the yield surface was not elliptical in shape, nor was it symmetrical about its consolidation axis. The undrained compression stress path proved to be a good first order approximation of the cap of the yield surface, while the undrained extension stress path was found to progressively overestimate the yield surface. MCC and MIT-E3 were found to not accurately predict the yield surface. With the conclusion that the undrained compression stress path provides a first order approximation of the cap of the yield surface, it is predicted that the geometry of the yield surface is stress dependent.

Thesis Supervisor: John T. Germaine

Title: Research professor of Civil and Environmental Engineering

ACKNOWLEDGMENTS

My greatest appreciation undoubtedly goes to my research supervisor, teacher and friend Dr. Jack Germaine (Dr. G). Dr. G's personality and sense of humor made working in the lab a pleasure, from running new exciting experiments to our daily trivia debates. The utmost respect and admiration is given to his knowledge of soil mechanics, laboratory testing, and indeed engineering as a whole. I am extremely grateful to have been taken under his wing over the past two years of my M.S degree. Outside of the laboratory we have also enjoyed some tense battles on the pool tables of Austin, as well enjoying my first Red sox's game. He has proven to be much more than a research advisor, but a close friend and role model.

I am also very much grateful to Ward and Burke Construction. Ltd, particularly Robert Ward, for providing me with a fully funded scholarship to pursue my Master's degree. Robert took me on as an intern engineer during my third year of my undergraduate degree, and the heavy civil engineering experience I have gained from working with him for such a short period has been invaluable. I look forward to returning to working with him in the near future.

I would like to thank the UT-GeoFluids research group members for their valuable contributions and insights into the work: Prof. Peter Flemings, Dr. Dick Plumb and Dr. Maria Nikolinakou. I would also like to acknowledge my committee members and teachers of geotechnical engineering; Prof. Laurie Baise, Prof. Luis Dorfmann and Dr. Lucy Jen. I recognize that I have been advised and educated by some of the best in the world.

Finally I am sincerely thankful for all my friends with whom I have spent many hours procrastinating writing this thesis. Without them, this work would have been finished two months earlier. Although, there company was very much appreciated every day, in particular Parker, James, David, Amer, Deniz, Lisa, Lechin, Chunwei, Amanda, Mark, and Liz The daily banter has made demanding times seem less daunting, and indeed often a lot of fun.

TABLE OF CONTENTS

LIST OF TABLES

LIST OF FIGURES

LIST OF SYMBOLS

QBASIC	Quick Beginner's All-purpose Symbolic Instruction Code
BBC	Boston Blue Clay
CIUC	Isotropically Consolidated Undrained Triaxial Compression Test
CH	High Plasticity Clay
CL	Low Plasticity Clay
CL-ML	Silty clay
CRS	Constant Rate of Strain
DSS	Direct Simple Shear
LIR	Load Increment Ratio
LVDT	Linear Voltage Displacement Transducer
MADC	Multi-channel Analogue to Digital Converter
MCC	Modified Cam Clay
MH	Elastic silt
MIT	Massachusetts Institute of Technology
NC	Normally Consolidated
OC	Overconsolidated
OCR	Overconsolidation Ratio
PSC	Plane Strain Compression
PSE	Plane Strain Extension
PVA	Pressure-Volume Actuator
R	Resedimented
RBBC	Resedimented Boston Blue Clay

RGoM-EI	Resedimented Gulf of Mexico Eugene Island Clay
SHANSEP	Stress History and Normalized Soil Engineering Properties
TAG	Tufts Advanced Geomaterials
TC	Triaxial Compression
TE	Triaxial Extension
TX	Triaxial
USCS	Unified Soil Classification System
VCL	Virgin Compression Line

$A_{cylindrical}$	Right cylinder area correction for a specimen
E	Young's modulus
e	Void ratio
Gs	Specific gravity
Ip	Plasticity index
K	Lateral stress ratio
K_0	Coefficient of lateral earth pressure at rest
$K_{0, NC}$	Coefficient of lateral earth pressure at rest for NC soil
p'	Average effective stress, $\frac{1}{2}(\sigma'_v + \sigma'_h)$
q	Shear stress, $\frac{1}{2}(\sigma_v - \sigma_h)$
s_u	Undrained shear strength
t	Time
u	Pore pressure

u_e	Excess pore pressure
w_c	Water content
w_L	Liquid limit
w_p	Plastic limit
ε	Strain
ε_a	Axial strain
ε_v	Volume strain
φ'cs	Secant critical state friction angle
σ'p	Preconsolidation pressure
σ'_v	Vertical effective stress
σ'_{vmax}	Maximum consolidation stress in the triaxial cell
τ	Shear stress

1 INTRODUCTION

1.1 PROBLEM STATEMENT

The yield surface is described as a contour that separates the state of stress from which a soil is behaving elastically from where it is behaving plastically. It is used as the basis for many computer modeling packages for analyzing soil behavior. While the mechanical characteristics of fine-grained soils is now believed to be well understood for the range of stresses conventionally encountered in geotechnical engineering practice, almost all of this research involved undrained testing procedures to describe these characteristics, limited successful drained tests have been performed. Thus, the yield surface for fine grained materials has not been experimentally characterized using drained triaxial tests. It has long been believed to be described by two undrained stress paths; a normally consolidated undrained compression stress path and a normally consolidated undrained extension stress path. Limited research has attempted to describe the yield surface using drained tests, as these types of tests are generally more difficult and take much longer. Bensari (1984) attempted to describe the yield surface for Resedimented Boston Blue Clay (RBBC) using drained shear triaxial tests in the MIT Geotechnical Laboratory in the early nineteen eighties. However, due to limitations in testing equipment at the time, he was only able to carry out a small number of tests. These tests consisted of manual incremental loading, in the form of weights being added or subtracted depending on the desired shearing condition. Incremental manual loading is not desirable for experimental research interpreting yielding as it does not produce a continuous stress path and often produces partially drained conditions. Advancements in modern technologies allows for fully automated drained tests to be performed and hence fully characterize the yield surface using drained triaxial shear tests.

Traditionally, the geotechnical engineering discipline has been focused on applications involving stresses less than about 1 MPa, with behavior at higher stresses being assumed to follow similar normalized trends i.e., strength increases proportionally with increasing consolidation stress (up to 100 MPa). However, in recent years a desire driven primarily by the petroleum industry to gain a deeper understanding of the behavior of fine grained materials has for applications in hydrocarbon reservoir development has led to the discoveries of these materials having stress dependence. Abdulhadi (2009) and Casey (2014) have shown that the strength of various soils is decreasing with increasing consolidation stress. Additionally, these recent discoveries would suggest that the normalized yield surface of an individual fine grained materials is stress dependent.

1.2 THESIS SCOPE AND OBJECTIVES

The overall goal of this research is to characterize the yield surface for fine grained materials at three orders of magnitude, 1, 10 and 100 MPa, and to determine if the yield surface is stress dependent. This is achieved through a program of K_0-consolidated drained triaxial tests on fully saturated specimens possessing similar degrees of over consolidation. All tests are performed in either, drained triaxial compression, or extension mode of shear, at room temperature. Test specimens are produced both by resedimenting natural source materials in the Tufts Laboratory and by intact samples. Resedimentation allows one to produce fully saturated samples of identical composition from source material with any desired preconsolidation stress or porosity, something which would be near impossible with the use of intact samples.

This thesis involves an extensive experimental investigation of the change in shear stress-strain behavior of fine-grained sediments as they are drain sheared from inside the yield surface to failure, or well beyond the yield surface. The work focuses particularly on the volumetric strain energy adsorbed by specimens as they are drain sheared, and examines the observed friction angle and drained strength properties. The research also aims to compare the characterized yield surfaces to the undrained effective stress paths, and to current model formulations, such as; MIT-E3 and Modified Cam Clay (MCC).

A secondary objective of the research is to determine the appropriate axial strain rate for K_0 consolidation inside the different triaxial systems. The strain rates currently used are based upon previous experimental experience in the MIT Geotechnical Laboratory for RBBC. However, these strain rates have never been verified to provide fully drained conditions throughout consolidation. Appropriate strain rates are based on the materials permeability, which for fine grained materials is stress dependent. Therefore, it is expected that the appropriate consolidation strain rate will have to be reduced as consolidation stress increases.

The research presented in this thesis represents a small fraction of the wider research objectives of the UT GeoFluids Consortium, a joint venture between Tufts University and the University of Texas at Austin. The main focus of the GeoFluids group is "to study the state and evolution of pressure, stress, deformation and fluid migration through experiments, theoretical analysis, and field study". The author's research focuses solely on mechanical behavior determined from experimentation, and provides a baseline behavior for use in analytical geomechanical models

1.3 ORGANIZATION OF THE THESIS

This thesis is organized into seven chapters, each of which has a separate and distinct function, as given below.

Chapter 2 presents a literature review of important background information relevant to the research. The aim is to establish an overall picture of the current level of knowledge regarding the characterization of the yield surface, and methods used to interpret yielding for fine-grained sediments. One dimensional yielding in the Oedometer device is discussed to aid in the understanding of the concept of the yield surface. Previous work on yielding in the triaxial cells is also discussed. Factors that affect the yield surface, such as secondary compression, cementation due to diagenesis and thixotropy are discussed. The concept of normalized soil behavior is then introduced. The development of MCC and MIT-E3 model formulations is presented and their limitations and input parameters are discussed. Chapter 2 also provides a review of the principle of effective stress.

Chapter 3 discusses the origin and index properties of Boston Blue Clay and Gulf of Mexico Eugene Island Clay. These fine-grained soils are very different in terms of mineral composition, geologic origin and mechanical properties. Chapter 3 also provides a detailed description of the procedures involved in both intact specimen preparation and the resedimentation process. The detailed description of the resedimentation process includes the processing method used, a brief background of resedimentation at both MIT and Tufts, the procedures and equipment used in this work, and an evaluation of sample uniformity.

Chapter 4 provides a detailed description of the equipment and procedures used in the triaxial testing program for the research. Three different automated triaxial systems, designed for low and medium stresses were available throughout the testing program. A more detailed discussion is provided of the low and medium pressure triaxial systems, as due to consolidation strain rate concerns, the high-pressure cell was not used in this testing program. The chapter also describes the control system hardware, software, pressure volume actuators, automated control systems and data acquisition system. The issue of apparatus compressibility in relation to increasing cell pressure and deviatoric load and their impact on measurements of axial strain is also addressed.

Chapter 5 presents the results of the K_0-consolidated drained triaxial testing program on RGoM-EI and intact BBC and briefly discusses the compression behavior observed from previous research. It also presents results on the K_0 swelling of RGoM-EI specimens and the stress path swelling of intact BBC specimens. The testing program consists primarily of triaxial compression and extension tests in which all specimens were consolidated to the same consolidation stress ~1 MPa. The variation in the lateral stress ratio was examined throughout the consolidation and swelling stages. The chapter also discusses the normalized behavior of the consolidation stress paths for both materials tested, in MIT stress space. In addition, there is a section summarizing the verification of drained consolidation results for both the low and medium stress systems

Chapter 6 presents results obtained during the drained shearing phase of triaxial tests. First, the method used to interpret yielding is described in detail, with the aid of the drained test shear stress paths. The normalized interpreted yield surfaces for RGoM-EI and intact BBC are presented, along with their corresponding yield transition zones. The secondary compression effect on the interpretation of the surfaces is also presented. The normalized undrained effective stress paths of both materials are compared to their individual interpreted yield surfaces. Following this, the RGoM-EI interpreted yield surface is compared to two model formulations (MIT-E3 and MCC). In addition, the shear stress–volumetric strain behavior observed from specific RGoM-EI tests is used to discuss the variations in the size of the interpreted yield transition zones. For specimens that were sheared to failure, the failure planes observed in compression and extension, can be predicted by the Mohr Coulomb Failure Criterion.

Chapter 7 summarizes the most important conclusions which can be drawn from the results of the research. Recommendations for future work are also given

Appendix A presents normalized volumetric strain energy plots for each drained shear test carried out on both BBC and RGoM-EI

2 BACKGROUND

2.1 INTRODUCTION

A yield surface is a contour separating the state of stress domain under which the soil behaves elastically from the state of stress having plastic behavior. More precisely, at stresses within the yield surface, the specimen strains are small and largely recoverable, whereas at stresses outside the yield surface, the strains are relatively large and mainly irrecoverable. When the stresses acting upon the soil lie on the yield surface, such as occurs during undrained shearing at OCR = 1, then the soil can undergo plastic deformation, i.e. progressive yielding.

This chapter begins with a review of previous experimental studies carried out on characterizing the yield surface for fine grained sediments for both intact and resedimented hard clays in triaxial compression at low and high stresses. Particular attention is paid to the findings of Casey (2014). Section 2.3 discusses the classification of fine-grained materials, with emphasis on clarifying the correct term for the materials used in the research. Section 2.4 examines the most common methods used to define yielding and the apparatuses used. Section 2.5 discusses the most common factors that affect the yield surface of fine-grained materials. Section 2.6 discusses normalized behavior and its importance when dealing with fine-grained soils, particularly, for this research. Section 2.7 describes the effects of soil anisotropy on the interpreted yield surface. Section 2.8 examines the multiple types of failure envelopes encountered with fine-grained materials. Finally, Section 2.9 describes two of the current model formulations used in industry to predict the yield surface; Modified Cam Clay (MCC) and MIT-E3.

2.2 PREVIOUS STUDIES ON EXPERIMENTAL CHARACTERIZATION OF THE YIELD SURFACE FOR FINE GRAINED MATERIALS

One of the earliest programs of triaxial testing at low stresses is that of Bensari (1984) on Resedimented Boston Blue Clay (RBBC). Figure 2-1 has been abstracted from Bensari's thesis, it plots the estimated yield surface for RBBC. Bensari combined the results obtained from three drained triaxial tests on overconsolidated soil with three undrained effective stress paths: a normally consolidated undrained compression stress path, a normally consolidated undrained extension stress path, and an over consolidated undrained compression stress path. He obtained yield points on the drained shear stress paths using the Casagrande Method of interpretation. However, his work was limited by equipment capabilities as load increments were added manually by the use of weights. This caused yielding and failure to occur suddenly in some specimens upon the addition of the new weight increment.

A more recent attempt to characterize the yield surface for RBBC at low and high confining stresses was performed by Casey (2014). Figure 2-2 plots the effective stress paths followed in TC and TE, together with the interpreted Mohr-Coulomb failure envelopes for RBBC in normalized MIT stress space. The plot also includes the Casey's interpretation of the soil's yield surface at the low and high stress levels. Casey combined the TC and TE effective stress paths, during undrained shearing, at OCR = 1, with the Mohr-Coulomb failure envelopes, to create the interpreted yield surfaces. Casey concluded that the fact that RBBC possesses no true cohesion means that the interpreted yield surface must pass through the origin of the normalized MIT plot,

The interpreted yield surfaces shown in Figure 2-2 synthesize many of the results presented previously, from high stress testing on fine grained materials. For RBBC, increasing consolidation stress changes the form of the yield surface such that it becomes more centered about the effective stress axis (i.e., the yield surface becomes more isotropic). This is reflected in a decrease in normalized undrained strength and friction angle and an increase in $K_{0, NC}$ with increasing consolidation stress, as observed by Abdulhadi (2009). Casey concluded that the shape and orientation of the yield surface has stress dependence, For example, high plasticity soils such as R. London Clay display a large reduction in normalized undrained strength and friction angle and a large increase in $K_{0, NC}$ with increasing stress (Casey, 2014). This reflects a yield surface which becomes elongated about the effective stress axis as consolidation stress increases.

2.3 CLASSIFICATION OF FINE-GRAINED MATERIALS

It is important to clarify the terminology used to describe and classify fine-grained materials. The materials referred to in this thesis lie in a transitional zone between hard clay and soft ductile argillaceous rock. This transitional nature can lead to confusion between researchers in soil mechanics, rock mechanics, and geology. For example, while one author may refer to a material as shale, others may refer to the same material as clay, clay shale or mudstone. A review of the various geological and engineering classification schemes which have been proposed for fine-grained materials is given in William (2007). For clarification, the following descriptions are given based on definitions suggested by Stokes and Varnes (1955):

Shale: A general term for lithified clays and silts which are fissile and break along planes parallel to the original bedding.

Clay shale: A shale that consists primarily of clay minerals.

Claystone: A clay which has become indurated by some means, e.g. due to cementation. It is the same as clay rock and is sometimes used to designate concretionary masses found in clay deposits. Unlike shale, claystone does not necessarily possess significant fissility.

Mudrock/Mudstone: Is a generic term for all fine-grained sediments including: clay, silt, siltstone, claystone, shale and argillite. It should be used when a deposit consists of a mixture of clay, silt and sand sized particles, or when there is doubt as to a precise identification or.

Clay and silt have more than one definition:

Clay Definitions:

1. Under the USCS classification system, a fine-grained soil whose Atterberg Limits (ASTM D4318) cause it to be plotted above the 'A' Line in the Casagrande Plasticity chart (Lambe and Whitman 1969).
2. A soil which, by weight, more than 50 % of its particles are smaller than 0.002 mm.
3. A soil consisting primarily of clay minerals, e.g. smectite, illite, kaolinite.

Silt Definitions:

1. A soil which, by weight, more than 50 % of its particles are smaller than 0.075 mm and whose Atterberg Limits cause it to be plotted below the 'A' Line in the Casagrande Plasticity chart
2. A soil which, by weight, consists primarily of particles in the size range 0.075 - 0.002 mm

It is therefore necessary for the author to adopt some reasonable terminology which can be used consistency throughout this literature review. Since the research presented in this thesis focuses on the mechanical behavior of fine-grained soils at and above 1 MPa, the materials will be regarded by the author as 'hard clays' (with clay being defined using Clay Definition 1 above). This is in accordance with the classification scheme proposed by Terzaghi et al. (1996) for clays exhibiting an undrained strength $S_u > 0.2$ MPa.

2.4 METHODS USED TO DEFINE YIELDING

2.4.1 Yielding in the Oedometer test

The oedometer test is one of the most common test run in problems which involve one dimensional settlement computations. It is also used in the application of the SHANSEP design procedure (Ladd and Foott, 1974) to evaluate undrained stability. A great number of empirical methods can be used to locate the maximum past pressure, i.e. yield stress (Casagrande, 1936; Schmertmann, 1955; Jambu, 1969; Butterfield, 1979) from oedometer test data. The two most common methods are the Casagrande method and the strain energy method (Becker et al. 1987) are discussed below. It should be recognized that the oedometer test is limited to only locating one point on the yield surface, as it can only apply one dimensional loading. Hence, it was not used as part of this research.

2.4.1.1 Casagrande Method

The Casagrande construction is performed on a plot of either, void ratio, or volumetric strain, versus axial effective stress on a log scale. The plotted curve generally has the following features.

- At low stress levels ($\sigma'_{vc} < \sigma'_{vm}$), the soil compression is small with a near linear shallow function of log
- At relatively high stress levels, the soil compression is large and increases linearly with log σ'_{vc} (virgin compression line)
- For intermediate stress levels, the compressibility increases progressively with log σ'_{vc}, with a maximum curvature in the vicinity of the maximum past pressure.

Casagrande's graphical technique provides the maximum past pressure or "yield stress" separating the two portions of the consolidation curve with a sharp difference in compressibility. Figure 2-3 summarizes the Casagrande method, it consists of the following steps:

a) Locating the point of maximum curvature on the consolidation curve
b) Constructing a horizontal line through this point of maximum curvature, and constructing a tangent line to the curve
c) Bisecting the angle formed between the two constructed lines
d) Extrapolating the virgin line to meet the bisection line.

The intersection of the extension of the normally consolidated line and bisecting line gives the yield stress. While it is very common to plot one - dimensional compression data in the log effective stress space, one should always review the compression results when stress is plotted on a natural scale. This often provides a very different impression of the measurements, and it is the natural stress scale that maps directly to depth (Germaine, 2009).

2.4.1.2 Strain Energy Method

Strain energy is the work done per unit volume on the specimen. Becker et al. (1987) proposed a work-based procedure to determine the preconsolidation stress. The method plots work against consolidation stress, with both plotted on a natural scale. The quantity of work is calculated for each increment as the sum of the average force for each increment multiplied by the increment in deformation, and divided by the current volume. For an Oedometer test, the strain energy is given by:

$$W_j = \sum_{m=1}^{j} \left(\frac{\sigma'_{v,m} + \sigma'_{v,m-1}}{2} \right) \left(\ln \frac{1 - \varepsilon_{a,m-1}}{1 - \varepsilon_{a,m}} \right) \tag{2-1}$$

Where:

W_j = work per unit volume of the specimen up to increment j (kN-m/m^3)

j = index value for stress increment (integer)

$\sigma'_{v,m}$ = vertical effective stress at current increment (MPa)
$\sigma'_{v,m-1}$ = vertical effective stress at previous increment (MPa)
$\varepsilon_{a,m}$ = axial strain at current increment (decimal)
$\varepsilon_{a,m-1}$ = axial strain at the previous increment (decimal)
$\sigma'_{r,m}$ = radial effective stress at current increment (MPa)
$\sigma'_{r,m-1}$ = radial effective stress at previous increment (MPa)
$\varepsilon_{r,m}$ = radial strain at current increment (decimal)
$\varepsilon_{r,m-1}$ = radial strain at the previous increment (decimal)
m = index used in summation (integer)

The work calculation is not unique. The quantity depends on the size of the stress increment added. This is because the stress-strain (or force-deformation) curve is not linear. This is an important consideration when applying the calculation to tests having an unload-reload cycle. Figure 2-4 plots the strain energy construction method. It involves, plotting the work versus axial effective stress on a natural scale. A line is drawn through the high stress linear portion of the data. The low stress range should also approximate a straight line. However, this can often times, be a matter of some judgment. The stress at the intersection of these two lines represents the yield stress (or preconsolidation stress). This method is advantageous, as plotting results in a natural scale reduces the variation in the yield stress, due to subjective decisions about the slope of the initial straight line. This method can also be used to approximate upper and lower estimates by varying the slope of the initial line.

2.4.2 Yielding During Triaxial Shearing

The triaxial system is capable of applying an infinite number of different loading situations to specimens. The system is also fully automated, and is capable of applying a constant shearing rate to specimens. This is why the triaxial system was adopted for this research. Both the Casagrande and strain energy methods can also be used to interpret yielding in triaxial test data. For this research the strain energy method was used to incorporate yielding for drained triaxial test results. The yield stress, using the strain energy curves, corresponds to an abrupt (or measurable) change in the strain energy curve during triaxial shear. For undrained tests, Mitchell (1969) showed that for overconsolidated tests the curvature of the undrained effective stress path (ESP) is an indication of yielding. The point of maximum curvature coincides with the yield stress.

2.5 FACTORS AFFECTING THE YIELD SURFACE

For a natural clay deposited under K_0 conditions, the yield surface is believed to be an ellipsoid centered on the K_0-line, with its apex at the maximum past pressure (Tavenas, 1977). Thus, the size of the yield surface is proportional to the maximum past pressure. Any change of the maximum past pressure would affect the yield surface. Time effects such as aging and thixotropy can be important. It is also recognized that anisotropy and strain rate affect the stress-strain-strength characteristics of soft clays and hence yielding. The following is a summary of the most recent findings on the effect of these factors:

- Diagenetic processes such as cementation can be a much more important cause of overconsolidation (i.e., shifting of the yield surface). This increase in overconsolidation due to non-mechanical processes such as cementation is commonly referred to as ‘apparent’ or ‘quasi’ preconsolidation (Gutierrez et al. 2008). The ratio of the apparent preconsolidation stress to the current in situ effective stress is often referred to as the yield stress ratio (YSR) rather than overconsolidation ratio (OCR). It should be noted that, apart from cementation, many other natural phenomenon may cause an apparent preconsolidation to develop in a soil. Desiccation caused by evaporation or freezing can also have a similar effect (Ladd 1985).
- Aging or secondary compression increases the maximum past pressure, causing a shift in the yield envelope. Tavenas(1977) concluded, based on experiments on Champlain Clay

from St Alban, Quebec, that aging causes an uniform displacement of the entire yield surface.

- It is recognized that thixotropy stiffens the soil with time, which would presumably affect the yield envelope. O'Neill (1984) data suggests that compression and extension strengths are equally affected. However, the magnitude and direction of the change of the yield surface due to thixotropy has not been investigated.
- Most natural clays are anisotropic and exhibit asymmetrical yield surfaces (Mitchell 1970, Tavenas, 1977, Lo, 1972, Bensari 1984, Casey 2014) The Kavvadas model (1982) assumes that soil elements consolidated along a radial stress path can be described by a yield surface centered on the radial stress path of consolidation (this applies equally for radial stress paths other than K_0 and isotropic stress paths).
- A change in the strain rate or duration of shear causes a displacement of the yield surface (Tavenas, 1977). Lo (1972) concluded that the displacement of the yield surface due to the strain rate is uniform.

2.6 NORMALIZED BEHAVIOUR

The Normalized Soil Parameter (NSP) concept is based on the empirical observation that clay samples having similar over consolidation ratios, but different consolidation stresses, and consequently different preconsolidation pressures, exhibit similar properties (i.e., strength, stress-strain, shear induced pore pressures, etc.) when normalized with respect to the maximum consolidation stress. This concept has led to the development of the SHANSEP (Stress History and Normalized Soil Engineering Properties) design method (Ladd & Foott, 1974). Furthermore, the NSP is also the foundation for other frameworks of soil behavior, such as: the Critical State Soil Mechanics (Schofield & Wroth, 1968), and "simple" clay (Ladd, 1960). It is also the basis of the two analytical soil models the Modified Cam Clay (Roscoe & Burland, 1968) and MIT-E3 (Whittle & Kavvadas, 1994).

The SHANSEP normalization method is applicable to cohesive soils that have been mechanically normally consolidated (i.e., in situ OCR = 1), or overconsolidated. This method is not intended to be used in cemented, highly sensitive clays, or in drying crust of a soil deposit. The technique can be used in either drained or undrained conditions. It is generally applied to undrained shear in triaxial compression (TC) and extension (TE), plane strain compression (PSC) and extension (PSE), and in direct simple shear (DSS). The premise of this technique is that the in situ stress history can be simulated in the laboratory that will provide accurate predictions of the in situ soil behavior at various OCRs. Figure 2-5 shows typical results of a SHANSEP test program results for AGS plastic marine clay with three modes of shearing: TC, TE, and DSS. The results can be represented by the SHANSEP equation:

$$S_u/\sigma'_{vc} = S(OCR)^m \tag{2-1}$$

where S_u is the undrained strength ratio for the NC clay, and m is the slope of the regression line. The variance in behavior for the three modes of shearing is a reflection of the anisotropic nature of soil. The method should ideally only be applied to K_0 consolidated test specimens. While isotropic consolidation is assumed to have little impact on the measured undrained strength of intact OC specimens, for resedimented specimens consolidated into the NC range where the yield surface changes, K_0 consolidation prior to shearing is especially important (Belviso et al. 2001, Ladd and Varallyay 1965).

2.7 SOIL ANISOTROPY

The experimental program conducted in this research comprises of drained triaxial compression and extension tests. The mode of shearing in these tests is different, which leads to variations in the stress-strain strength properties due to anisotropy. The change in soil behavior with direction of loading (i.e., anisotropy) can arise from several factors, such as: the depositional environment, the consolidation stress-strain history of the material, and due to subsequent changes in the loading conditions. Definitions of anisotropy have been discussed extensively (e.g., Casagrande & Carillo, 1944; Hansen & Gibson, 1949; Ladd et al., 1977; Jamiolkowski et al., 1985; Ladd, 1991). Ladd (1991) stated that the initial anisotropy (i.e., inherent and initial shear stress) denotes differences in the stress-strain-strength response of a K_0 consolidated soil with variations in the applied principal stress direction. Inherent anisotropy is developed during 1-dimensional (K_0) deposition. Initial shear stress anisotropy represents the directionally dependent undrained response of soils whenever shearing starts from an anisotropic initial state of stress (i.e., $K_0 \neq 1$). Evolving anisotropy describes how the initial cross anisotropic properties of the K_0 consolidated soil change due to subsequent stressing and straining.

When evaluating laboratory shear devices available for testing, two parameters are used to describe the basic differences in the applied stress system (Germaine, 1982): 1) direction of the applied major principal stress relative to the vertical (depositional) direction denoted by the δ angle; and 2) the relative magnitude of the intermediate principal stress defined by $b = (\sigma_2 - \sigma_3)/(\sigma_1 - \sigma_3)$. Figure 2-6 shows the combinations of b and δ that can be achieved by laboratory shear devices, these being triaxial compression and extension (TC/TE), plane strain compression and extension (PSC/PSE), direct simple shear (DSS), true triaxial apparatus (TTA), torsional shear hollow cylinder (TSHC), and the directional shear cell (DSC).

The triaxial system is the most commonly shearing device used to evaluate the stress-strain strength behavior of fine grained materials. This is because of its relative simplicity for testing and in the interpretation of results. In addition, drainage conditions can be well controlled and the results are generally consistent and repeatable. The conventional triaxial cell is used to test solid cylindrical specimens by applying an equal fluid pressure to each side of the specimen, and imposing a deviatoric load (positive or negative) in the axial direction. The device is capable of performing any drained consolidation stress path; with isotropic or K_0 consolidation stress paths being the most common. However, the major principal stress can act only in the axial, or radial direction, resulting in two possible b-δ combinations: 1) b =0 and δ = 0° for triaxial compression (TC); and 2) b = 1 and δ = 90° for triaxial extension (TE).

2.8 FAILURE ENVELOPES

Failure envelopes for fine-grained soils are highly influenced by: natural micro-structure, OCR and stress level. Burland (1990) examined the behavior of various types of intact and resedimented clays, and demonstrated that the peak undrained strength of undisturbed clays is often significantly greater than that of the corresponding resedimented material at the same void ratio, due to the effects of natural micro-structure. Burland concluded that four failure envelopes can be defined for fine-grained materials: 1) a peak strength envelope defining brittle failure of undisturbed OC clays; 2) a post-rupture strength envelope representing the end of rapid post-peak strain softening of undisturbed OC clays; 3) an 'intrinsic' critical strength envelope defined by the failure of resedimented samples; and 4) a residual strength envelope reached only after very large strains as particles become aligned parallel to the failure surface. Figure 2-7 plots the four types of failure envelopes defined by Burland (1990). The peak strength envelope is curved, displays a cohesive intercept, and lies above the intrinsic critical state envelope. This is because of the influence of natural micro-structure possessed by undisturbed OC clay. Alternatively, undisturbed NC clay (i.e., intact clay which possesses no mechanical or apparent preconsolidation) will tend to fail on the intrinsic critical state envelope and then travel down this envelope. The intrinsic critical state envelope may be interpreted as a basic property independent of the undisturbed state of the material and can be viewed as providing a good basis for comparison of the properties of different clays. The post-rupture envelope traces very close to the intrinsic critical state envelope. After very large shear strains, both undisturbed and resedimented clay will reach a common residual strength envelope as the platy clay particles become aligned parallel to a shear surface.

2.9 MODEL FORMULATIONS

2.9.1 Modified Cam Clay

Modified cam clay is a stress-strain model based on plasticity theory and the critical state concept. It was developed at Cambridge University to model the generalized stress-strain behavior of clay. It regards soft clay as an isotropic, elastoplastic, strain-hardening material with irrecoverable strains occurring only outside its elliptical yield locus. It incorporates the condition of normality that governs the direction of plastic strain increments. It has proven to reasonably well predict the behavior of soft clays in isotropic triaxial compression and extension during both undrained and drained shear. However, its major shortcoming is that it is an isotropic model which does not include important effects due to rotation or reversal of principal stress directions.

Kavvadas (1982) and Kavvadas and Baligh (1982) significantly extended the MCC model by incorporating an elliptical yield surface centered along the radial stress path during one dimensional (K_0) consolidation. This model is known as MIT-E1. It predicts a yield surface that is free to rotate in the effective stress space and change in size to account for the influence of stress strain history. It provides a more realistic treatment of stress-strain anisotropy, and strain softening.

Both the MIT-E1 and the MCC model require initial definitions of state of stress. However MIT-E1 requires 11 input parameters compared to only five for the MCC model.

2.9.2 MIT-E3

MIT-E3 is a model formulation developed at MIT in the early 1990's. It was developed for describing the behavior of overconsolidated clays that obey normalized behavior and are rate-independent. The model incorporates observations of overconsolidated clay behavior including: hysteretic stress-strain response; small strain nonlinearity; coupling of volumetric and shear deformations; and transitional yielding as the NC stress state is approached. For normally consolidated clays, the model describes anisotropic stress-strain strength for K_0 consolidated clays, as well as strain softening that occurs in certain modes of deformation. Figure 2-8 shows the conceptual framework used by the MIT-E3 formulation for hydrostatic unloading and reloading. The formulation assumes that the soil can be modeled as a rate-independent material (i.e., creep effects are not incorporated). The measured behavior of a clay is most closely described by A-B-C [Figure 2-8(b)]. For modeling purposes, MIT-E3 subdivides this behavior into two components:

1. A closed, symmetric, hysteresis loop [Figure 2-8(a)] that matches the materials unloading behavior. This response is referred to as perfectly hysteretic and is described through a formulation similar to that proposed by Hueckel and Nova (1979).
2. Upon reloading, irrecoverable plastic strains are assumed to develop as the virgin consolidation line (VCL) is approached, resulting in residual plastic strains, Δp, at A. The magnitude of plastic strains is determined by the proximity of the current stress state to the VCL.

The mechanical behavior of NC soil elements, consolidated along radial effective stress paths, can be described by a yield surface which is initially oriented along the direction of consolidation. The model used a number of input parameters and variables to determine the position of the yield surface. Figure 2-9 presents the MIT-E3 yield surface and parameters, where α' controls the size of the yield surface; **b** = a second-order tensor describes the orientation of the yield surface in effective stress space; and c = the ratio of the semiaxes of the ellipsoid. For the case when b = 0, the model reduces to the same form as that used in the MCC model (Roscoe and Burland 1968). More information on the calibration parameters of MIT-E3 can be found in Whittle and Kavvadas, 1994.

Another component of MIT-E3 is an elastoplastic model to describe the generalized behavior of K_0 NC clays, based on earlier work of Kavvadas (1982). This model describes the anisotropic properties of K_0 consolidated clays, and their evolution with loading, and strain-softening behavior that is observed experimentally for certain modes of deformation. The model, in its most general form, uses 15 input parameters to characterize a given clay. These parameters are either directly measured in standard laboratory tests, or are obtained from parametric studies that identify clear roles for each of the input parameters. Complete evaluation of input parameters and model predictions are presented in Whittle (1990, 1993) and in a companion paper Whittle et al.(1994).

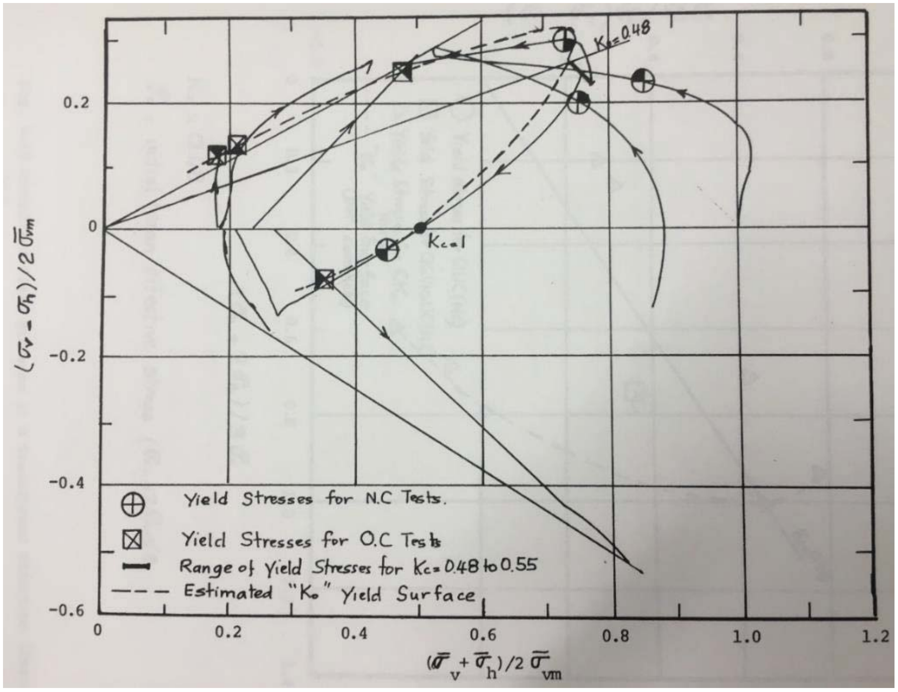

Figure 2-1: Estimated K_0 yield surface for RBBC using a combination of drained and undrained tests (Bensari, 1981)

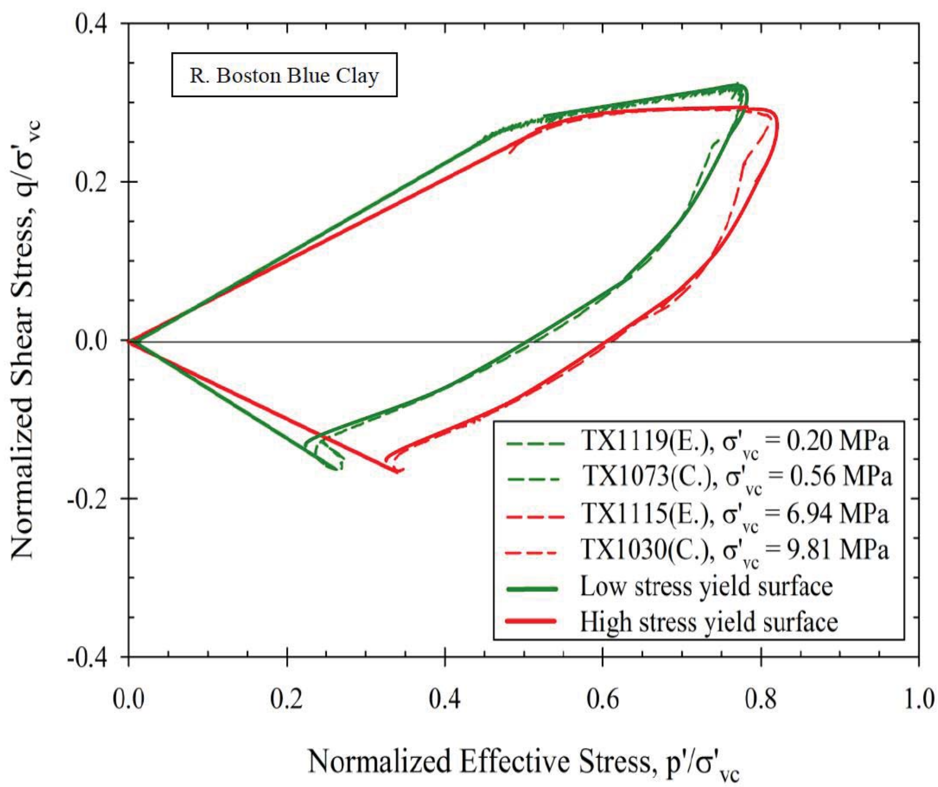

Figure 2-2: Interpreted yield surfaces of RBBC at low and high consolidation stresses based on the results of TE and TC tests performed on the soil at OCR = 1 (Casey, 2014)

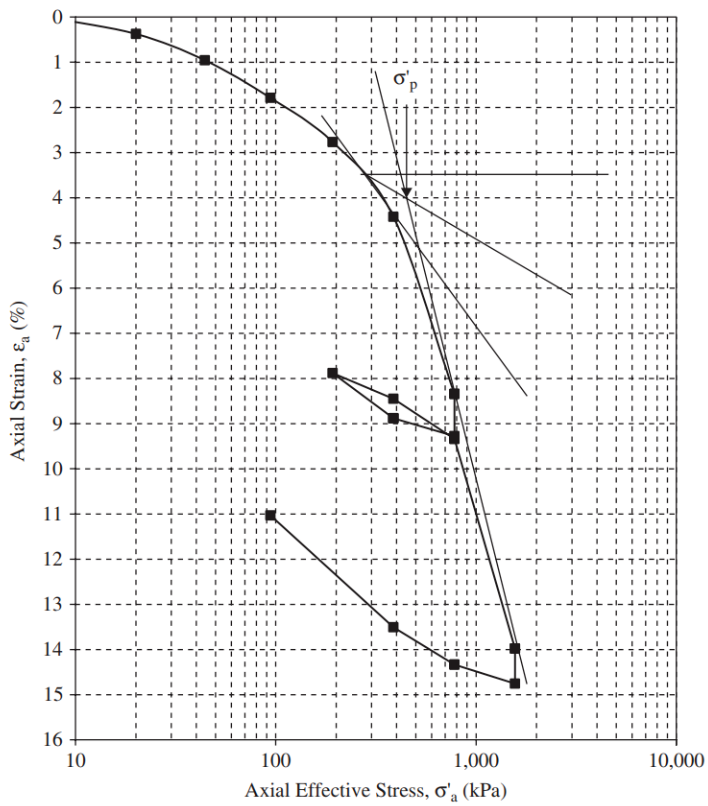

Figure 2-3: Casagrande construction to determine the preconsolidation stress (Germaine & Germaine, 2009)

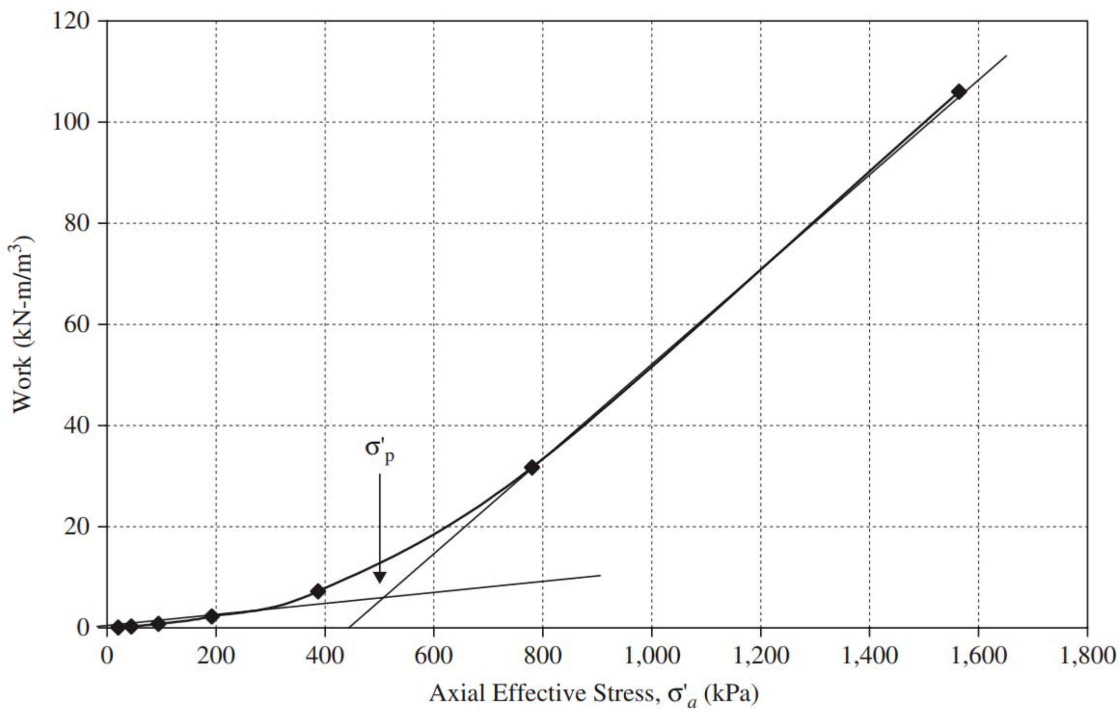

Figure 2-4:Strain energy method to determine the pre-consolidation stress (Germaine & Germaine, 2009)

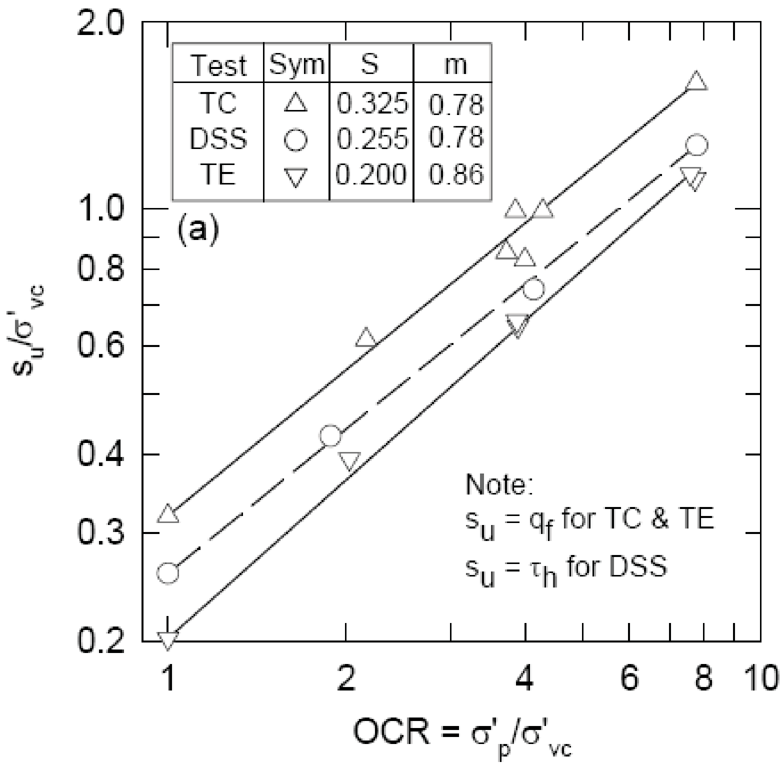

Figure 2-5: Normalized undrained shear strength versus OCR from a SHANSEP test program on *AGS Plastic Marine Clay* (Koutsoftas & Ladd, 1985)

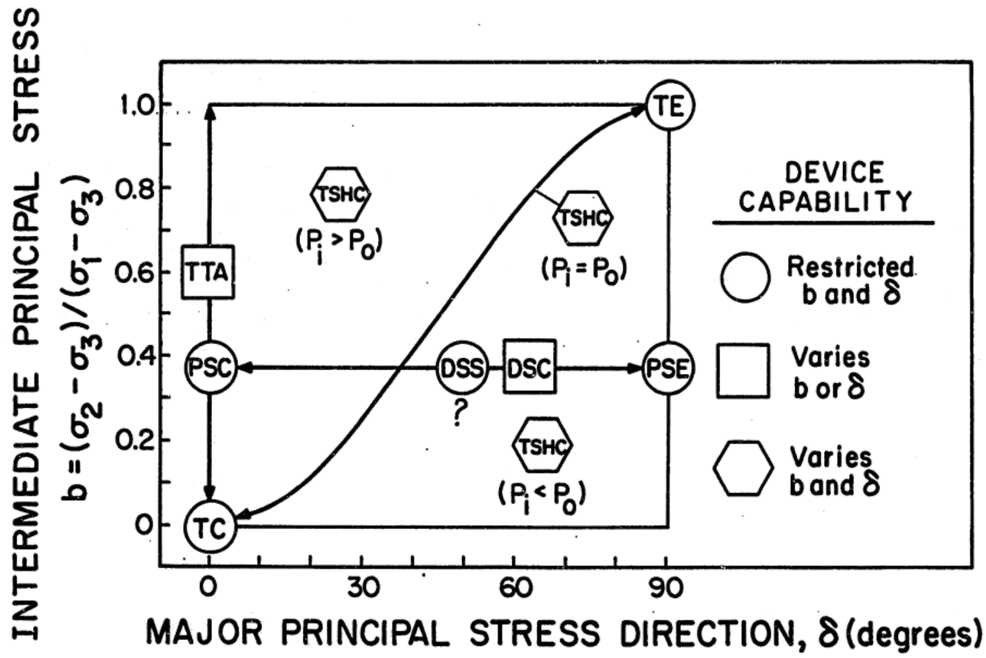

Figure 2-6: Stress systems achievable by shear devices for K_0 consolidated specimens (Ladd, 1991 after Germaine, 1982)

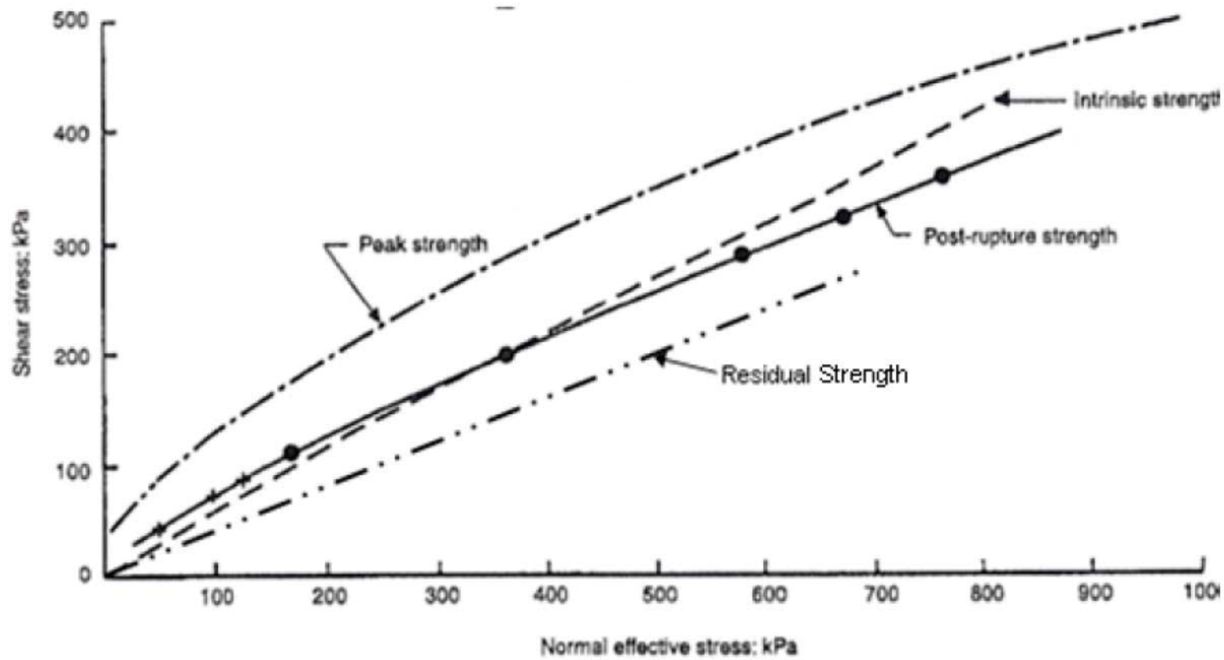

Figure 2-7: Conceptual form of failure envelopes for fine-grained soils by Burland (1990)

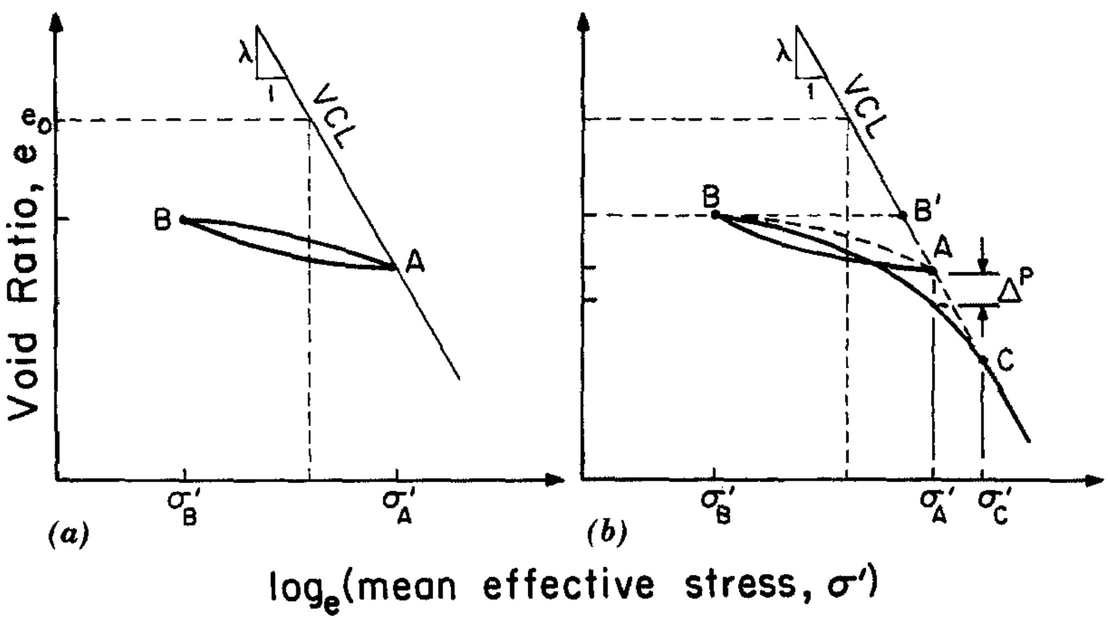

Figure 2-8: Conceptual model of unload-reload used by MIT-E3 for hydrostatic compression: (a) perfect hysteresis; and (b) hysteresis and bounding surface plasticity(Whittle and Kavvadas, 1994)

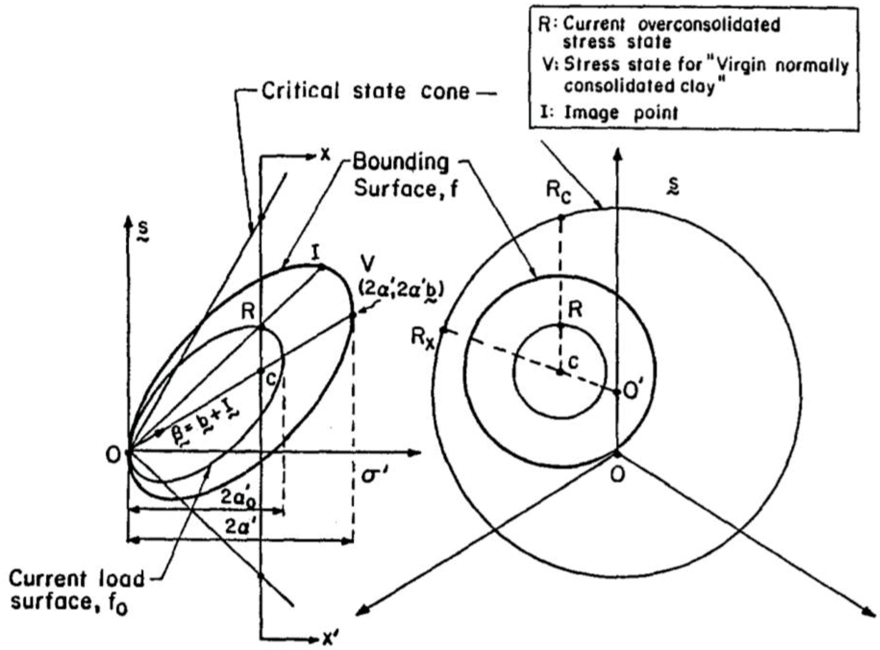

Figure 2-9: Yield, failure and load surfaces used in the MIT-E3 mode (Whittle and Kavvadas, 1994)

3 RESEDIMENTATION AND TEST MATERIALS

3.1 INTRODUCTION

This chapter describes the origin and index properties of the soil types tested as part of this work. It also explains the process of resedimentation and how it is used to produce samples of soils for laboratory testing. Section 3.2 provides background information on Boston Blue Clay, and Gulf of Mexico Eugene Island Clay. These two fine-grained soils are very different in terms of composition, mechanical properties and geologic origin. In addition to being tested as part of this thesis, these soils have been previously investigated to a larger extent by individual researchers. The dissertations of these researchers provide additional information on the geologic origin and techniques in the processing of these soils. They also provide knowledge on the particular aspect of mechanical behavior, which was examined during the course of this investigation.

Resedimentation enables one to produce samples of identical composition from a given source material, free from the blemishes that can be found in individual intact samples. It is an advantageous procedure, as samples can be formed with any desired preconsolidation stress, porosity, or pore fluid salt concentration. This enables an individual to separate out each of these important variables and subject a given material to systematic laboratory investigations; a process which would not be possible with the use of intact samples. More importantly, resedimenting soil samples for laboratory testing overcomes the practical problems of sampling disturbance, and more economically, reduces the cost associated with intact samples (particularly in this case for deep or offshore samples of GOM-EI). The resedimentation technique eliminates sample variability; produces uniform specimens with K_0-consolidation histories, and ensures complete saturation. Resedimentation is therefore, an essential asset in the development and proofing of new laboratory testing equipment, as well as the modification of existing equipment. Section 3.3 describes the process of resedimentation, including a brief background of resedimentation at Tufts University and MIT, the procedure and equipment used as part of this work, an evaluation of sample uniformity, and the procedures involved in intact specimen preparation.

3.2 TEST MATERIALS

3.2.1 Introduction

Table 3-1 presents the origin, liquid limit, plasticity index, specific gravity, and clay fraction - where clay fraction is defined as the percentage of particles with an equivalent diameter < 2 μm as determined by sedimentation (ASTM D422). Liquid limits were determined by either the Casagrande cup method (ASTM D4318) or the fall cone method (BS 1377). The classification of each soil as per the Unified Soil Classification System (USCS) (ASTM D2487) is also provided. In addition, relevant citations for previous investigations by other researchers are included in Table 3-1. Figure 3-1 presents the location of the two soils on the plasticity chart. The particle size distributions of the soils as determined from hydrometer tests (ASTM D422) by previous researchers are shown in Figure 3-2. It can be observed from Figure 3-2 that RBBC, the lower plasticity soil, is comprised of larger sized silt particles, and thus, possesses a lower fraction of clay sized particles than RGOM-EI. This result is consistent with the perception that the Atterberg limits of soils decrease with decreasing clay fraction.

The clay mineralogical compositions of soils investigated in this work are provided in Table 3-2. The mineralogy analyses were carried out by Macaulay Scientific Consulting Ltd. of Aberdeen, U.K. The samples primarily contain quartz, plagioclase, K-feldspar and clay minerals in varying proportions, as well as several other minerals in minor proportions. Table 3-2 shows the percentages of clay minerals determined for the bulk (whole) samples, as well as the relative proportions of these minerals in the < 2 μm fraction of each sample. The bulk samples were wet ground in ethanol and spray dried to produce random powders (Hillier 1999). X-ray powder diffraction (XRPD) patterns were recorded from 2-75° 2θ using Cobalt Kα radiation and quantitative analysis was done by a normalized full pattern reference intensity ratio method. Uncertainty in the concentration of an individual mineral is given within 95 % by ± X0.35, where X = concentration in percent, e.g. 20±2.9 % (Hillier 2003). The < 2 μm fractions were separated from the bulk samples by timed sedimentation. They were then prepared as oriented mounts and scanned from 2-45° 2θ in the air-dried state, after glycolation and after heating to 300°C for one hour. Clay minerals identified were quantified using a mineral intensity factor approach based on calculated XRPD patterns. For clay minerals present in relative amounts > 10 %, uncertainty is estimated as better than ± 5 % at the 95% confidence level (Hillier 2003)

3.2.2 Boston Blue Clay

Natural Boston Blue Clay is a glacio-marine clay of low sensitivity and has a USCS classification of CL (low plasticity clay). It is comprised of glacial outwash deposited in a marine environment about 12,000 to 14,000 years ago, in the period immediately following deglaciation of the Boston basin (Kenney 1964). It exists throughout the Boston area, roughly 9 m below the surface, varying in thickness from 20 to 40 m. A stiff overconsolidated crust (OCR of 2 – 5) forms the upper 12 to 20 m of the deposit, below this, the clay is close to normally consolidated (Santagata 1998). Although the depositional and general characteristics of BBC are; for the most part similar throughout the Boston area, some variability is inevitable for clay samples retrieved from different locations. The index properties of the clay may vary slightly, depending on several factors, including; particle size distribution, pore fluid chemistry and mineralogy. These properties can vary at a given location as a function of depth. Intact samples of BBC were obtained from the construction site of Harvard University's Klarman Hall in Cambridge MA. The pore fluid of natural BBC contains salt which varies in concentration as a function of both location and depth. For this research the pore fluid salt concentration was estimated to be 16 g/l.

Resedimented Boston Blue Clay (RBBC) has been studied extensively at MIT since 1961 (Bailey 1961), and a large database exists on its properties. Its engineering behavior is similar to many other natural uncemented clays, including; low to medium sensitivity, stress-strain behavior, strength anisotropy, significant strain rate dependency and typical consolidation characteristics. Combined with its virtually infinite local supply, it is no surprise that the soil has been an ideal research material for investigating fundamental aspects of soil behavior over the past five decades. Since 1961, several different sources have been used to produce RBBC, with these sources defining different RBBC series. RBBC research referenced in this thesis has come from previous researchers who have studied RBBC from Series IV. Series IV was obtained in 1992 from the base of an excavation for MIT's Biology Building. Approximately 2500 kg of BBC was excavated at a depth of about 12 m where the OCR of the clay varied from 1.3 to 4.3 (Berman 1993). Due to time constraints associated with the early part of this work, and the transition of the laboratory from MIT to Tufts University, RBBC was not used for initial test specimens, as it can takes a month to produce a specimen (see section 3.3).

3.2.3 Gulf of Mexico-Eugene Island Clay

This high plasticity clay originated from the Eugene Island region, located off the coast of Louisiana in the Gulf of Mexico (see Figure 3-3). Resedimented Gulf of Mexico-Eugene Island Clay (RGoM-EI) stemmed from two 10.2 cm cores drilled in the 1990's; specifically, from boreholes A-20 in Block 330 and A-12 in Block 316. In this region, the basin consists of over 4 km of Pliocene and Pleistocene sedimentary fill deposited over a salt-weld. A considerable quantity of core material was abstracted from each borehole at depths ranging from approximately 2200 m to 2500 m. The in situ salinity of the clay at this depth is approximately 80 g/l (Betts 2014). The core material was removed from their individual tubes at the University of Texas at Austin. Hand tools were used to carefully remove the material, and any sandy intervals present in the tubes were discarded. Despite the A-20 core being sealed in wax, most of the core was in a damp to dry condition when it was opened. The clayey material was broken down into fist-sized pieces and evenly distributed on plastic sheeting, and allowed to air-dry for 18 days. It was then roller ground into a fine powder by an external company, to the specification that 99 % should pass through a #100 sieve (nominal diameter of 0.15 mm). Finally, the material was manually blended to produce a homogenous powder, before being stored in 40 gallon drums. RGoM-EI has a high plasticity (w_L = 85.8 %) and a clay fraction of 63 % as determined by sedimentation (Casey 2014). The mineralogical clay fraction was found to be 53.9 %, the dominant clay mineral being smectite. A detailed description of the geologic origin, processing and consolidation behavior of RGOM-EI is given in Betts (2014). Results of a large number of undrained triaxial tests performed on RGoM-EI are provided in Fahy (2014).

3.3 RESEDIMENTATION AND SAMPLE PREPERATION

3.3.1 Introduction

Resedimentation refers to the process of one-dimensionally consolidating a dilute slurry of clay material in a rigid-walled cylindrical container; also known as a consolidometer. Early techniques of resedimentation were developed and performed on BBC at MIT (Ladd and Varallyay 1965). This involved the production of large diameter 'soil cakes' that were subsequently divided into smaller samples for testing. The main flaw associated with this method was that it produced partially saturated clay samples, which could only be saturated using a 200 kPa back-pressure. This became a major concern when RBBC was being used in the directional shear cell by Germaine (1982). Germaine revised and improved upon the original resedimentation technique to produce fully saturated uniform samples, with salt concentrations of approximately 16 g/l. Additional reforms were later introduced by Seah (1990), who modified; the system layout to increase productivity; the technique for extrusion of the soil cake from the consolidometer, and also, implemented a remote data acquisition system to provide continuous monitoring throughout the consolidation process. Abdulhadi (2009) modified the technique further, by preparing individual resedimented samples for each separate test specimen. This approach reduced the cross-sectional area of the consolidometer; therefore, substantially reducing the load that has to be applied to consolidate the specimen to a particular preconsolidation stress. Abdulhadi's technique was particularly beneficial to the process of preparing samples for testing in the higher stress triaxial systems.

3.3.2 Resedimentation Procedure

Abdulhadi's technique of preparing individual resedimented samples for each test specimen was adopted and modified as part of this work. Irrespective of the clay type to be resedimented, the resedimentation procedure remains the same. It can be divided into four main stages: powdering, deposition, consolidation, followed by sample extrusion and preparation. These stages are explained in more detail below.

(i) Powdering

Once the natural material has been abstracted from the field it is shipped to the Tufts Advanced Geomaterials Laboratory. It is then broken up into relatively small clumps (< golf ball) and left to air dry in plastic containers, as shown in Figure 3-4. After air drying the material is ground into a fine power using the industrial disk grinder shown in Figure 3-5. This powder is then blended thoroughly to produce a homogenous mixture and stored in sealed 5 gallon buckets. The procedure of powdering may have differed slightly for the different soils in the laboratory, since the soils were processed by several different researchers during different time periods. Further information on powdering techniques used for different soils can be found in Cauble (1996), Jones (2010), Kontopoulos (2012), Grennan (2010), Betts (2014), and Casey (2014).

(ii) Mixing & Deposition

An Excel spreadsheet is used to determine the individual amounts of clay powder, water and salt required for an individual sample. It calculates these quantities based upon user defined input parameters of final volume, final void ratio, batching water content and salt concentration, of the intended specimen. It is important to note that the salt added at this point is in addition to any already naturally existing salt in the clay powder. This factor is very significant for this work, as the GoM-EI clay powder used had ≈ 14 g/kg natural salt content. This is by far the highest natural salt concentration of any of the materials in the laboratories data base. The spreadsheet also has a factor of safety parameter that accounts for slurry lost throughout the mixing process (i.e. left in the mixing bowl and spatulas etc.). Once the desired mass of clay powder has been calculated, it is thoroughly mixed with calculated amounts of distilled water and sea salt (optional) using an electric blender. This process produces a homogenous slurry of a required pore fluid salt concentration without lumps, as shown in Figure 3-6.

As a rule of thumb the mixing water content is generally taken to approximately equal twice the liquid limit of the soil. This usually results in a workable yet stable slurry with no free surface water present. After mixing, the slurry is left to hydrate over a period of at least 24 hours. Following hydration, the slurry is remixed and then placed in a sealed container and exposed to negative pressure (under > 25 inches Hg) using a vacuum. This process removes any entrapped air that may be present in the mixture. The vacuum pump setup is shown in Figure 3-7, a) and slurry placed under negative pressure is shown in Figure 3-7, b). The container used to vacuum the slurry has two ports, one is connected to the vacuum pump while the second port is used to steadily re-pressurize the container after the process is complete. Post vacuuming, previous researchers used to take the de-aired slurry and carefully tremie it into a pre-prepared consolidometers (see section 3.3.3 Resedimentation Equipment) using a funnel in such a manner, as to minimize entrapment of air bubbles. However, for this work a different approach was adopted for transferring the vacuumed material to the consolidometer, as the author found that the funnel method was not inadequate.

Both Fahy (2014) and Marjanovic (2015) recommended a water content of 120 % for a pore fluid sea-salt concentration of 80g/l to be used on RGoM-EI samples. However, during the early part of this work, the author noticed that there was significant surface water present in the mixture after it had been left to hydrate for 24 hours. This indicated that the slurry was not stable. The batching water content was then reduced from 120 % to 110 % and the slurry was observed to be stable after it had been left hydrate for 24 hours. The new mixture was then observed to be too viscous to flow down the treaming funnel without entrapping air. To eliminate the tremie funnel method altogether the author adopted the use of a modified 0.6 ltr suction gun. This method involved placing the de-aired material into a funnel with the suction gun securely sealed to the spout, as shown in Figure 3-8. The material is then drawn down into the gun under negative pressure to fill it and forced out under pressure into the consolidometer. This method was much more successful, as it produced samples; with no entrapped air; that had a lower water content and hence would take less time to consolidate; and it also has a lower loss factor of slurry associated with it. In the early portion of use, the suction gun parts began to rust from the high salt concentration in the RGoM slurry mixture. The corroded parts, seen in Figure 3-9, had the potential to alter the chemical composition of the slurry, and thus, needed to be replaced. To eliminate the corrosion issue, the author modified the suction gun by replacing all the parts that either corroded or had the potential to corrode, with PVC and stainless steel. Table 3-3 summarizes the water contents and salt concentrations used for resedimenting both soils as part of this work.

(iii) Consolidation

After deposition is complete, a porous stone lined with nylon filter fabric is placed on top of the slurry. Porous stones placed at the top and bottom of the sample allow for double drainage which in turn speeds up the consolidation process. The nylon filter fabric openings are large enough to allow water to permeate through, but small enough to prevent clay particles from passing through. Thus, the nylon filter fabric acts as a barrier that prevents small clay particles from entering and clogging the pores in the porous stones. The specimen is loaded incrementally in the consolidometer using a Load Increment Ratio (LIR) of one. Each load increment is monitored by an external displacement transducer, and maintained until at least the end of primary consolidation, as determined by the root time method. Once the desired maximum vertical stress, i.e. $\sigma'_{v,max}$, has been achieved, the resedimented sample is allowed additional time for, at least, one cycle of secondary compression, before being rebounded to OCR = 4, using a single unload increment. At an OCR = 4, the clay is assumed to be close to isotropic effective stress conditions, i.e. $K_0 \approx 1$. This minimizes the shear strains associated with sample extrusion from the consolidometer, as confirmed by the work of Santagata (1994).

(iv) Extrusion & Preparation

Once the consolidation stage is complete, the sample is extruded from the consolidometer and prepared for triaxial testing. Samples resedimented to below approximately 1 MPa (low stress) can be extruded manually from the consolidometer with moderate effort. These samples are subsequently trimmed to the required diameter for testing using the combination of: a soil sample trimmer stand, a wire saw and a specimen mold. The last portion of trimming is performed with a razor blade to achieve high quality samples of identical volume. A typical sample being trimmed is shown in Figure 3-10. Excess material or trimmings are taken and used for water content measurements. More information on low stress sample preparation can be found in Germaine (2009). Samples resedimented to above 1 MPa (med-high stress) require a hydraulic jack for extrusion. In addition, samples resedimented to above 5 MPa (high stress) are typically not soft enough to be manually trimmed down to a smaller diameter using the standard procedure mentioned above. To overcome this issue, these higher stress samples are resedimented in a consolidometer of the same inside diameter as a triaxial specimen (35.0 mm). This type of resedimented sample only needs to be placed in the specimen mold and have the ends cut off with a wire saw to achieve the required height, while ensuring that the two ends of the specimen are parallel. The pieces sliced off the ends are taken for water content measurements. Finally, the ends of the specimen are smoothed down using a razor blade. This method was only adopted to overcome difficulties in trimming high stress samples. The author believes that trimming the larger diameter lower stress samples removes the film of silicone oil (see Section 3.3.3 below) surrounding the specimen, and hence the material being tested is believed to have no silicone oil in its chemical composition.

3.3.3 Resedimentation Equipment

Traditionally consolidometers used to resediment samples consisted of a smooth acrylic tube, in which the clay consolidated between top and bottom porous stones. PVC tubes were used for this work over traditional acrylic as it was found that at high salinity the salt would react with the acrylic and cause crystallization of the salt. These salt crystals would continuously grow up the acrylic tubes and bases, as shown in Figure 3-11, and reduce the salinity of the pore fluid, causing uncertainty in true pore fluid concentration. This reaction does not occur with the PVC tubes and bases.

Prior to the slurry being added, a thin film of silicon oil is used to lubricate the inside of the tubes in order to reduce friction acting between the tube walls and the consolidating sample. A PVC spacer, topped with a porous stone and nylon filter fabric, is placed at the bottom of the oiled PVC tube. The bottom portion of the tube is then submerged in a PVC bath filled with water of the same salt concentration as the pore fluid of the clay slurry. The basic setup of a consolidometer is illustrated in Figure 3-12. The water level in the bath is filled to the top of the bottom porous stone prior to adding the clay mixture to ensure no air gets trapped between the bottom of the specimen and the outside bath water. Nylon filter fabric is then placed between the deposited clay mixture and the top porous stone. Load is applied to the sample through a top spacer which rests on the top porous stone. Clamps are used to ensure that the entire setup is maintained vertical throughout the consolidation process. During each consolidation increment, axial deformation can be measured using a linear voltage displacement transducer (LVDT) to determine the end of primary consolidation. This monitoring also enables one to gain information on the consolidation properties of a given soil. For the first set of load increments, up until roughly 30 kPa, the load is applied by simply stacking weights on top of the PVC spacer. Upon reaching higher loads, the weights are placed on a hanger which in turn transfers load to the top piston, as shown in Figure 3-12. When the consolidometer is initially set up, the PVC tube rests on the base of the water bath for increased stability. Once reaching the point at which the method of load application is changed to the hanger system, the bottom spacer is replaced with a taller one so that the PVC tube no longer makes contact with the base of the water bath. This allows the sample to vertically strain from both ends (i.e. as is achieved in a floating ring Oedometer), thereby halving the amount of side wall friction experienced by the sample. The hanger system can apply a maximum gross load of 0.7 kN to a given consolidometer. The corresponding stress imposed on the sample is calculated by simply dividing the load applied by the hanger system by the cross-sectional area of the consolidometer. For a 10.87 cm^2 sample (area of a low stress tube), this corresponds to a maximum consolidation stress of roughly 0.7 MPa.

For medium to high stress samples that need to be loaded above 0.7 kN to achieve their desired consolidation stress, the consolidometer is removed from the hanger system and transferred to either a pneumatic actuator or lever arm load frame. This pneumatic actuator, shown in Figure 3-13a, has a maximum capacity of 6.8 kN. For a 10.87 cm2 sample, this corresponds to a maximum consolidation stress of about 6.3 MPa. The lever arm load frame, shown in Figure 3-13b, has a similar maximum capacity to that of the pneumatic actuator. The transfer from the hanger system to the pneumatic actuator or lever arm load frame is performed rapidly to prevent significant swelling of the sample. High stress samples are placed inside a large pneumatic industrial load frame, shown in Figure 3-14. This device has the capacity to apply 80 MPa to a resedimented specimen.

The time required to produce a resedimented sample depends very strongly upon the individual samples coefficient of volume compressibility (m_v) and its hydraulic conductivity (k). These parameters vary for different soils. For example, while a sample of RBBC may require approximately four weeks to reach to 2 MPa (Casey 2014), a sample of RGoM-EI may take approximately 8 weeks to reach the same stress level. This is one of the major reasons why RBBC is favored in laboratory investigations of soil behavior over higher plasticity materials such as RGoM-EI.

3.3.4 Evaluation of Specimen Uniformity

Side wall friction reduces the actual stress imposed upon the soil specimen, it also encourages sample non-uniformity during resedimentation in both the axial and radial directions, and may create a slightly smeared outer layer. Germaine (1982) and Seah (1990) evaluated the uniformity and quality of resedimented samples produced by the larger diameter (30 cm) consolidometers. Uniformity of individual soil cakes was examined by: measuring the variation of water content throughout the sample; utilizing X-ray diffraction pattern methods, and air-drying vertical and radial slices to check for stratification. Results from all these procedures verified that the batches were uniform. However, as mentioned previously in Section 3.3.2., many of the samples resedimented as part of this research have been done so in consolidometers of much smaller internal diameters, i.e.≈ 3.75 cm. These samples have a height to diameter ratio (H/D) of approximately 2.5 at the end of consolidation (in contrast to a H/D of about 0.4 for the large diameter soil cakes that Germaine tested). Therefore, side wall friction acting between the consolidometer tube and the soil specimen has a much larger impact on samples prepared for this research. By allowing the samples to consolidate from both ends, as described in Section 3.3.3, the impact of side wall friction is reduced to some extent.

Casey (2014) compared the virgin compression curve of RBBC measured in a typical CRS test against compression curves exhibited by two RBBC samples that underwent resedimentation in consolidometers to [applied] preconsolidation stresses of 2 and 10 MPa. The results are shown in Figure 3-15. The void ratios for the resedimented samples were calculated based upon the final heights and water contents of the extruded samples, combined with LVDT readings at the end of each load increment. At a given applied stress, the void ratios of the samples in smaller diameter consolidometers are significantly higher than in the CRS test. Casey concluded that this was due to the fact that the stress applied to a sample in a consolidometer only truly acts at the top and bottom of the sample, as side wall friction reduces the applied stress as you move closer to the center. Thus, the void ratio of a resedimented sample is lowest at either end and highest in the middle. Casey averaged the void ratio of the specimen and this averaged value is displayed in Figure 3-15. However, following the SHANSEP reconsolidation procedure (described previously in Chapter 2), the effects of side wall friction, or indeed any other disturbance effects caused by extrusion from the consolidometer, should be effectively eliminated following K_0-consolidation in the triaxial device to stresses twice that of the preconsolidation stress imposed during resedimentation. This ensures that any specimen non-uniformity is eliminated prior to the shearing or unloading phase of a triaxial test.

Abdulhadi (2009) also confirmed this when he compared the consolidation and shear results of two CKOUC tests on RBBC. One specimen was prepared in a 3.45 cm internal diameter consolidometer, while the other was prepared in a 6.35 cm internal diameter consolidometer (actually a modified Oedometer) and then trimmed prior to triaxial testing. The results of the two tests are presented in Figure 3-16 and Figure 3-17 (Abdulhadi refers to the small diameter consolidometer as 'Plexi.' and the larger consolidometer as 'Stnd.'). The two specimens were consolidated to the same target stress (σ'_p = 0.1 MPa) in their respective consolidometers and then K_0-consolidated in the triaxial apparatus to a σ'_p = 0.35 MPa. Figure 3-16 displays the compression curves obtained during the K_0-consolidation phase of both triaxial tests. At 0.35 MPa the two specimens have converged to an almost identical void ratio. However, Abdulhadi did record slightly different values of K_0 and axial strain at this stress. The specimen prepared in the small diameter consolidometer exhibited a compression curve which had a yield stress significantly lower than the preconsolidation stress of 0.1 MPa that was supposedly imposed upon it during resedimentation. Its yield point is also quite difficult to interpret. In addition, the initial void ratio of the specimen is significantly higher than the initial void ratio of the specimen prepared in the larger diameter consolidometer. These observations could reasonably be attributed to a greater impact of side wall friction occurring in the smaller diameter consolidometer. However, as can be seen in Figure 3-17, the stress-strain responses during undrained shearing are approximately identical for the two tests. Both tests have the same strain to peak, undrained strength and shear resistance at large strains. Since the consolidation and shear behavior measured by Abdulhadi (2009) for RBBC at low stresses strongly agrees with results measured by previous researchers, who tested specimens trimmed from large diameter soil cakes, it is concluded that the impact of side wall friction on specimens prepared in small diameter consolidometers has a negligible effect on the shearing behavior, provided the SHANSEP reconsolidation procedure is adopted.

3.3.5 Intact Specimen Preparation

As mentioned earlier, intact samples of BBC were used as substitute for RBBC samples to save time in the earlier parts of this research. The samples were extracted from the Harvard business school campus and were delivered to the TAG Laboratory in late 2015. Prior to testing, the tubes were first x-rayed to identify the level of sample disturbance present (if any).A radiograph of an intact sample of BBC tested as part of this work is shown in Figure 3-18 .The radiograph highlights the presence of sand, stones, layering and internal voids or cracks. Pebbles and stones show up as round clear zones, while voids show up as patches of darkness. Differences in density, or layering is displayed as different color shade changes. Overall, the tubes were determined to have minimum levels of sample disturbance, but many had stones present. Prime sections of the tubes (≈100 mm in length) which had minimal sample disturbance were identified and were marked for cutting using a mechanical cut off saw. Once a section had been removed from the tube, the tube was sealed with wax to preserve it for further use. In an effort to reduce frictional forces between the sample and the side walls of the Shelby tube, piano wire is inserted between the sample and the wall of the tube using a small diameter (just larger than that of the piano wire) hollow rigid tube. The rigid tube is then removed and the piano wire is taughtened using a hand vice grips. The sample tube is then rotated slowly while keeping the piano wire taught against the edge of the tube. This process breaks the skin frictional bonds between the sample and the Shelby tube walls, which in turn reduces the amount of shear imposed on the specimen during the extrusion process. The samples for this work were removed from the Shelby tube sections by hand. Further information on intact sample preparation can be found in Germaine (2009). Once a sample is extruded from the Shelby tube it is prepared in the same manner as the resedimented samples described in Section 3.3.2, (iv).

Table 3-1: Origin, index properties and USCS classification of soils included in this thesis

Soil	Abbreviation	Origin	Contributing researchers	Liquid Limit, W_L (%)	Plasticity Index, I_P (%)	Clay fraction (%)	Specific Gravity	USCS classification
Boston Blue Clay	BBC	Boston, Massachusetts	author, Sheahan (1991), Santagata (1994, 1998), Abdulhadi (2009), Moniz (2009), Horan (2012), Casey (2014)	46.5	22.7	56	2.779	CL
Gulf of Mexico-Eugene Island Clay	GoM-EI	Eugene Island, Gulf of Mexico	author, Betts (2014), Fahy (2014)	85.8	62.9	63	2.775	CH

Table 3-2: Mineralogy of soils included in this thesis. Mineral quantities are quoted as both absolute percentages of the bulk sample by mass, as well as the relative percentages of these minerals in the < 2 μm fraction of each sample. Expandables in the < 2 μm fraction are given as a relative percentage of the mixed-layer illite-smectite

Soil		Chlorite (%)	Kaolinite (%)	Illite (%)	Illite-Smectite (%)	Expandables (%)	Total clay (%)
BBC	Whole sample	6.2	2.9		7.3*	N/A	16.4
	<2 μm fraction	5	2	65	28	5-10	
GoM-EI	Whole sample	0.4	9.1	0.0	44.4	N/A	53.9
	<2 μm fraction	1	4	8	87	70-80	

*includes both illite and mixed layer illite-smectite

^from Di Maio et al. (2004)

Table 3-3: Water contents and salt concentrations at which resedimented samples are mixed to form a slurry

Soil	Mixing water content (%)	Salt content of mixing fluid (g/L)	Natural salt content of powder (g/kg)
BBC	100	16	2.7
GoM-EI	110	80	~ 14

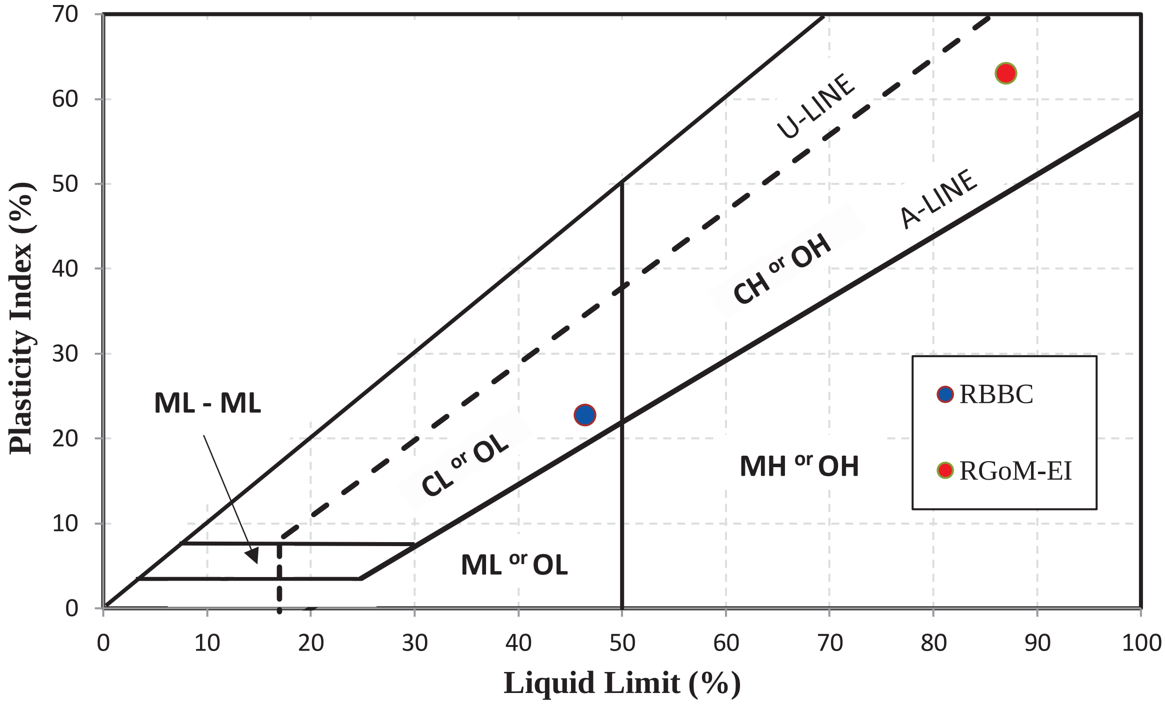

Figure 3-1: Plasticity chart showing the location of soils tested as part of this work

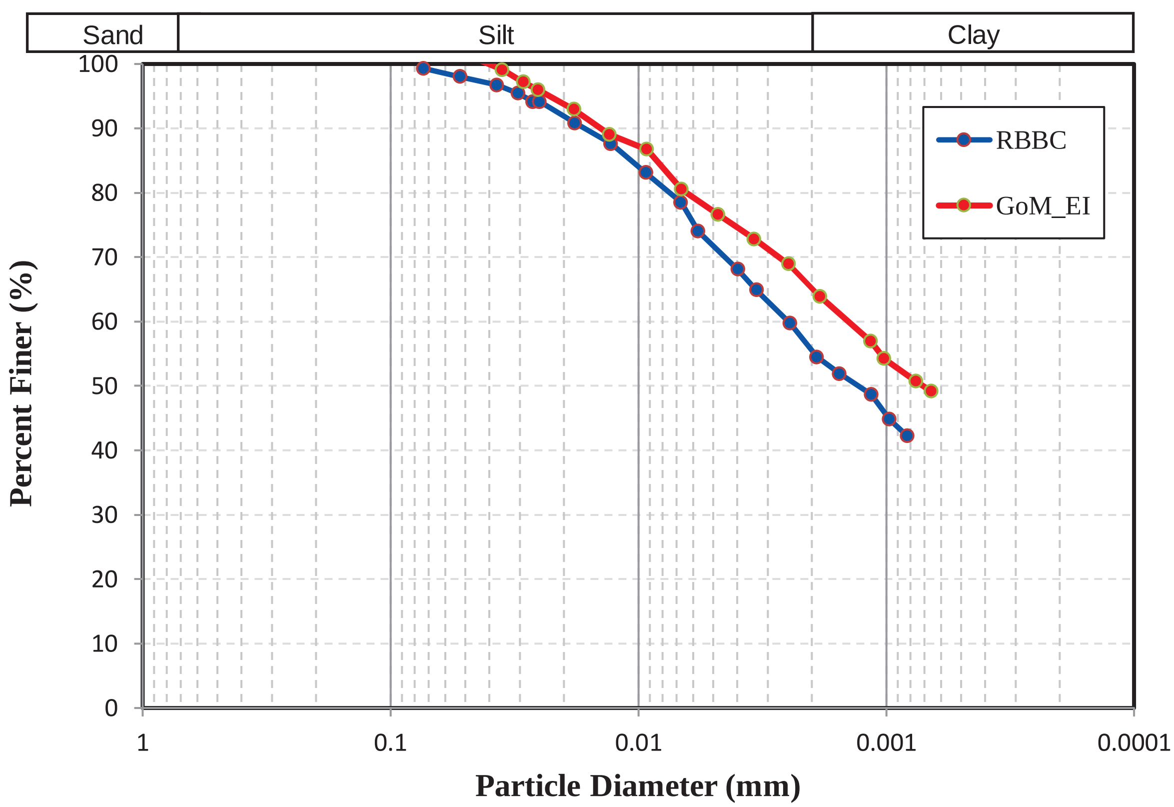

Figure 3-2: Particle size distributions of both soils tested as part of this work as determined from hydrometer tests

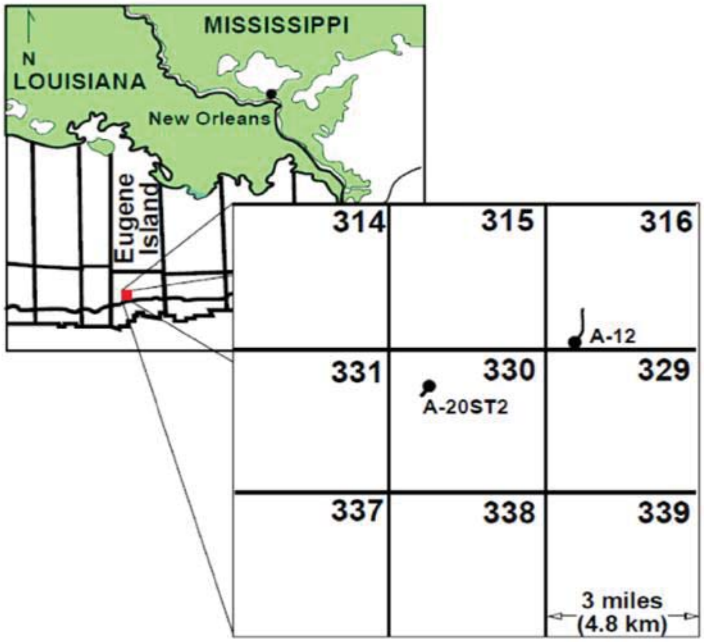

Figure 3-3: Location of boreholes A-12 and A-20 in the Eugene Island region of the Gulf of Mexico (Betts 2014)

Figure 3-4: Broken down raw clay material being left to air dry in large surface area containers

Figure 3-5: Industrial grinder used to grind dried raw clay material into fine clay powder

Figure 3-6: Stable slurry mixture of sea salt, clay powder, and water in a KitchenAid blender

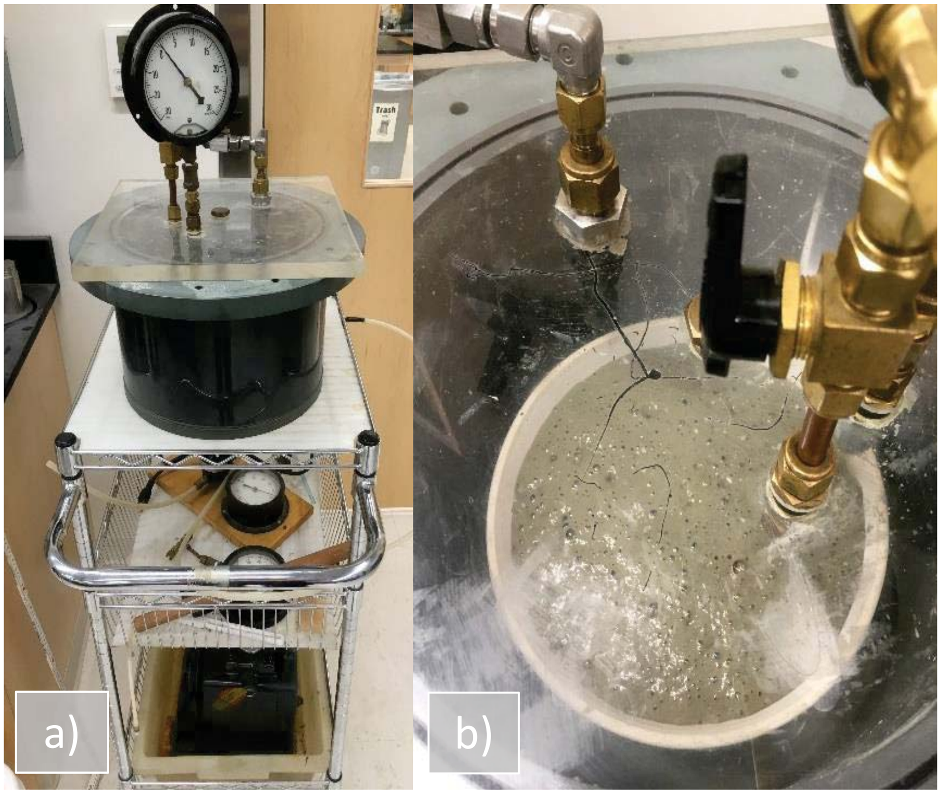

Figure 3-7: a). Vacuum pump system used to de-air slurry. b). Slurry under negative pressure inside sealed container

Figure 3-8: Filling of the suction gun with de-aired slurry

Figure 3-9: Corroded parts of the original suction gun

Figure 3-10: Resedimented specimen in the final stages of trimming with a razor blade

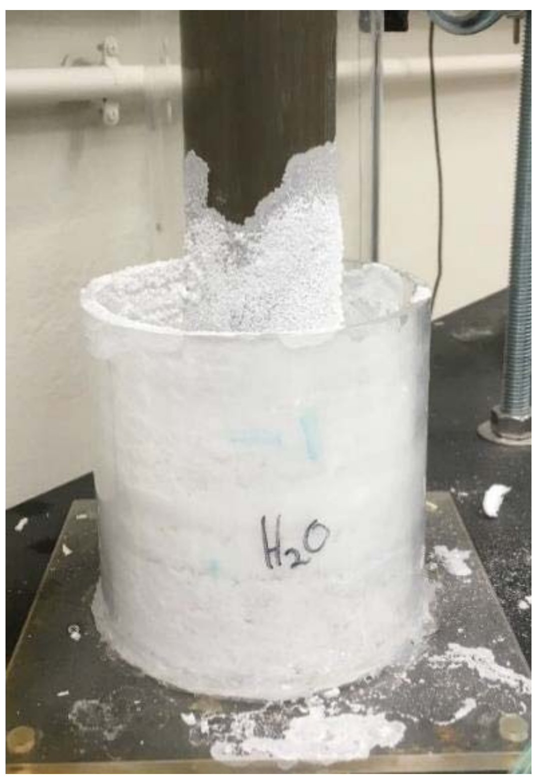

Figure 3-11: Salt crystallization on the acrylic resedimentation tube and base as a result of high salinity pore fluid concentration

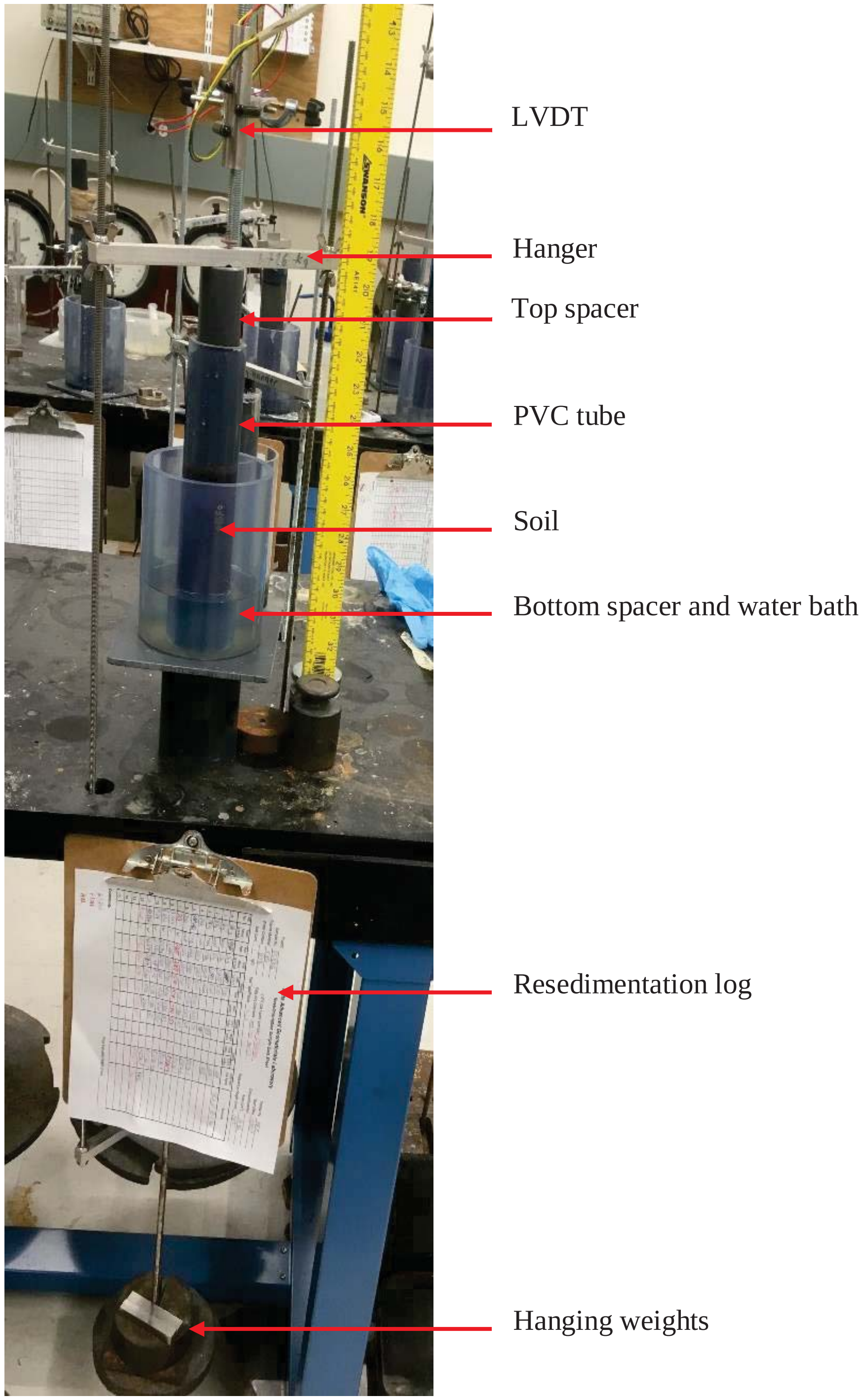

Figure 3-12: Setup of consolidometer with hanger system

Figure 3-13: a). Pneumatic actuator. b). Lever arm load frame. Both used to resediment samples to 6 MPa

Figure 3-14: High stress pneumatic load frame used for resedimenting specimens

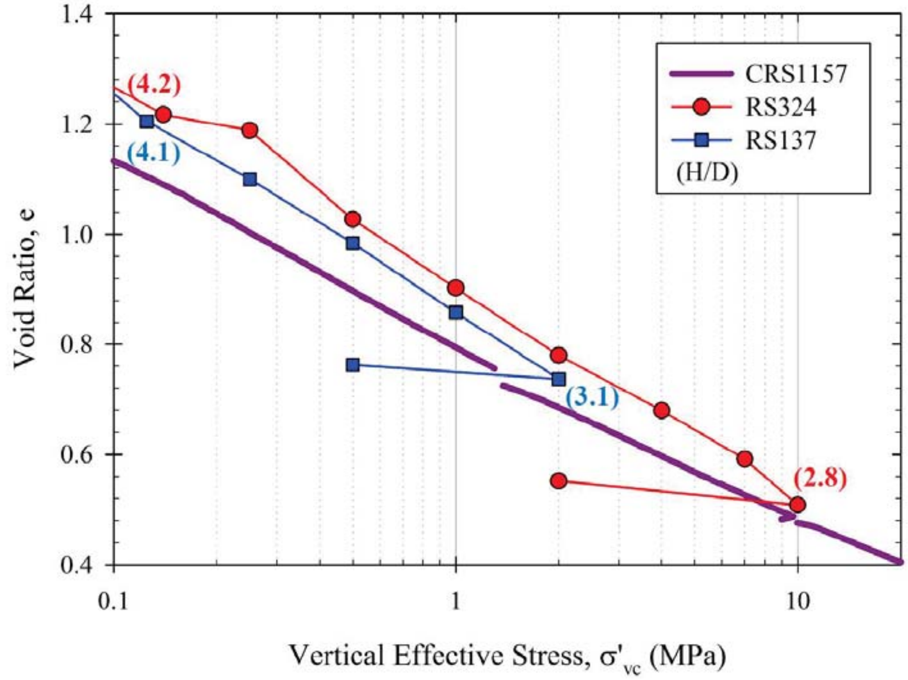

Figure 3-15: Comparison of virgin compression curves for RBBC as measured in a typical CRS test and during resedimentation in consolidometers. (Casey 2014)

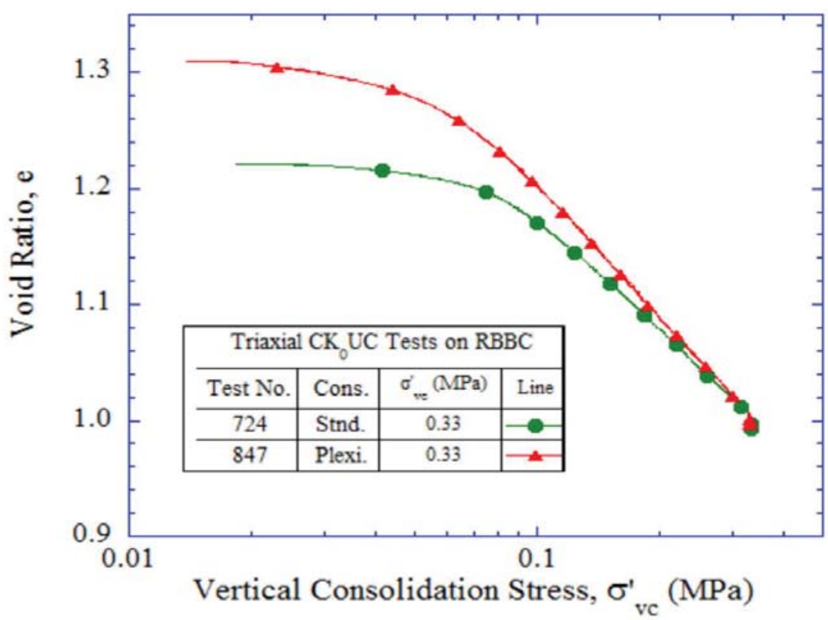

Figure 3-16: Comparison of compression behaviours measured during the K_0-consolidation phase of triaxial tests for RBBC samples prepared in 3.45 cm diameter ('Plexi.') and 6.35 cm diameter consolidometers ('stnd.') (Abdulhadi 2009)

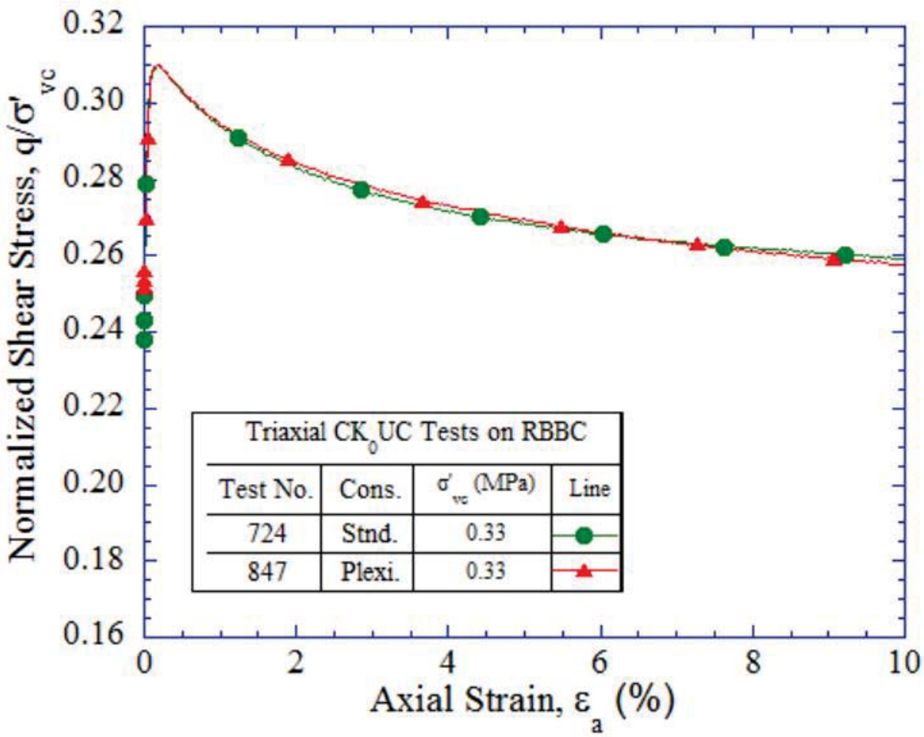

Figure 3-17: Comparison of shear stress-strain responses measured during the undrained shear phase of triaxial tests for RBBC samples prepaired in 3.45 cm diameter ('Plexi.') and 6.35 cm diameter consolidometers ('stnd.') (Abdulhadi 2009)

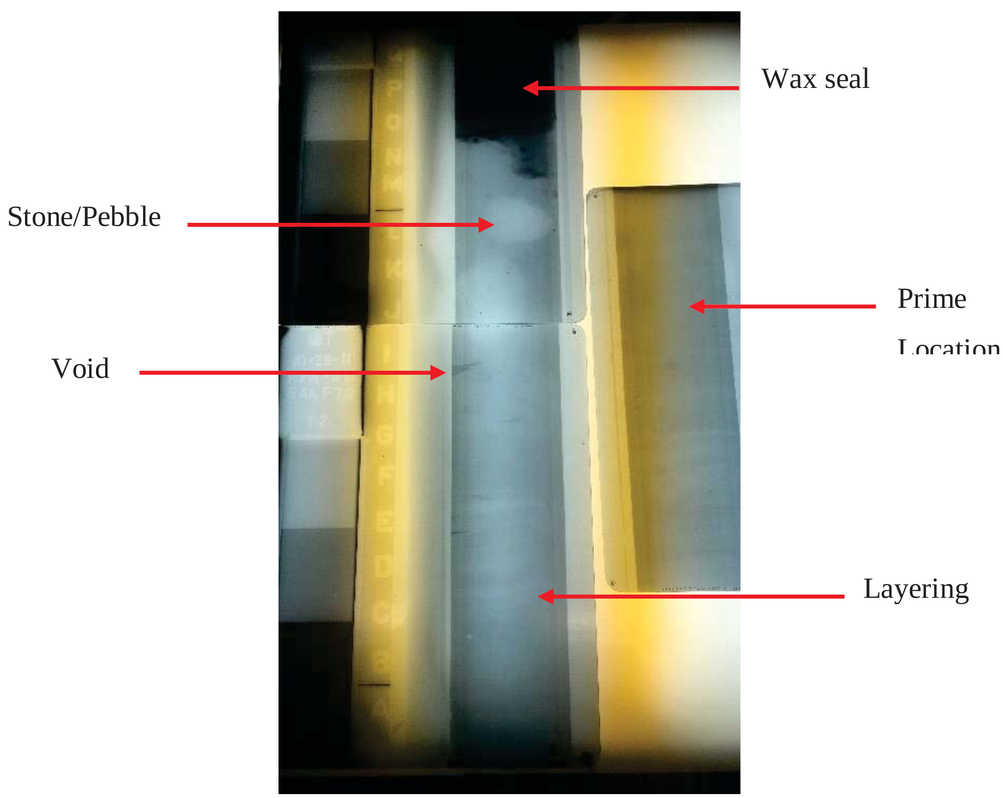

Figure 3-18: Radiograph of intact BBC sample tested as part of this research

4 EQUIPMENT AND PROCEDURES

4.1 INTRODUCTION

This chapter describes the equipment and procedures incorporated as part of this work. It involved fine-grained specimens being consolidated to two different orders of magnitudes of effective stresses. A single triaxial system could not successfully test specimens over this stress range, this is due to accuracy and range constraints of individual transducers. There are three different automated triaxial systems in the TAG laboratory, designed for; low, medium, and high stresses. All three triaxial systems were designed and fabricated within the MIT Geotechnical Engineering Laboratory. Section 4.2 describes the triaxial systems used in this work. It also provides a detailed discussion of the triaxial cells themselves, end platen design, pressure volume actuators (PVAs), automated control systems and data acquisition. Section 4.3 evaluates the reproducibility and reliability of test results obtained using both types of triaxial system. It also investigates apparatus compressibility in relation to system stiffness. The procedures followed in the testing program are described in detail in Section 4.4.

4.2 TRIAXIAL EQUIPMENT

4.2.1 Overview of Triaxial Systems

In order to characterize the shape of the yield surface for fine-grained sediments over an order of magnitude of consolidation stress, two different automated triaxial systems were used. To achieve a consistent degree of resolution throughout a testing program, a reduction in magnitude of a triaxial system capacity must coincide with a corresponding increase in the precision of both load/pressure application and test variable measurements. Essentially, anticipated material properties must be matched with testing device capacity. The low pressure system was used for tests where specimens were to be consolidated to a maximum σ'_p of 1 MPa. The medium pressure system was used for tests where specimens were to be consolidated to a maximum σ'_p of 10 MPa. Sheahan (1991) made significant contributions to the design of the low pressure system, which has been progressively improved upon over the past two decades. The medium pressure system was first developed by Anderson (1991) for the testing of frozen sand. It was then modified for the testing of fine-grained materials by Abdulhadi (2009).

Figure 4-1 shows the components associated with a typical low pressure triaxial system, though the general configuration is the same for both systems. Both systems consist of the following: a triaxial cell to act as a sealed chamber, a load frame to apply axial load, pressure volume-actuators (PVAs) to provide cell, back, and in the case of the medium stress system-load frame pressures, a control box containing servoamplifiers, a power supply for the transducers, a computer to run the necessary control software and provide real-time readouts of the test data, and a central data acquisition system to record the test data. The triaxial cell, load frame and PVAs are located inside a temperature controlled enclosure, in which the temperature can be maintained to within ± 0.5˚C.

4.2.2 Triaxial Cells

Both the low and medium stress triaxial cells test a standard sized specimen of approximately 3.50 cm diameter and 8.13 cm height. In both stress systems, PVA's are used to control the cell and back pressures. Changes in volume of the specimen are computed from LVDT's monitoring the motion of the back pressure PVA (see Section 4.3.2). Specimens are subjected to top and bottom drainage to accelerate the consolidation process. Porous stones are located at the top and bottom of the specimen to facilitate drainage and measurement of pore pressures. Axial strain is measured externally on all cells by means of a displacement transducer. Axial force is measured by means of an internal load cell. All pressures are measured using externally mounted pressure transducers.

The low pressure cell uses a transparent 6 mm acrylic cell wall to constrain a maximum internal cell pressure of 1.5 MPa. Figure 4-2 shows a schematic of a typical low stress cell and Figure 4-3 shows a photograph of the low stress apparatus used in this work. Both the cell and back pressures are monitored with high performance diaphragm type (200 psi [1.4 MPa] capacity) pressure transducers, located on the base of the cell. The internal load cell is connected to a piston which is restricted to vertical movement only, through a low friction, linear bearing with O-ring seal. The top cap is securely fixed to the load cell which allows a negative deviator load to be applied to the specimen, thereby making it possible to perform triaxial extension tests. The top drainage line is made of coiled flexible nylon tubing which enables sufficient axial strains during the consolidation and shearing stages. The entire system is axially loaded using a 1 Tonne [9.8 kN] capacity benchtop Wykeham Ferrance screw driven loading frame with adjustable gear ratios.

The medium pressure cell requires a 10 mm carbon steel cell wall to withstand the internal cell pressure of 12 MPA. It is zinc-plated to prevent corrosion. Figure 4-4 shows a schematic of the medium pressure triaxial chamber and Figure 4-5 shows a section view of the apparatus. The triaxial chamber encloses the soil specimen, base pedestal, floating top cap, top and bottom drainage lines, and an internal shear-beam load cell. Because the top cap is not fixed to the load cell, an alignment cap is placed between the load cell and top cap. The alignment cap is securely attached to the load cell, but merely rests upon the floating top cap, with an O-ring seal around the edges. The void left between the alignment cap and the top cap is vented to the atmosphere, which creates a pressure gradient that essentially fixes the top cap. The axial load is applied to the specimen via a 25 mm diameter hardened steel piston which enters the top of the chamber through a double O-ring seal. The entire system is axially loaded through the use of a 2 Tonne [19.6 kN] capacity benchtop Mossco-Oslo (Type TP-2) screw driven loading frame. Due to higher cell pressures, the top drainage line is made of copper tubing to minimize system compliance, it is also coiled to increase flexibility and enable sufficient axial strains during consolidation and shearing (Figure 4-4). The assembly of the medium pressure triaxial cell requires the top back pressure drainage line to be disconnected prior to each test. After re-connecting the lines, they have to be saturated by applying vacuum to remove the air and then flushed with water. The cell and pore pressures are measured using 1,000 psi [7 MPa] capacity diaphragm type pressure transducers.

In both triaxial systems, cell pressure is applied to the specimen using low viscosity silicone oil (Dow-Corning® 200 fluid, 20 centistokes). This type of silicone oil is; optically transparent, nonconductive, non-toxic, and chemically inert. It exhibits extremely low viscosity under a wide range of temperatures and does not degrade the seals or latex membranes used in testing. Silicon oil is used instead of water because, unlike water, it does not permeate through latex membranes over long periods of testing (Bellwald, 1990). Because it is electrically non-conductive, it allows electronic devices such as a load cell or displacement transducer to be located inside the cell chamber. The latex membranes used to seal the soil specimen from the silicon oil are different for each triaxial cell. Unlubricated latex condoms are used in the low pressure cell due to their high reliability, but have been found to leak at pressures above about 3 MPa (Abdulhadi, 2009). Two commercial latex membranes of 0.30 mm thickness are placed over an unlubricated latex condom in the medium pressure cell. Vacuum greased O-rings are used in both triaxial cells to seal the latex membranes to the base pedestal and top cap.

The two cells possess electrical feed-through connections located at the base to allow for the use of an internal load cell as well as on-specimen displacement transducers. Internal displacement transducers were not used in this work. An internal load cell eliminates the effect of piston seal friction, allowing for accurate measurement of true deviator load applied to the specimen. In low and medium cells, Honeywell® 'S-beam' type load cells of 2.2 kN [500 lb] and 8.9 kN [2000 lb] capacity are used, respectively. These internal load cells should ideally have a voltage output that is unaffected by cell fluid pressure. Casey (2014) investigated this aspect for the low stress cell by varying cell pressure while keeping the true deviator load acting on the load cell constant. Figure 4-6 plots the effect of varying cell pressure on the output of the low stress 2.2 kN load cell. The cell pressure was varied between 0-10 MPa for three consecutive cycles, while the applied deviator load was kept at a constant value of zero (the initial reading of -1 N for the first loading cycle is due to submersion of the load cell in silicon oil). There is a slight hysteretic effect within each cycle and the recorded output between cycles is non-repeatable. However, the hysteretic effect induced by the cell pressure only varies the output of the load cell by < 2 N (corresponding to < 0.1 % of its capacity) over the entire 10 MPa cell pressure range. This is regarded as a negligible amount in comparison to the shear strength of soil specimens. It was therefore ignored in the analysis if the results in this work. In addition, since the 8.9 kN load cell is of the same type and manufacturer, it was assumed to have a similarly negligible sensitivity to cell pressure (even assuming a calibration factor 4 times that of the 2.2 kN load cell).

4.2.3 End Platens

The two systems possess a standard type end platen configuration with a base pedestal and top cap of the same diameter as the specimen. Carborundum porous stones of 5 mm thickness are placed in contact with the base pedestal and top cap. Nylon filter paper is placed between the porous stones and the soil specimen. A thick 0.5 mm commercial latex sleeve is placed around the pedestals, porous stones and extremities of the soil specimen as shown in Figure 4-7. This prevents the edges of the porous stones from tearing the thin latex membranes that surround the specimen, while also providing additional alignment stability for the specimen throughout the test assembly process. This type of end platen configuration is considered 'fixed' because it prevents radial displacement of the specimen at the top and bottom interfaces. It results in non-uniform stresses and strains being developed throughout the shearing phase of a triaxial test. However, Casey (2014) compared the fixed end configuration to a smooth end plate configuration and concluded that the fixed end plate design did not have significant impacts upon test results. Internal drainage lines in the base pedestal and top cap allow for pore fluid flow and pressure measurement.

4.2.4 Pressure Volume Actuators

Custom-built PVAs are used to generate the required cell and back pressures for each system. The PVA design consists of a pressure chamber containing either silicon oil or salt water (depending on use); one end of the chamber is connected to the triaxial cell base and external reservoir via Swagelok valve. The opposite end of the chamber is connected to a moving piston which in turn, controls the pressure in the chamber. This type of PVA has been used in the MIT Geotechnical Engineering Laboratory for many years for a variety of test systems, including triaxial, constant rate of strain (CRS) and flow-through permeability. This type of PVA has a maximum pressure capacity of 14 MPa and a volume capacity of 47 cm^3. It is also versatile and compact, which enables it to be placed inside the temperature control enclosure. The PVAs accommodate a 0.5-ton Duff-Norton® inverted ball screw jack, which can be driven by a Maxon

Motors® servomotor with 80 mNm continuous output (geared at 84:1). PVAs are fitted with limit switches, which shut off the power to the servomotor to prevent damage in the case of the piston running out of stroke within the chamber. Figure 4-8- shows a schematic of the high capacity pressure-volume controller.

4.2.5 Control System

The low and medium pressure triaxial systems are automated using control hardware and software that was originally developed by Sheahan (1991). Measurement of test variables, such as force, pressure, and displacement is performed by transducers located both inside and outside the triaxial cell. The continuous analogue output from each transducer is converted to a digital signal using a multichannel analogue-to-digital converter (MADC) device, located within each systems local computer system. The computer operates a control program written in QBASIC that is capable of performing all aspects of a triaxial testing. This includes: initial pressure-up, back pressure saturation, B-value check, consolidation (K_0 or stress path), and shearing (drained or undrained). The program compares the actual output measurements from the transducers with the time-dependent target values and automatically calculates the command signal required to reduce the difference between the two values. This command signal is converted back into an analog signal through a digital to analog (D/A) converter board that is located within the computer. The computer displays real time output readings of all transducers along with associated command signals on its monitor. The monitor also displays the stage at which the test is operating at. From the D/A card, the analog command signals are sent through an external control box via electric pulses to the electric motor, thus completing control loop. This allows for continuous and very precise control of cell pressure, pore pressure, and axial load throughout the testing period. The control box allows the user to manually adjust each motor in the system. An image of the computer system containing the MADC device and the control box is shown in Figure 4-9. Figure 4-10 shows individual components located inside the interior of the control box. A more detailed description of the control system can be found in Abdulhadi (2009).

4.2.6 Data Acquisition

The control system described above incorporates two data acquisition systems: a central system used to record data from every operating system in the laboratory for subsequent analysis, and a local one for each individual system based around the MADC device. A key component for the MADC device is the Analog Devices® AD1170 analogue-to-digital converter. The AD1170 is a high resolution, integration-type converter which allows for user specified integration times (from 1 to 350 ms) and a maximum resolution of 22 bits. At a 10 V scale (±5 V), this corresponds to a maximum precision of 0.0024 mV. The maximum output of both pressure transducers and load cells is typically in the range of 2–150 mV. These values are too small and require amplification to provide accurate readings for closed loop feedback control of the system. This is achieved by using a channel specific AD624 instrumentation amplifier which amplifies the output signal by a factor of 10, 100, or 1000 prior to digital conversion, thereby increasing the precision to 0.00024 mV, 0.000024 mV, or 0.0000024 mV respectively. This is more than sufficient to provide accurate readings for closed loop feedback control of the system. The high degree of signal averaging provided by the integration-type AD1170 converter reduces noise from the input signal and thus provides stable readings of test variables.

The central data acquisition system present in the TAG Laboratory is based around a Hewlett Packard HP3497A data acquisition unit interfaced with a desktop computer. This system incorporates an integration-type analogue-to-digital converter combined with auto-ranging signal amplification to four voltages scales; 0.1, 1, 10, 100 V. This auto-ranging capability removes the need for any amplification of analogue input signals. The central system is not used for feedback control of any testing equipment; therefore, it is not necessary for its resolution to be as high as that of the MADC device. The system is capable of monitoring recording 254 channels simultaneously at a maximum rate of 1 Hz.

Table 4-1 summarizes the precision of both the central data acquisition system and the MADC device (in engineering values and voltages) for both triaxial systems, as well as the corresponding resolutions for each device. For axial displacements and specimen volume, resolutions are based on specimen dimensions. For cell pressure, pore pressure and load cell force, resolutions are based on the maximum range of the transducer during a typical test. To achieve a comparable degree of resolution across each triaxial system, axial load, cell pressure and pore pressure must be measured with far greater precision when testing at lower stresses. In reality, the MADC device is capable of performing analogue-to-digital conversion with greater precision than measurements can be taken using commercially available displacement and pressure transducers. As a result, the resolution of test variables may be controlled by the transducers used, and would be lower than the values quoted in Table 4-1.

4.3 EVALUATION OF TRIAXIAL EQUIPMENT

4.3.1 Introduction

It is important to demonstrate that reproducible test results can be obtained using the different triaxial systems. This is necessary to ensure that observed trends in soil properties are not being influenced by the testing equipment, and that any measured variations in strength with increasing stress level, reflect true soil behavior. Previous work has been done to demonstrate reproducibility of tests performed on samples of the same composition, under the same test conditions, across all three stress level systems. The resedimentation technique has proven ideal for this purpose as it can produce identical saturated samples consolidated to any desired preconsolidation stress. However, no attempt was made to investigate the effects of consolidation rates on the development of pore pressure in the sample in each system. This section briefly describes the previous work done on samples of RBBC, and evaluates work done as part of this research on samples of RGoM-EI. It also investigates the effects of apparatus compressibility on each system.

4.3.2 Consolidation

Casey (2014) compared the compression behavior of RBBC determined from the K_0-consolidation phase of different triaxial systems to the compression behavior as determined from a CRS test. Figure 4-11 shows the virgin compression behavior of the soil from 0.1 MPa up to 100 MPa, and includes two medium and high pressure systems tests performed by Casey, as well as a test performed with the low pressure system by Abdulhadi (2009). Casey concluded that each of the tests followed a unique virgin compression curve and that there was excellent agreement between the compression behavior determined using the CRS device and using each of the triaxial systems. He observed that the compression index (Cc) of the soil decreased with increasing stress level, from about 0.35 in the 0.1–1 MPa stress range, to 0.33 in the range of 1–10 MPa, to 0.23 in the range of 10–40 MPa. He also observed a change in the value of $K_{0,\,NC}$ during consolidation for all the materials tested, as shown in Figure 4-12. All the clay materials Casey tested exhibited a trend of increasing $K_{0,\,NC}$ with increasing confining pressure. The results of medium stress triaxial tests carried out as part of this research, and that of Abdulhadi (2009) also show a consistent increase in $K_{0,\,NC}$ of RGoM-EI, from~0.62 at 1 MPa to~0.8 at 10 MPa, and of RBBC from~0.51 at 0.1 MPa to 0.60 at 100 MPa.

The appropriate axial strain rate to be used is dependent upon the permeability of the soil, with low permeability soils requiring much slower rates to prevent large excess pore pressures from developing within the specimen. Casey (2014) recommends 0.15 %/hr is sufficiently slow for RBBC, based on CRS data results. However, he applied this axial strain rate to all the clay types tested as part of his research. The applicability of applying this strain rate to RGoM-EI samples was investigated in both the low and medium stress apparatuses as part of this research. This topic is discussed in more detail in section 5.5 verification of consolidation test results.

4.3.3 Apparatus Compressibility

Extensive research has been done on the effects of apparatus compressibility, particularly during the undrained shearing process. Drainage lines, valves and the pore water contained within them necessarily involve a finite compressibility that alters the excess pore pressure generated in a specimen from its true value, since some amount of pore fluid must inevitably drain from the specimen into the drainage lines when the pore pressure increases (Wissa 1969, Bishop 1976). Casey (2014) investigated this over all three stress ranges and concluded that the effect of apparatus compressibility during undrained shearing had a larger influence at higher stresses. He also concluded that this effect lowers the achievable Skempton's B-Value (i.e., it becomes impossible to achieve a B-value greater that 90% above 30 MPa). Since drained tests were used as part of this research, and the confining stresses were never greater than 10 MPa, the effect of apparatus compressibility due to induced pore pressures was neglected as part of this work.

Both the effect of increasing cell pressure and increasing axial load on axial strain apparatus compressibility were analyzed as part of this work. This was done in both low and medium triaxial cells by replacing the clay specimen with a solid steel specimen of similar dimensions, and recording the change in axial strain as the two quantiles were independently varied. In the first case the cell pressure was varied from 0 MPa to the individual apparatuses safe maximum cell pressure capacity, while the deviator load being applied the specimen was kept constant. Figure 4-13 corresponds to the cell pressure in the low stress cell being varied between 0–1.3 MPa, while the applied deviator stress was kept relatively constant at 17.9 kPa. The graph consists of an unload cycle, followed by a complete load and unload cycle. At a maximum cell pressure of 1.3 MPa, the system is recording a corresponding axial strain of ≈ 0.15% strain. Thus, it can be concluded that increasing cell pressure has a significant effect on apparatus compressibility in the low stress cell. There is a clear hysteresis present in the data that appears to be repeatable, thus a linear regression would be the best approximation for this.

Figure 4-14 plots to two separate cycles of axial strain against deviatoric load in the low stress cell being varied between 0–0.6 kN and 0–1.2 kN, while the cell pressure was being held constant at 0.29 MPa (this was an arbitrary value). Between the two loadings the testing apparatus was disassembled and reassembled to mimic two separate tests being performed. There appears to be an initial non-linear loading trend up to ~ 0.15 kN, which has an associated strain of ~ 0.08%. After this, the loading trend becomes more linear with increasing deviatoric load. After the first unloading phase has occurred, there is a clear hysteresis that is somewhat repeatable between loading and unloading cycles. However, the hysteresis from both tests do not trace each other, and appear to be dependent upon the deviatoric load applied. Increasing deviatoric load imposes an increasing associated permanent axial strain. For both tests, permanent axial strains of 0.05 and

0.075 % are observed from the first unload cycle. It is assumed that this is due to misalignments in connections between individual components of both the triaxial cell and load frame reaching equilibrium in compression. Comparing the initial loading of both tests to the hysteresis observed, it is concluded that there is a 0.04 % axial strain (based on a standard sized specimen) apparatus compressibility effect from the system reaching equilibrium after assembly. After reaching equilibrium the apparatus experiences ~0.12 % axial strain apparatus compressibility in loading to 1.2 kN. Even though the two hysteresis loops do not trace each other, the associated error is minimal (~ 0.02%), thus a linear regression is acceptable can be used to account for apparatus compressibility due to the deviatoric load effect.

Two displacement transducers, placed at separate locations, were used to monitor the axial strain and check for uniform deformations of the medium pressure device. Figure 4-15 shows the effect of the cell pressure being varied from 0–10 MPa on the recorded axial strain in both displacement transducers. The deviatoric load on the specimen was kept constant at 0.36 kN (this was an arbitrary value) throughout the test. There is a clear reproducible hysteresis present, and there are uniform deformations for cell pressures up to ~5 MPa. Above 5 MPa the cycles begin to deviate, indicating that the cell may be undergoing non-uniform deformations at higher stresses. Increasing cell pressure has a very significant impact on axial strain apparatus compressibility; at a maximum cell pressure of 10 MPa the system is recording a corresponding axial strain of ~0.7 % strain. The hysteresis effect caused by increase in cell pressure can be approximated by a linear regression function.

A similar approach was used when varying the deviator load in the cell while keeping the cell fluid at a constant value of 1 MPa (this was an arbitrary value). The deviator load was varied between 0–3.1 kN for two complete cycles, while the axial strain was monitored at opposite sides of the loading piston. The cell was then disassembled and resembled to mimic actual procedures, and the test was repeated three more times. Figure 4-16 plots the results of these tests, the circular and triangular data points represent opposite sides of the loading piston, and each trial is color coded (i.e. green circular and triangle points make up one trial). There results show that there is non-uniform straining taking place, it appears that the piston is not remaining vertically aligned as the applied load increases. This would suggest the piston is inducing additional shear stressed in the sample. Each test produces a different offset hysteresis loop. The strain recorded by the apparatus varies dramatically depending on where the transducer is placed. At a deviatoric load of 3 kN the axial strain recorded by the device could be recorded as 0.1% or 0.28% (blue data points), depending on the position of the displacement transducer. Some hysteresis loops appear to be reproducible, producing low strains~0.1% for 3 kN deviatoric load. However, the majority of loops are offset from each other and vary up to 0.38% axial strain for 3kN deviatoric load. Therefore no trend can be correctly established.

It is important to note that these apparatus compressibility tests were run in the latter part of this research, when the author became concerned about apparatus compressibility in the medium stress cell. As a result, all data presented in this thesis have not been corrected for this newly established apparatus compressibility. For future work, the author recommends that the triaxial control program be modified to account for these additional strains and that the medium stress cell be remediated to eliminate the piston loading alignment issue.

4.4 TESTING PROCEDURES

This section describes the procedures for setting up and performing tests in the low and medium triaxial systems. Test specimens are prepared using the resedimentation process, as described in Chapter 3. Prior to inserting the specimen, the base pedestal and top cap of both systems needs to be prepared. Both systems require a thorough cleaning of the top and base pedestals to remove any grit/residue left behind from the previous test. After cleaning, a light film of vacuum grease is applied to the sides of the top cap and base pedestal, to help form the seal with the latex membrane. The 0.5 mm thick protector latex strip (as discussed in Section 4.2.3) is then applied to both platens. Half the strip surrounds the platen, while the other forms a recess for the porous stone to sit in. Both systems require 6 O-rings to fulfill the design seal criterion. All O-rings are cleaned and lightly coated with vacuum grease prior to every test. The specimen preparation is essentially the same for both test types. The resedimented specimen is extruded from its consolidometer and trimmed (Chapter 3). Its dimensions are measured with a caliper and recorded to calculate specimen area and volume. Moist nylon filter fabric pieces, of the same diameter as the specimen are placed over the top and bottom of the specimen to complete the setup preparation.

The assembly procedure varies slightly between the low and medium stress apparatuses, but the finished assemblies are similar. Figure 4-17 shows a cross-section schematic of a typical medium stress specimen. The cross-section of a low stress specimen is similar, with the exception that it has two membranes instead of three. The preparation of the low stress involves, first placing a moist porous stone into the recess created from the thicker latex strip. A thin unlubricated, unrolled latex condom (with the tip cut off) is then placed around the lower part of the base platen, and rolled up to just below the porous stone. Two O-rings are then placed over the latex, around the base platen. A second unrolled condom is placed below the two O-rings, and then rolled out over the two O-rings to a position just below the first membrane. A third O-ring is placed outside the second membrane in between the first two O-rings. The remaining three O-rings are placed around a split piece O-ring stretcher, and the stretcher is placed around the lower part of the base pedestal. The prepared specimen is then placed on the moist porous stone which is now confined within the recess of the thick latex sleeve and triaxial cell base pedestal. A second porous stone is placed on top of the specimen and the top cap is gently lowered down to meet the specimen. The output reading of the load cell is closely monitored during this process to ensure no additional load is placed on the specimen. The first internal membrane is then rolled up the specimen, the O-ring stretcher is raised up, and two O-ring seals are removed to seal the inner membrane against the top cap. The second outer membrane is then rolled up over the top two O-rings and sealed with the third remaining O-ring on the stretcher. The split ring then splits into two separate pieces and is removed. After this, the cell is assembled and secured into the load frame for testing.

The set up for the medium stress cell is similar to the low stress, with the exception that three membranes (1-thin, 2-thick, see Figure 4-17) were used, and applied using a different technique. Only one thin membrane is applied to the base platen, and it is not immediately sealed with two O-rings. The prepared specimen is placed on the moist porous stone and the prepared floating top cap and second porous stone are placed on top of the specimen. A custom-built positioner holds the floating top cap in the correct position throughout the setup procedure. Filter paper strips may now be placed around the specimen to speed up the rate of consolidation for soils having low values of cv. Filter paper strips were used when testing RGoM-EI samples as part of this research. The first thin latex membrane is then rolled up the specimen and around the top cap. The second (first thick) membrane is placed over the specimen using a membrane stretcher connected to a vacuum. Four O-rings are then placed over the two membranes, two around bottom pedestal and two around the top cap. The third (outer thick) membrane is then placed in the same way. Two O-rings (one top one bottom) are positioned outside the outer membrane, but in between the first two O-rings, as shown in Figure 4-17. The top drainage line, which spirals around the specimen, is then connected to the cell base and top cap. The custom-built positioner is now removed and the steel cell chamber is placed in position using a wall-mounted gantry crane. The cell is then bolted together, in place, on the load frame. The zero value of the load cell is recorded and the load cell is then slowly brought into contact with the top cap (similar to the low tress system). The piston is then fixed into place by assembling the load frame.

Following assembly, both systems are filled with silicone oil via an air pressurized reservoir. Once filled, the cell oil is pressurized slightly to prevent the specimen from swelling. In the low stress system, this is done with the back-pressure valves closed (as the lines are already saturated) to generate positive pore pressure in the specimen before commencement of the saturation process. The cell is typically pressurized to a value equal to the rebound pressure applied during resedimentation. The specimen is then allowed to equilibrate for 24 hours, after which the sampling effective stress is recorded. Back pressure saturation then proceeds, provided the sampling effective stress is positive. If the pore pressure is negative, the cell pressure is increased by a quantity equal to this amount and the sample is left to equilibrate once more.

In the medium stress system, the cell is not immediately pressured up to the rebound pressure applied during resedimentation. This is due to concerns relating to consolidation of the specimen, as at this point, the drainage lines are not saturated like those in the low stress system. The magnitude of the initial cell pressure needed to prevent the specimen from changing volume at this time (so that it neither swells nor consolidates) is estimated to be about 0.5 MPa for specimens resedimented to σ'_p = 3-4 MPa, though this value is empirical and difficult to establish. The drainage lines then are vacuumed (under approximately 20 inches Hg) using a portable vacuum pump, for approximately 5 minutes to remove air before being flushed with water. The pore pressure transducer is then installed and the drainage valves are closed. At this point the cell pressure is increased to the rebound pressure applied during resedimentation. Like the low stress, the specimen is allowed to equilibrate overnight, and the following day the sampling effective stress is recorded. The specimen is then back-pressure saturated, provided the sampling effective stress is positive. Similar to the low stress cell, if the pore pressure is negative, the cell pressure is increased by a quantity equal to this amount and the sample is left to equilibrate once more.

For both systems, specimens are back pressure saturated to 0.2 MPa, while the sampling effective stress is held constant. A small deviator stress of approximately 100 kPa is maintained on the specimen throughout the initial pressure-up and back-pressure saturation phases. This is done so that any axial strain which the specimen undergoes can be recorded using the external displacement transducer. At the end of back-pressure saturation, a B-value check is performed using a cell pressure increment of 0.02 and 0.1 MPa for the low and medium systems respectively. If a low B-value (< 0.97 for low stress and <.7 for medium stress) is recorded the sample is left to equilibrate for an extra 24 hours and the check it repeated. As discussed earlier, Casey (2014) has shown that achievable B-Value decreases with increasing stress level, hence why the medium stress criterion for B-value is lower.

After the B-value check has been deemed satisfactory, specimens are K_0-consolidated to at least twice the stress level applied during resedimentation, as per the standard SHANSEP method of laboratory reconsolidation (discussed in Section 2.4.4). The K_0-consolidation algorithm used to control the triaxial system applies a constant axial rate of strain and ensures zero radial strain of the specimen by continuously adjusting cell pressure to keep volumetric and axial strains equal. At the end of K_0 virgin consolidation specimens are allowed a hold stress cycle to ensure the specimen has reached equilibrium. This is typically 24 – 30 hours for BBC and RGoM-EI respectively. Specimens are then swelled using an axial swelling strain rate of 0.15%/hr to the desired OCR along a prescribed path given by the equation:

$$K_{0,OCR} = K_{0,NC}(OCR)^{1-K_{0,NC}} \tag{4–1}$$

Where $K_{0,\ NC}$ is the average value of K_0 throughout the hold stress cycle at the end of the consolidation phase. This is an empirical correlation developed by Ladd (1992), which is believed to describe the path the path of K_0-unloading for any given fine grained material. After swelling the specimen is allowed a further hold stress cycle to equilibrate. Prior to drained shearing, a leak check is performed by closing the drainage valves and monitoring the pore pressure. Provided no internal or external leak is detected, the specimen is sheared in what is assumed to be "drained conditions" (an investigation into this is undertaken in chapter 5) using an axial strain rate of 0.15 %/hr. Shearing is generally carried out to ε_a > 20 %, failure of the specimen, or until the system has reached capacity (whichever comes first), in each test, by which point yielding is clearly visible in the unprocessed voltage output test data.

The raw test data is converted to engineering values using a QBASIC computer program. The program converts the transducer voltages recorded by the central data acquisition system into engineering values of deviator load, axial displacement; change in volume, cell and pore pressures. These values are in turn used to compute effective stresses and strains. During the consolidation and drained shearing phases of tests a right cylinder correction is used to compute the area ($A_{cylindrical}$), defined as:

$$A_{cylidrical} = A_0(1 - \varepsilon_{vol}/1 - \varepsilon_a) \tag{4–2}$$

Where A_0 is the initial specimen area. And ε_a is the axial strain since the beginning of the test stage. In addition, the computations of axial and radial stresses involve a correction for membrane resistance using the method of Berre (1985). For tests in which filter paper strips are used to speed up consolidation, axial stress is further modified using the filter paper correction of Bishop and Henkel (1962). Additional cross sectional area correction factors applied in testing can be found in Casey (2014)

4.4.1 Maintenance

The high pour fluid salinity concentration used when testing RGoM-EI specimens can create problems in the testing equipment. The salt particles tend to flocculate together and stick to the interior walls of the copper drainage lines, particularly around connections and openings. This dramatically reduces the pore fluid flow, and in some situations can lead to clogging if left un-remediated. Low permeable/impermeable lines cause changes in internal specimen pore pressure, increases consolidation times, and causes uncertainties in true specimen effective stress. To prevent the excess salt build up in the pore fluid drainage lines, after every third experiment, boiling hot water is flushed through the lines to remove any salt residue. Because air pressure being used to fill and empty the triaxial cells with silicon oil, the oil becomes super saturated with air. This increases the compressibility of the oil, which can lead to errors in the applied cell pressure. To prevent this, the oil is placed under negative pressure once a month, using the portable vacuum pump. This removes any entrapped air from the oil reservoir.

Table 4-1: Precision and resolutions of the central data acquisition system and MADC device. For axial displacements and specimen volume, resolutions are based on specimen dimensions. For cell pressure, pore pressure and load cell force, resolutions are based on the typical range of the transducer utilized during testing

Transducer	Working Range (%)	Precision		Resolution	
		MADC	Central acq.	MADC	Central acq.
Low Pressure					
Axial displacement	1.8 cm	0.00001 mm (0.0024 mV)	0.00045 mm (0.1 mV)	0.00001%	0.00056%
Specimen volume	47 cm^3	0.01 mm^3 (0.0024 mV)	0.41 mm^3 (0.1 mV)	0.00001%	0.00055%
Cell pressure	1.4 Mpa	0.003 kPa (0.00024 mV)	0.012 kPa (0.001 mV)	0.0002%	0.0009%
Pore pressure	1.4 Mpa	0.003 kPa (0.00024 mV)	0.012 kPa (0.001 mV)	0.0003%	0.0014%
Load cell	2.2 kN	0.001 N (0.00024 mV)	0.005 N (0.001 mV)	0.0001%	0.0004%
Medium Pressure					
Axial displacement	3 cm	0.00001 mm (0.0024 mV)	0.0006 mm (0.1 mV)	0.00002%	0.00074%
Specimen volume	47 cm^3	0.01 mm^3 (0.0024 mV)	0.4 mm^3 (0.1 mV)	0.00001%	0.00054%
Cell pressure	7 Mpa	0.015 kPa (0.00024 mV)	0.063 kPa (0.001 mV)	0.0002%	0.0009%
Pore pressure	7 Mpa	0.015 kPa (0.00024 mV)	0.063 kPa (0.001 mV)	0.0004%	0.0018%
Load cell	8.9 kN	0.012 N (0.00024 mV)	0.05 N (0.001 mV)	0.0001%	0.0004%
High Pressure					
Axial displacement	7.6 cm	0.00003 mm (0.0022 mV)	0.0014 mm (0.1 mV)	0.00004%	0.00174%
Specimen volume	47 cm^3	0.01 mm^3 (0.0024 mV)	1. mm^3 (0.1 mV)	0.00006%	0.00233%
Cell pressure	69 Mpa	1.45 kPa (0.00024 mV)	6.03 kPa (0.001 mV)	0.0021%	0.0087%
Pore pressure	34 Mpa	0.08 kPa (0.00024 mV)	0.31 kPa (0.001 mV)	0.0002%	0.001%
Load cell	222 kN	0.040 N (0.0000024 mV)	18.6 N (0.001 mV)	0.0001%	0.0317%

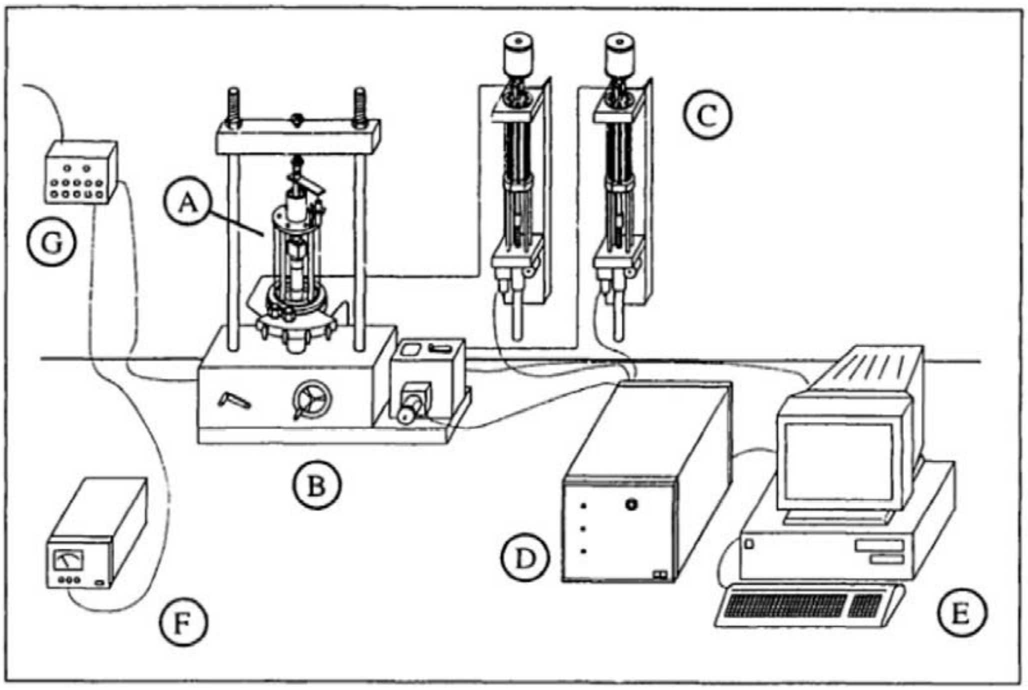

A - Triaxial Cell
B - Load Frame
C - Pressure/Volume Controllers
D - Motor Control Box
E - Personal Computer
F - DC Power Supply
G - Data Acquisition Channels

Figure 4-1: Schematic of the standard automated triaxial testing system used in the Tufts Advanced Geomaterials Laboratory (Santagata, 1998)

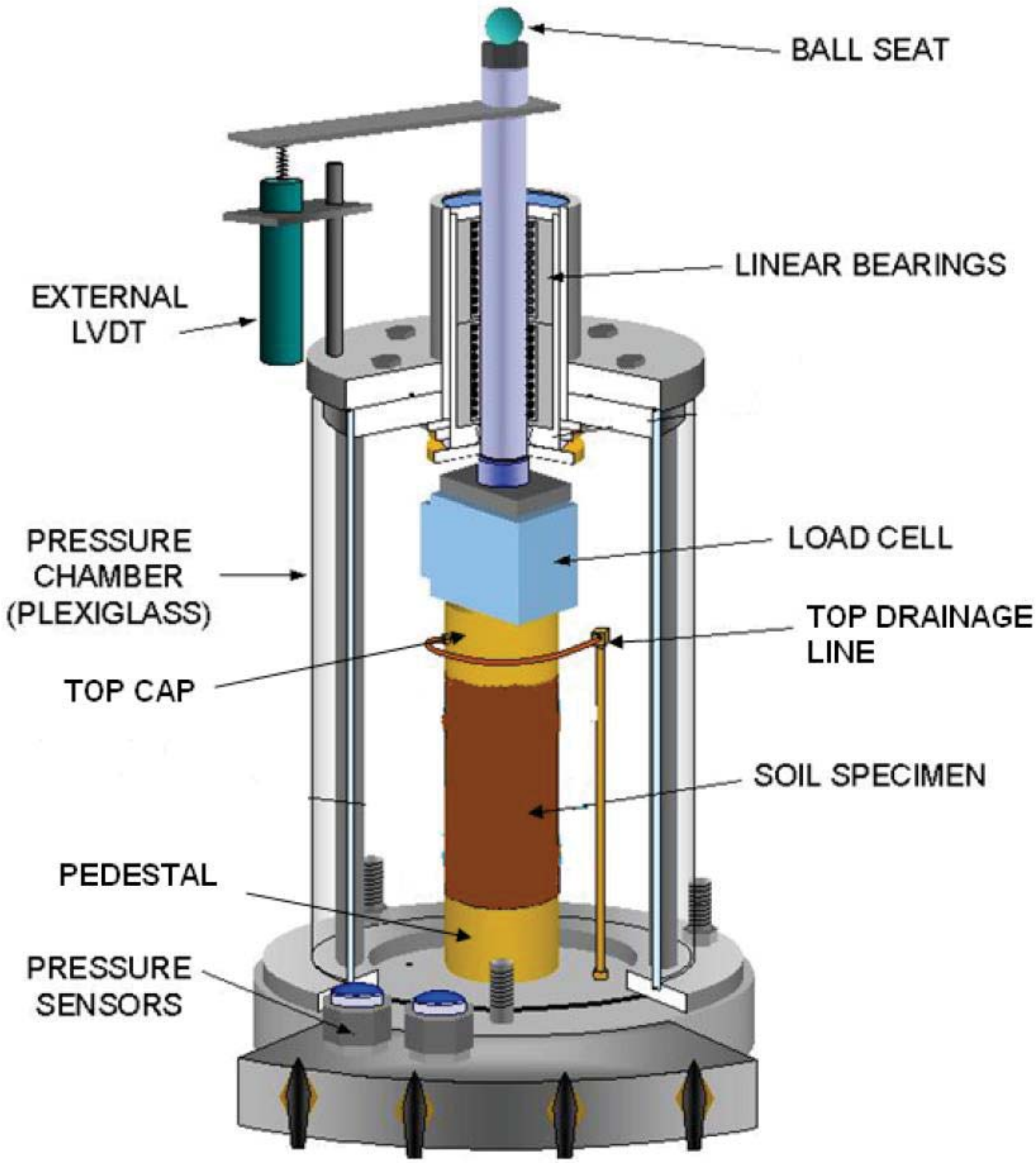

Figure 4-2: Schematic of low pressure triaxial chamber (Santagata 1998)

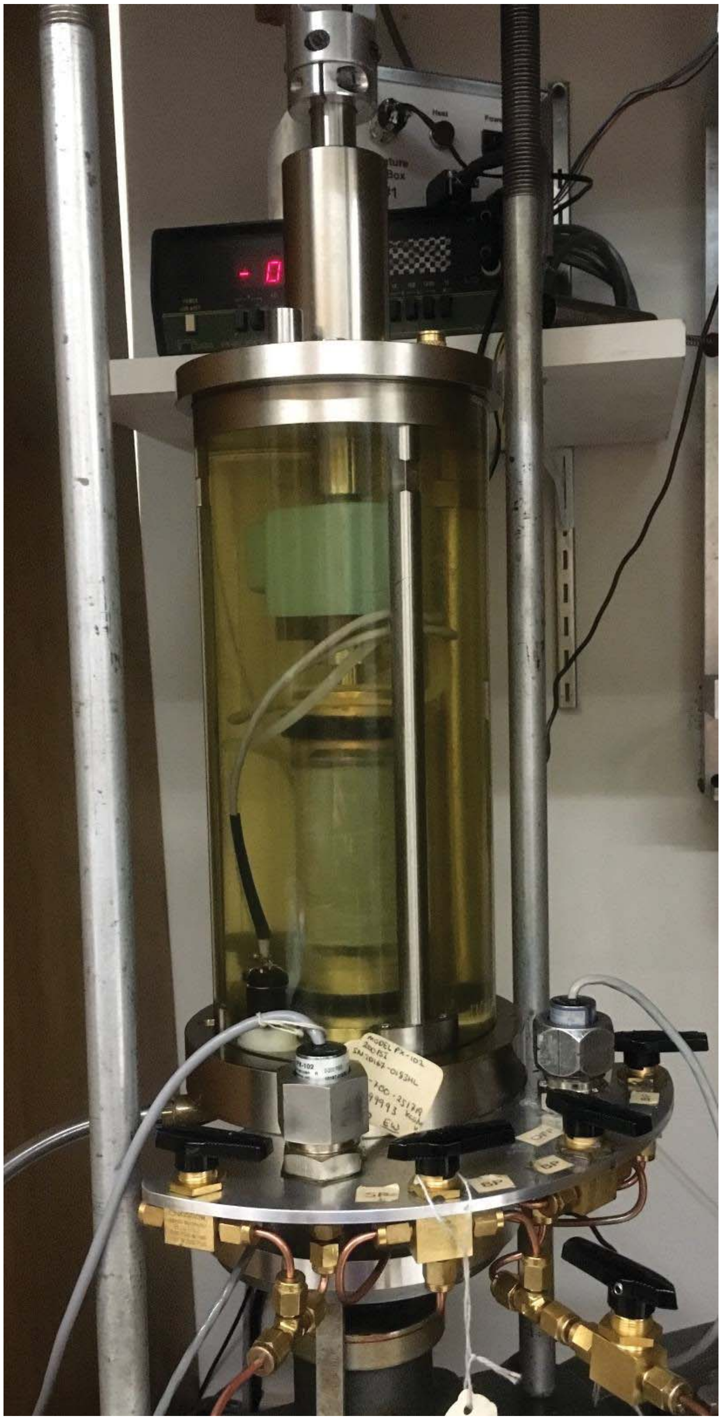

Figure 4-3: Photograph of the low pressure triaxial apparatus

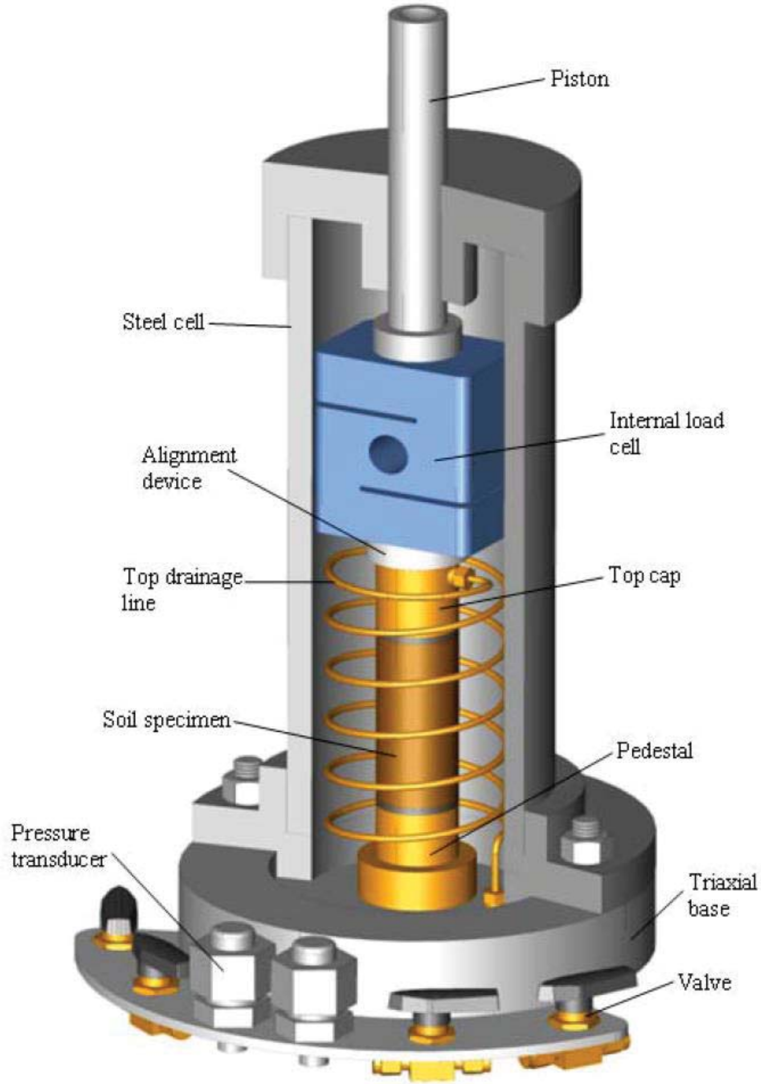

Figure 4-4: Schematic of medium pressure triaxial chamber (Abdulhadi 2009)

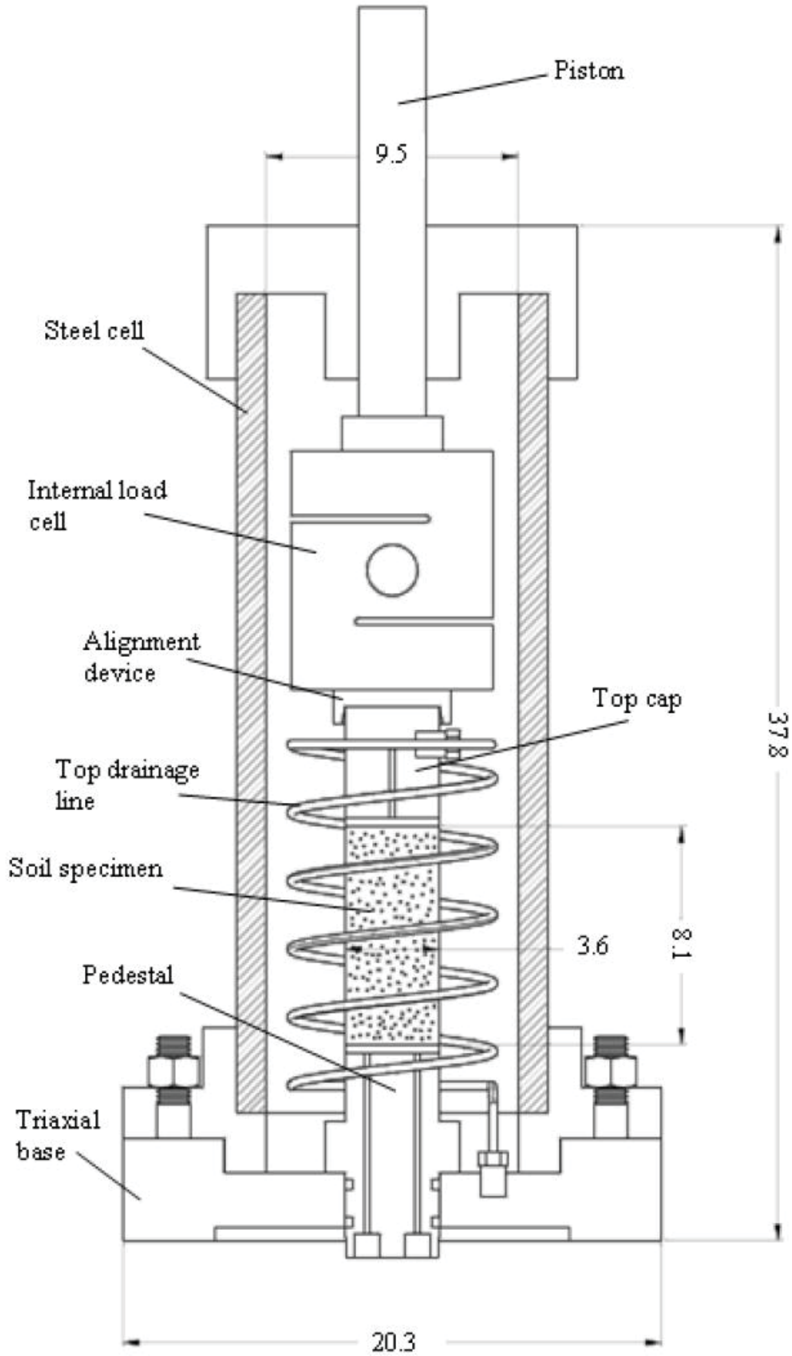

Figure 4-5: Section view of medium pressure triaxial apparatus. Note all dimensions are given in cm

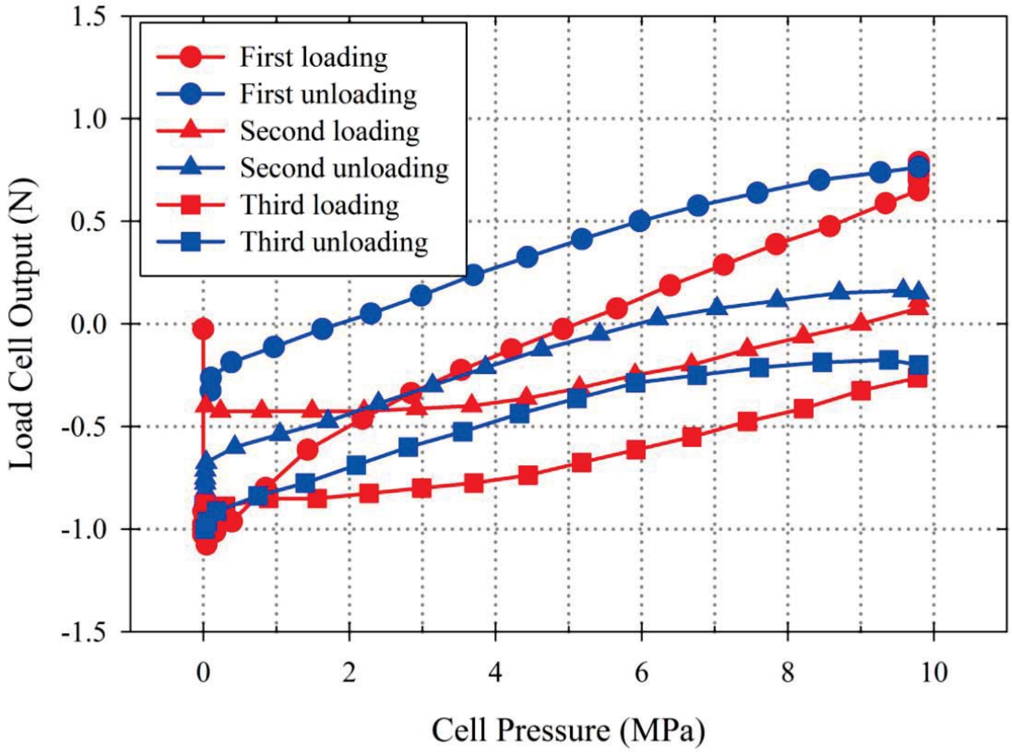

Figure 4-6: The effect of cell fluid pressure on the output of a 2.2kN Honeywell® S-beam load cell

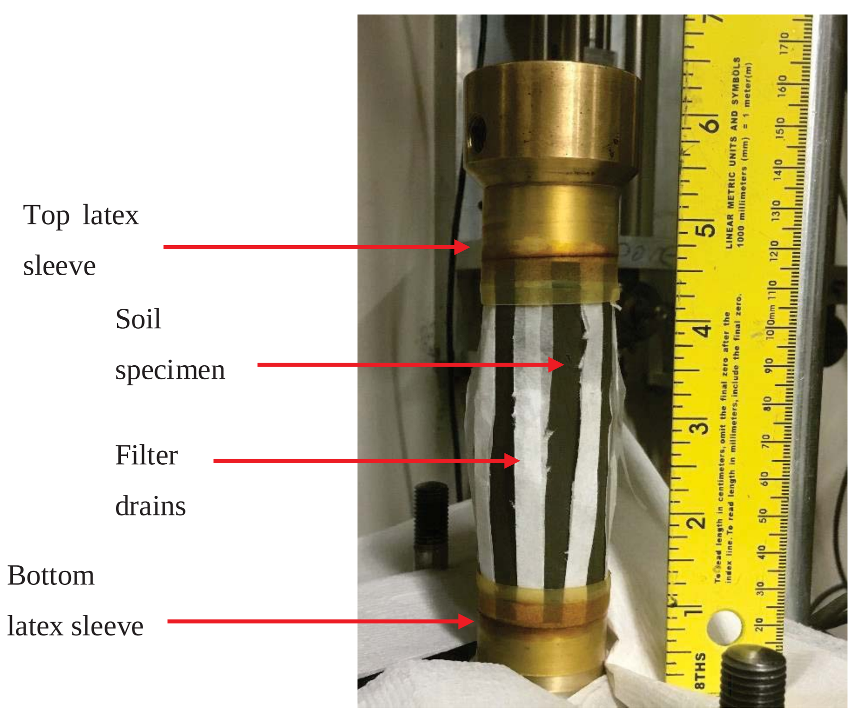

Figure 4-7: Photograph showing the top and bottom thick latex sleeves in place on a medium stress triaxial specimen.

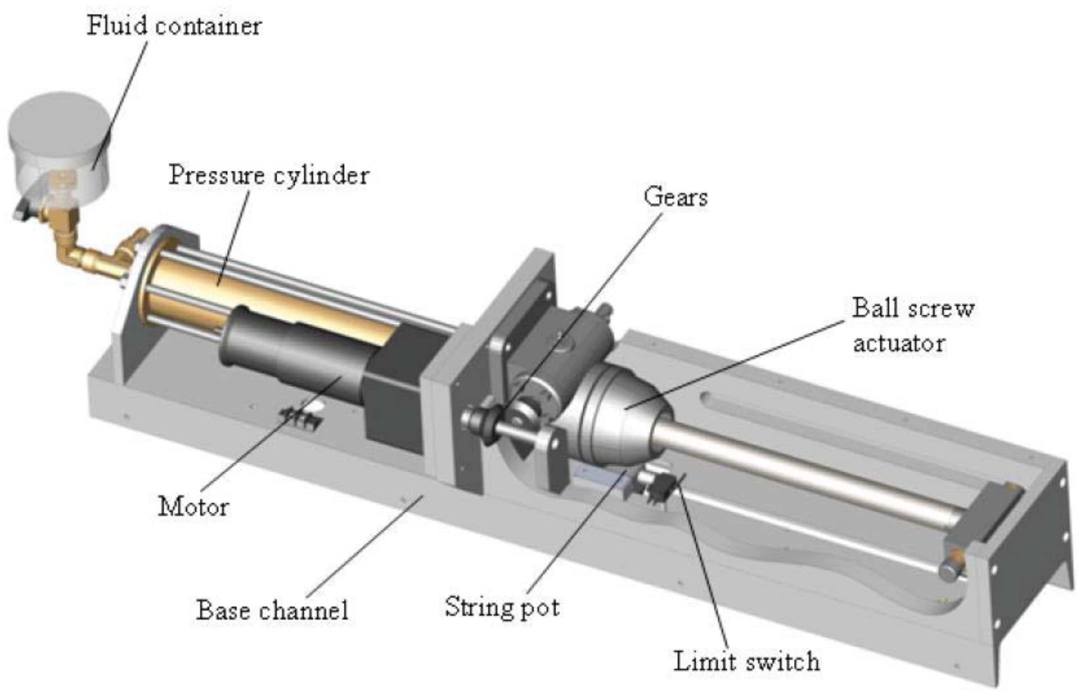

Figure 4-8: Schematic of high capacity Pressure Volume Controller (PVC) used for the medium stress apparatus

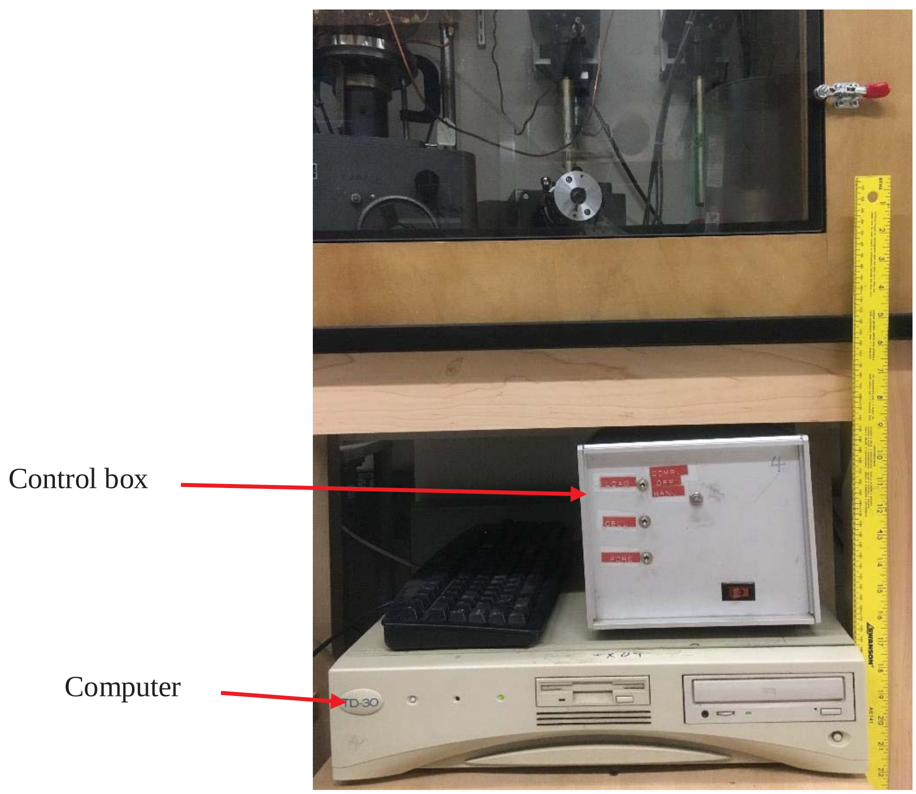

Figure 4-9: Image of local computer system containing MADC device and control box

Figure 4-10: Interior of control box for the triaxial system

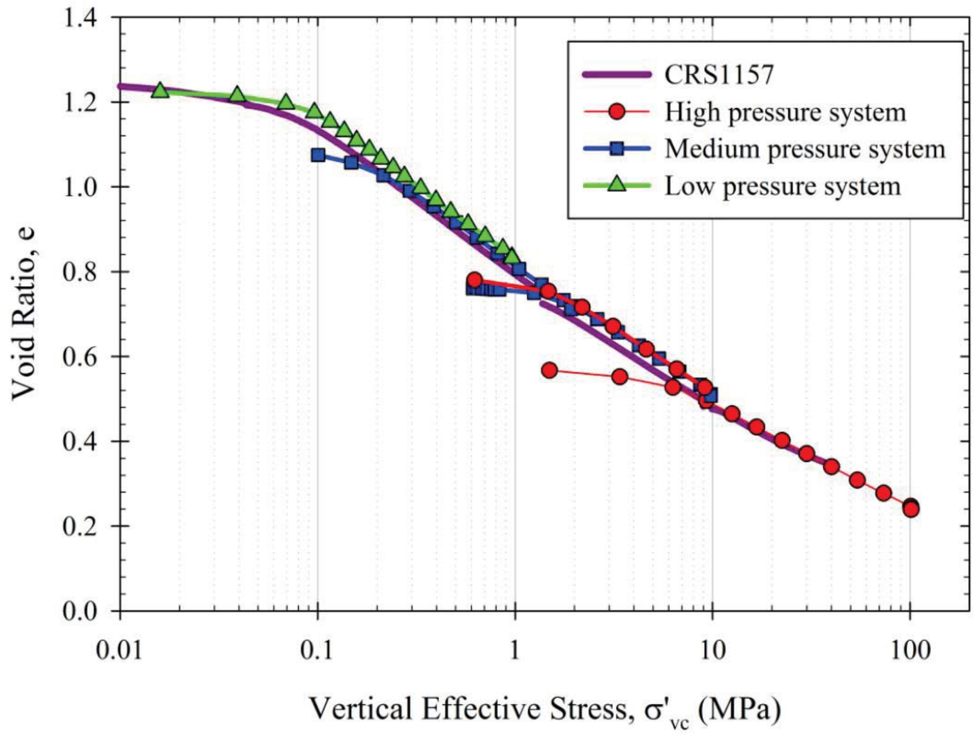

Figure 4-11: Compression behavior of RBBC as measured using the CRS device and the low, medium and high pressure triaxial systems

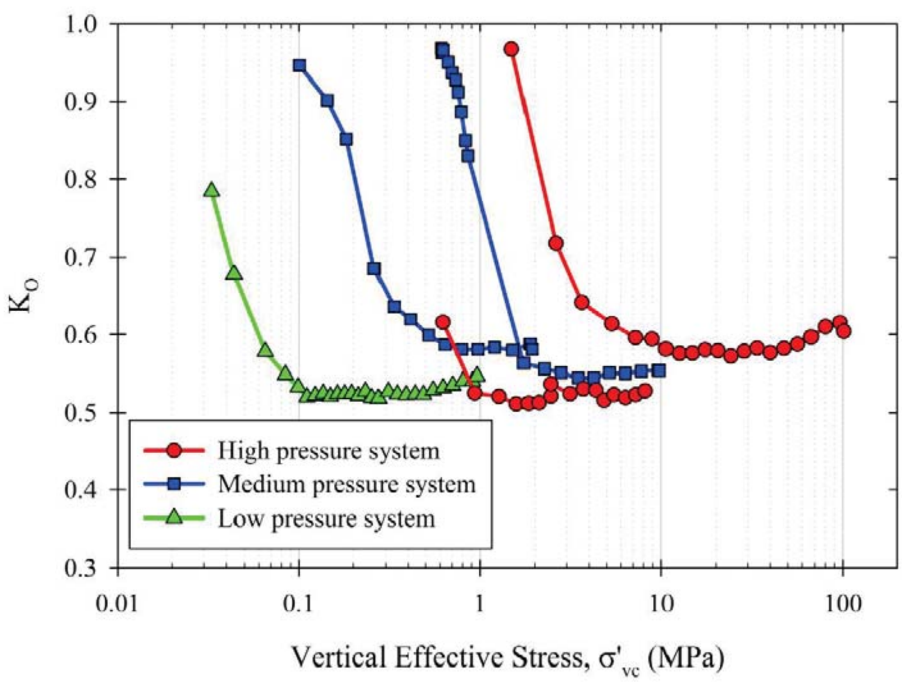

Figure 4-12: Change in K_0 of RBBC during the consolidation phase of triaxial tests using the low, medium and high pressure triaxial systems

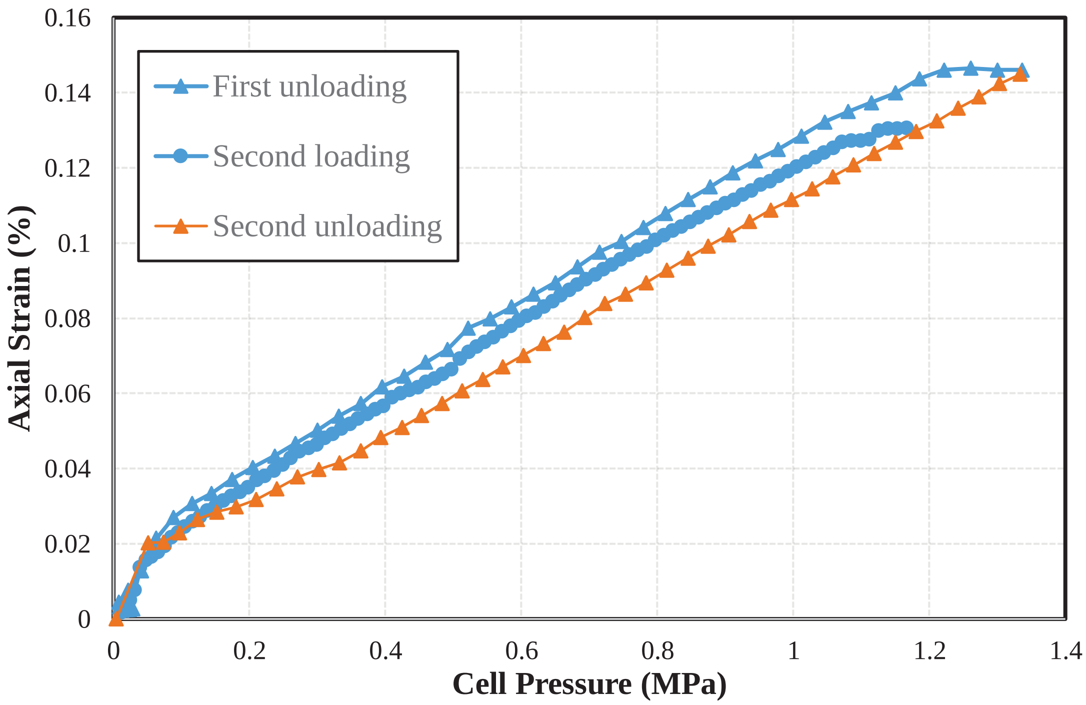

Figure 4-13: The effect of cell fluid pressure on the output of the recorded axial strain in the low stress triaxial apparatus

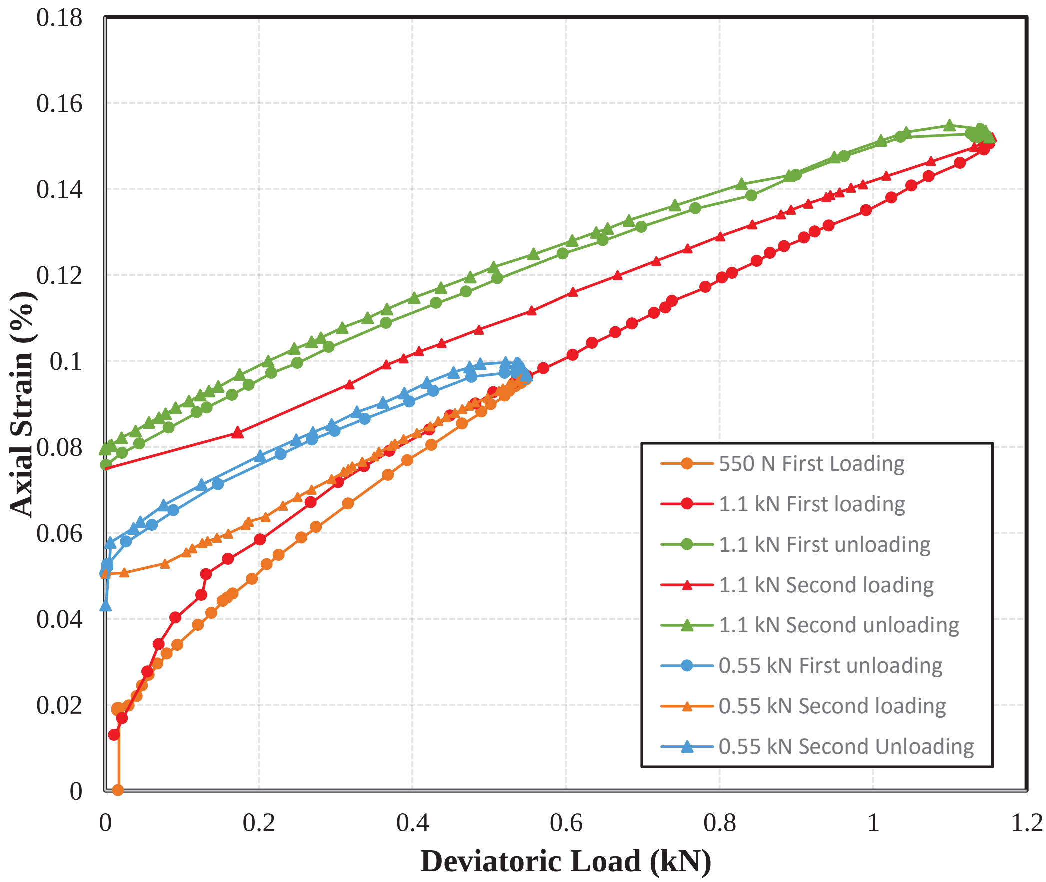

Figure 4-14: The effect of deviatoric load on the output of the recorded axial strain in the low stress triaxial apparatus

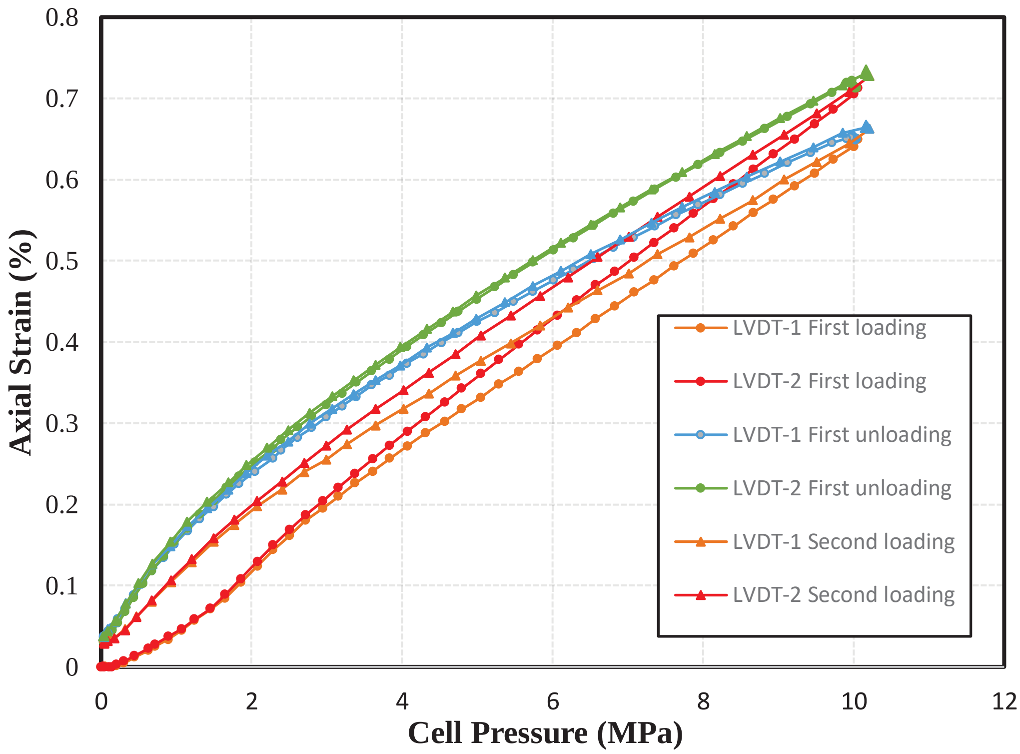

Figure 4-15: The effect of cell fluid pressure on the output of the recorded axial strain in the low stress triaxial apparatus. Note two axial displacement transducers were used to investigate non-uniform straining

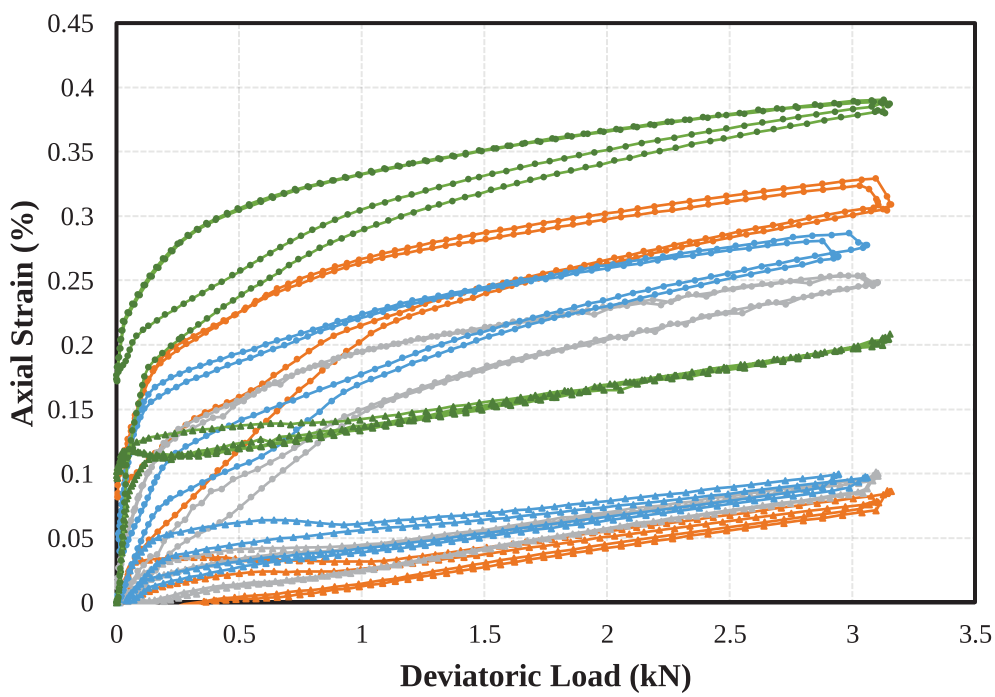

Figure 4-16: The effect of deviatoric load on the output of the recorded axial strain in the low stress triaxial apparatus. Note two axial displacement transducers were used to investigate non-uniform straining

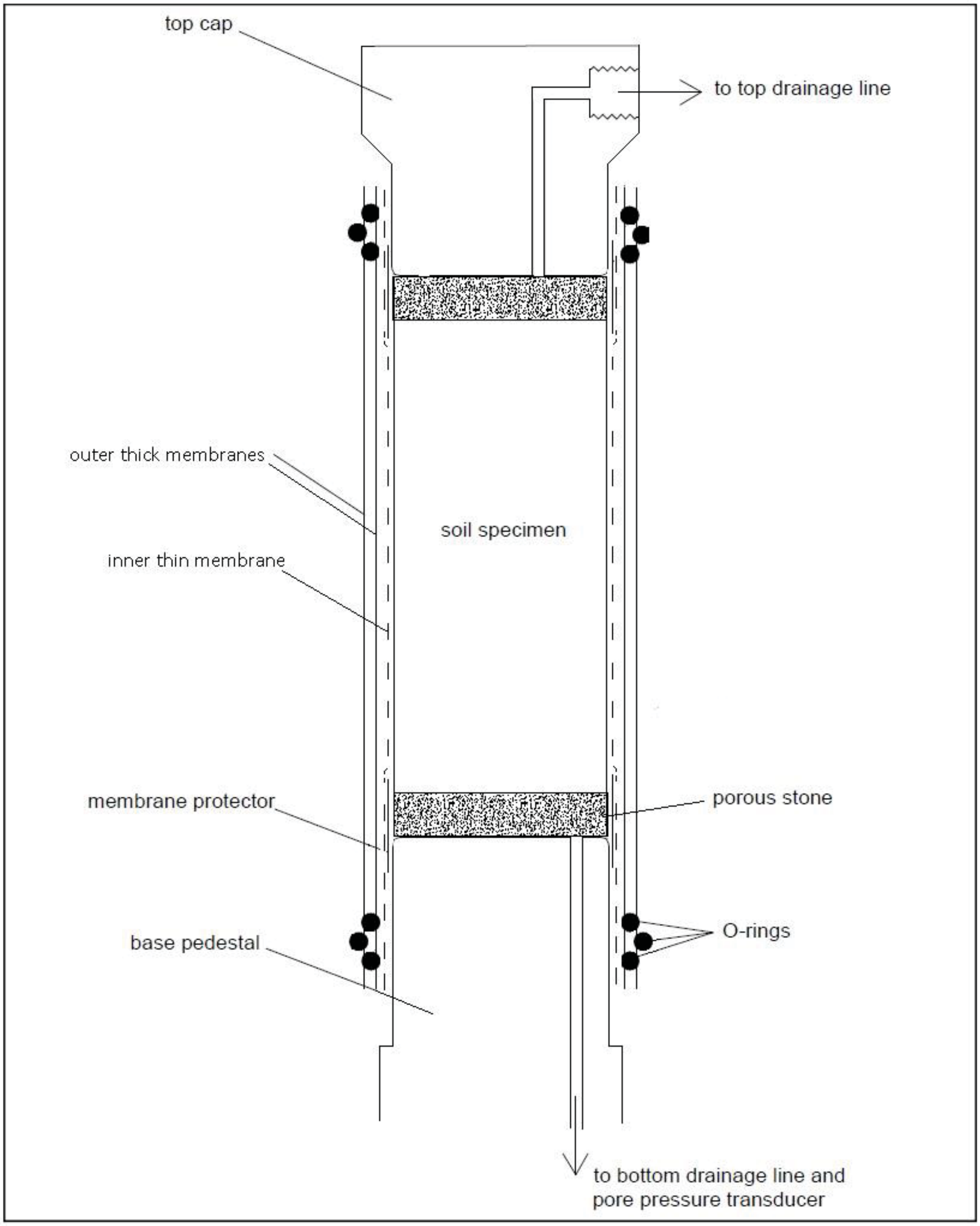

Figure 4-17: Cross-section of fixed end platen specimen setup in the medium stress apparatus

5 CONSOLIDATION RESULTS

5.1 INTRODUCTION

This chapter presents and discusses some of the consolidation properties of both soils investigated as part of this work. These properties are determined from results of resedimentation and the K_0-consolidation phase of triaxial tests. Section 5.2 presents the one-dimensional virgin compression behavior of RGoM-EI and RBBC, respectively, and describes stress dependency behavior as a function of soil type and stress level. Section 5.3 presents data on the K_0 of soils as determined from triaxial tests and discusses the dependence of K_0 on soil type, stress level, and OCR. Section 5.4 discusses normalized consolidated stress paths plotted in MIT-E3 stress space. Finally, Section 5.5 presents results determined from the investigation into the development of excess pore pressure during K_0 drained consolidation in the triaxial systems.

Tables 5-1, 5-2 and 5-3 provide a summary of initial triaxial setup pressure up, saturation, and consolidation results for all of the successful low stress triaxial tests performed during the course of the research. The data presented includes the triaxial system used, soil tested, resedimented sample number, specimen phase relations, maximum effective consolidation stresses, lateral stress ratios, and pre-shear effective stresses.

5.2 COMPRESSION BEHAVIOR

Extensive research has been performed by previous researchers in the MIT Geotechnical Laboratory on the compression behavior of both materials investigated as part of this research. Abdulhadi (2009), Horan (2012), Fahy (2014) and Casey (2014) are the most recent researchers who studied the compression behavior over large stress ranges (0.1-100 MPa). It is not necessary to redo the work of previous researchers, and thus, the compression behavior of the materials were not thoroughly investigated as part of this work. Figure 5-1 has been abstracted from Casey (2014).The graph plots the virgin compression behavior for both soils investigated. It can be observed from Figure 5-1, that RGoM-EI, the higher plasticity, smectite rich clay, possess a much larger void ratio at low stresses compared to RBBC, the siltier, low plasticity clay. As both soils undergo consolidation to higher stresses, RGoM-EI displays a much greater compressibility and a corresponding larger decrease in void ratio compared to RBBC. The void ratios of the two soils then converge together at high stresses. Casey also correlated compression behavior to liquid limit for both these soil types amongst a wide range of others.

5.3 FACTORS INFLUENCING MEASURED K_0

5.3.1 Introduction

The K_0-consolidation algorithm used in the triaxial systems allows for continuous measurements of the K_0 value of a specimen throughout the consolidation phase. The control algorithm applies a user defined constant axial rate of strain, while ensuring zero radial strain of the specimen by continuously adjusting the cell pressure to keep volumetric and axial strains equal. The loading portion of the algorithm has proven successful in both maintaining constant cross-sectional area of specimens, and proportional axial strain deformation, during virgin consolidation. However, the algorithm can be less effective during the swelling portion of tests. This is due to backlash of the axial loading gear mechanism used in both the low and medium stress systems. The backlash effect, combined with small changes in axial strain involved in swelling compared to virgin compression, creates a small control issue in the device. This issue manifests itself as erratic changes in K_0 during the initial portions of swelling (below an OCR of ~1.5), though K_0 tends to become more stable as swelling progresses and the control system achieves true one-dimensional conditions. As a result of this issue, previous researchers who have examined the strength behavior of OC soil in the MIT Geotechnical Engineering Laboratory (e.g. Sheahan 1991, Santagata 1998, Abdulhadi 2009, Casey 2011) have typically relied on stress path swelling rather than K_0-swelling. All RGoM-EI tests performed as part of this research were unloaded using the stress path swelling algorithm combined with the $K_{0,\ OCR}$ equation discussed in Section 4.4

5.3.2 Effect of OC and NC on RGoM-EI K_0

Figure 5-2 shows the variations in K_0 during the consolidation phase of a select number of triaxial tests carried out on RGoM-EI. The graph plots the lateral stress ratio imposed on the specimen against vertical effective stress. Data obtained during the swelling portion of tests are omitted from Figure 5-2 for clarity. The similarities between all tests, with relation to the vertical effective stress axis, reflect the similar preconsolidation stresses which specimens were consolidated to during resedimentation. Specimens were typically resedimented to nominal preconsolidation stresses of 0.5 MPa (though side wall friction reduces the actual preconsolidation stress imposed on specimens, as discussed in Section 3.3.4.) before being swelled to OCR = 4 prior to extrusion. The broad range of starting points with relation to lateral stress ratio axis, at low stress levels, reflects a slight variability in the pressure up and saturation procedures of each test. During the initial pressure-up and back-pressure saturation phases of a test, the OC specimen is subjected to near isotropic stress conditions. Thus, the value of K_0 is approximately unity at the beginning of consolidation. The broad starting range has no effect on the consolidation process as the K_0-consolidation computer algorithm will auto correct for this.

The variation in K_0 during the consolidation process follows the same trend in all tests. K_0 reduces sharply during the recompression stage and then begins to stabilize upon reaching the σ'_p imposed on the specimen during resedimentation (the dip in all the curves). From here, K_0 remains relatively constant as the specimen undergoes virgin consolidation. It can be seen from Figure 5-2, that there is an overall trend for $K_{0, NC}$ to increase very slightly with increasing stress level. Both Abdulhadi (2009) and Casey (2014) concluded that $K_{0, NC}$ increases steadily over increasing orders of magnitudes of vertical effective stress. RGoM-EI had an average value of $K_{0, NC} = 0.62$ for a vertical effective stress ($\sigma'_{v, max}$) of ≈ 1 MPa. Figure 5-3 additionally includes the variation in K_0 during the swelling stages of RGoM-EI tests. It can be seen that there is a slight variation in the vertical effective stress between each unloaded specimen. This is due to slight variations in individual specimen consolidation stress (i.e., some specimens were consolidated to a slightly lower stress due to strain limitations). The effects of slight variations in consolidation and unloading stresses are considered to be negligible as each individual test is normalized by its own unique consolidation stress $\sigma'_{v, max}$.

5.3.3 Effect of OC and NC on Intact BBC K_0

Figure 5-4 shows the variations in K_0 during the consolidation phase of Intact BBC specimens. The general behavior observed is the same as that described above (i.e., a rapidly decreasing K_0 during recompression followed by a steadiness during virgin consolidation). However, the curves are not as reproducible as those of RGoM-EI; there is a variation in the stress at which each test transitions from OC to NC. This is due to the variation in σ'_p associated with each intact sample. There is also a significant variation in $K_{0, NC}$ at 1 MPa. This is most likely due to the different composition of each individual specimen, as intact specimens are not homogenous throughout like the resedimented samples. Figure 5-5 shows the unloading cycles of these tests. The specimens were not unloaded by Equation 4-1, they were unloaded under the criteria that they would have an OCR of ~10 and be at a lateral stress ratio of 1. This was because these tests were conducted during the earlier parts of this research when the author was not aware of this equation. One test was unloaded to an OCR of 2 to assess the effects of OCR on interpreting the yield surface.

5.4 NORMALIZED CONSOLIDATION RESULTS

5.4.1 Introduction

As mentioned in Section 2.6, the Normalized Soil Parameter concept is based on the SHANSEP empirical observation that clay samples having a similar OCR but different consolidation stresses. Therefore, different preconsolidation pressures exhibit similar properties when normalized with respect to their individual consolidation stress. Casey (2014) concluded that material has stress dependency and the SHANSEP equation needs an adjustment factor to account for this. For the purpose of this research, the SNANSEP theory is applicable as all tests (with the exception of a few of trial experiments) have been consolidated to the approximately the same consolidation stress and unloaded to the same OCR. All RGOM-EI and BBC tests have been normalized and the results are shown in the following two sections.

5.4.2 RGOM-EI Normalized Results

Figure 5-6 shows the normalized results of a single K_0 consolidation and $K_{0,\,OCR}$ unloading test, plotted in MIT stress space. The grey stress path is the K_0 consolidation loading path; it is seen to start at the isostatic axis (i.e., consistent with having a K_0 of 1) and travels upwards at a steep incline, followed by a gradual decrease in slope, as the specimen transitions from OC to NC. This is consistent for each specimen starting at a high K_0 value and decreasing to a lower K_0 value, as previously mentioned in section above. The stress path then follows a relatively straight path as it undergoes virgin consolidation. The large red point on the graph is the normalized stress point associated with a vertical effective stress of~1 MPa. This point essentially sets the interpreted yield surface in the normalized stress space. From here the specimen is unloaded along the prescribed $K_{0,\,OCR}$ equation to an OCR of 2, as represented by the blue straight stress path. The end point of this stress path is where the drained shearing phase of the tests begin.

Figure 5-7 plots the majority of the RGoM-EI K_0 consolidation and $K_{0, OCR}$ unloading tests in normalized MIT stress space. The figure shows the significant reproducibility associated with resedimented samples. It can be seen that independent of where individual tests start, they all converge onto the same normalized K_0 consolidation stress path and are loaded to the same normalized stress point (red point). Again, all tests are seen to converge along the same $K_{0, OCR}$ unloading stress path and are unloaded to the same stress point. Figure 5-8 fits a linear regression line from the origin through the $K_{0, NC}$ consolidation stress paths. This is a line having a constant $K_0 = 0.62$, which is in agreement with a previous empirical correlation for estimating $K_{O, NC}$ proposed by Jâky (1944). Jâky correlated $K_{0, NC}$ to ϕ'cs, where ϕ'cs is assumed to be constant. This relationship holds through for the low stress ranges (0-1MPa) tested as part of this research. However, Casey (2014) demonstrated that ϕ'cs can vary considerably for a given soil as a function of effective stress level and that this relationship breaks down at higher stress levels.

5.4.3 BBC Normalized Results

The normalized K_0 consolidation stress paths of all BBC tests, plotted in MIT stress space are shown in Figure 5-9. Again, all stress paths start from the isostatic axes, consistent with having $K_0 = 1$. The stress paths do not converge together like as observed in the RGoM-EI tests. Rather, there is a considerable amount of scatter in the plot. As mentioned above, this is most likely due to the different composition of each individual specimen. However, a number of normalized stress paths do appear to trace each other closely and converge to the red stress point ($K_{0, NC} = 0.54$). This point is taken as the best estimate for all the BBC tests. The unloading portion of the BBC tests have been omitted from the graph for clarity as they simply trace back along a straight line stress path to 0.1 on the isostatic axis. Again, the K_0 consolidation paths fall below a normally consolidated failure envelope. The envelope shown in this figure has a ϕ'cs of 33°, this is a commonly assumed normally consolidated failure envelope for BBC (shown in the image for clarity purposes).

5.5 VERIFICATION OF CONSOLIDATION TEST RESULTS

5.5.1 Introduction

The K_0 Consolidation axial strain rates used in the triaxial systems are based upon historical empirical experience. These values are recommended by Sheahan (1991) to be in the range of 0.15 – 0.25 %/hr and have been adopted by all researchers in the MIT geotechnical laboratory over the past two decades. Casey (2014) has adopted a 0.15 % strain rate when consolidating to stresses of up to 100 MPa. However, Casey showed that the permeability of fine grained sediments decreases by orders of magnitude with increasing $K_{0, NC}$ consolidation vertical effective stress, as shown in Figure 5-10. Applying constant rate of vertical strain to a material of decreasing permeability is likely to cause increased internal pore pressure generation as the pore water has not been given significant time to permeate to the free draining ends of the specimen. Internal pore pressure generation will subsequently cause a reduction in the effective stress being applied to the specimen.

The standard configuration of the triaxial cell does not measure excess pore pressure generated in the specimen, and therefore the true vertical effective stress being imposed upon the specimen may in fact be much lower than the system is recording. This research modified the triaxial system by isolating the top drainage line from the specimen and connecting it to a separate pore pressure transducer via a three-way Swagelok valve. The schematic of the modification and the device itself are shown in Figure 5-11. This system modification allowed the samples to be pressured up and saturated in the same way as other tests, while making it possible to monitor the pore pressure developed within the specimen during the consolidation stage. Diverting the top drainage line changes the specimen's boundary conditions from double drainage (top and bottom), to single drainage (bottom only) conditions. The second pore pressure transducer is used to monitor the maximum internal pressure generation in the specimen throughout the K_0 consolidation procedure.

5.5.2 Low Stress Testing

Figure 5-12 plots the results obtained from the internal pressure monitoring of an RGoM-EI specimen in the low stress cell. The graph plots pressure as a function of time throughout the entire testing procedure. It can be seen that the vertical total stress, radial total stress, and internal pressure generation all rise throughout the K_0 consolidation process. All three paths stop rising upon reaching the end of the K_0 consolidation procedure (i.e. the sample has been loaded to its target stress of~1 MPa), from here, the triaxial system enters into hold stress mode, signified by the constant values of both vertical and radial total stress. The internal excess pressure then begins to dissipate in a trend resembling an exponential decay until the test was stopped after 11 days. The maximum excess pore pressure generated at the top of the one way draining specimen was 0.39 MPa, at the end of K_0 consolidation after 2.5 days. It then takes a further 8.5 days for the excess pore pressure to dissipate almost fully. The back pressure at the base of the specimen was kept constant at 0.2 MPa throughout the entire experiment.

The excess pore pressure generated in Figure 5-12 is only representative of a one way draining triaxial consolidation test. All tests performed as part of this research were consolidated under double drainage conditions in the triaxial cell and thus the experimental results presented in Figure 5-12 were modified to account for double drainage conditions by Equation 5-1.

$$Average\ Pore\ Pressure\ = {}^{2}/_{3}\left(\frac{u_e}{4}\right) \tag{5-1}$$

Where u_e is the excess pore pressure generated at a given point in time in the one way drainage test. The denominator of 4 in the equation is derived from Terzaghi's one dimensional consolidation equation (half the drainage height squared). The 2/3 term converts what is assumed to be a parabolic distribution of internal excess pore pressure, (maximum at center, zero at extreme boundaries) to a constant average pore pressure throughout the specimen. This predicted average pore pressure for a conventional two-way drainage system, K_0-consolidated to 1 MPa is shown in Figure 5-13. The total vertical, radial, and back pressures are the same as in Figure 5-12. The predicted average pore pressure generated in the specimen has been significantly reduced. At the end point of K_0 consolidation, the total vertical stress has reached ~ 1.2 MPa, the back pressure remains constant at 0.2 MPa, the average internal pore pressure in the specimen has risen to 0.25 MPa (an increase in pressure of 0.05 MPa). This causes a 5 % error in the interpreted vertical effective stress being imposed upon the sample at this point (i.e., the computer program reads a σ'_v of 1MPa, but the specimen is actually experiencing a σ'_v of 0.95 MPa). All tests are left in the hold stress condition for ~ 30 hours to allow one cycle of secondary compression. This extra time allows some of the excess pore pressure generated in the specimen to dissipate, and the associated error in σ'_v reduces from 5 % to ~3 %.

Constant rate of strain tests have been used to correlate strain rates to excess pore pressure generation inside the specimen as far back as three decades ago. The correlation was first developed by Wissa (1971), who proposed the following equation:

$$Excess\ Pore\ Pressure, \qquad U_e = \frac{\varepsilon H_o\ H_n \gamma_w}{2K_v} \tag{5-2}$$

where ε is the axial strain rate, H_0 is equal to the initial height of the specimen, H_n is equal to the height of the specimen at a given strain, and K_v is the hydraulic conductivity of the material in the vertical direction. Extensive CRS research has been performed by the MIT geotechnical laboratory on RGoM-EI, and further information can be found in Nordquist (2013) and Fahy (2014). Figure 5-14 compares the predicted excess pore pressure for RGoM-EI derived by the Wissa CRS equation against the triaxial experimental results. A constant axial strain rate of 0.15 %/hr was used in the experiment, and thus, was adopted into the prediction equation. The CRS relationship continuously predicts a higher excess pore pressure than what was measured experimentally. There is a larger discrepancy between the two data series at low strains. As the strain increases the experimental results begin to converge slightly towards the CRS prediction pressure. The discrepancy between the two curves is relatively small considering two different devices are being compared, this gives confidence in the CRS prediction equation for the low stress region (0-1 MPa).

5.5.3 Medium Stress Testing

Due to the large decreases in permeability shown in Figure 5-10, the axial strain rate was reduced from 0.15 to 0.1 %/hr in an attempt to reduce the anticipated internal pore pressures generated in the medium stress device. The results obtained from this testing procedure are shown in Figure 5-15. Similar to Figure 5-12 the vertical total stress, radial total stress and internal pressure generation all rise throughout the K_0 consolidation process. The target vertical effective stress to be imposed upon the specimen in the medium stress device was 10 MPa. Due to an axial motor control issue, the vertical total stress continued to rise slightly after the end of K_0 consolidation, but it returned back to its target constant value of 10.2 MPa after 3 days. This motor control issue in turn, caused a slight fluctuation in the internal pore pressure generated. At the end of K_0 consolidation (2 days), it can be seen to rise and fall slightly over a period of ~2.5 days, before beginning to dissipate in a trend resembling an exponential decay, similar to the low stress system. Unlike the low stress system, the internal pore pressure generated in the medium stress system was much higher. For a total vertical consolidation stress of 10.2 MPa the internal pore pressure rose to 7.7 MPa (75.5 % of σ_v) compared to the low stress system, where the total vertical consolidation stress was 1.2 MPa and internal pore pressure only rose to 0.58 MPa (48.3 % of σ_v). The medium stress strain rate used was also reduced by 33 %, compared to the low stress cell. Due to time constraints, the test was stopped after 14 days, before the excess pore pressure could fully dissipate. However, it had dissipated by ~ 76 % which was enough to distinguish the dissipation curve. The time taken for excess pore pressure to fully dissipate in this one way drainage system can be obtained by extrapolating this curve.

The predicted average pore pressure for a conventional two-way drainage system, K_0-consolidated to 10 MPa is shown in Figure 5-16. Again, the total vertical, radial and back pressures are the same as in Figure 5-15. Although the predicted average pore pressure generated in the specimen has been considerably reduced, it still has a significant presence. At the exact end point of K_0 consolidation, the total vertical stress has just reached ~10.2 MPa, the back pressure remains constant at 0.2 MPa, and the average internal pore pressure in the specimen has risen to ~1.5 MPa (i.e., an increase in pressure of 1.3 MPa). This results in a 13.3 % error in the interpreted vertical effective stress being imposed upon the sample at this point (i.e., the computer program reads a σ'_v of 10 MPa, but the specimen is actually experiencing a σ'_v of 8.67 MPa). The predicted dissipation curve also decreases at a much slower rate than that of the low stress system. The 30 hours extra time allowed for a cycle of secondary compression would reduce the error in σ'_v by 2

% at most. A 13 % error in σ'_v has a significant effect, and medium stress tests on RGoM-EI having an axial strain rate of 0.1 %/hr, or greater, are concluded to be partially-drained.

Wissa's CRS prediction equation (Equation 5-2) was also used to theoretically predict internal pressure generation in the medium stress cell. Results generated from Wissa's equation are compared to the experimental results in Figure 5-17. The axial strain rate deviated slightly from 0.1 %/hr in the experimental test and this was accounted for in the CRS prediction equation. The slight variation in axial strain rate is the reason why the two data series are not smooth curves like those shown in Figure 5-14. At strains below 2 % the CRS equation predicts higher internal pore pressures than actual generated pressures. However, the experimental data series is continuously converging towards the CRS prediction curve, and at just over 2 % axial strain the curves converge together. At axial strains greater than 4 % the experimental excess pore pressure exceeds the CRS prediction, and continues to rise at a greater rate than that of the CRS. At 6 % strain the test entered into hold stress mode when the specimen had reached its target σ'_v of 10 MPa (Actual σ'_v was~8.7 MPa). At this point actual excess pore pressure generated is significantly higher than the pressure predicted by the CRS equation (5.7 MPa vs 3.2 MPa). It is concluded that Wissa's CRS prediction equation is conservative, but acceptable, at predicting internal excess pore pressures in triaxial specimens at low stresses. (Below 2 MPa). The relationship under predicts internal excess pore pressure at stresses exceeding 5 MPa.

Table 4-2: Summary of low stress triaxial test setup results

Test No:	Sample No:	Soil	TX System	Initial W_C	Initial e_o	End of Pressure up ε_a %	σ_c (MPa)	σ_v (MPa)	u (MPa)	ε_v %
TX1249	KL15-01	BBC	STA-02	27.0	0.770	0.20	0.098	0.083	-0.004	0.06
TX1250	KL15-01	BBC	STA-02	43.4	0.785	0.22	0.098	0.101	0.014	0.00
TX1251	KL15-01	BBC	STA-02	29.5	0.879	0.23	0.048	0.052	0.000	0.02
TX1252	KL15-01	BBC	STA-02	25.1	0.739	0.18	0.097	0.101	0.025	0.01
TX1253	KL15-01	BBC	STA-01	23.4	0.666	0.18	0.070	0.068	0.009	-0.02
TX1254	KL15-01	BBC	STA-02	23.9	0.711	0.18	0.096	0.093	0.048	0.01
TX1255	KL15-01	BBC	STA-01	26.8	0.774	0.03	0.098	0.098	0.034	0.00
TX1256	KL15-01	BBC	STA-02	31.0	0.872	0.04	0.097	0.095	0.066	0.01
TX1257	KL15-01	BBC	STA-01	27.8	0.813	0.01	0.098	0.096	0.048	-0.01
TX1260	RS466	RBBC	STA-01	34.1	1.023	0.26	0.137	0.137	0.015	0.00
TX1261	RS460	RGoM-EI	STA-02	44.3	1.372	0.27	0.098	0.100	0.031	0.00
TX1262	RS464	RGoM-EI	STA-01	44.2	1.335	0.47	0.137	0.147	0.098	0.00
TX1264	RS463	RGoM-EI	STA-01	51.1	1.130	0.29	0.147	0.174	0.042	0.00
TX1265	RS461	RGoM-EI	STA-02	35.9	1.108	0.30	0.149	0.167	0.038	0.02
TX1268	RS477	RGoM-EI	STA-02	36.7	1.111	0.22	0.147	0.159	0.025	0.00
TX1269	RS474	RGoM-EI	STA-01	35.5	1.076	0.05	0.147	0.169	0.038	0.00
TX1270	RS475	RGoM-EI	STA-02	36.4	1.083	0.16	0.147	0.148	0.015	0.02
TX1271	RS476	RGoM-EI	STA-01	36.3	1.076	0.04	0.147	0.153	0.005	0.00
TX1273	RS479	RGoM-EI	STA-02	36.9	1.084	0.21	0.148	0.162	0.018	0.03
TX1276	RS482	RGoM-EI	STA-01	33.4	1.018	0.06	0.146	0.150	0.027	0.00
TX1279	RS480	RGoM-EI	STA-02	34.7	1.048	0.15	0.147	0.146	0.018	0.02
TX1282	RS478	RGoM-EI	STA-01	35.7	1.282	0.06	0.147	0.150	0.004	0.00
TX1287	RS483	RGoM-EI	STA-02	41.7		0.14	0.147	0.145	0.010	0.00
TX1288	RS486	RGoM-EI	STA-01	37.6	1.106	0.07	0.146	0.153	0.009	0.02
TX1290	RS484	RGoM-EI	STA-01	37.4		0.27	0.147	0.201	0.007	-0.01
TX1292	RS487	RGoM-EI	STA-02	37.2	1.059	0.23	0.228	0.230	0.077	0.03
TX1295	RS495	RGoM-EI	STA-01	37.9	1.138	0.09	0.147	0.155	0.017	0.00
TX1298	RS496	RGoM-EI	STA-02	35.9	1.069	0.22	0.147	0.185	0.076	0.02
TX1304	RS504	RGoM-EI	STA-01	37.4	1.100	0.12	0.147	0.148	0.015	0.04
TX1305	RS510	RGoM-EI	STA-02	36.1	1.058	0.14	0.147	0.187	0.098	0.00
TX1308	RS512	RGoM-EI	STA-01	37.1	1.085	0.05	0.146	0.150	0.005	0.03
TX1313	RS514	RGoM-EI	STA-01	41.4	1.221	0.23	0.097	0.111	-0.008	0.09

Table 4-3: Summary of low stress triaxial saturation results

Test No.	Sample No:	Soil	TX System	At End of Saturation ε_a %	σ_c (MPa)	σ_v (MPa)	u (MPa)	ε_v %	B-value	e
TX1249	KL15-01	BBC	STA-02	0.24	0.294	0.294	0.2	-0.88	0.54	0.766
TX1250	KL15-01	BBC	STA-02	0.24	0.282	0.285	0.2	-0.86	0.70	0.781
TX1251	KL15-01	BBC	STA-02	0.41	0.245	0.248	0.2	0.13	0.79	0.871
TX1252	KL15-01	BBC	STA-02	0.18	0.270	0.268	0.2	-0.49	0.76	0.736
TX1253	KL15-01	BBC	STA-01	0.26	0.259	0.253	0.2	-3.83	0.40	0.662
TX1254	KL15-01	BBC	STA-02	0.25	0.247	0.244	0.2	-0.55	0.83	0.707
TX1255	KL15-01	BBC	STA-01	2.18	0.260	0.294	0.2	-0.62	0.50	0.736
TX1256	KL15-01	BBC	STA-02	0.08	0.228	0.227	0.2	-1.18	0.85	0.870
TX1257	KL15-01	BBC	STA-01	0.21	0.246	0.244	0.2	-0.22	0.50	0.809
TX1260	RS466	RBBC	STA-01	0.38	0.317	0.317	0.2	-1.92	0.22	1.015
TX1261	RS460	RGoM-EI	STA-02	0.27	0.263	0.264	0.2	-2.60	0.40	1.365
TX1262	RS464	RGoM-EI	STA-01	0.48	0.234	0.258	0.2	-0.86	0.97	1.324
TX1264	RS463	RGoM-EI	STA-01	0.31	0.300	0.325	0.2	-1.42	0.85	1.123
TX1265	RS461	RGoM-EI	STA-02	0.34	0.308	0.332	0.2	-2.24	0.71	1.101
TX1268	RS477	RGoM-EI	STA-02	0.22	0.319	0.338	0.2	-0.85	0.70	1.107
TX1269	RS474	RGoM-EI	STA-01	0.09	0.305	0.338	0.2	-1.18	0.79	1.074
TX1270	RS475	RGoM-EI	STA-02	0.16	0.329	0.334	0.2	-0.69	0.95	1.080
TX1271	RS476	RGoM-EI	STA-01	0.05	0.337	0.350	0.2	-0.74	0.87	1.075
TX1273	RS479	RGoM-EI	STA-02	0.20	0.327	0.340	0.2	-0.70	0.81	1.080
TX1276	RS482	RGoM-EI	STA-01	0.07	0.316	0.323	0.2	-0.18	0.87	1.017
TX1279	RS480	RGoM-EI	STA-02	0.15	0.326	0.330	0.2	-0.71	0.84	1.046
TX1282	RS478	RGoM-EI	STA-01	0.08	0.338	0.351	0.2	-0.84	0.94	1.280
TX1287	RS483	RGoM-EI	STA-02	0.19	0.342	0.344	0.2	-0.60	0.99	
TX1288	RS486	RGoM-EI	STA-01	0.08	0.333	0.343	0.2	-0.94	0.94	1.104
TX1290	RS484	RGoM-EI	STA-01	0.28	0.335	0.363	0.2	-0.95	0.86	
TX1292	RS487	RGoM-EI	STA-02	0.20	0.347	0.347	0.2	-0.40	0.91	1.055
TX1295	RS495	RGoM-EI	STA-01	0.19	0.326	0.329	0.2	-0.93	1.00	1.134
TX1298	RS496	RGoM-EI	STA-02	0.22	0.267	0.310	0.2	0.14	0.98	1.065
TX1304	RS504	RGoM-EI	STA-01	0.15	0.329	0.330	0.2	-0.98	0.96	1.070
TX1305	RS510	RGoM-EI	STA-02	5.99	0.392	0.529	0.2	5.48	1.00	0.935
TX1308	RS512	RGoM-EI	STA-01	0.06	0.337	0.348	0.2	-0.97	0.97	1.053
TX1313	RS514	RGoM-EI	STA-01	0.23	0.244	0.288	0.2	-2.18	0.64	1.216

Table 4-4: Summary of low stress triaxial consolidation results

Test No.	At Maximum Vertical Effective Stress							Pre-Drained Shear						
	ε_a %	σ'_v (MPa)	σ'_c (MPa)	e	ε_v %	$K_{0,\,NC}$	Hold stress hr	ε_a %	σ'_v (MPa)	σ'_c (MPa)	e	ε_v %	OCR	K_{OCR}
TX1249	3.82	0.690	0.371	0.703	3.80	0.537	47.12	2.30	0.068	0.069	0.735	1.97	10.20	1.000
TX1250	4.85	0.979	0.521	0.700	4.77	0.532	14.88	3.57	0.095	0.097	0.731	3.00	10.04	1.024
TX1251	8.09	0.925	0.574	0.726	8.13	0.621	25	6.99	0.109	0.111	0.754	6.63	8.79	1.022
TX1252	4.08	0.976	0.542	0.669	4.05	0.556	24.05	2.82	0.099	0.100	0.697	2.42	9.85	1.011
TX1253	4.56	0.958	0.515	0.592	4.42	0.537	24	3.42	0.145	0.102	0.615	3.04	6.60	0.699
TX1254	4.82	0.980	0.551	0.629	4.80	0.562	24.07	3.64	0.097	0.098	0.655	3.28	10.10	1.008
TX1255	5.94	0.996	0.453	0.672	5.74	0.455	30	4.60	0.129	0.105	0.700	4.18	7.71	0.812
TX1256	8.33	0.968	0.569	0.722	8.02	0.588	26.1	6.41	0.096	0.098	0.767	5.62	10.01	1.025
TX1257	4.49	0.768	0.404	0.733	4.42	0.542	24.6	4.20	0.439	0.288	0.740	4.03	1.75	0.657
TX1260	9.58	1.369	0.760	0.827	9.47	0.555	27	9.08	0.547	0.439	0.841	9.01	2.50	0.802
TX1261	17.78	0.777	0.486	0.944	18.06	0.626	28	17.49	0.509	0.380	0.959	17.42	1.53	0.748
TX1262	21.35	0.816	0.534	0.834	21.47	0.654	40	NO SWELLING STAGE						
TX1264	10.92	0.735	0.454	0.891	11.20	0.618	32.4	10.05	0.368	0.301	0.914	10.15	2.00	0.817
TX1265	11.05	0.709	0.434	0.874	11.12	0.613	33	10.13	0.350	0.286	0.895	10.13	2.02	0.817
TX1268	11.01	0.852	0.524	0.874	11.25	0.615	30	10.10	0.424	0.346	0.895	10.21	2.01	0.818
TX1269	12.41	0.855	0.532	0.807	12.97	0.622	30	11.41	0.429	0.353	0.829	11.90	1.99	0.824
TX1270	11.03	0.841	0.523	0.848	11.28	0.623	28.5	10.10	0.416	0.346	0.868	10.31	2.02	0.832
TX1271	11.00	0.928	0.593	0.838	11.46	0.639	29	10.05	0.463	0.392	0.858	10.51	2.01	0.847
TX1273	11.02	0.869	0.539	0.851	11.18	0.620	32	10.08	0.429	0.356	0.874	10.09	2.03	0.831
TX1276	10.93	0.843	0.523	0.792	11.18	0.620	30	10.08	0.421	0.346	0.809	10.34	2.00	0.822
TX1279	11.07	0.816	0.507	0.812	11.53	0.622	30	10.17	0.403	0.336	0.835	10.42	2.02	0.833
TX1282	10.98	0.907	0.562	1.023	11.37	0.620	32	10.06	0.449	0.371	1.045	10.38	2.02	0.825
TX1287	12.71	0.976	0.606		13.07	0.621	36	11.79	0.483	0.401		11.89	2.02	0.830
TX1288	10.93	0.808	0.505	0.868	11.29	0.625	30.7	10.03	0.403	0.335	0.892	10.18	2.00	0.830
TX1290	12.07	0.974	0.610		12.26	0.626	29	11.19	0.484	0.403		11.33	2.01	0.831
TX1292	11.91	0.976	0.612	0.807	12.22	0.627	44.8	NO SWELLING STAGE						
TX1295	13.00	0.968	0.589	0.855	13.24	0.608	118.5	NO SWELLING STAGE						
TX1298	13.05	0.967	0.577	0.785	13.73	0.597	37	12.17	0.483	0.381		13.45	2.00	0.597
TX1304	11.30	0.982	0.708	0.919	12.45	0.721	72	NO SWELLING STAGE						
TX1305	13.22	0.870	0.497	0.754	14.75	0.572	30	12.42	0.433	0.330	0.771	13.96	2.01	0.763
TX1308	11.34	0.980	0.620	0.915	11.92	0.633	123	10.49	0.487	0.413	0.989	10.92	2.01	0.848
TX1313	10.74	0.484	0.289	0.979	10.91	0.598	38	9.97	0.238	0.167	1.003	9.81	2.04	0.702

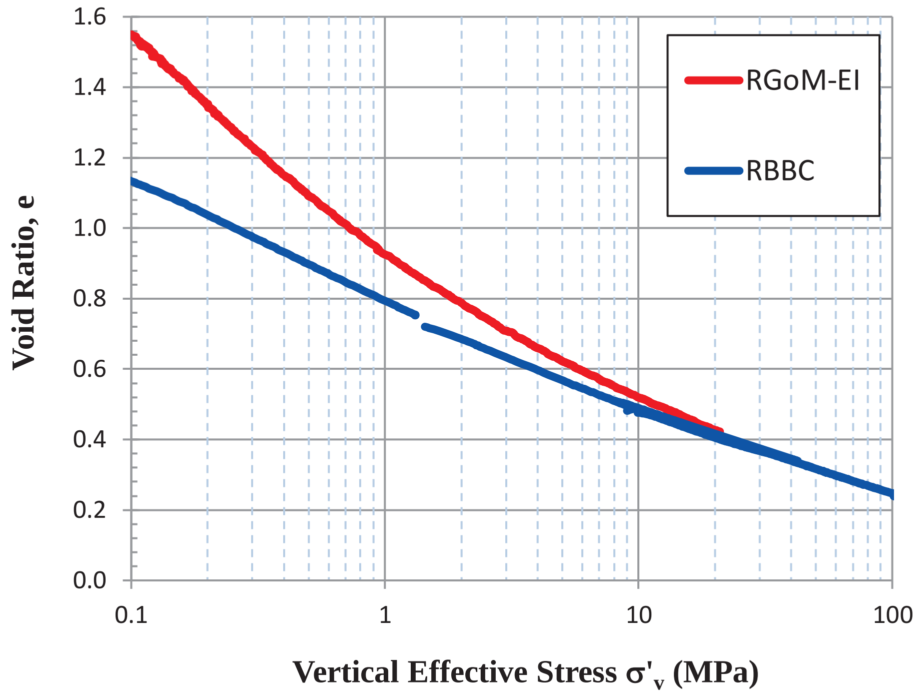

Figure 4-18: One dimensional virgin compression behavior of soils obtained from CRS tests ran by Casey (2014)

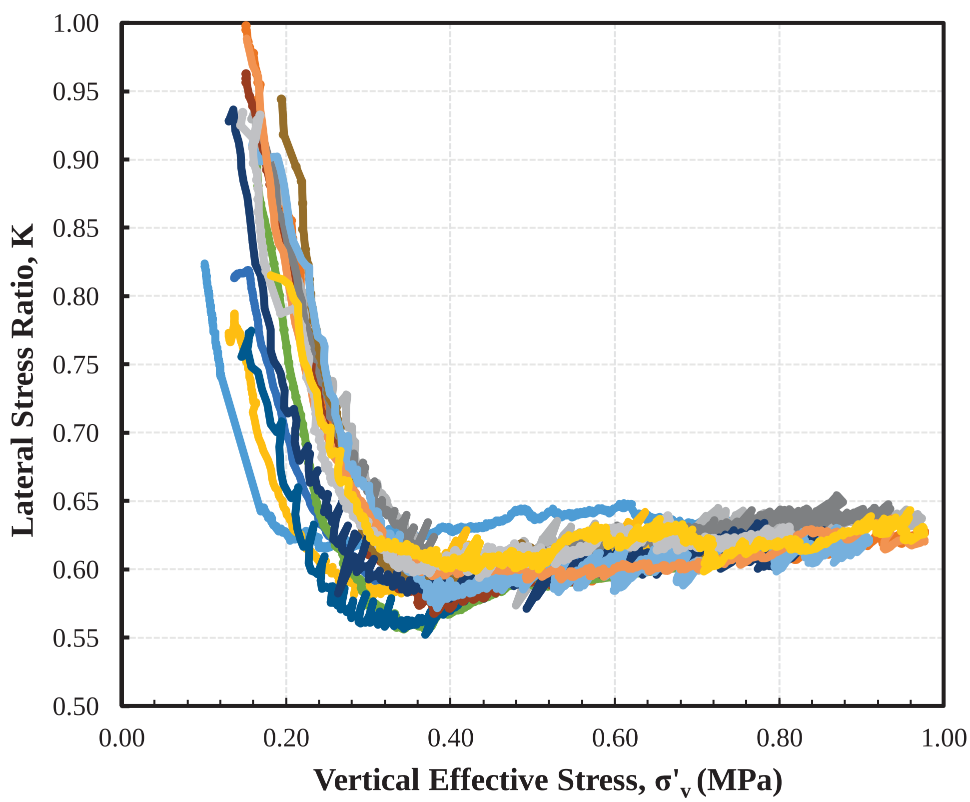

Figure 4-19 : The variation in measured K_0 during the consolidation phase of selected triaxial tests performed on RGoM-EI

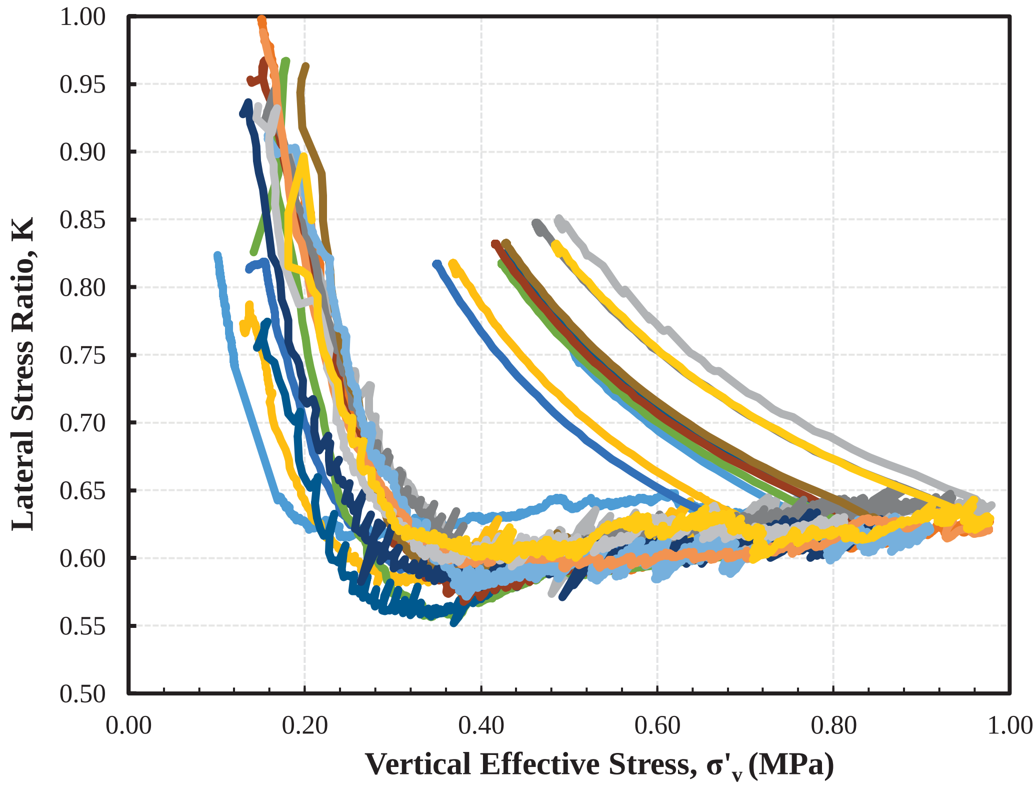

Figure 4-20: The variation in measured K_0 during the consolidation and swelling phases of selected triaxial tests performed on RGoM-EI

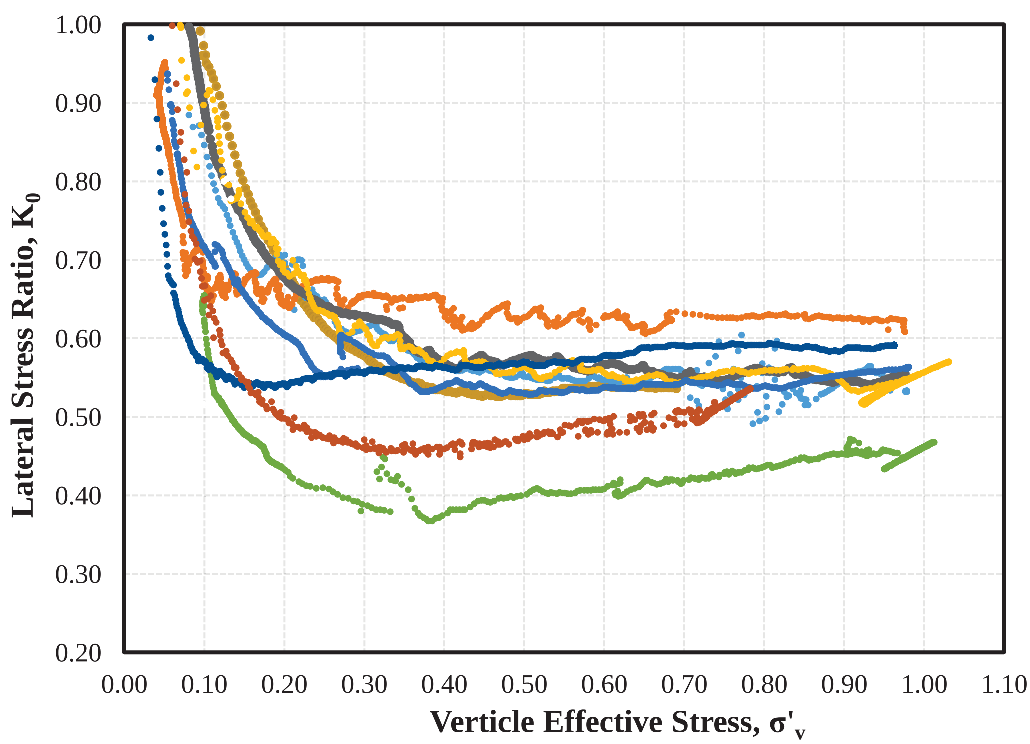

Figure 4-21: The variation in measured K_0 during the consolidation phase of triaxial tests performed on intact BBC specimens

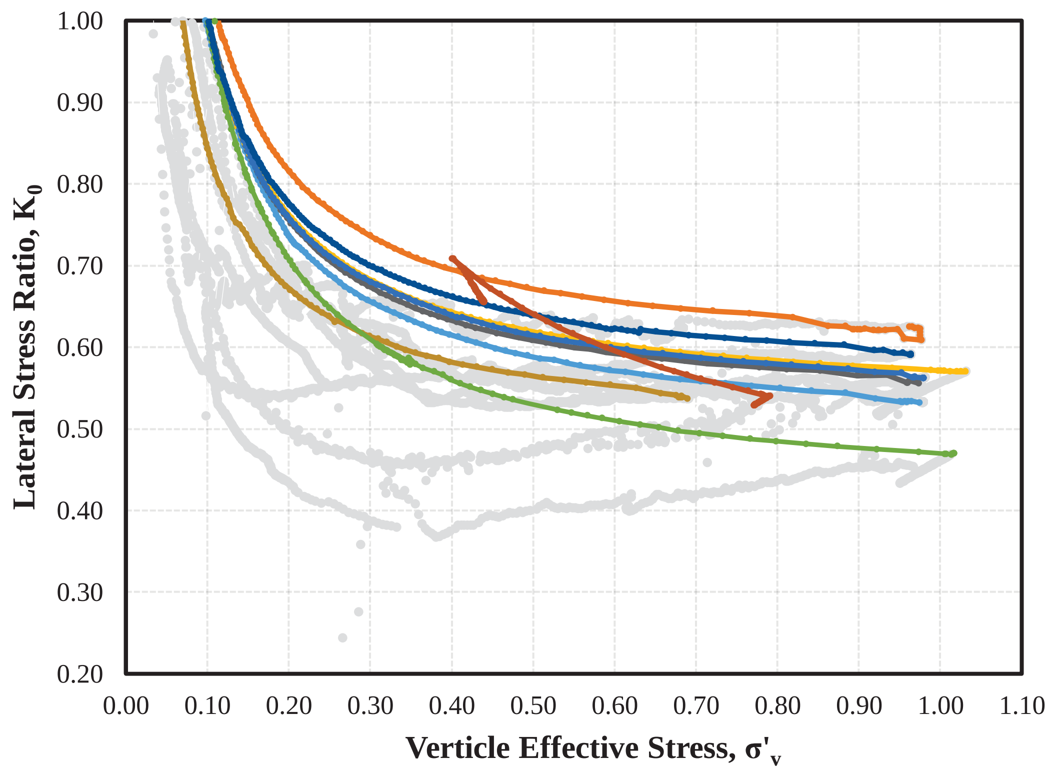

Figure 4-22: The variation in measured K_0 during the swelling phases of triaxial tests performed on intact BBC specimens

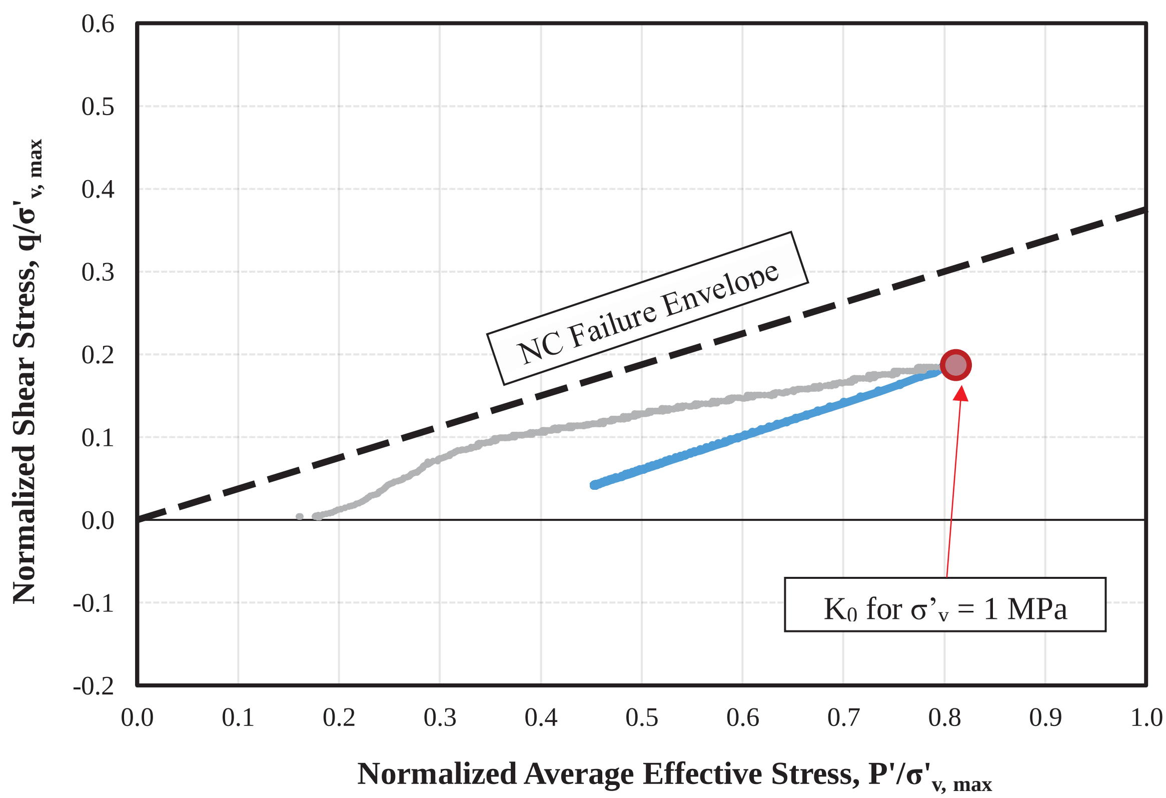

Figure 4-23: K_0 consolidation loading and K_{OCR} unloading stress paths of a single RGoM-EI triaxial test plotted in MIT stress space

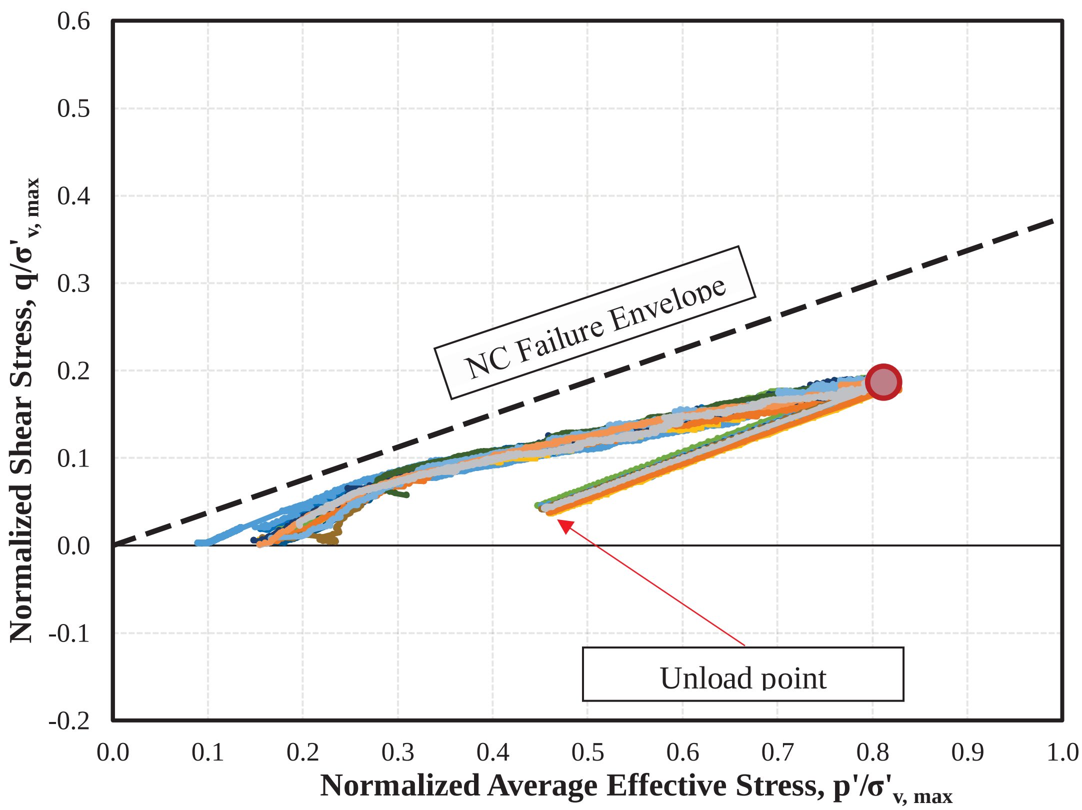

Figure 4-24: Combined K_0 consolidation loading and K_{OCR} unloading stress paths of selected RGoM-EI triaxial tests plotted in MIT stress space

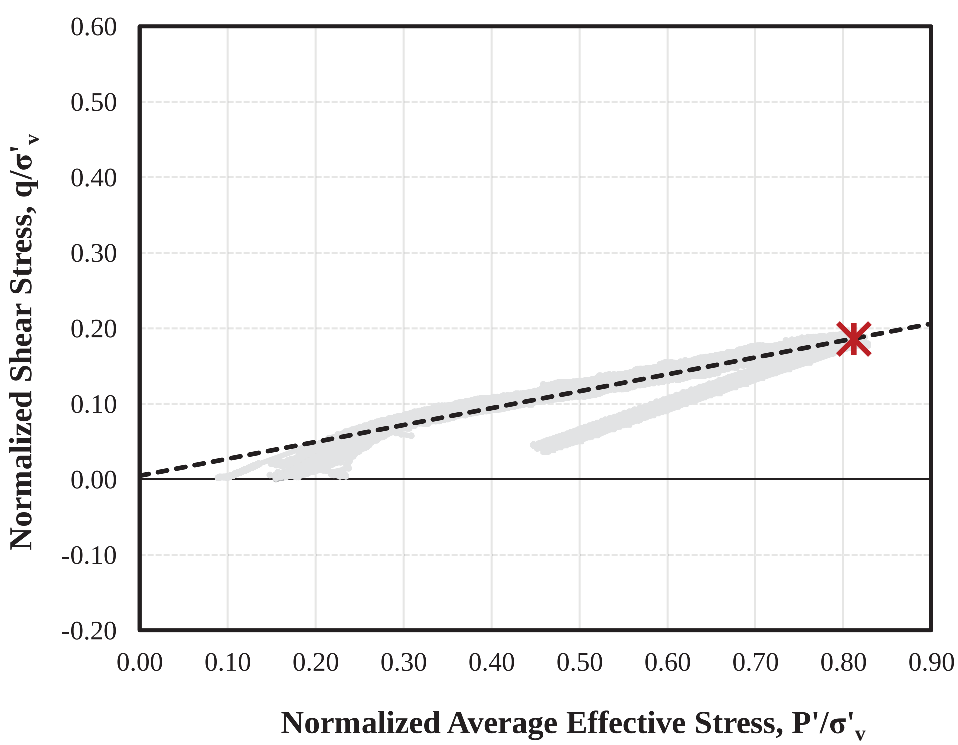

Figure 4-25: Linear regression line of constant K_0 through the K_0 consolidation loading paths shown in Figure 5-7

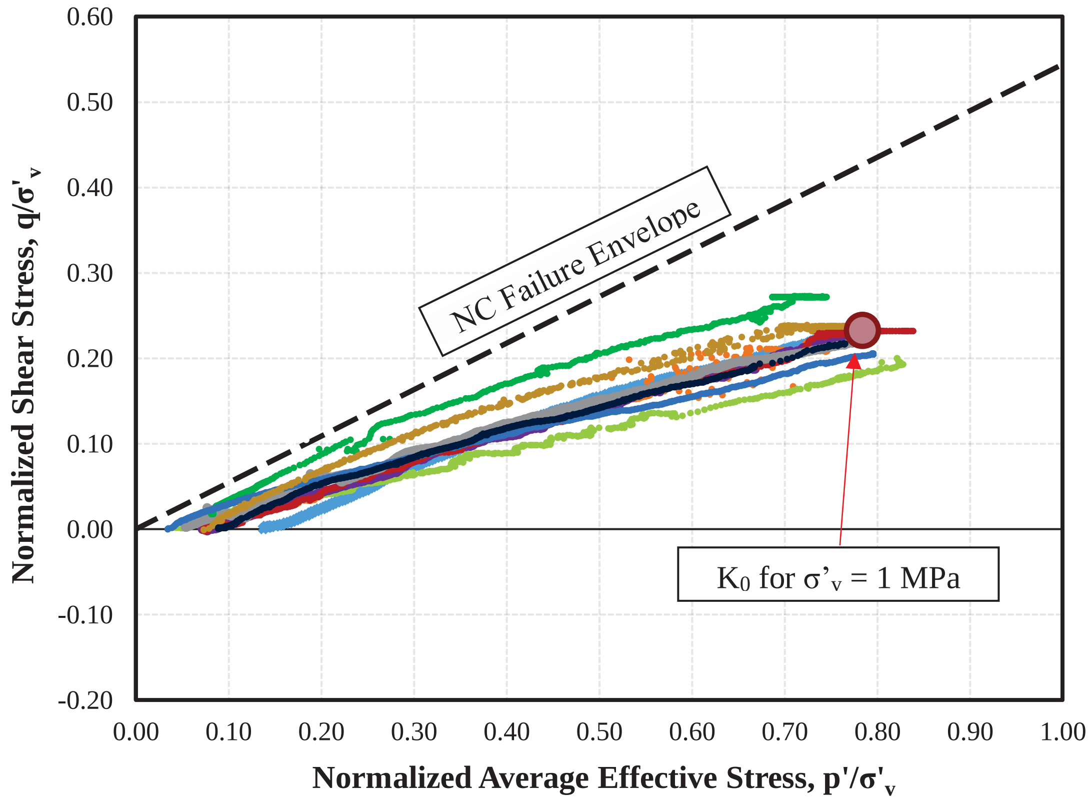

Figure 4-26: K_0 consolidation loading stress paths of intact BBC triaxial tests plotted in MIT stress space

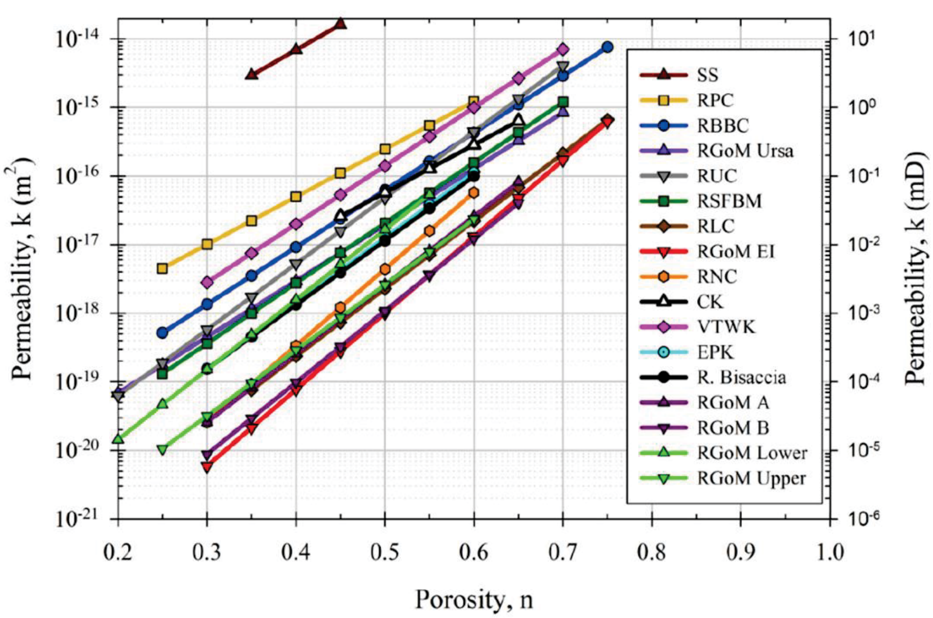

Figure 4-27: Permeability-porosity relationships for various soils determined by Casey (2014)

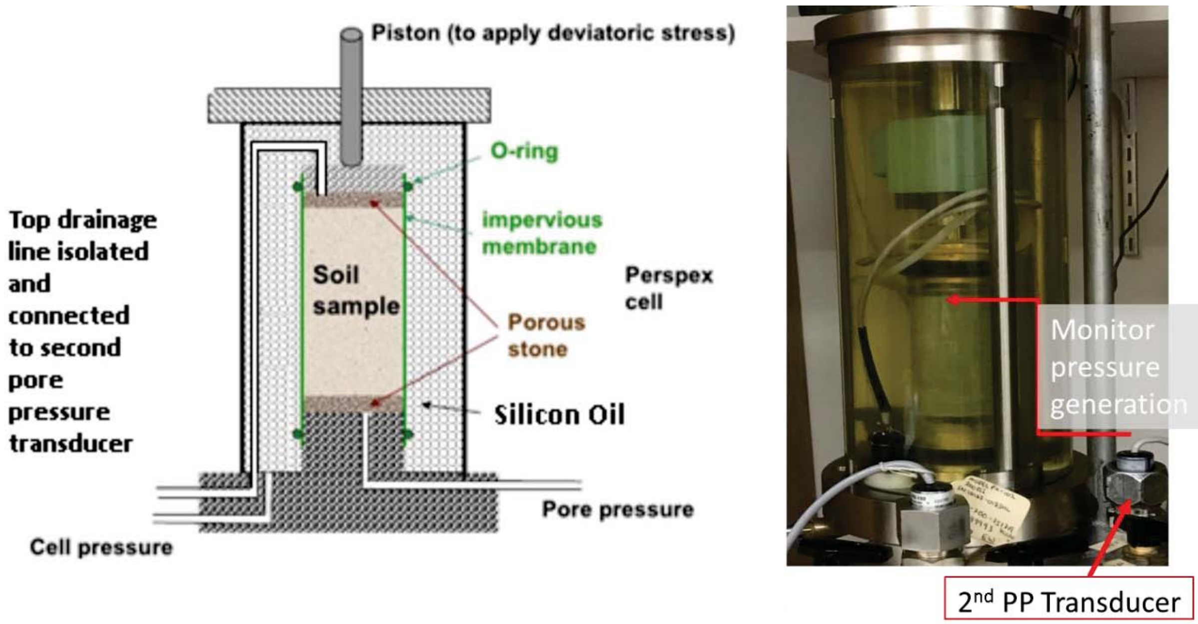

Figure 4-28: Schematic of modified triaxial cell & image of actual modified triaxial device

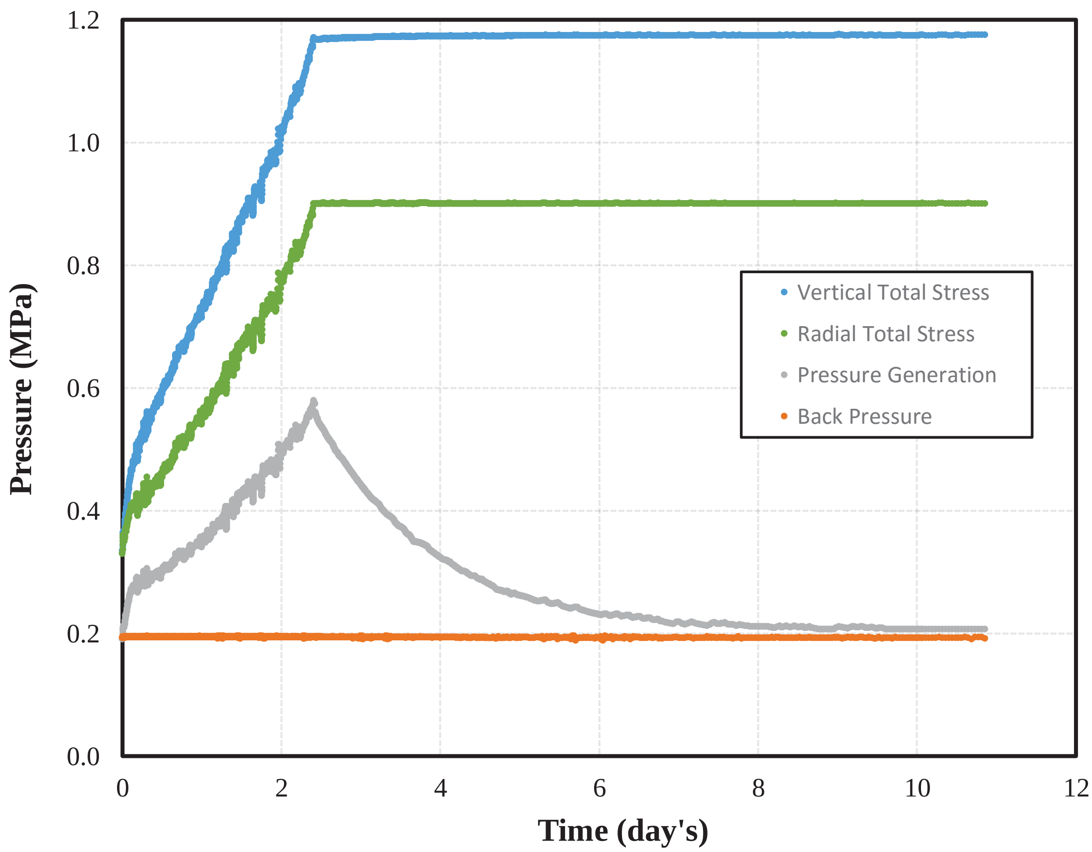

Figure 4-29: Experimental results derived from a one-way drainage K_0 consolidation and hold stress portion of a low stress triaxial test on RGoM-EI

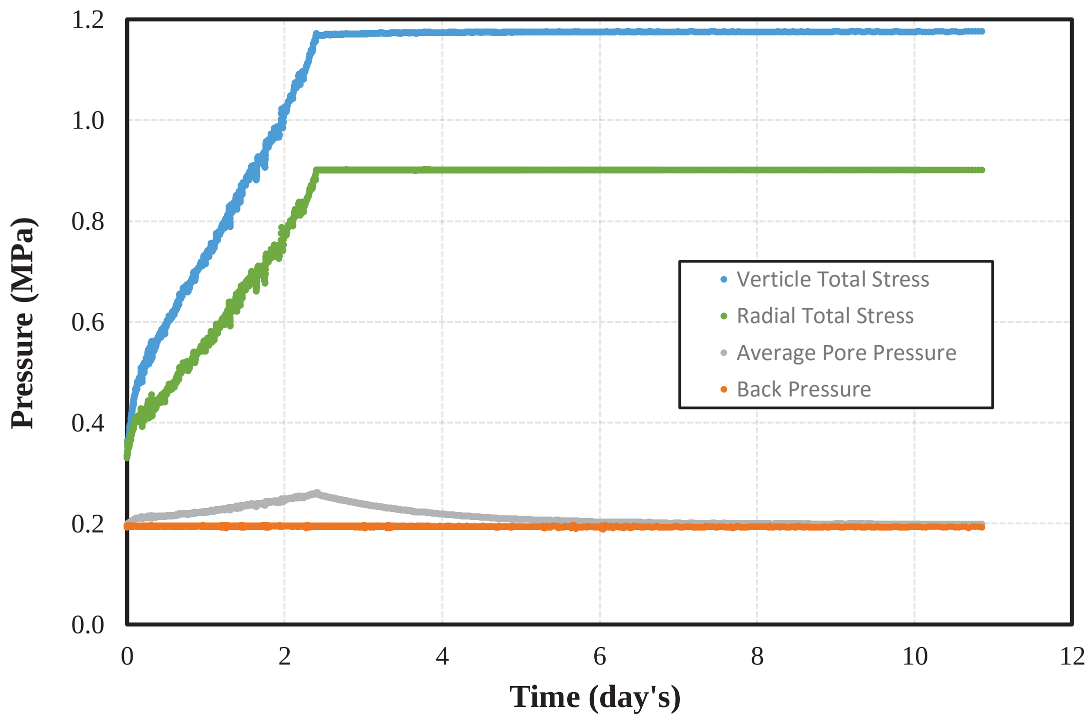

Figure 4-30: Predicted pore pressure generated in a two-way draining RGoM-EI specimen during the K_0 consolidation and hold stress portion of a low stress triaxial test

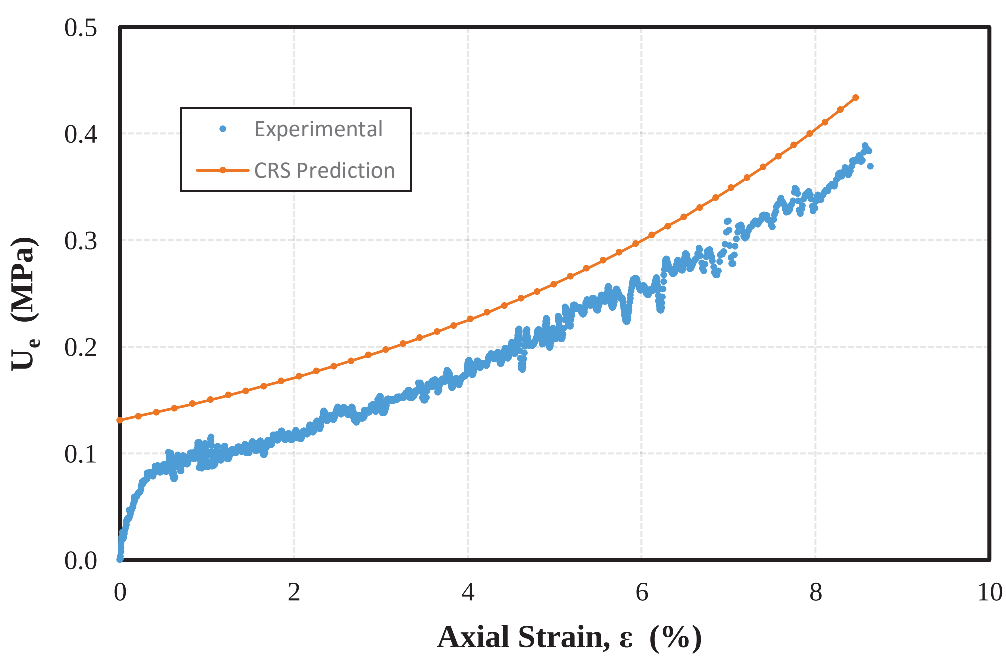

Figure 4-31: Comparison of experimental results and CRS predicted results for internal pore pressure generation in a low stress triaxial test on RGoM-EI

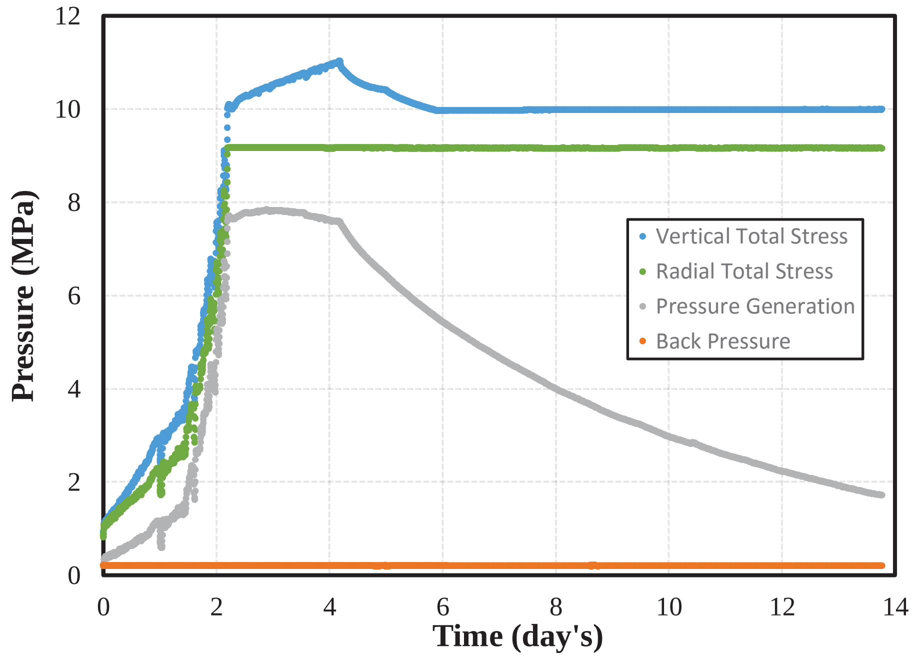

Figure 4-32: Experimental results derived from a one-way drainage K_0 consolidation and hold stress portion of a medium stress triaxial test on RGoM-EI

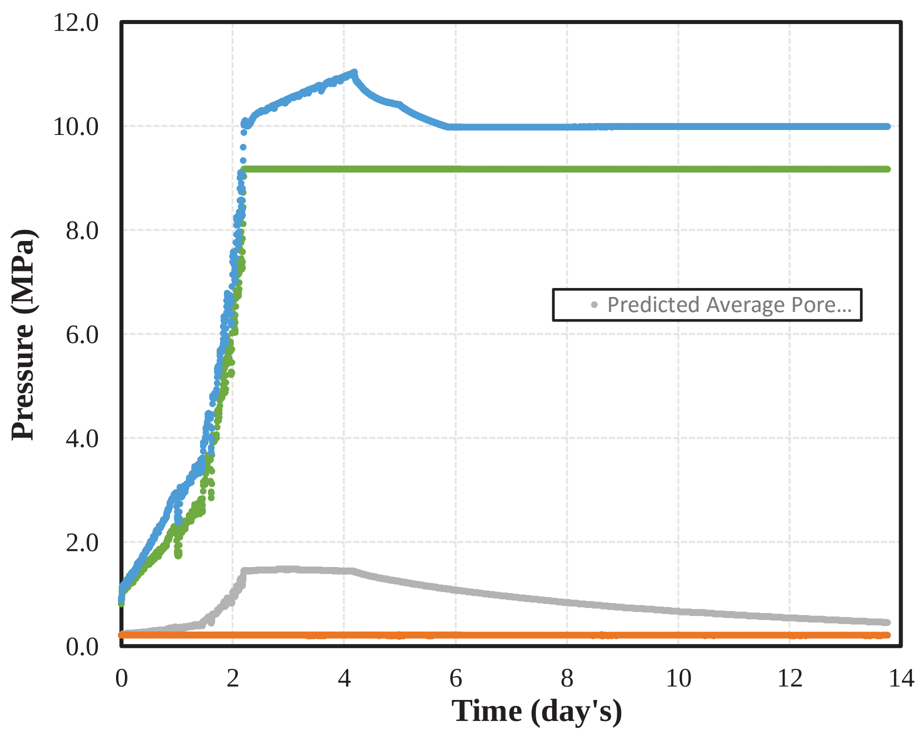

Figure 4-33: Predicted pore pressure generated in a two-way draining RGoM-EI specimen during the K_0 consolidation and hold stress portion of a low stress triaxial test

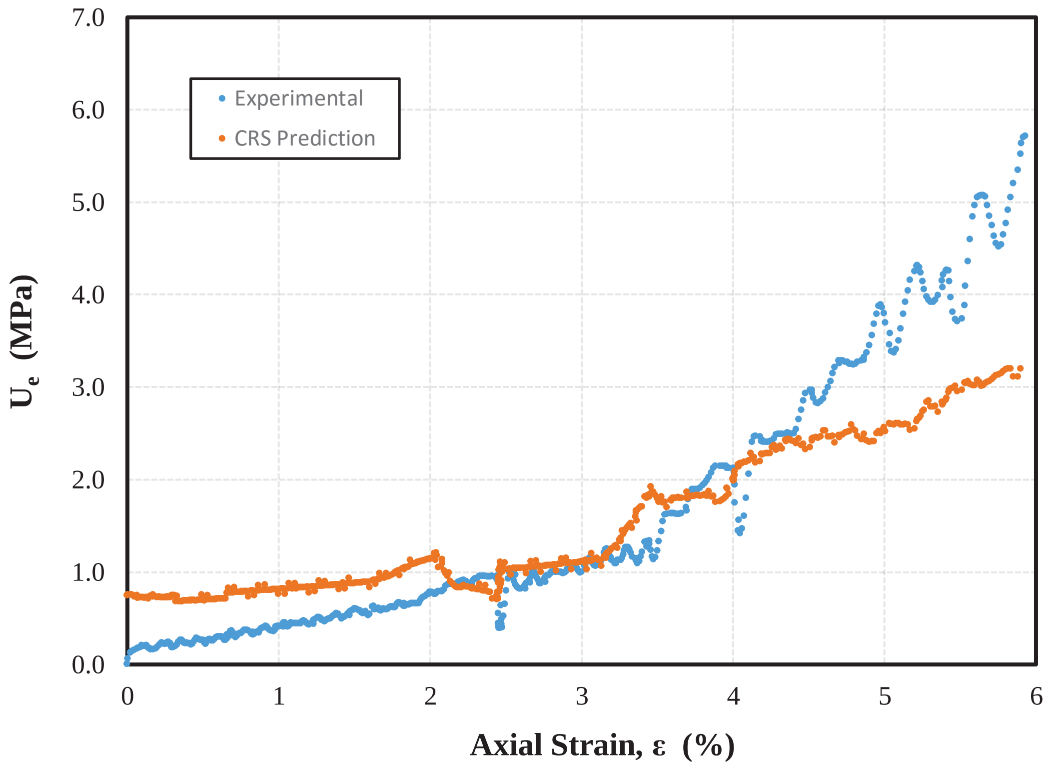

Figure 4-34: Comparison of experimental results and CRS predicted results for internal pore pressure generation in a medium stress triaxial test on RGoM-EI

6 DRAINED SHEAR RESULTS

6.1 INTRODUCTION

This chapter presents the results obtained during the drained shear phase of low stress triaxial tests carried out during the course of this research. Section 6.2 describes in detail, the methods used to interpret yielding transition zones and best estimate yield points, for both materials, in normalized MIT stress space. Section 6.3 briefly describes the effects of secondary compression on the interpreted yield surface and how the hold stress phase at the end of the consolidation phase contributes to secondary compression effects. Section 6.4 compares undrained effective stress path test results to the interpreted yield surface obtained from drained results. Section 6.5 evaluates the failure planes observed on specimens and compares them to the Mohr Coulomb failure criterion. Section 6.6 evaluates the volumetric strain of specimens post yielding, and compares the stiffness's observed in both extension and compression. Section 6.7 compares the interpreted yield surfaces to one another. Finally, Section 6.8 discusses the comparison of the interpreted RGoM-EI yield surface to model formulations.

6.2 INTERPRETING YIELDING

In order to characterize the yield surface, specimens are drained sheared a long different stress paths from their corresponding unload points. (Unload point shown in Figure 5-7 in normalized MIT space). Figure 6-1 plots a single triaxial compression loading stress path in MIT stress space. The K_0 consolidation and $K_{0,\ OCR}$ stress paths are also shown for completeness. Equation 2-1 was modified to account for three dimensional straining effects:

$$W_j = \sum_{m=1}^{j} \left(\left(\frac{\sigma'_{v,m}+\sigma'_{v,m-1}}{2} \right) \left(\ln \frac{1-\varepsilon_{a,m-1}}{1-\varepsilon_{a,m}} \right) + 2 \left(\frac{\sigma'_{r,m}+\sigma'_{r,m-1}}{2} \right) \left(\ln \frac{1-\varepsilon_{r,m-1}}{1-\varepsilon_{r,m}} \right) \right) \qquad (6\text{-}1)$$

Where:

W_j = work per unit volume of the specimen up to increment j (kN-m/m^3)
j = index value for stress increment (integer)
$\sigma'_{v,m}$ = vertical effective stress at current increment (MPa)
$\sigma'_{v,m-1}$ = vertical effective stress at previous increment (MPa)
$\varepsilon_{a,m}$ = axial strain at current increment (decimal)
$\varepsilon_{a,m-1}$ = axial strain at the previous increment (decimal)
$\sigma'_{r,m}$ = radial effective stress at current increment (MPa)
$\sigma'_{r,m-1}$ = radial effective stress at previous increment (MPa)
$\varepsilon_{r,m}$ = radial strain at current increment (decimal)
$\varepsilon_{r,m-1}$ = radial strain at the previous increment (decimal)
m = index used in summation (integer)

Equation (6-1) allows the energy absorbed by the specimen to be continuously monitored as the specimen undergoes drained shear along any stress path. This absorbed energy is then plotted against the specimens stress path vector. Plotting the absorbed energy against stress path vector is advantageous as it allows for comparison of infinitely different loading conditions in a uniform fashion. Because, normalized MIT stress space is being used, both the Strain Energy and the stress path vector are normalized by the consolidation stress of~1 MPa (depending on each specimen's individual consolidation history). Figure 6-2 plots the normalized strain energy absorbed by the specimen against its unique normalized stress path vector. The figure shows that there appears to be an initial linear region, followed by a transitional curved region as the specimen transitions to plastic deformation, and then finally a somewhat linear plastic region as the specimen continues to undergo large deformations with increasing load. A scaled image of the initial portion of the plot is also superimposed on the image. The scaled image shows that the results are constantly curving from the beginning of the shearing process. However, since this initial curve appears to be somewhat linear on a larger scale, in comparison to the more clearly defined transition curve to plastic deformation, for the analysis of the results this initial slightly curved portion is taken to be representative of a linear region.

To accentuate changes in the transition from the initial curved portion to the transition to larger deformations, the normalized stress path vector axis in Figure 6-2 is transformed into a logarithmic scale. Figure 6-3 plots the results of this transformation. This graph shows a much clearer liner initial stage, followed by a significant energy absorption region, and linear plastic region, than that shown in Figure 6-2. Similar to Figure 6-2, a scaled image of the initial portion of the results is superimposed on Figure 6-3. A point is taken just before the onset of the transitional period in this scaled image graph, signified by the blue point at an x-axis value of 0.03. This point is also plotted on the unscaled plot for clarity. This point obtained from the semi log plot is then transformed back into normalized natural stress space and used to define a linear elastic line. Figure 6-4 shows this point transferred back into real space (blue point), it also shows the interpreted linear elastic region (shown as a blue line drawn from the origin to the blue point). This line is then extrapolated outwards until it meets a best fit line drawn through the plastic deformation region. These lines are shown as two black hatched lines, the intersection of these lines is taken as the best estimate yield point, having a value of~0.29 on the normalized stress path vector axis (shown as a gold star).

The yield point obtained is dependent on where one chooses to fit the best estimate line through the linear elastic region and plastic region. Transferring the point just before curvature takes place in the semi log plot (blue point Figure 6-3) produces, a consistent estimate of the pre-yield line. This method eliminates the need for estimation of the elastic region in real space, and has been adopted for the analyzation of all test results as part of this work. The line drawn through the plastic region is not as easily defined, and its position can vary depending on the scale used when analyzing the results. To overcome this issue, the author proposes that a yield transition be used instead of a single yield point. This is done by magnifying the early part of the curve plotted in Figure 6-4 to determine a minimum yield point, and then increasing the scale, to plot all data up peak stress, to determine a maximum yield point. Figure 6-5 plots the magnification of the results. The method used to interpret the yield point is exactly the same as described above in Figure 6-4. This minimum interpreted yield point has a value of~0.27 on the normalized stress path vector axis. Figure 6-6 plots all of the data beyond failure of the specimen. Again, the yield point was determined using the same method described above. The maximum interpreted yield point has a value of~0.32 on the normalized stress path vector axis.

Figure 6-7 combines the minimum, best estimate, and maximum yield points obtained from figures 6-4, 6-5, and 6-6. This figure clearly shows the three lines that could be drawn through the data set to obtain a yield range, consisting of minimum, maximum, and best estimate yield points. Figure 6-8 plots the yield range shown in Figure 6-7 on the drained shear stress path shown in Figure 6-1, in MIT stress space. The best estimated yield surface point is the first interpreted point on the predicted yield surface. The minimum and maximum point's show the range at over which yield transitioning is taking place. This method of interpretation is repeated for each test to characterize the yield surface in MIT stress space.

The size of the interpreted yield transition zone varies with stress path direction. Figure 6-9 plots normalized volumetric strain energy plot for a triaxial extension loading test (drained stress path travels at 45^{o} below the isostatic axes in MIT stress space). The energy curve obtained from this stress path displays a more gradual transition period that that shown in Figure 6-7. This corresponds to the interpreted yield transition zone from Figure 6-9 being significantly larger than that that observed in Figure 6-7. The corresponding interpretation plots of all tests are shown in

Appendix A. Table 6-1 summarizes the interpreted yield transition zones and best estimate yield points for all test specimens.

Figure 6-10 plots each individual drained shear stress path for the tests carried out on RGoM-EI. It can be seen from this figure that all tests start from the same point, with the exception of one extension loading test that started from an OCR of 1.5 (TX1261), and one extension unloading test that started directly from the consolidation stress of 1MPa (TX1292). These two tests were carried out to analyze the effect of OCR on the interpreted yield surface. Figure 6-11 plots all the best estimate yield points and yielding transition regions superimposed onto the drained stress paths shown in Figure 6-10. Figure 6-11 also plots a best estimate interpreted yield surface and interpreted failure lines for both extension and compression.

Figure 6-11 highlights the anisotropy associated with the RGoM-EI yield surface. It is not symmetrical along the isostatic axis, nor is it symmetrical about its K_0 consolidation axis. It is somewhat elliptical in shape and appears not to trace back to the origin. The yielding transition regions are much smaller above the K_0 consolidation axis than they are below. Above the K_0 consolidation axis yielding takes place more rapidly with small changes in stress. Below the K_0 consolidation axis the material appears to be stiffer and yielding takes place over a larger stress change. Figure 6-11 also shows the stress changes that each specimen undergoes after yielding before reaching the interpreted failure lines. On the compression side of the yield surface, specimens undergo relatively lower changes in stress post yielding prior to failure, than what they do on the extension side of the yield surface. It is important to recognize that the failure envelopes shown in Figure 6-11 are the results of a best fit line through the termination points of specimen shear stress paths. It is also important to note that these failure lines have an OC effected associated with them, in that specimens were unloaded to an OCR of two prior to shearing. Specimens sheared at lower stresses would then show increased strength due to the effects of their previous consolidation history (Ladd, 1992).

From Figure 6-11, it can be seen on both the extension and compression side of the yield surface that some stress paths were heading towards failure, but the plotted stress paths never reached failure. This is because the triaxial apparatus had reached its capacity and the tests had to be terminated early. If the loading conditions were continued, these stress paths would continue to undergo shear deformation until reaching the failure envelops. Some drained shear stress paths, particularly those around the isostatic axis, can be seen to be travelling at such shallow angles that they would never come into contact with the failure envelops. These tests were also terminated when the system reached capacity. Specimens being sheared along these stress paths will never reach failure. They will continue to undergo shear deformations and densification with increasing changes in applied stress. Two of the stress paths on the compression side of the surface that can be seen not to reach the interpreted compression failure line. These two tests were terminated early due to power outages associated with ongoing construction in Tufts University.

6.2.1 Interpreted yield surface for Boston Blue Clay

The characterization of the BBC yield surface was done using the same method described above. However, during the consolidation process of BBC specimens, the majority of specimens were unloaded to an OCR of 10. Figure 6-12 plots the drained shear stress paths of all intact BBC specimens tested as part of this work. One test (TX1257) was unloaded to an OCR of 2, to assess the effects of OCR on the Yield Surface. Another test (TX1260R) was carried out on a resedimented sample that was unloaded to an OCR of 2.5. All tests were drain sheared until failure, or until the system had reached capacity. Similar to RGoM-EI, a linear OC failure envelope was drawn through the termination points of all the failed specimens on both the extension and compression sides. All tests carried out on the compression side failed on this OC failure envelope, independent of their OCR. One triaxial extension loading test was terminated early due to a power shut down in the Laboratory, its stress path can be seen to terminate at; $p/\sigma'_{vm} \approx 0.35$, $q/\sigma'_{vm} \approx -0.1$.

Figure 6-13 plots the interpreted yield surface for BBC in MIT stress space. The surface is seen to have a complex geometry that may be described as being somewhat elliptical, being linear on the compression side. Similar to RGoM-EI, the BBC yield transition ranges are much smaller above the K_0 consolidation axes than below the axis. However, at lower stresses on the extension side of the surface, these yield transition zones begin to condense again. One triaxial compression loading test (identified by the orange stress path), sheared at higher confining stresses, appears to have a larger yield transition zone. This is believed to be due to the shallow angle at which the specimen was sheared at in relation to the yield surface. The stress path can be seen to travel along the yield surface momentarily ($p/\sigma'_{vm} \approx 0.52$, $q/\sigma'_{vm} \approx 0.25$ – $p/\sigma'_{vm} \approx 0.57$, $q/\sigma'_{vm} \approx 0.27$), and hence increase the interpreted transition zone, making yielding more difficult to interpret.

6.3 SECONDARY COMPRESSION EFFECTS ON THE YIELD SURFACE

Figure 6-14 plots the RGoM-EI end of K_0 consolidation point for $\sigma'_v = 1$ MPa, and the interpreted RGoM-EI yield surface in Normalized MIT stress space. The interpreted yield surface is seen to be offset outwards from the K_0 consolidation point (i.e. previous max stress history point). This is believed to be due to the effects of secondary compression which takes place during the 30 hour hold stress cycle the end of the K_0 consolidation procedure. During this hold stress cycle, the specimen continuous to undergo strain deformations as the stress being applied is kept constant. This effect causes the yield surface to evolve or push outwards, and this is believed to cause the interpreted yield surface to extend beyond the maximum previous stress point. However, the K_0 consolidation point does fall within the interpreted yield transition zone, and so, while the effects of secondary compression are considered to be consistent with what we understand for clays, due to the low hold stress times (30 hours), the magnitude of secondary compression is not considered to be high enough to have a significant effect in this research.

Figure 6-15 plots the BBC K_0 consolidation point of 1 MPa and the interpreted BBC yield surface in Normalized MIT stress space. No tests were successfully drain sheared through the cap of the yield surface, so the K_0 consolidation stress point was used as a yield point on the interpreted yield surface. Taking the results from Figure 6-14 into consideration, it is expected that the cap of the interpreted yield surface would also be slightly shifted outwards due to the secondary compression effect. But as the RGoM-EI K_0 point fell inside the transition region in Figure 6-14, the BBC K_0 consolidation point was used as a best estimate yield point to avoid estimating an approximate offset yield point.

6.4 UNDRAINED EFFECTIVE STRESS PATHS AND THE YIELD SURFACE

Historically, the trace of the NC undrained compression and extension stress paths have been taken as near approximations of the trace of the yield surface. Figure 6-16 combines the results obtained from this work on RGoM-EI with a low stress NC undrained compression stress path for RGoM-EI (TX1175), obtained from Fahy (2014). The undrained effective stress path begins at the K_0 consolidation, which signifies repeatability between this work and the work of Fahy (2014). It then moves to just outside the interpreted yield surface as undrained shearing commences, and begins to trace the cap of the interpreted yield surface as it shears to failure. Failure of the NC undrained compression stress path takes place at a normalized p', q value of~ 0.56, 0.22 respectively. It does not fail at the interpreted compression failure envelope, this is because the

Interpreted failure envelope has been offset due to the effects of OC, as mentioned previously. However, for the most part, the undrained compression stress path is within the yielding transition region, and therefore can be concluded to be a good first order approximation of the cap of the yield surface. An undrained extension stress path is not available for RGoM-EI material.

Figure 6-17 combines the results obtained from this work on intact BBC with low stress NC undrained compression and extension stress paths for RBBC, obtained from Casey (2014). The two stress paths start at a different stress point, because the K_0 consolidation stress point is not the same as the point obtained in this work. It is believed that this is due to variations in K_0 values obtained during the consolidation process, as Casey used resedimented samples, whereas the samples used as part of this work were intact, and an average value of K_0 from all tests was used. Similar to RGoM-EI, the undrained compression stress path provides a first order approximation of the cap of the interpreted yield surface. It also fails before the interpreted OC failure envelope. The undrained extension stress path does not trace the interpreted yield surface. As the undrained specimen is sheared in extension, it is believed to strain harden and continuously shift the yield surface outwards until failure of the specimen occurs. The extension stress path also appears to fail at the interpreted OC extension failure envelope. At this point the stress path has strain hardened to well outside the maximum yield points in the low stress extension region.

6.5 GEOMETRY OF FAILED SPECIMENS

6.5.1 RGoM-EI

Figure 6-18 shows a select number of the RGoM-EI specimens that were sheared to failure in both extension and compression. The images of the failed specimens have been super imposed upon their individual drained shear stress paths, in normalized MIT stress space, for clarity purposes. Specimens that were drain sheared to failure in compression, below normalized average stresses of~0.4, displayed dramatic shear failure planes and little change in cross sectional area or bulging. Specimens that were sheared to failure in compression, between normalized average stresses of~0.45-0.7, displayed both dramatic shear failure planes and significant bulging in the middle of specimens. The bulging effect increased as confining pressure increased. Specimens that were sheared to failure in compression under normalized average effective stresses above~0.7, displayed no shear failure planes, but displayed excessive bulging. Specimens that were drain sheared to failure in extension displayed reductions in cross sectional area and shallow shear failure planes. The cracking shown in the specimen that failed in extension occurred during the oven drying process.

6.5.2 BBC

Figure 6-19 shows a select number of BBC specimens that were sheared to failure in both extension and compression. The images of the failed specimens have also been super imposed upon their individual drained shear stress paths, in normalized MIT stress space, for clarity purposes. Similar to the RGoM-EI specimens, failure planes are observed to be: dramatic with no bulging below normalized average effective stresses of~0.3, and dramatic with minor bulging between normalized average effective stresses of~0.3-0.5. No failure plane was observed in the specimen that was sheared to failure at high confining stresses (above~0.55), significant bulging was observed in the specimen mid-section. Shallow failure planes were observed in both specimens that were sheared to failure in extension. A small reduction in cross-sectional area was also observed in both specimens.

6.5.3 Mohr Coulomb Failure Criterion

The Mohr Coulomb Failure Criterion equation predicts that specimens sheared to failure would exhibit failure planes inclined at angle, θ, dependent upon the materials ϕ' and if the specimen was sheared in compression or extension:

$$\theta = 45^{o} \pm \frac{\varphi'}{2} \tag{6-2}$$

Where ϕ' is the materials friction angle. Specimens sheared in compression are predicted to display failure planes inclined at 45^{o} plus the addition of the friction angle term. Specimens sheared to failure in extension are predicted to display failure planes inclined at 45^{o} minus the friction angle term. Failure planes observed in both RGoM-EI and BBC specimens showed good agreement with the Mohr Coulomb Failure Criterion equation. BBC specimens displayed average shear failure planes inclined at~63^{o} and~28^{o} in compression and extension respectively. This is consistent with a 34^{o} friction angle of BBC. RGoM-EI specimens displayed average shear failure planes inclined at~ 56^{o} and 34^{o} in compression and extension respectively. This is consistent with normally consolidated RGoM-EI having a friction angle of 22^{o}.

6.6 CONTOURS OF VOLUMETRIC STRAIN INCREMENTS BEYOND YIELD SURFACE

Figure 6-20 shows contours of volumetric strain increments plotted on specific RGoM-EI stress paths in MIT stress space, which were sheared well beyond the yield surface. These contours points were obtained by resetting the volumetric strain increment measured on a test specimen to zero once it had reached the best estimate yield point (i.e. yellow star on drained stress path of interpreted red yield surface). The volumetric strain increment was then measured continuously as the specimen was drained sheared. Specific values of volumetric strain were chosen for contour lines, and plotted along the specimens drained shear stress path. The process was then repeated for six other tests, in both compression and extension. Tests were chosen that had significant post yield increments of stress change. One of the tests shown in Figure 6-20 was drain sheared in a direction parallel to the isostatic axis (i.e. p' axis). This test was terminated early, and so the volumetric strain points of 1% and 1.5% were obtained by linear extrapolation. The volumetric strain contours were constructed by joining the data points plotted with straight lines. In reality, these lines would be expected to be continuous curves similar to the interpreted yield surface. The contours show that above the K_0-consolidation axis, the material is much softer. The material undergoes large changes in volumetric strain with relatively small changes in stress, signified by the converging volumetric strain contours. Below the K_0-consolidation axis the material becomes much stiffer undergoing much larger changes in stress to achieve the same associated volumetric strains. This is signified by the broadening of the volumetric strain contours. Below the isostatic axis, the material begins to soften again, signified by the converging of the strain contours. However, the contours do not converge as closely on the extension side of the yield surface as they did above the K_0-consolidation axis. This suggests that the material is stiffer in extension than in compression above the K_0-consolidation axis. The material is stiffest in the direction of the normalized average effective stress axis. Increasing shear stress then leads to contraction of the structure once the material is normally consolidated.

The plotted contours of volumetric strain in Figure 6-20 provide a good insight into the variability of the transitional yield ranges. In compression above the K_0-consolidation axis, the yield transitions are smaller, and this is supported by the larger changes in volumetric strain observed with smaller changes in stress. Below the K_0-consolidation axis the yield transition zones are larger and yielding is more difficult to interpret. This is supported by the broadening of the strain contours, with larger confining stress changes needed to achieve the necessary strain changes to interpret yielding. This is also a good explanation as to why more gradual changes are seen in the strain energy curves below the K_0-consolidation axis. The procedure was not repeated for the intact BBC surface, as there were an insufficient amount of appropriate shear stress paths

6.7 COMPARISON OF YIELD SURFACES

6.7.1 Comparison of Interpreted BBC and RGoM-EI Yield Surfaces

Figure 6-21 plots the interpreted yield surfaces for both intact BBC and RGoM-EI in normalized MIT stress space. The interpreted failure lines of BBC and RGoM-EI are plotted in green and black respectively. The two interpreted yield surfaces vary in a number of ways. The RGoM-EI surface is rotated downwards, closer to the isostatic axis. This is due to the higher K_0 value at the end of consolidation. RGoM-EI had typical K_0 values~0.62 at the end of consolidation compared to K_0 values of 0.55 observed in BBC specimens. The BBC yield surface is also significantly more linear than the RGoM-EI surface along the compression side of the surface. The RGoM-EI surface also seems to converge towards the isostatic axis at lower stresses, it appears to have permanent deformation associated with it (i.e. it does not appear to trace through the origin). The intact BBC surface appears to trace through the origin. The RGoM-EI yield surface is much broader, this could be due to the differences in the clay mineralogy, RGoM-EI being a dominantly smectitic clay, compared to BBC, which is a dominantly ilitic material. It could also be due to the large difference in liquid limits. BBC is classified as a low plasticity clay, whereas RGoM-EI is classified as a high plasticity clay.

Interpreted failure envelops of BBC are also have greater angles, α'=25.4^o and 24.9^o in compression and extension respectively, compared to the shallower failure envelopes of α'=15.4^o and 19.3^o in compression and extension respectively. BBC is believed to have broader failure envelopes due to the higher shear stresses imposed upon the BBC specimens during K_0 consolidation (synonymous with BBC having a lower $K_{0,NC}$). RGoM has larger cohesion intercepts than BBC, but both failure envelopes are expected to curve towards the origin with decreasing stress. As a result, the intercepts shown in Figure 6-21 are not believed to be accurate, and their corresponding magnitudes have been omitted from this thesis.

6.8 Comparison of Interpreted RGoM-EI Yield Surface with Model Formulations

Figure 6-22 compares the interpreted RGoM-EI yield surface and failure envelopes, with two of the commonly used model formulations in industry, MIT-E3 and Modified Cam Clay. The MIT-E3 model presented is the normally consolidated model yield surface. It also includes the normally consolidated failure envelopes commonly associated with RGoM-EI. These NC failure envelopes are consistent with a friction angle of 22^o. The NC failure envelope shown in extension is a mirror image of the compression envelope. In reality, the NC extension failure envelope should be drawn at a more obtuse angle, but due to the lack of extension test data available on RGoM-EI, the true extension failure envelope could not be constructed. The mirror image NC failure envelope is purely drawn for clarity purposes only. The image also contains the RGoM-EI $K_{0,\ NC}$ – consolidation point associated with a σ'_v of 1 MPa and the NC undrained compression effective stress path.

Neither model formulations accurately predict the yield surface for RGoM-EI. The MIT-E3 model formulation was calibrated to a $K_{0,\ NC}$ of 0.62 and friction angle of 22^o. The model incorporates the $K_{0,\ NC}$ value into its calibration and it accounts for anisotropy of the material. The model is over estimating yielding in compression, above the $K_{0,\ NC}$ consolidation point. The majority of specimens sheared in compression have surpassed yielding and reached failure, while the model predicts that they are still elastically straining inside the yield surface. Below the $K_{0, NC}$ –consolidation point the model formulation is under predicting yielding at normalized average effective stresses above 0.3. At normalized average stresses between 0.45-0.75 the model is predicting yielding before the minimum yield point interpreted from the experimental tests. The model formulation accurately predicts yielding in the region surrounding the $K_{0, NC}$-consolidation point. However, this is because the model is calibrated by the $K_{0, NC}$ value and the friction angle of the material.

The MCC model formulation was calibrated to a friction angle of 22^o. It does not account for anisotropy of materials, and so its predicted RGoM-EI yield surface is orientated around the isostatic axis. Below the $K_{0, NC}$ consolidation point the MCC formulation is excessively overestimating yielding. Its predicted yield surface also surpasses the experimental failure envelope in lower confining stresses (<0.4) in both extension and compression. The model formulation is predicting yielding moderately well in compression between normalized average effective stresses of 0.45-0.8. However, this is only due to the model formulation curve passing through the underside of the cap of the yield surface. The MCC formulation is also predicting a much broader yield surface than what is experimentally interpreted. This is most likely due to the model limitations, failure to include anisotropy in its calibration causes the model to over predict yielding along the isostatic axis to compensate for predicting the correct $K_{0, NC}$ consolidation point.

The NC undrained effective stress path in compression starts at the $K_{0, NC}$ point and initially traces the MIT-E3 yield surface before veering in to the left, following the interpreted yield surface until it reaches the NC failure envelope. The termination of the NC compression stress path at the NC failure envelope provides good confidence in the position of the envelope. The interpreted yield surface is located above the NC failure envelope on the compression side. This is due the over consolidation effect, and is believed to be the reason why we are interpreting an offset failure envelope at confining stresses lower than the consolidation confining stresses.

Table 4-5: Summary of interpreted yield results for both soils

Test	Probing direction from p' axis	Starting position		Interpreted Yield Points					
				Minimum		Best Estimate Yield Point		Maximum	
No.	(deg)	p'	q	p'_{min}	q_{min}	p'_{yield}	q_{yield}	p'_{max}	q_{max}
RGoM-EI:									
TX1261	-45	0.571	0.082	0.646	0.007	0.686	-0.033	0.714	-0.061
TX1262	27.7	0.813	0.187			0.303	-0.082		
TX1264	90	0.455	0.046	0.455	0.154	0.455	0.180	0.455	0.196
TX1265	80.1	0.450	0.045	0.471	0.165	0.475	0.188	0.477	0.203
TX1268	64.6	0.452	0.045	0.516	0.180	0.524	0.196	0.532	0.213
TX1269	49.8	0.457	0.044	0.577	0.185	0.597	0.210	0.610	0.224
TX1270	40	0.454	0.042	0.674	0.226	0.681	0.232	0.692	0.242
TX1271	30	0.461	0.038	0.764	0.213	0.783	0.224	0.820	0.246
TX1273	19.7	0.452	0.042	0.768	0.154	0.839	0.180	0.883	0.196
TX1276	0	0.456	0.044	0.698	0.044	0.736	0.044	0.814	0.044
TX1279	9.5	0.453	0.041	0.737	0.089	0.779	0.096	0.877	0.112
TX1282	-45	0.451	0.043	0.522	-0.027	0.572	-0.077	0.600	-0.105
TX1287	-90	0.453	0.042	0.453	-0.053	0.453	-0.086	0.453	-0.130
TX1288	135	0.457	0.042	0.365	0.135	0.359	0.140	0.348	0.152
TX1290	23.7	0.455	0.042	0.771	0.181	0.830	0.207	0.851	0.215
TX1292	-153	0.813	0.187	0.338	-0.059	0.299	-0.079	0.262	-0.098
TX1298	34.6	0.445	0.050	0.682	0.214	0.704	0.229	0.719	0.239
TX1305	16.1	0.439	0.059	0.783	0.158	0.846	0.177	0.894	0.190
TX1308	155	0.463	0.038	0.330	0.100	0.318	0.105	0.306	0.111
TX1313	27.1	0.417	0.070	0.698	0.214	0.721	0.226	0.732	0.231
BBC:									
TX1249	90	0.700	-0.007	0.700	0.330	0.700	0.358	0.700	0.377
TX1250	-90	1.001	0.027	1.001	-0.354	1.001	-0.478	1.001	-0.513
TX1251	-47	1.117	-0.011	1.550	-0.477	1.668	-0.603	1.814	-0.759
TX1252	-20	1.018	-0.006	2.045	-0.379	2.434	-0.521	2.766	-0.642
TX1253	43	1.256	0.223	2.109	1.019	2.185	1.090	2.294	1.191
TX1254	45	1.014	-0.003	1.895	0.878	2.016	0.998	2.084	1.067
TX1255	30	0.118	0.012	0.508	0.238	0.556	0.265	0.601	0.291
TX1256	0	0.100	-0.001	0.348	-0.001	0.459	-0.001	0.564	-0.001
TX1257	90	3.705	0.768	3.705	1.539	3.705	1.726	3.705	1.819
TX1260	13	0.360	0.040	0.532	0.079	0.622	0.100	0.679	0.113

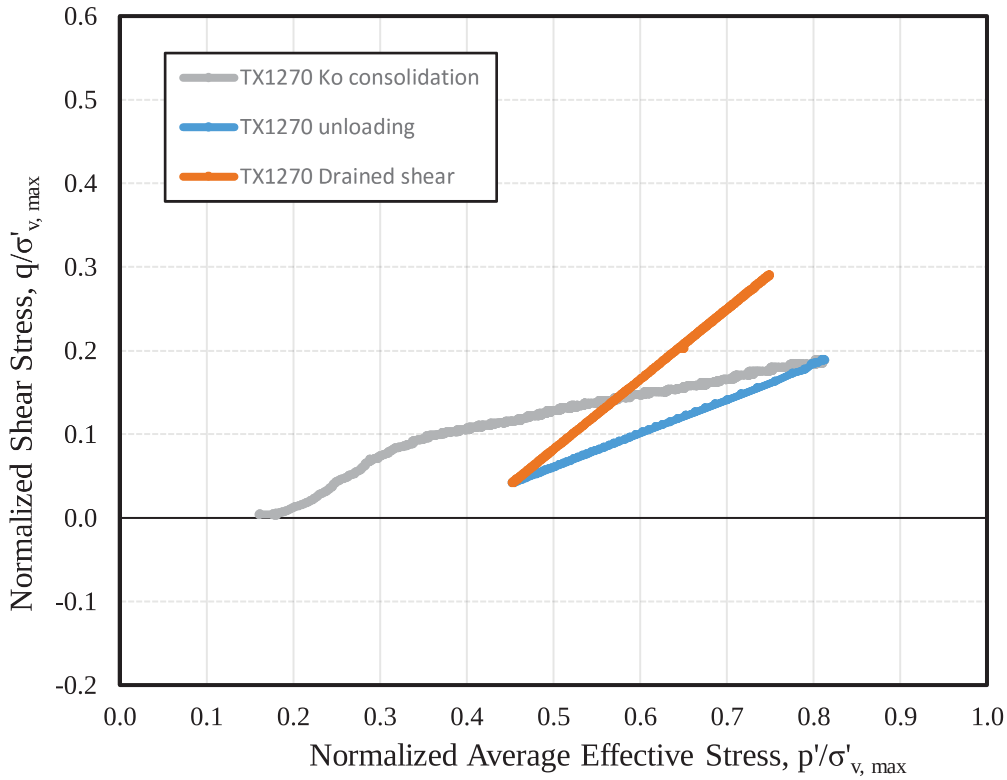

Figure 4-35: A select drained shear stress path in normalized MIT stress space

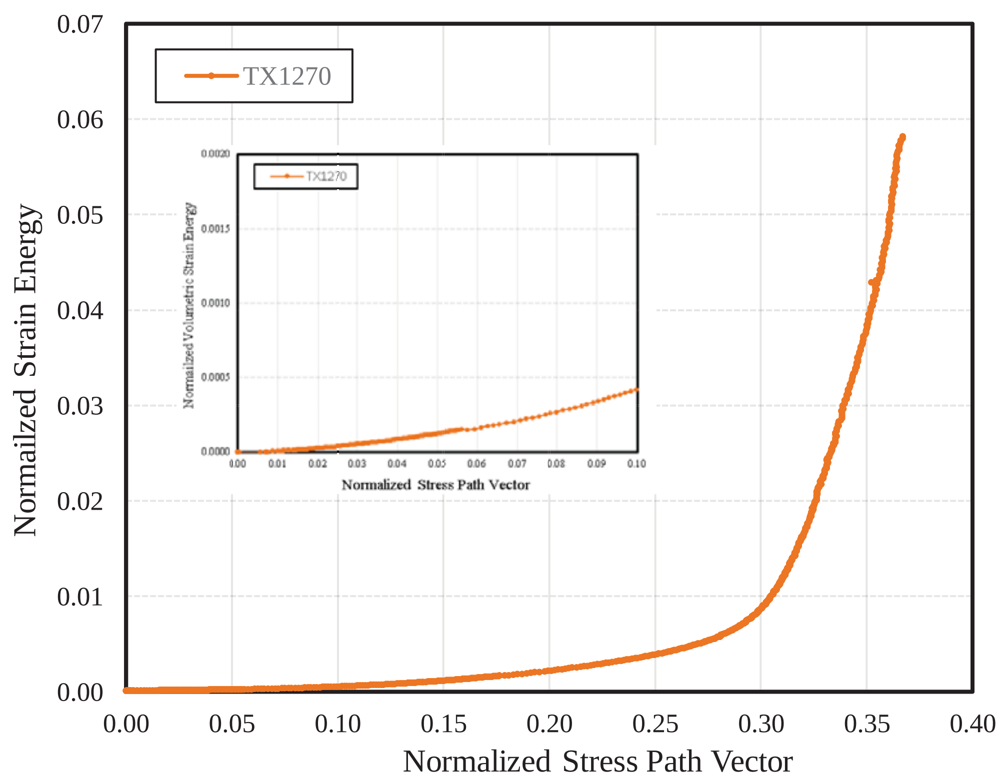

Figure 4-36: Normalized strain energy adsorbed by the specimen sheared in Figure 6-1

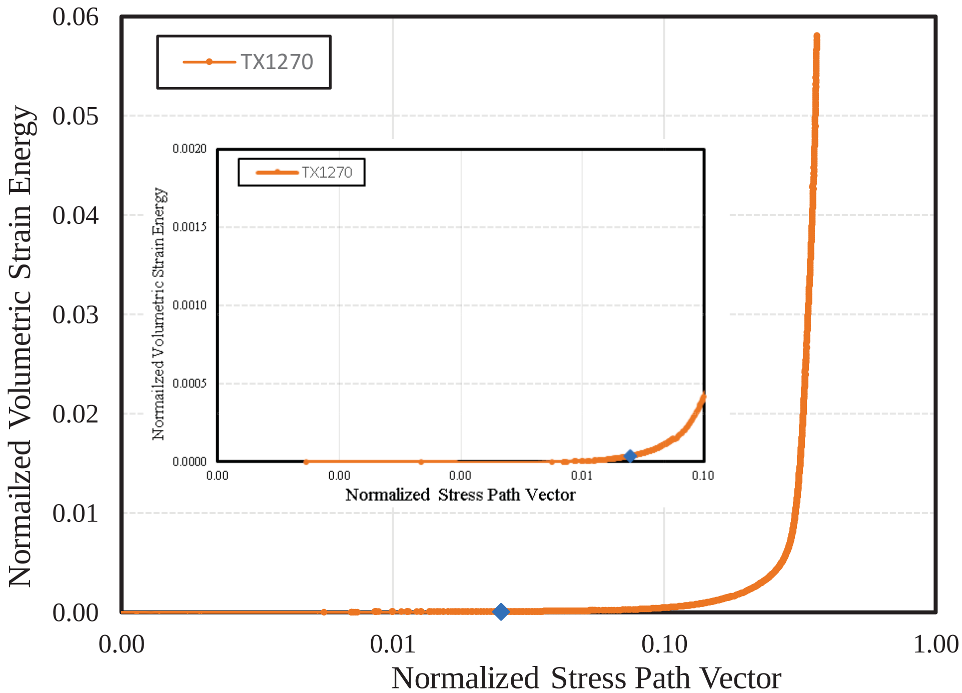

Figure 4-37: Normalized strain energy adsorbed by the specimen plotted in semi-log space to accentuate changes in curvature

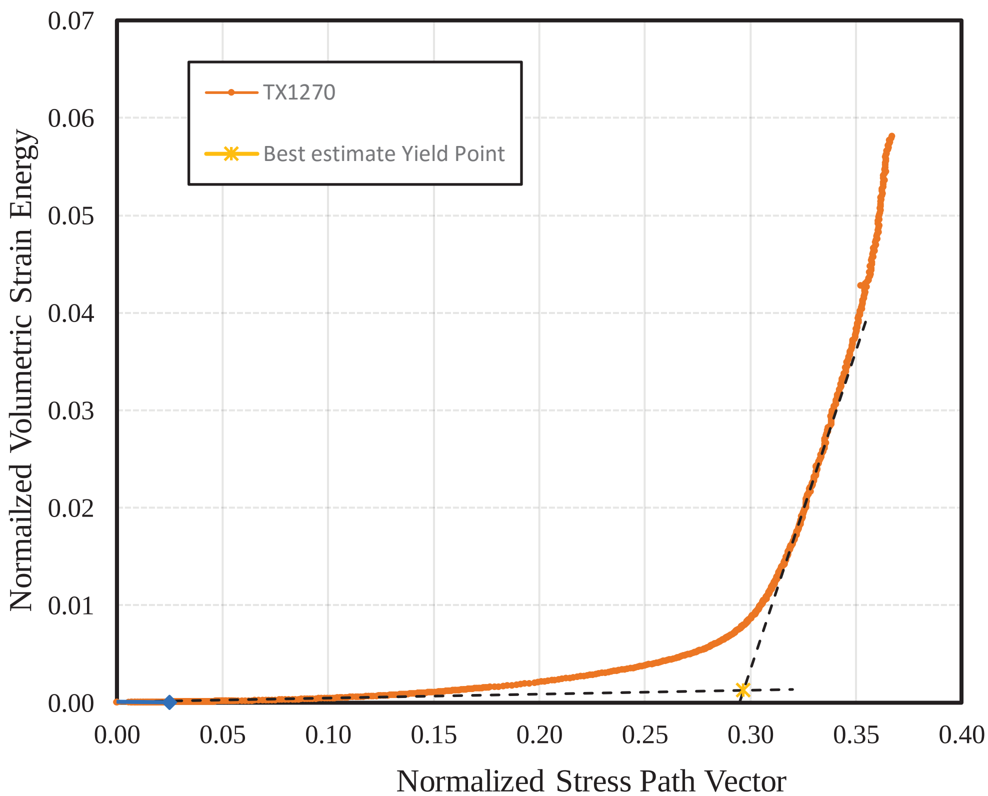

Figure 4-38: Normalized strain energy plot from Figure 6-2 combined with end of linear region point obtained from Figure 6-3. Linear extrapolation is used to obtain best estimate yield point

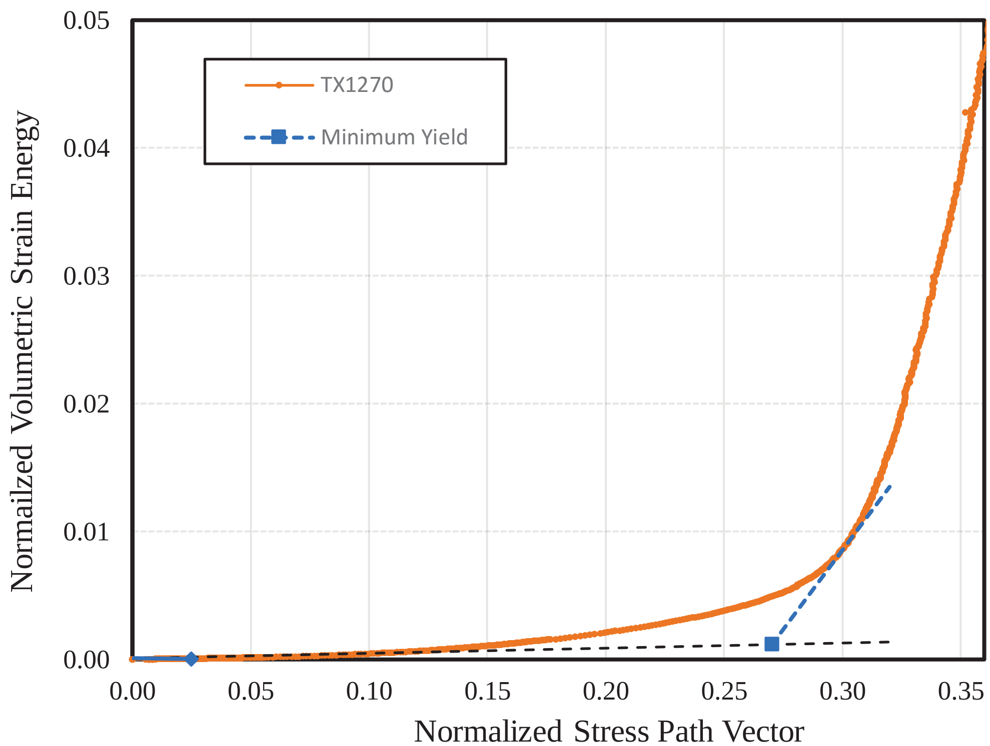

Figure 4-39: Closer scale view of normalized strain energy adsorbed by specimen used to interpret minimum yield point

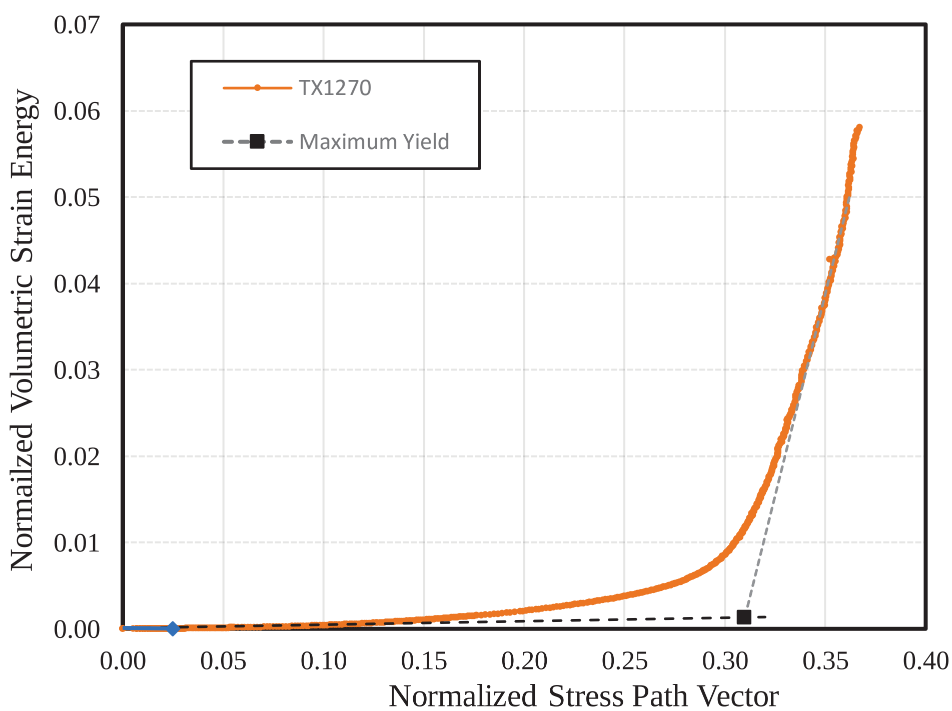

Figure 4-40: Reduced scale plot of normalized strain energy adsorbed by the specimen. This plot was used to interpret the maximum yield point

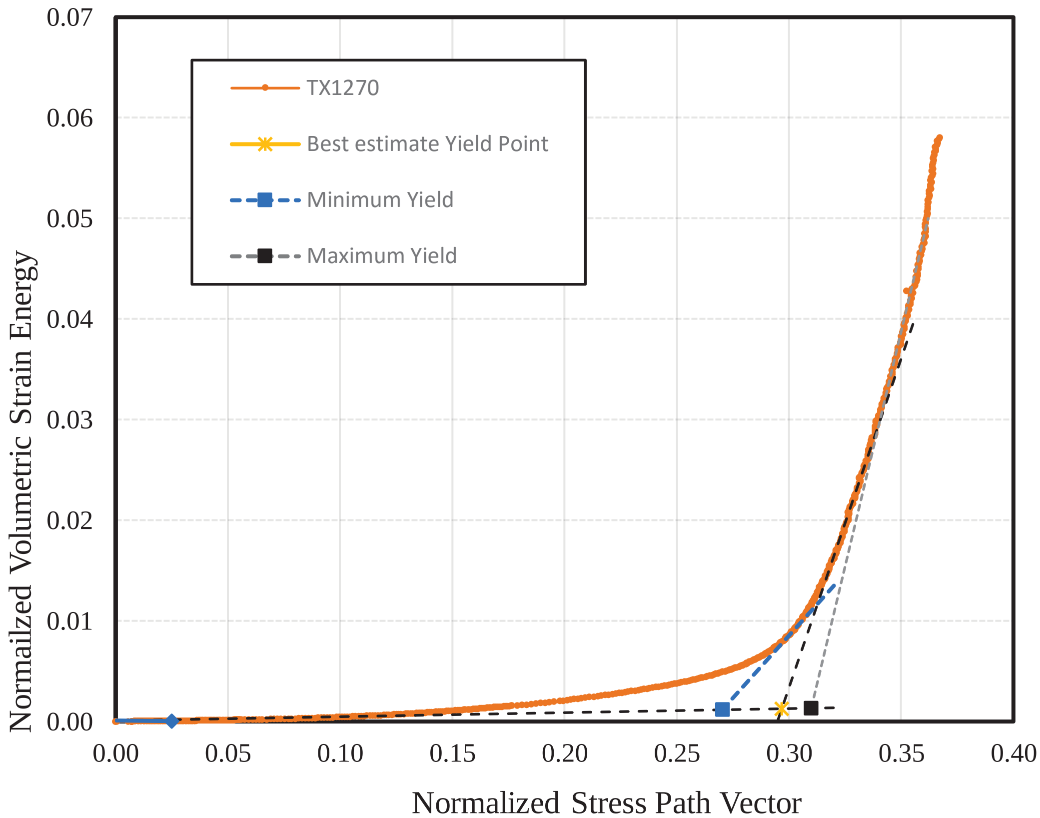

Figure 4-41: Normalized strain energy curve showing interpreted minimum, best and maximum yield points

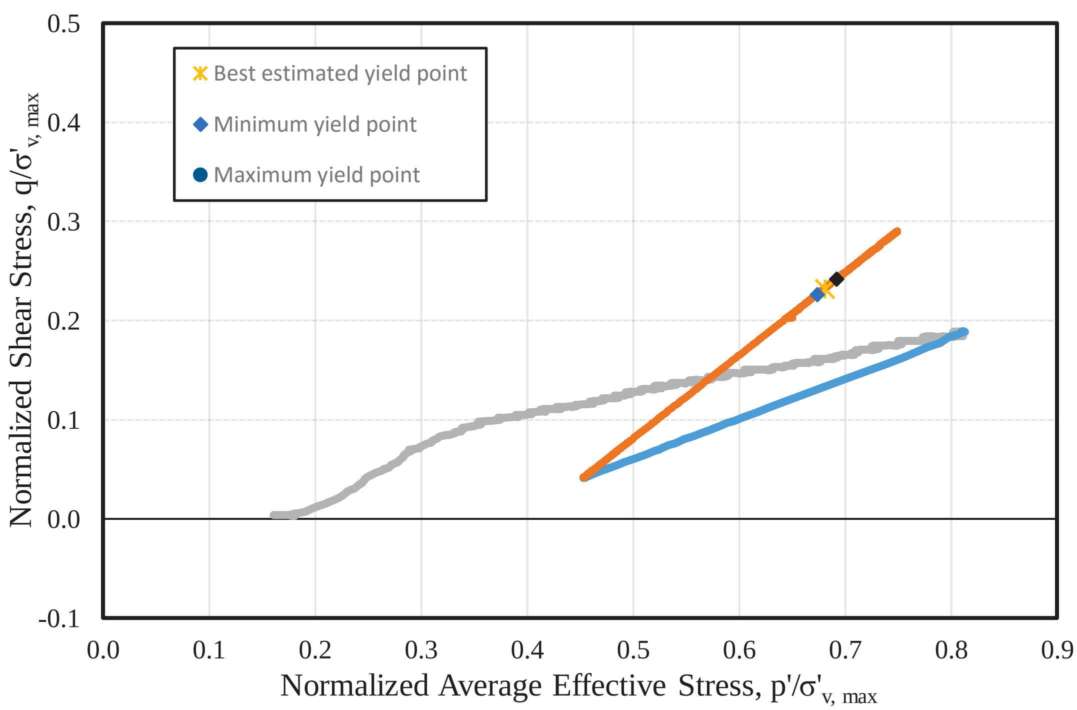

Figure 4-42: Interpreted yield range of plotted onto drained shear stress path in MIT stress space

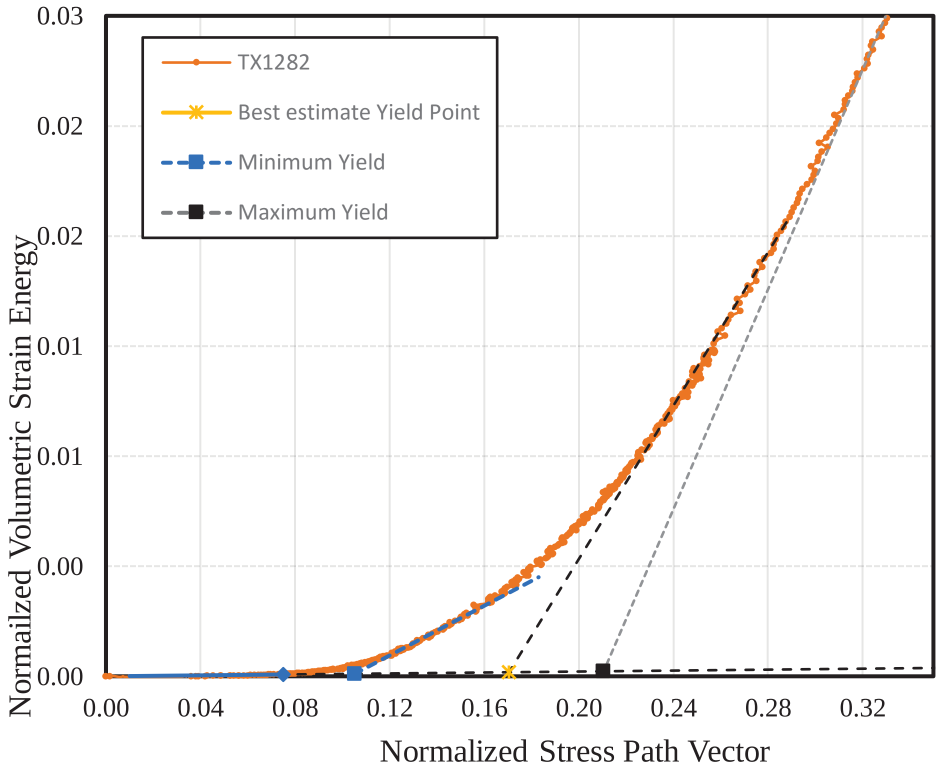

Figure 4-43: Normalized strain energy curve showing interpreted minimum, best and maximum yield points for a triaxial extension loading test on an RGoM-EI specimen

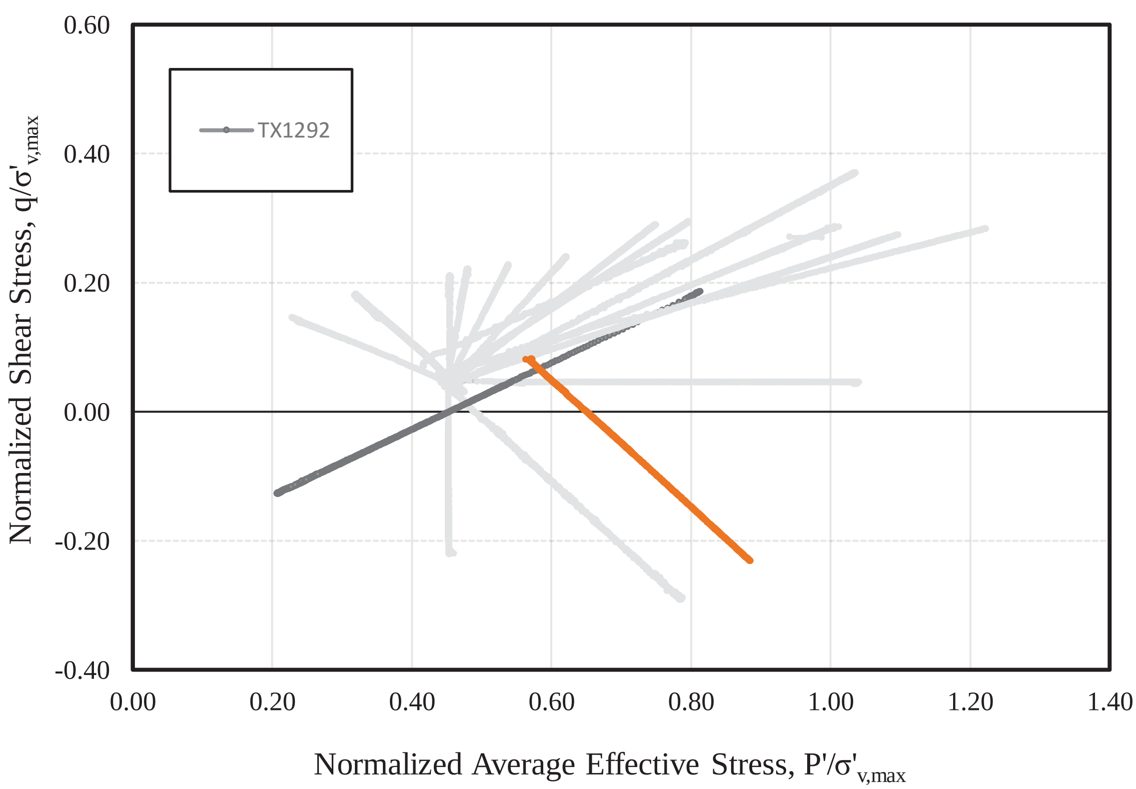

Figure 4-44: Plot of all RGoM-EI drained shear stress paths

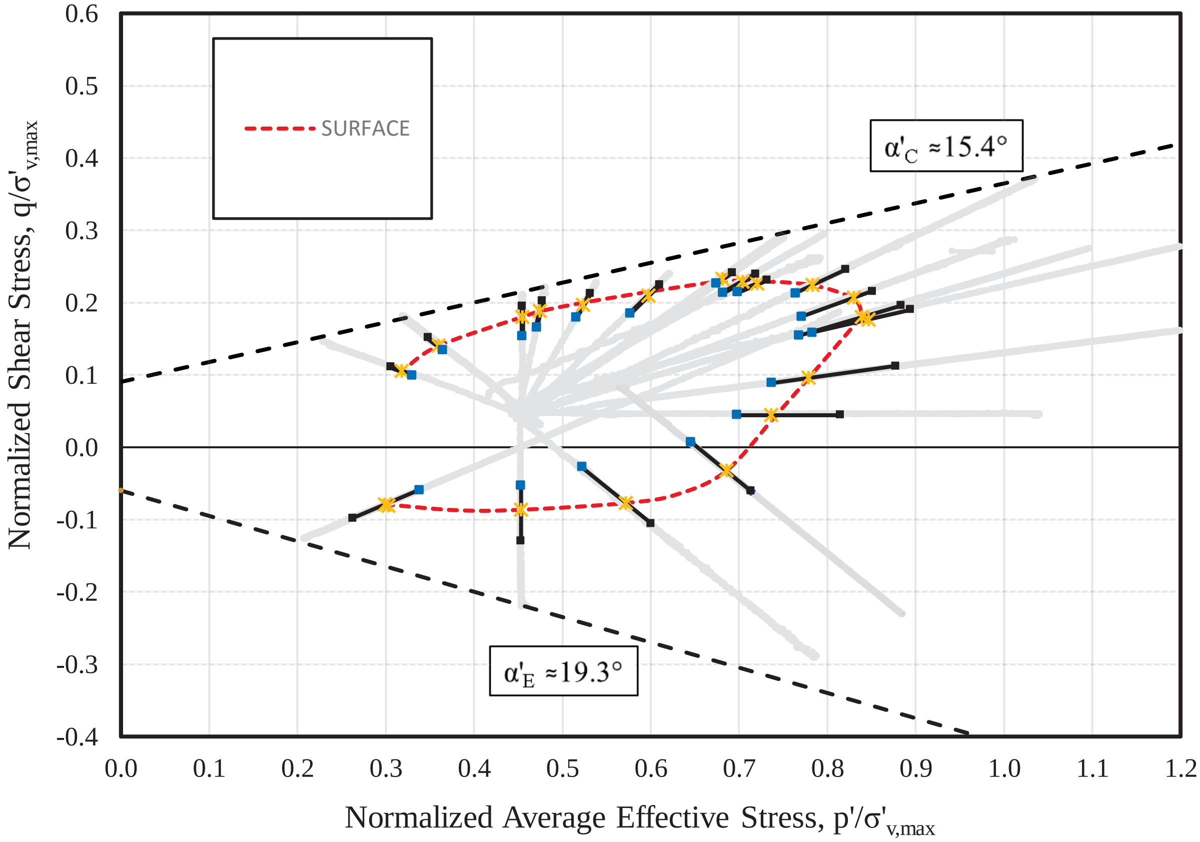

Figure 4-45: Plot of best estimate interpreted yield surface and yielding transition zones for RGoM-EI specimens

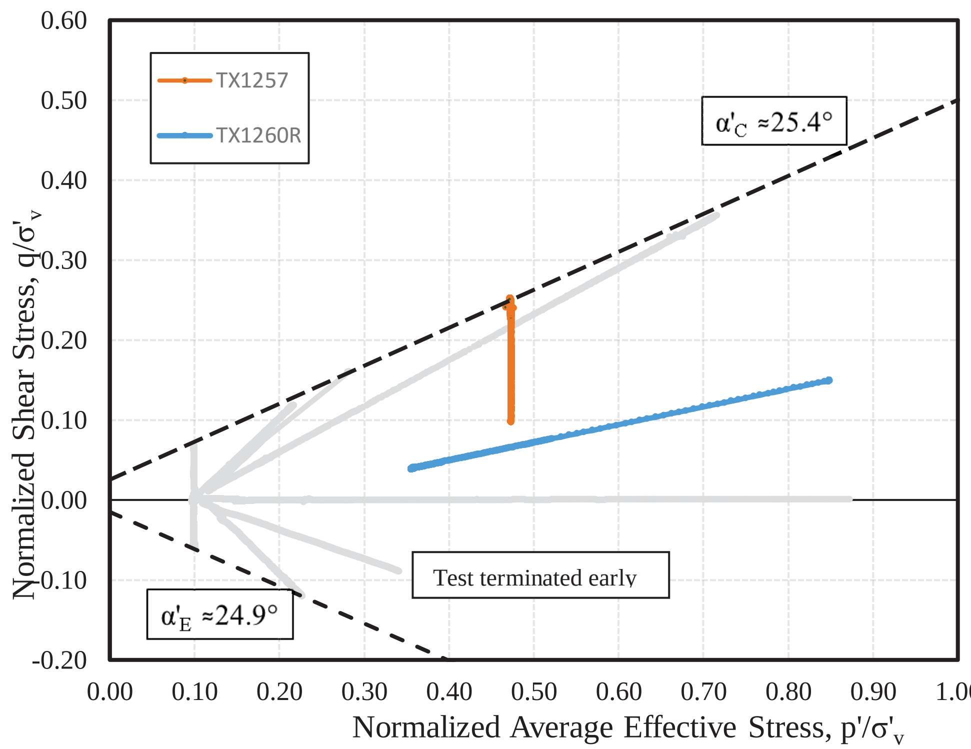

Figure 4-46: Plot of all intact BBC drained shear stress paths combined with one RBBC drained shear stress path

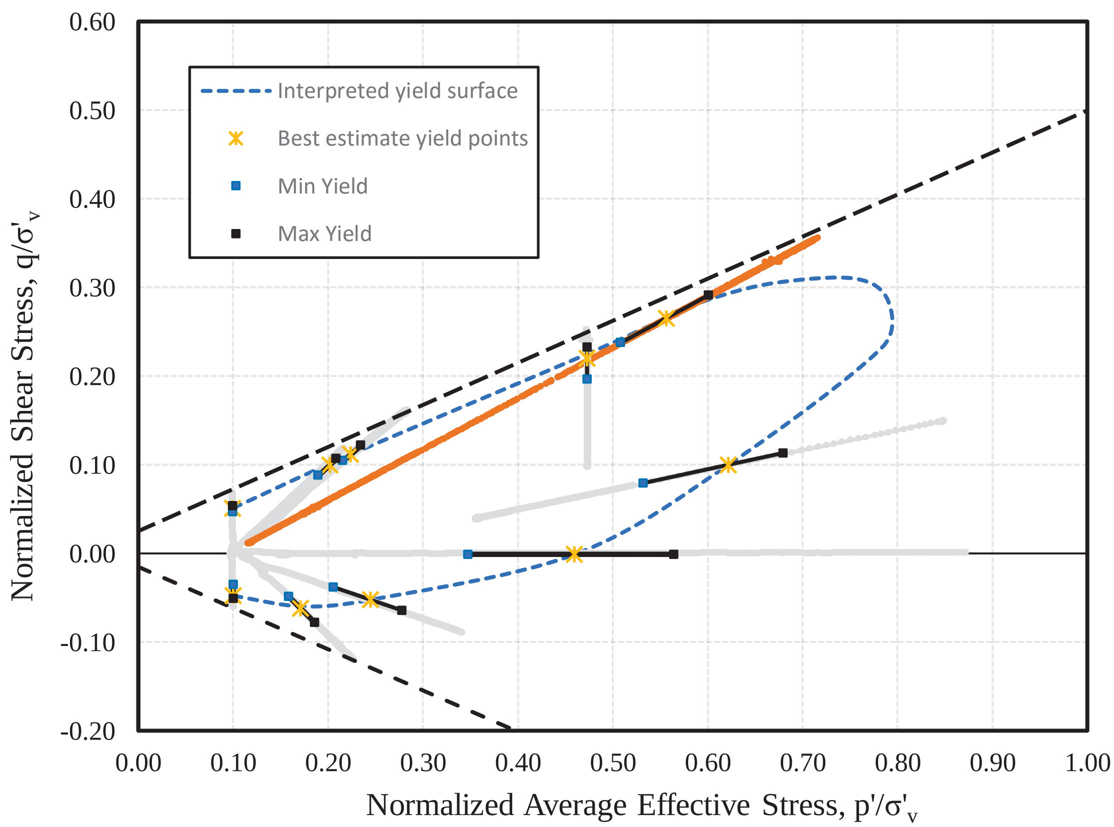

Figure 4-47: Plot of best estimate interpreted yield surface and yielding transition zones for intact BBC specimens

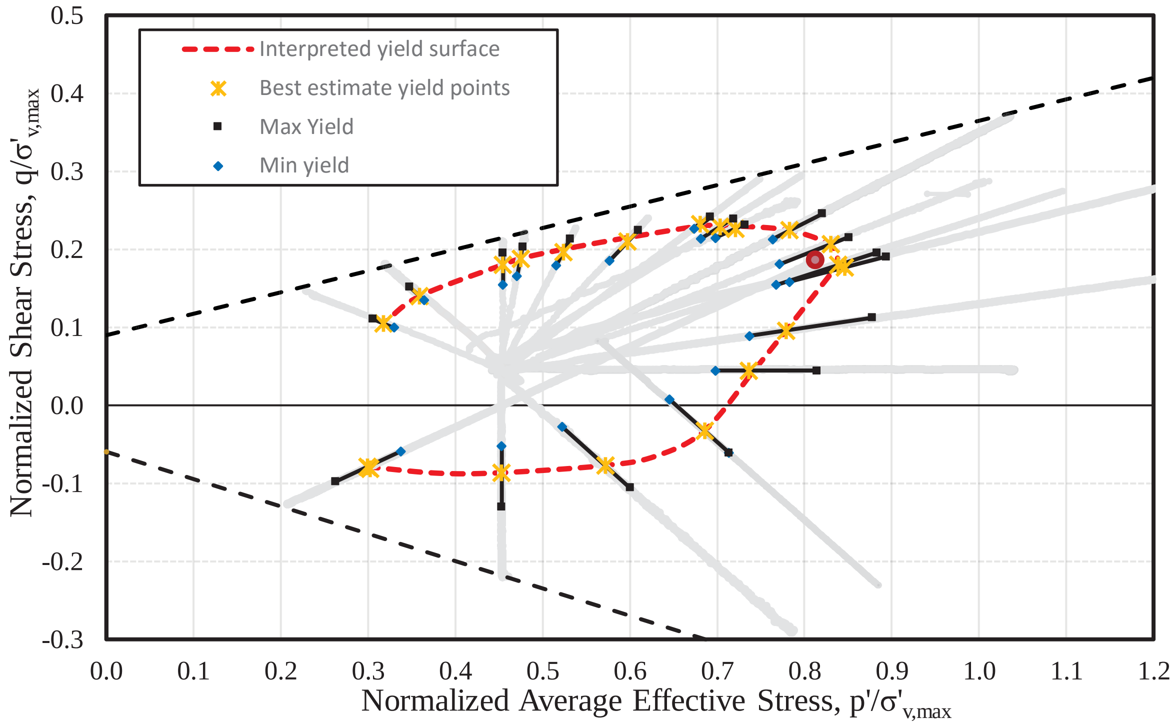

Figure 4-48: Comparison of the interpreted RGoM-EI yield surface to the previous maximum K_0 consolidation stress point in normalized MIT stress space

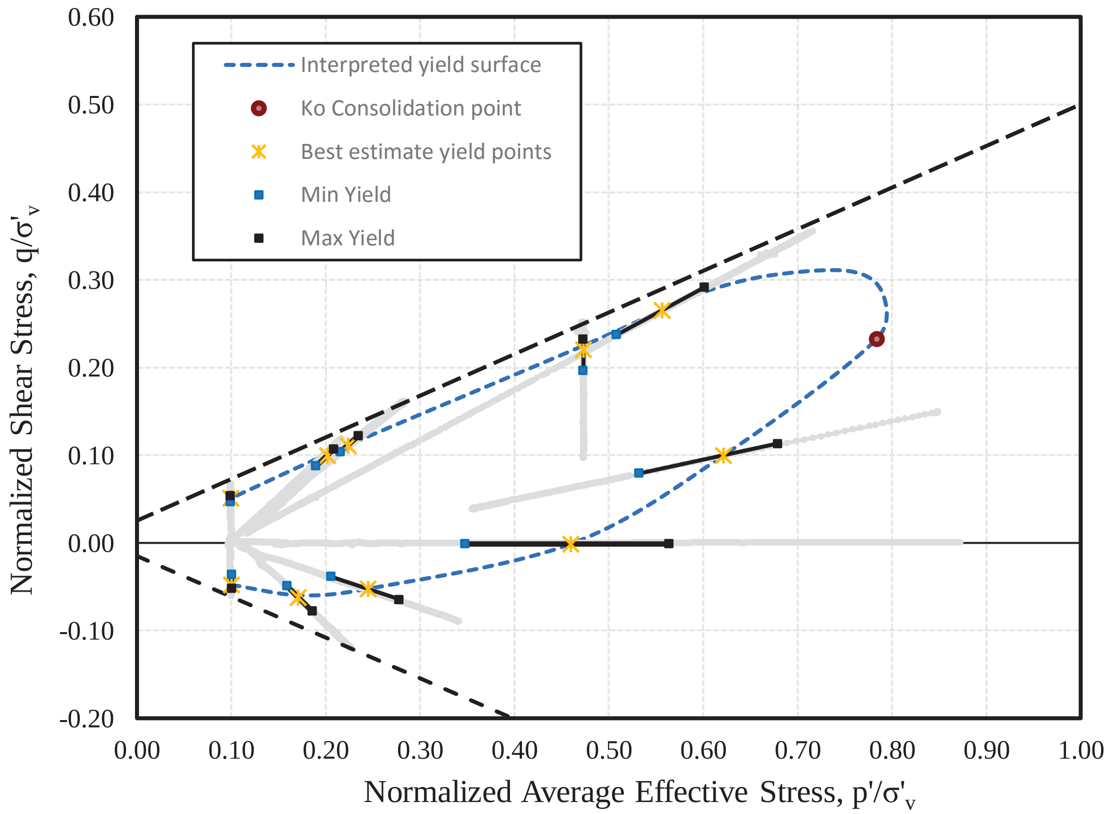

Figure 4-49: Comparison of the interpreted intact BBC yield surface to the previous maximum K_0 consolidation stress point in normalized MIT stress space

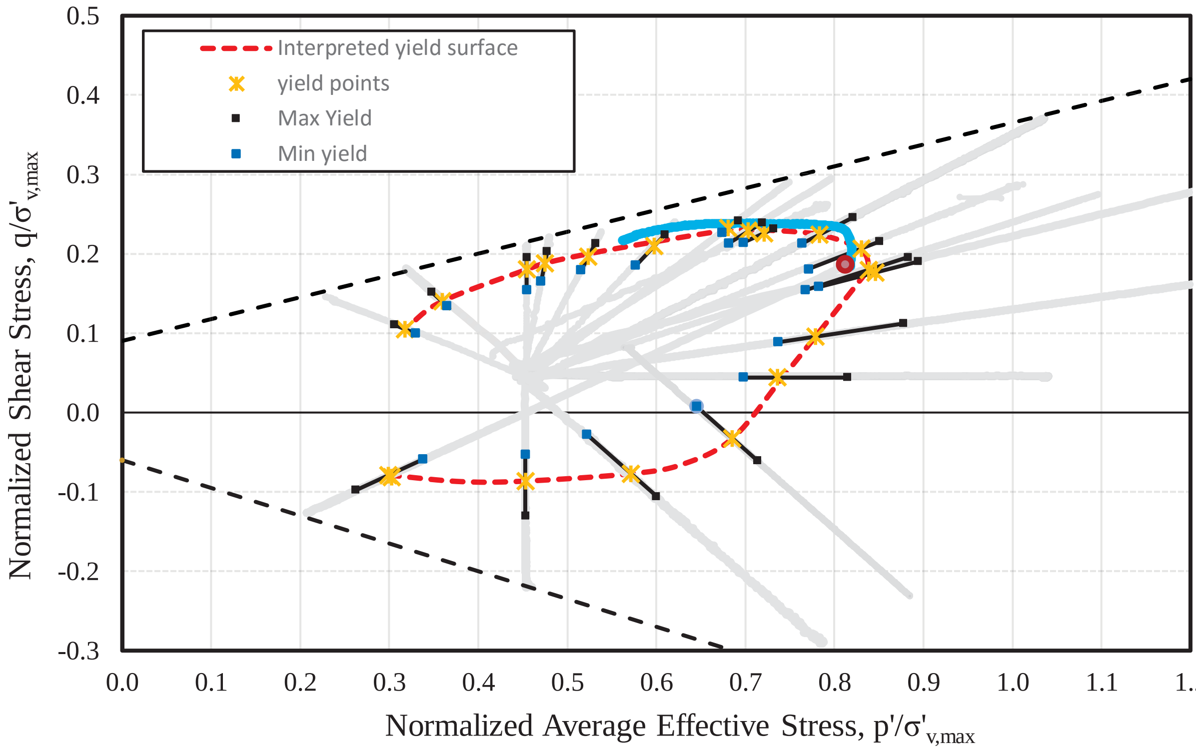

Figure 4-50: Comparison of the interpreted RGoM-EI yield surface to the normally consolidated undrained compression stress path in normalized MIT stress space

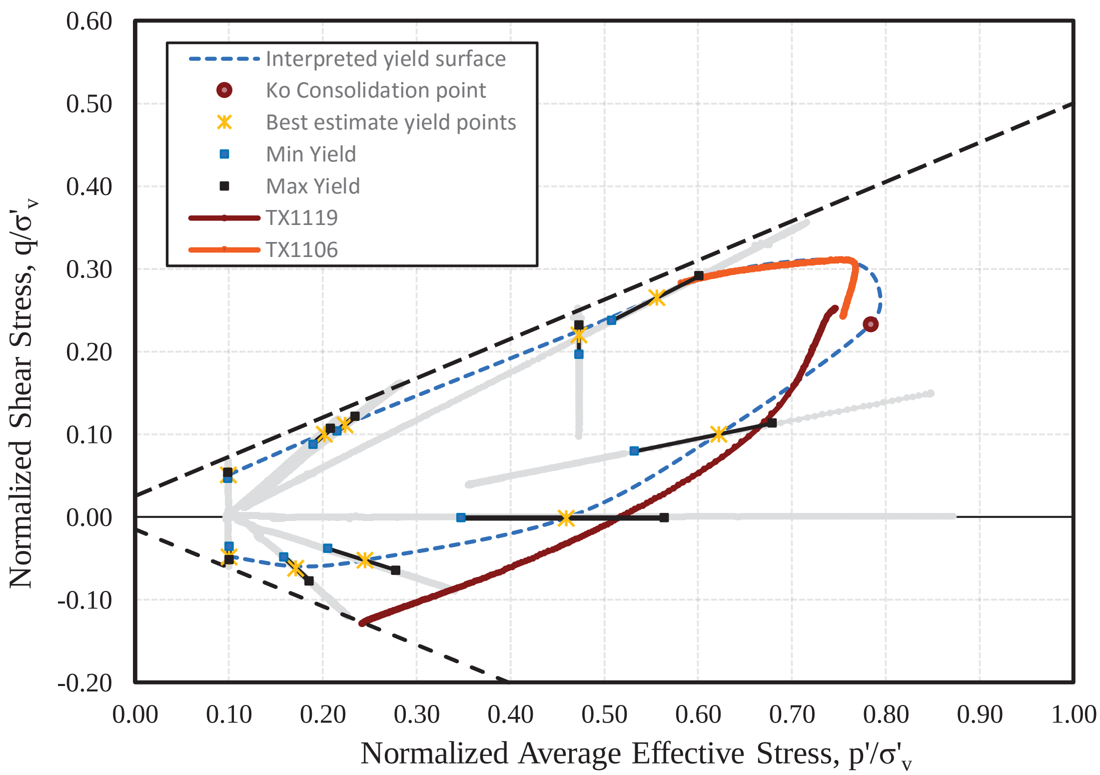

Figure 4-51: Comparison of the interpreted intact BBC yield surface to the normally consolidated undrained effective stress paths in extension and compression, MIT stress space

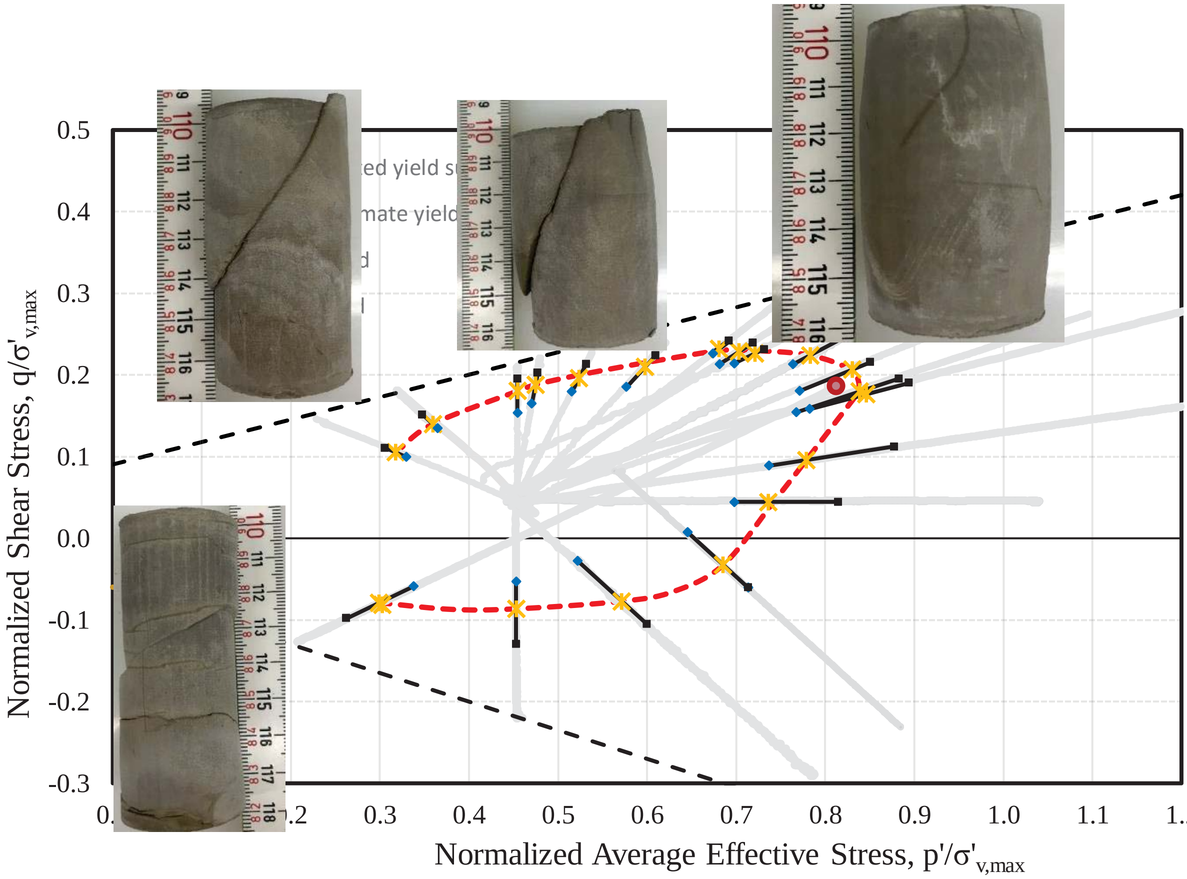

Figure 4-52: Failed RGoM-EI specimens superimposed onto their corresponding stress paths in normalized MIT stress space

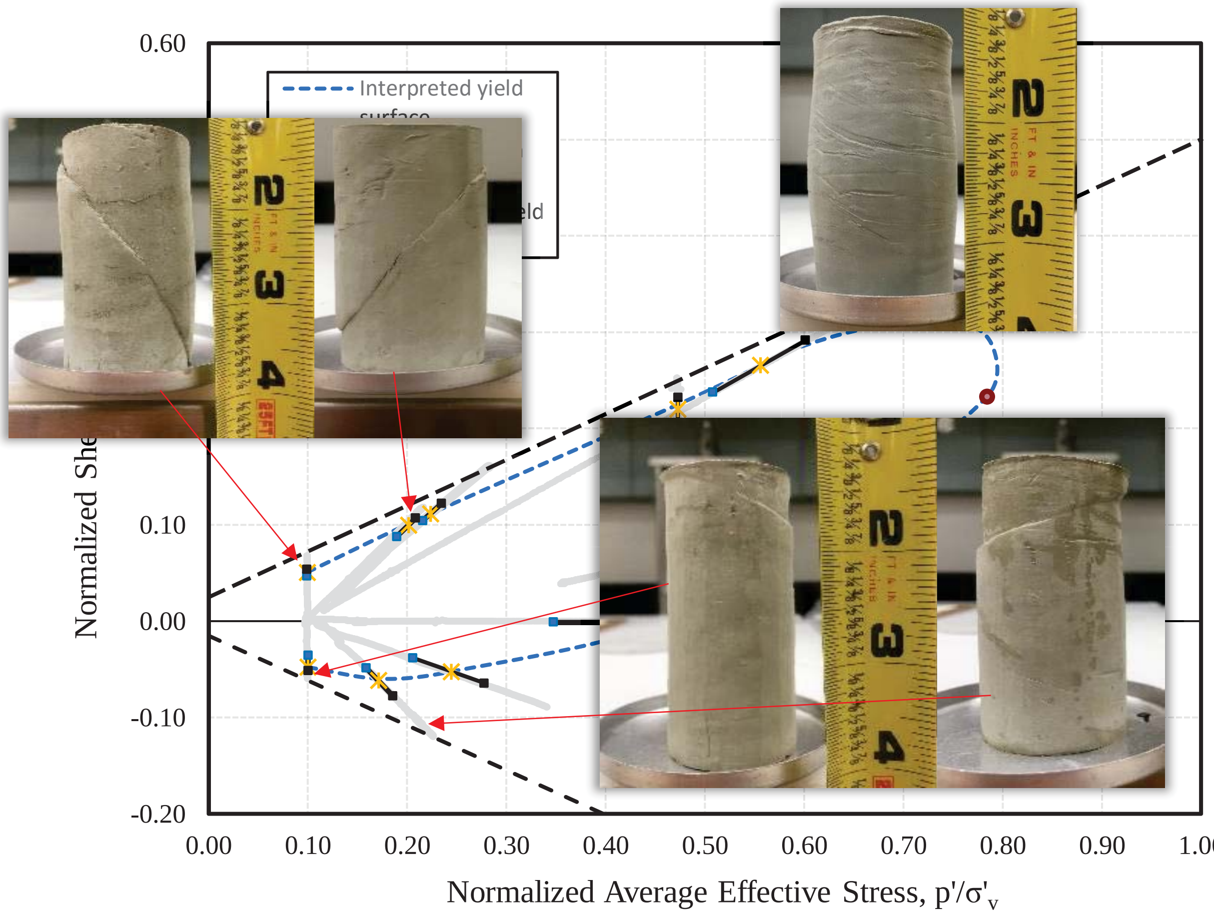

Figure 4-53: Failed intact BBC specimens superimposed onto their corresponding stress paths in normalized MIT stress space

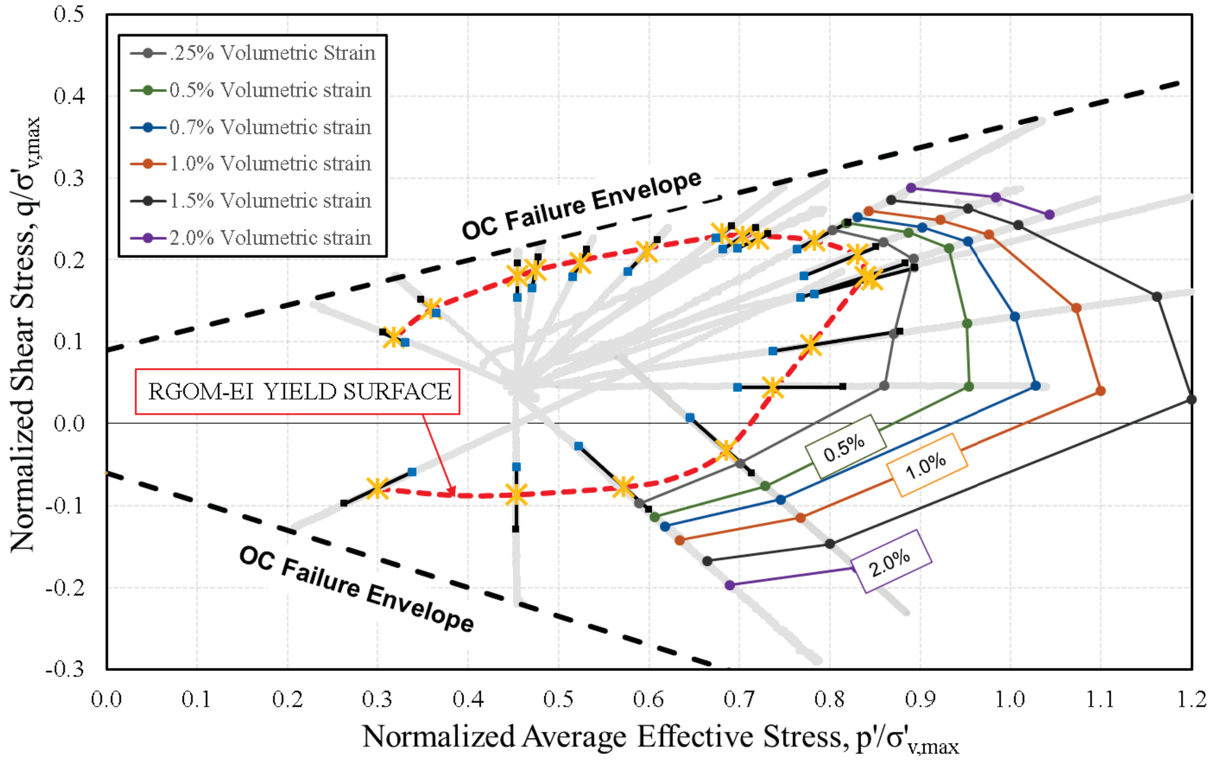

Figure 4-54: Contours of volumetric strain increments for RGoM-EI in normalized MIT stress space

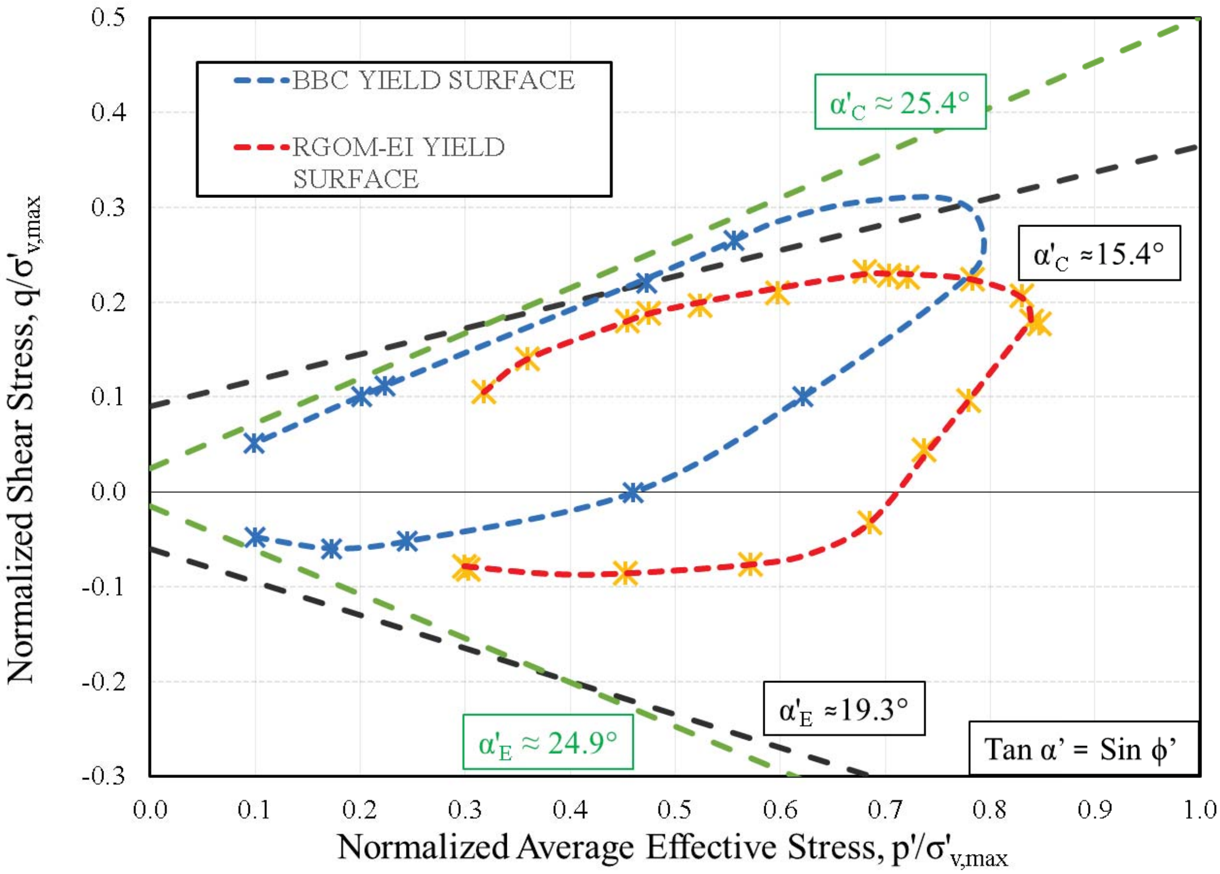

Figure 4-55: Comparison of RGoM-EI and intact BBC yield surfaces in normalized MIT stress space

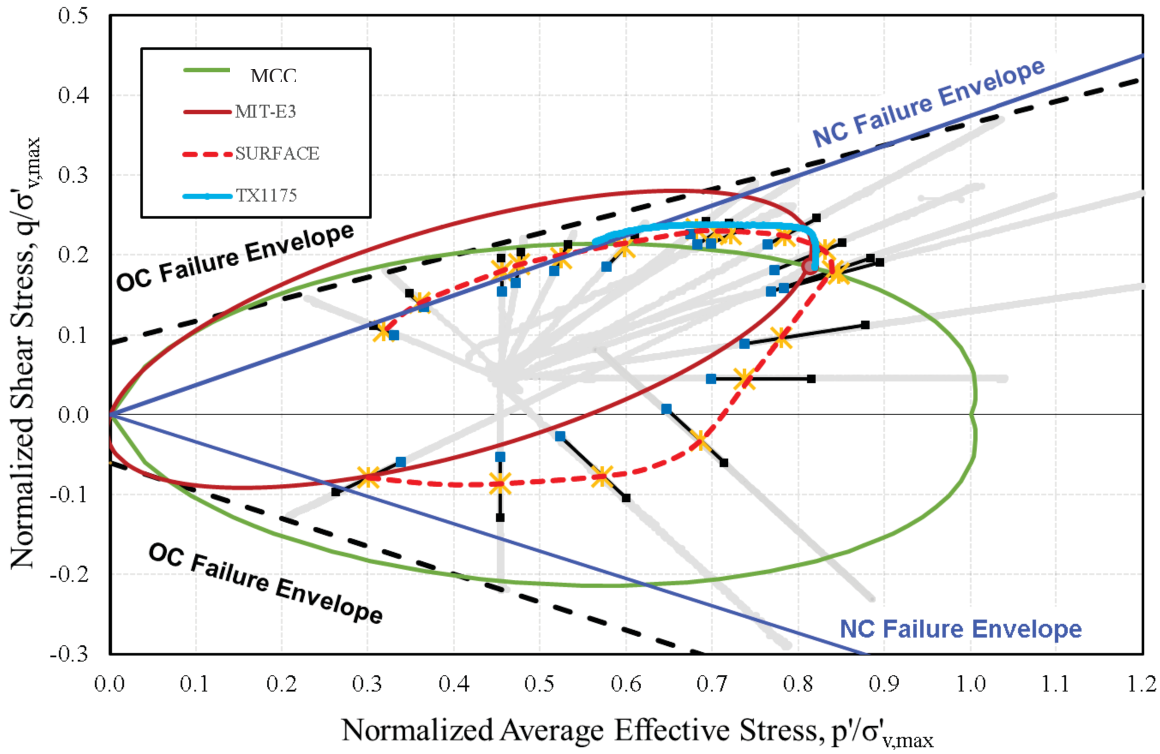

Figure 4-56: Comparison of interpreted RGoM-EI yield surface to model formulations

7 SUMMARY, CONCLUSIONS, AND RECOMMENDATIONS

7.1 SUMMARY OF WORK

This research involved the use of drained triaxial shear tests on two different fine- grained sediments, intact Boston Blue Clay (BBC), and Resedimented Gulf of Mexico Eugene Island clay (RGoM-EI), to characterize the shapes of the materials yield surfaces. The strain energy method was used to determine a yield transition zone, and best estimate yield points for all test stress paths. The interpreted yield surfaces for both materials were then plotted in normalized MIT stress space and compared to model formulations, including MIT-E3 and Modified Cam Clay (MCC). The yield surfaces were also compared to their corresponding undrained effective stress paths. This work also examined the use of appropriate consolidation strain rates to be used in the triaxial systems for ensuring uniform drained conditions.

7.1.1 RESEDIMENTATION

The majority of the research presented in this thesis adopted the use of soil samples which are resedimented in the laboratory from natural source materials. These source materials were derived from two separate geologic origins, RBBC from MIT's campus in Cambridge, and RGoM-EI from of the coast of Louisiana. From a practical viewpoint, resedimented samples are much easier and far less expensive to obtain than high quality intact samples, with minimum disturbance. This is extremely advantageous, particularly for deep offshore GoM-EI sediments, subjected to very high in situ pressures that are a special focus of the research. In addition to the considerable practical and financial benefits, resedimentation is also a technical necessity. The author's research involves consolidating specimens to specific stresses. This is far more difficult with the use of intact samples, since no two intact samples, even of the same sediment, will possess an identical composition and stress history. In addition, intact samples of a similar composition and OCR do not exist over a significant range of in situ consolidation stresses. For these reasons, the use of resedimentation is a technical requirement for the research, especially when investigating the yield surface over orders of magnitudes of stress.

Limited research has investigated the yield surface of soils using resedimented soil. The most relevant work up to this point has been that of Casey (2014) and Bensari (1984). Casey carried out a comprehensive experimental investigation to systematically quantify the effects of stress history and stress level on behavior for stresses up to 100 MPa, for a number of different materials. He also made an attempt to quantify material yield surfaces over different stress ranges using undrained effective stress paths. Bensari (1984) carried out a limited number of drained tests on RBBC specimens. His method included manually adjusting both cell pressure and axial load by small increments, and then allowing time for drainage to occur, before making another manual adjustment, as he did not have automated modern loading systems at the time.

7.2 NORMALIZED CONSOLIDATION BEHAVIOUR

Normalizing each specimens test data by its corresponding individual maximum consolidation stress ($\sigma'_{v,\ max}$) is essential for this research. Normalization allows specimens of the same material that were consolidated to slightly different consolidation stresses to be compared in a uniform fashion. It is also advantageous as the interpreted normalized yield surface for a vertical effective stress of 1MPa can be scaled to represent other consolidation stresses. Although, Casey 2014 has shown that undrained shear behavior is stress dependent, which would imply that yield surface is stress dependent.

Normalized K_0-consolidation stress paths of RGoM-EI specimens all display significant reproducibility, all tests carried out at low confining stresses (< 1 MPa) tests display linear normally consolidated stress paths of constant $K_{0, NC}$, ($K_{0, NC}$ =0.62) which are in agreement with the empirical correlation proposed by Jâky (1944). Normalized K_0-consolidation stress paths of intact BBC specimens displayed a more scattered reproducibility, due to their non-homogenous composition. $K_{0, NC}$ values of BBC varied between ~0.47-0.61, compared to the relatively constant values of 0.62-0.64 $K_{0, NC}$ values observed from RGoM-EI specimens. This highlights the benefits of using resedimented samples, as varying $K_{0, NC}$ values in turn imposes varying shear stresses on specimens at their corresponding maximum consolidation stress. The $K_{0, NC}$ value essentially sets the position of the cap of the interpreted yield surface in MIT stress space, thus the interpreted yield surface from intact samples would have an additional uncertainty associated with it. As resedimented samples have been proven to produce reproducible $K_{0, NC}$ values, the interpreted yield surface will not contain this additional uncertainty.

7.3 CONSOLIDATION STRAIN RATES

Appropriate consolidation strain rates to be used in the triaxial cell are dependent upon the permeability of the material being tested. This work has shown that axial consolidation strain rate of 0.15 %/hr is producing a 3% error in σ'_v during K_0 consolidation in RGoM-EI specimens up to 1 MPa. Wissa's equation has been found to provide a reasonable prediction of internal excess pore pressures generated in low stress triaxial specimens. When selecting an appropriate strain rate for consolidation the permeability of the material and the allowable percentage error in σ'_v should be taken into consideration. Wissa's equation should be used to provide a first approximation of the appropriate consolidation strain rate. Because RGoM-EI has a very low permeability in comparison to many other clays in the TAG database, it can be concluded that axial consolidation strain rates of 0.15 %/hr is acceptable (depending on one's allowance for error in σ'_v) for almost all other soils of higher permeability, when consolidating up to 1 MPa.

The strain rate was reduced to 0.1 %/hr for medium stress testing. Results from the medium stress testing show that large internal pore pressures are being generating at an almost exponential rate at stresses above~3 MPa. The work concludes that appropriate consolidation strain rates in the triaxial cell are stress dependent. Consolidation strain rates should be reduced to much slower rates as consolidation stress increases. Although, the exact appropriate strain rate reduction has not been verified as part of this research, the author would estimate that reducing the strain rate to 0.05 %/hr would be a near acceptable first approximation for consolidation up to 10 MPa.

7.4 YIELDING AND YIELD SURFACE

Plotting the work adsorbed by the specimen as it shears against the direction of the stress path is considered to be advantageous in interpreting yielding over traditional methods. This method allows for comparison of test data from any shear stress path in a uniform fashion. Traditional methods of plotting shear stress against axial strain or volumetric strain break down for stress paths travelling parallel, or at shallow angles, to the isostatic axis. Little to no shear stress change occurs when travelling along these particular stress paths, because compression governs and shear loading is marginal. Thus, yielding is impossible to determine when using these methods. The strain energy method is one of the few methods capable of interpreting yielding along these paths. The method is also advantageous as it allows a yield transitioning zone to be distinguished, as in reality yielding of soils does not occur at a specific point.

The orientation of the yield surface is believed to be dependent upon the orientation of the virgin consolidation stress path. All tests carried out as part of this research were K_0 consolidated and so the interpreted yield surface presented in this research would only represent one dimension consolidation conditions. Results from both materials tested show that the yield surface is not symmetrical about its virgin consolidation axis. However, its orientation is dependent upon the virgin consolidation axis. The interpreted yield surfaces incorporate significant anisotropy due to their K_0 consolidation history. Both the shape and degree of anisotropy of the interpreted yield surface is material dependent

Each stress path had and interpreted yield transition zone (i.e., a zone where yielding was gradually occurring). Interpreted yield transition zones are much narrower above the consolidation axis than they are below it. This is concluded to be due to the material behaving more brittle above the K_0 consolidation axis. Yield transition zones are much larger at higher confining stresses between the K_0 consolidation axis and the isostatic axis, as the material is ductile in this region. The yield transition zones begin to reduce in size again as you travel further below the isostatic axis and reduce confining pressure.

The size of the interpreted transition zone mentioned previously, also appears to have dependency upon the angle made between the interpreted yield surface and the shear stress path. If the stress path crosses the interpreted yield surface with a high angle trajectory, the yield transition zone observed will be narrower than similar stress paths travelling at shallower angles to the interpreted yield surface. This is because stress paths travelling at shallow angle trajectories relative to the yield surface travel in the yielding region for a longer duration. The majority of tests carried out in this work had larger associated stress path-yield surface angles, as a result the yield transition zones presented are considered to be accurate.

The NC undrained compression effective stress path is a good first order approximation of the cap of the yield surface. While the NC undrained extension stress path is not accurately tracing the yield surface of the material. The undrained extension stress path continues to deviate away from the interpreted yield surface throughout the shearing process, as the material is believed to be strain hardening and pushing out the yield surface. The effects of secondary compression cause the yield surface to shift/grow outwards from the point of previous maximum consolidation.

The normally consolidated MIT-E3 and MCC model formulations are not accurately predicting the yield surface of clay materials. This is because the model formulations are based on simplistic shapes (mainly elliptical) described by mathematical equations. As shown in Figure 6-22, the measured yield surface has a complex geometry that cannot be simply described by a single mathematical function. The normally consolidated MIT-E3 model formulation incorporates the effects of anisotropy into its calibration, and can be seen to be making a much better estimate of yielding than MCC

7.5 RECOMMENDATIONS FOR FUTURE WORK

Based on the results and conclusions of this work, the following are areas in which the author feels further research would be most beneficial and impactful:

- The research presented in this thesis has involved investigating the effects of using a constant axial strain rate throughout the K_0 consolidation process up to 10 MPa. It has proven that a constant axial strain rate generates exponentially increasing internal pore pressures as confining stress increases. Future research should investigate appropriate strain rates to achieve fully drained K_0 consolidation. Incorporating the use of a variable strain rate into the system would be particularly useful and economic. The author recommends modifying the system to incorporate a pore pressure transducer to monitor the internal pore pressure in the center of the specimen. Also, adopting a starting strain rate of 0.1 %/hr for low stresses (i.e., <1 MPa) and reducing it accordingly to keep the pressure in the center of the specimen relatively constant throughout the consolidation process.

- Based on the results obtained from this research, an elastic plastic model will never be able to accurately capture the observed anisotropic and non-linear soil behavior. For situations where understanding soil behavior is critical, it would be most beneficial if a computer model formulation was developed and calibrated to produce yield surfaces for RGoM-EI and BBC based upon the results presented in this work.
- Once an appropriate consolidation strain rate has been developed. The work presented in this thesis should be continued to investigate the yield surface at different orders of magnitude (i.e., 10 MPa and 100 MPa). This would determine whether the yield surface of soil is stress dependent as suggested by Casey (2014). When testing up to 100 MPa the effects of increasing temperature should also be taken into consideration as it is well known that the mechanical properties of soil and rock are significantly affected by temperature (particularly above 80˚C - 100˚C when the recrystallization of clay minerals such as smectite alters the microfabric of fine-grained soils). The author's experimental program has only involved laboratory testing at room temperature (~23º). It would be of great benefit to systematically evaluate the effects of temperature on consolidation and strength properties as a function of composition. This could be successfully achieved by a laboratory investigation involving a revision of the triaxial equipment, a controlled temperature setting, and the use of resedimented soil samples.

- All shear data presented in this thesis was obtained from triaxial tests. However, most design applications in which shear strength properties need to be considered involve a combination of multiple modes of shearing. Interpreting yielding from a Direct Simple Shear device would provide validation of the yield surface obtained from the triaxial device. In addition, an undrained TE test is required for RGoM-EI, to investigate if it is also progressively overestimating yielding.
- All triaxial tests performed by the author relied on external measurements of axial strain. As a result, the small strain behavior of the soils could not be determined accurately at strains less than about 0.01 %, by which point soils may already have experienced a significant reduction in Young's modulus. Santagata (1998) measured small strain behavior at axial strains as low as 0.0001 %, though only for a single material (RBBC) and for σ'p up to 2 MPa. It would be useful to modify all triaxial cells to accommodate internal strain measurement. This would allow an extension of the work of Santagata (1998) to stresses as high as 100 MPa. Internal strain measurement would also be beneficial to accurately monitor changes in cross-sectional area of specimens. The two yield surfaces presented in this research have different shapes. This is believed to be due to differences in Atterberg limits and mineral content in both materials. Previous research presented by Casey (2014) and Marjanovic (2016) has correlated the mechanical properties of fine-grained soils to liquid limit. If more soil types were to be investigated as part of future research, perhaps a correlation could be developed between the yield surface shape and liquid limit.
- Time-dependent diagenetic processes such as cementation were not investigated as part of this research. Such processes cannot [currently] be imitated inside a laboratory setting. If

substantial finances were to be made available, it would be beneficial to carry out laboratory testing of intact materials subjected to these time-dependent processes, and to examine the extent to which their measured behavior can be predicted by testing of corresponding resedimented material.

APPENDIX A

RESEDIMENTED GULF OF MEXICO EUGENE ISLAND CLAY PLOTS

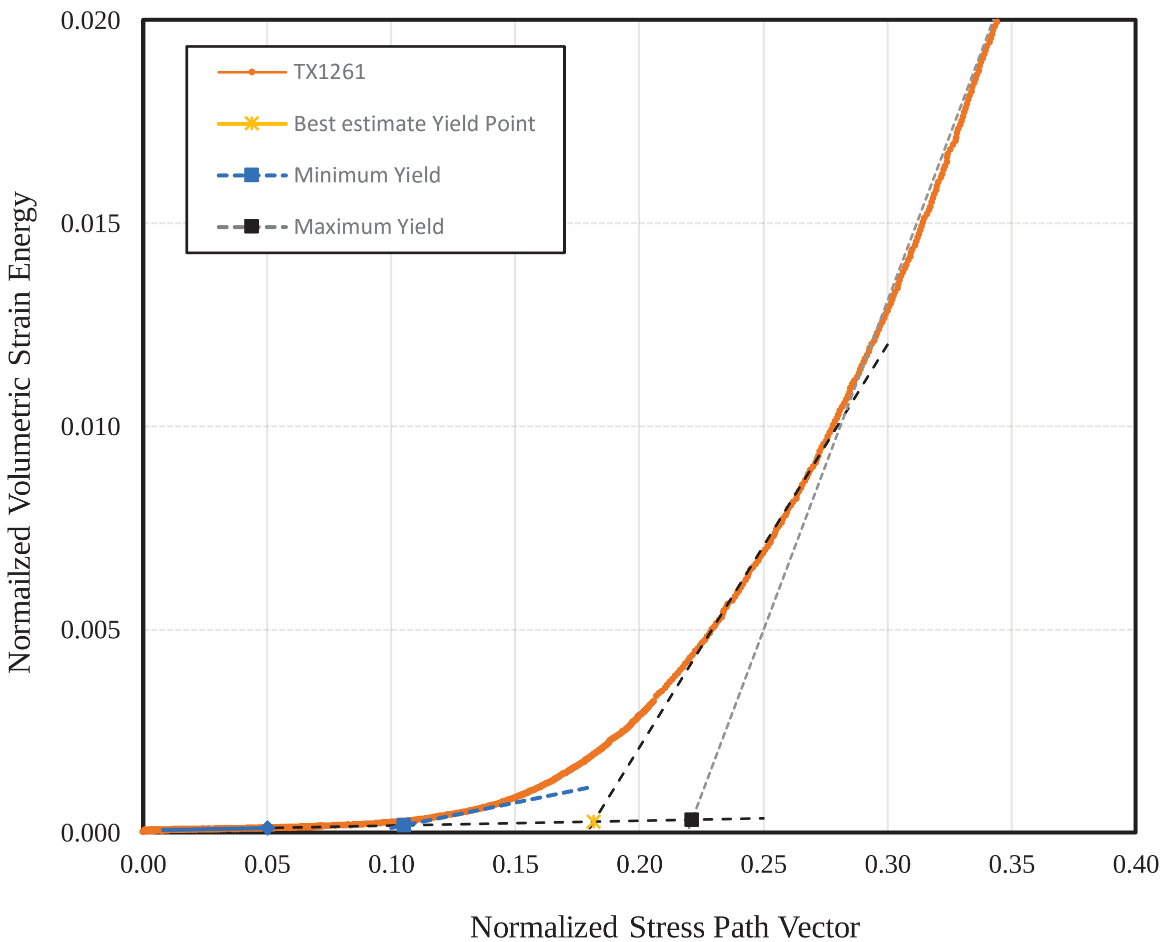

Figure 0-1: Interpreted yield transition zone for test no. TX1261

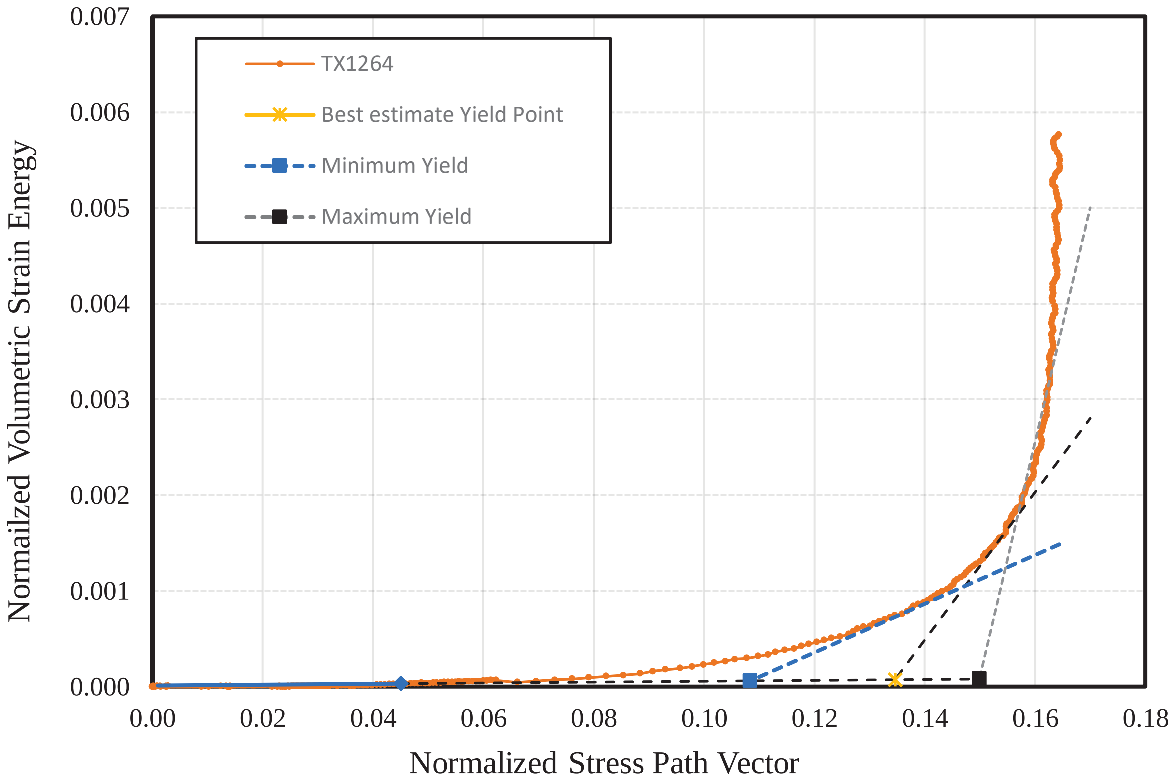

Figure 0-2: Interpreted yield transition zone for test no. TX1264

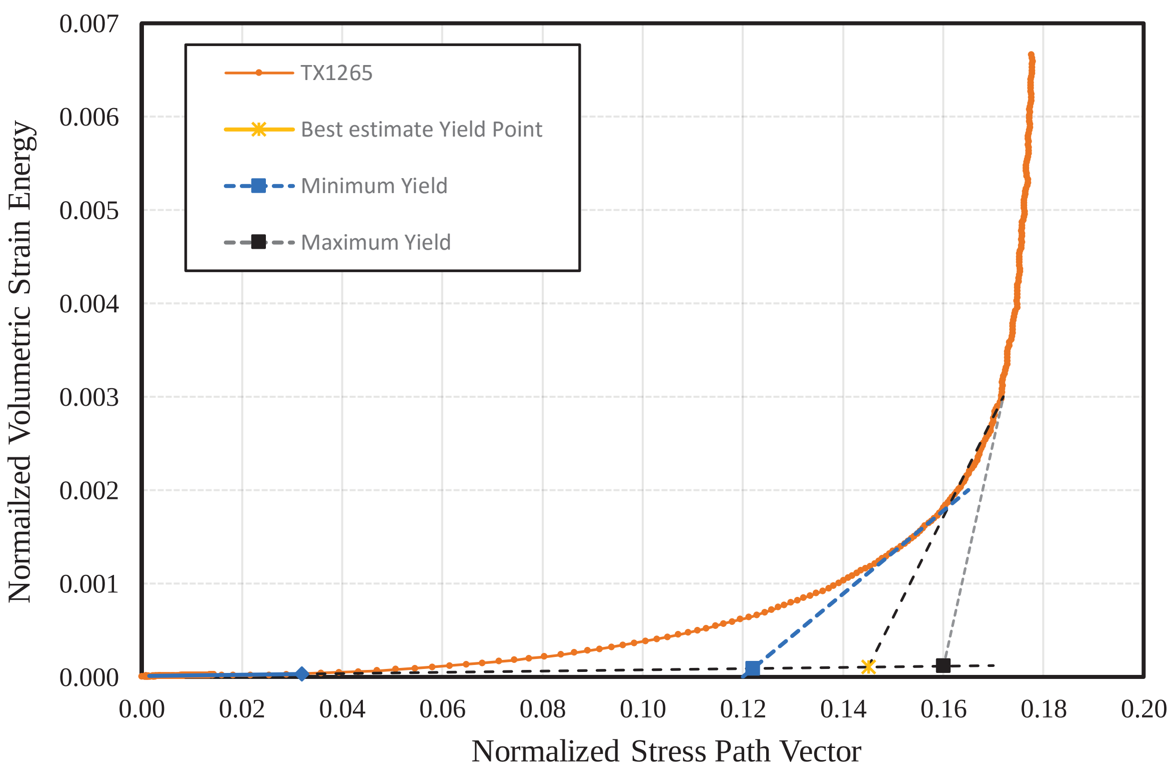

Figure 0-3: Interpreted yield transition zone for test no. TX1265

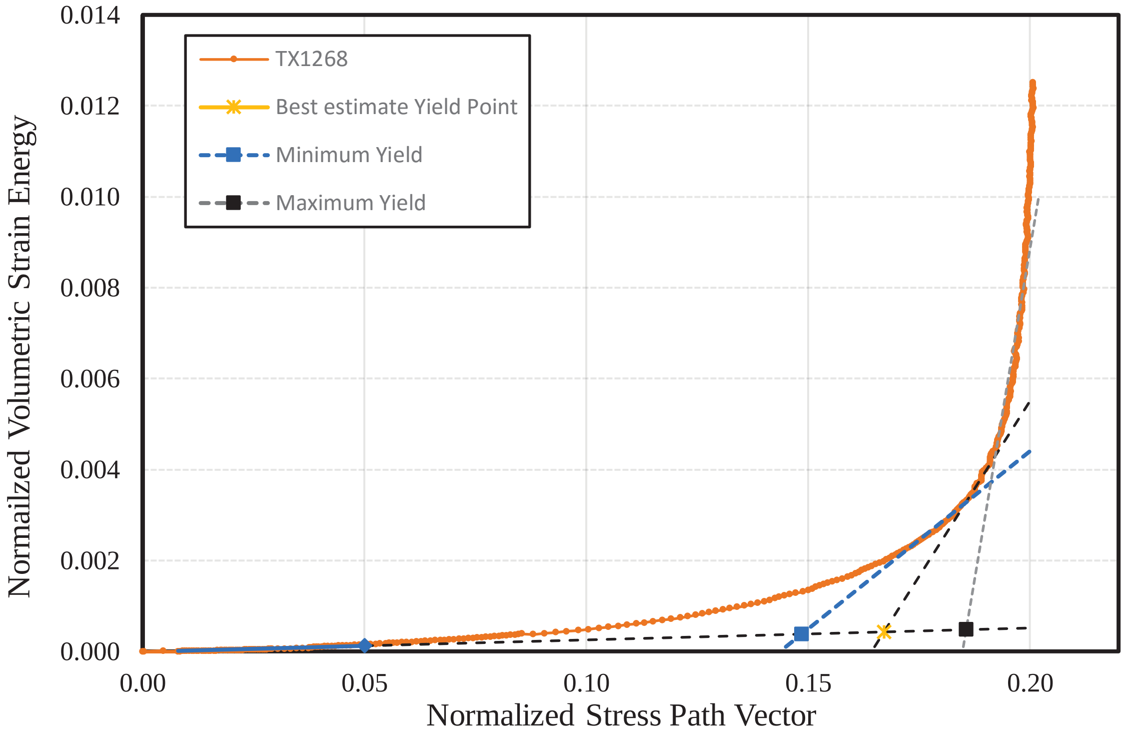

Figure 0-4: Interpreted yield transition zone for test no. TX1268

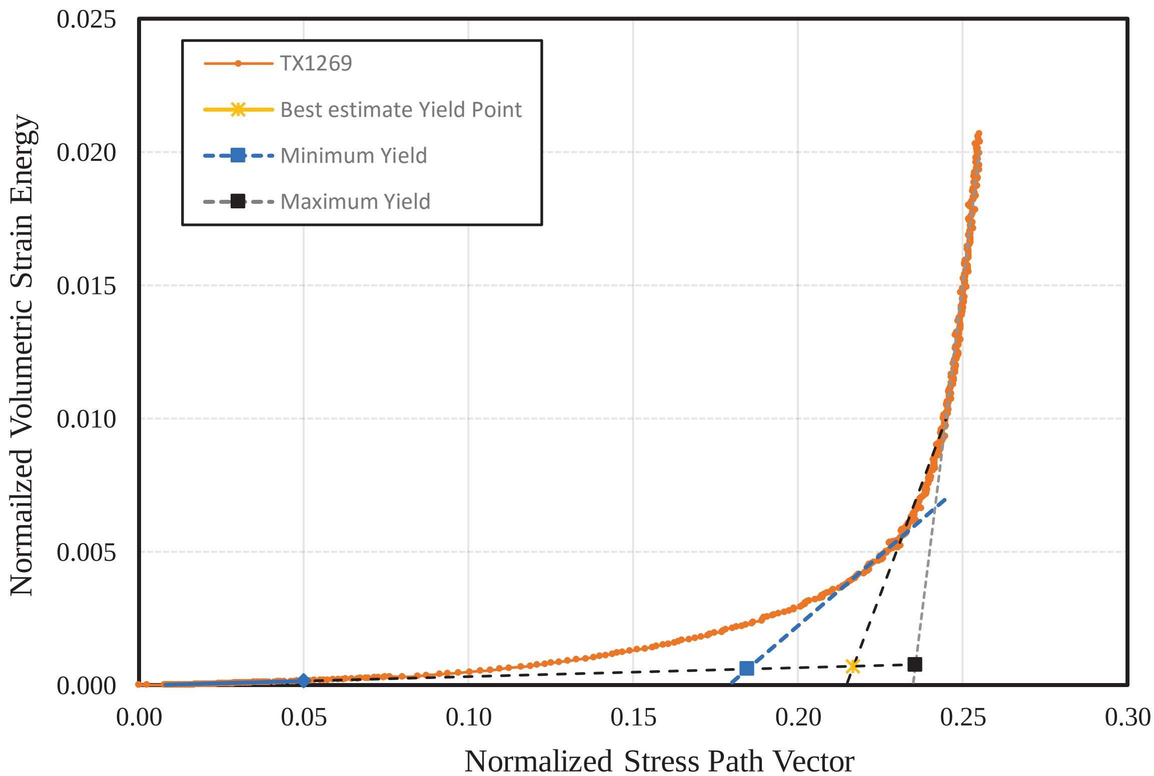

Figure 0-5: Interpreted yield transition zone for test no. TX1269

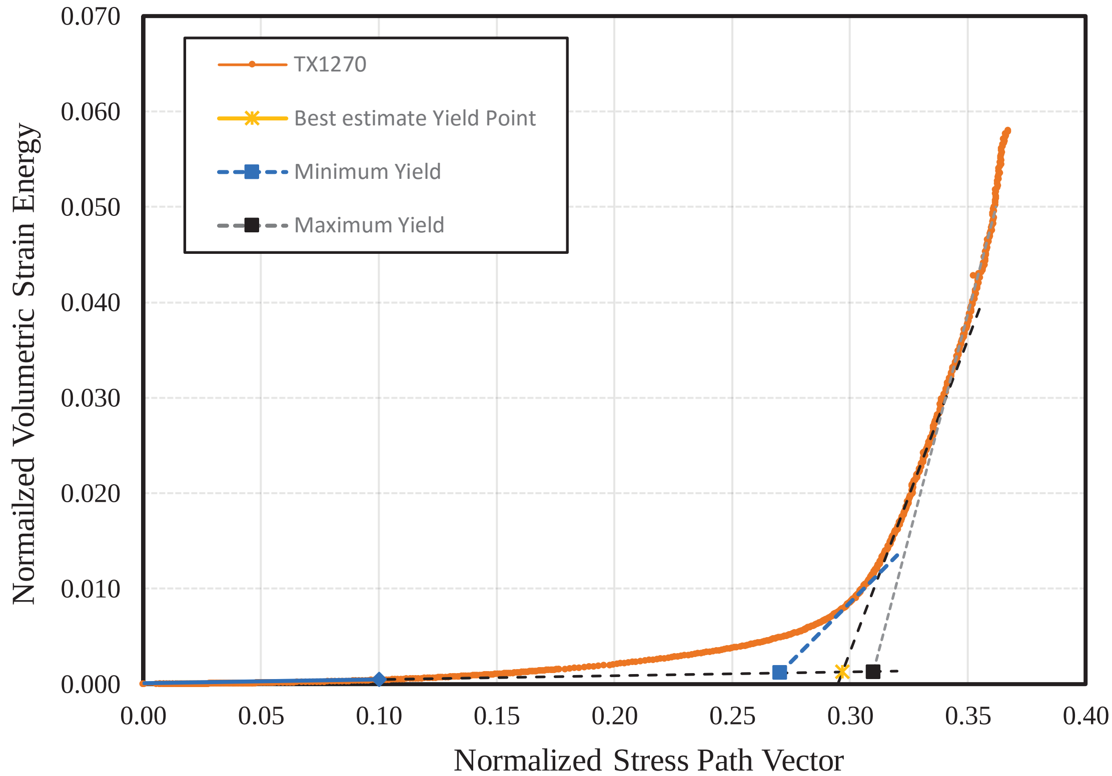

Figure 0-6: Interpreted yield transition zone for test no. TX1270

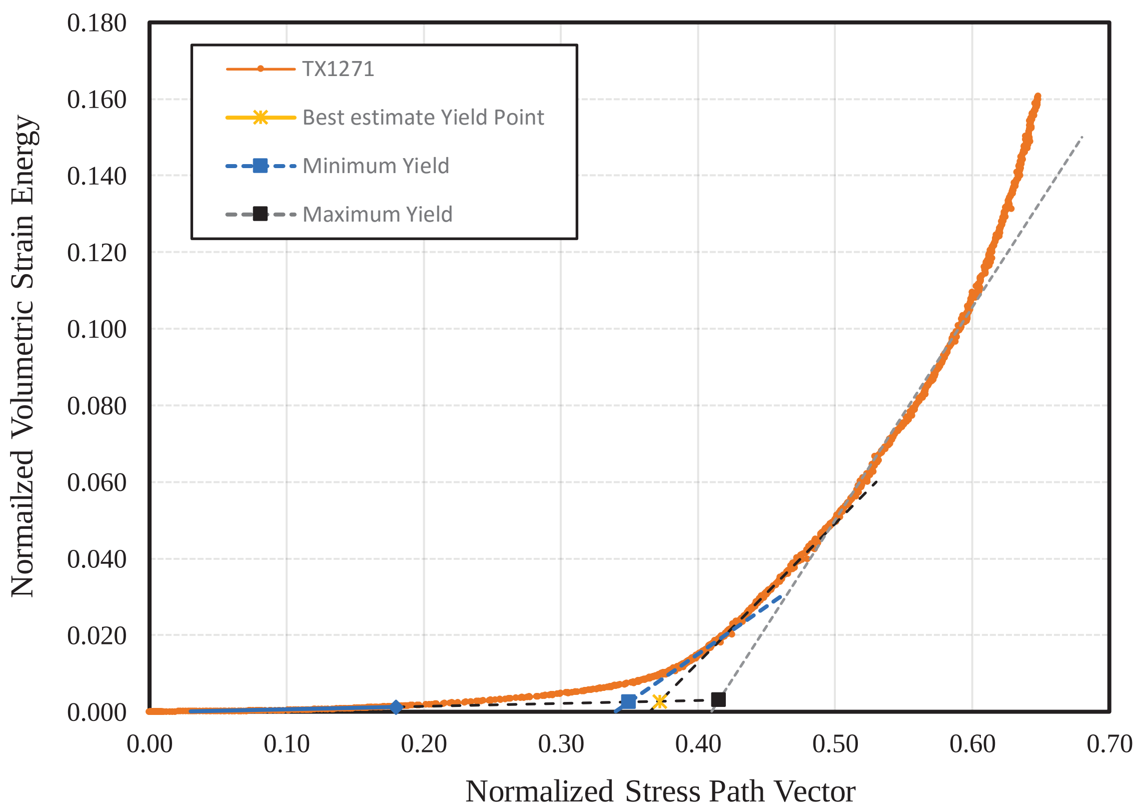

Figure 0-7: Interpreted yield transition zone for test no. TX1271

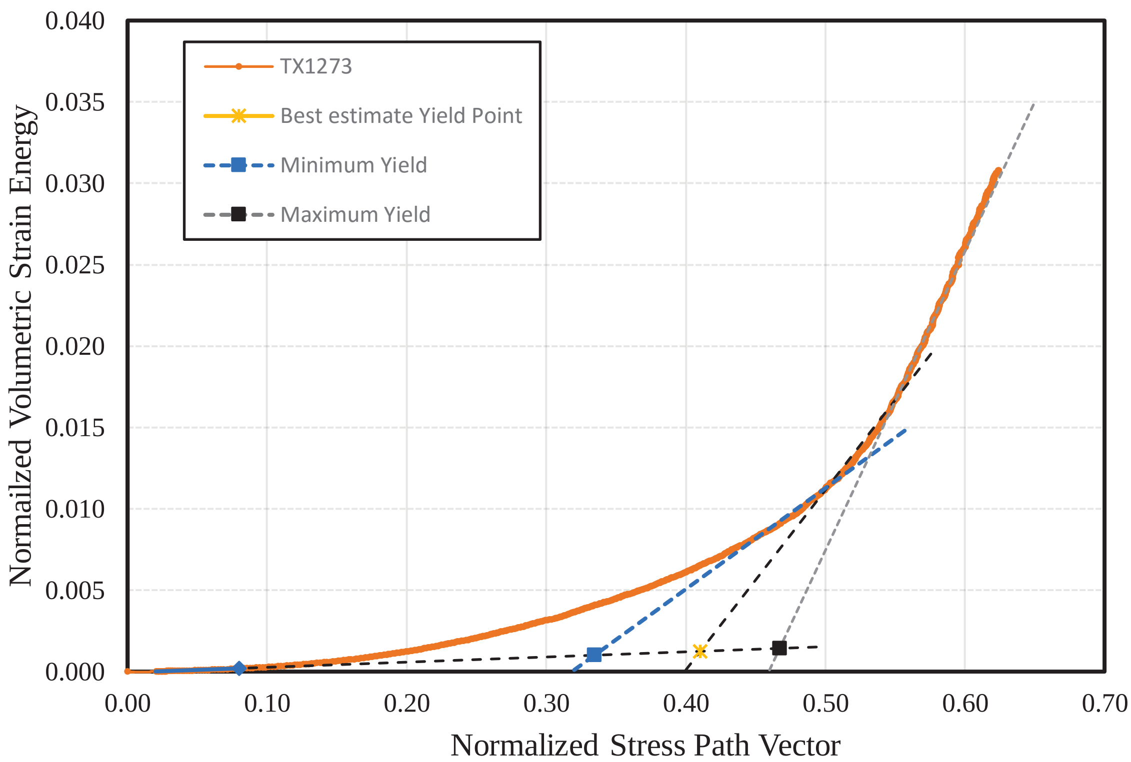

Figure 0-8: Interpreted yield transition zone for test no. TX1273

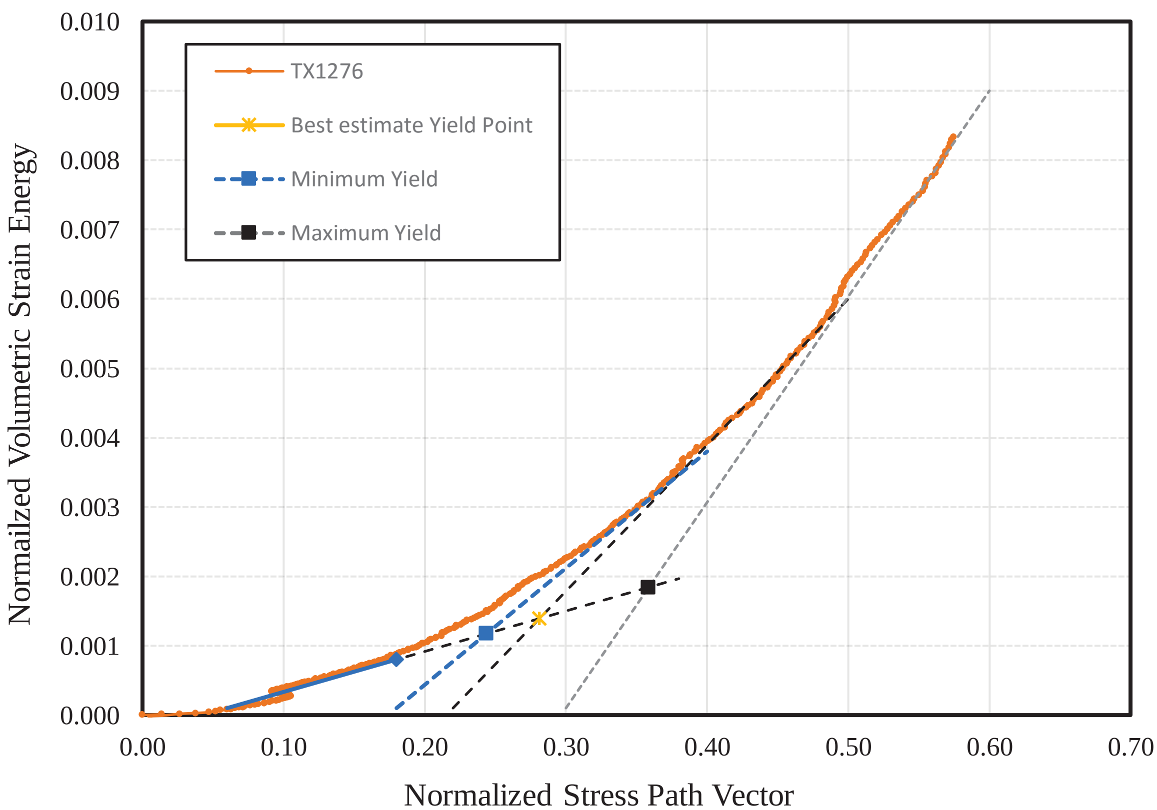

Figure 0-9: Interpreted yield transition zone for test no. TX1276

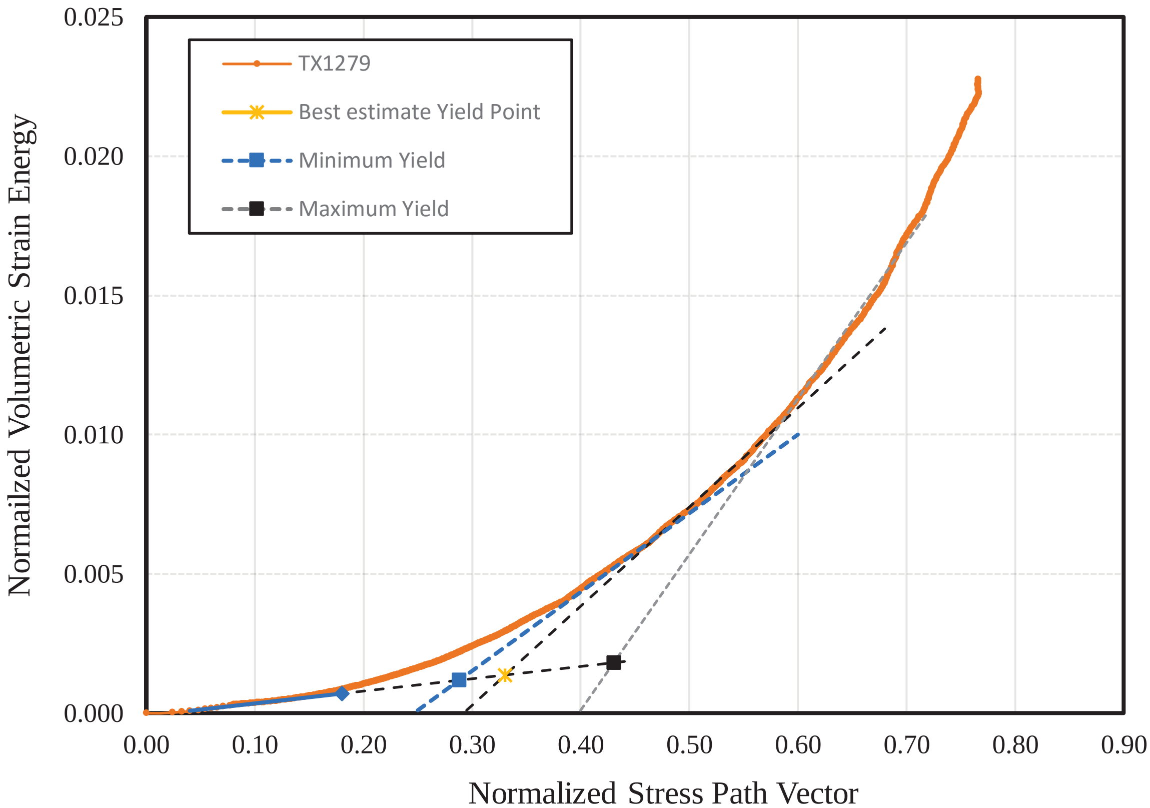

Figure 0-10: Interpreted yield transition zone for test no. TX1279

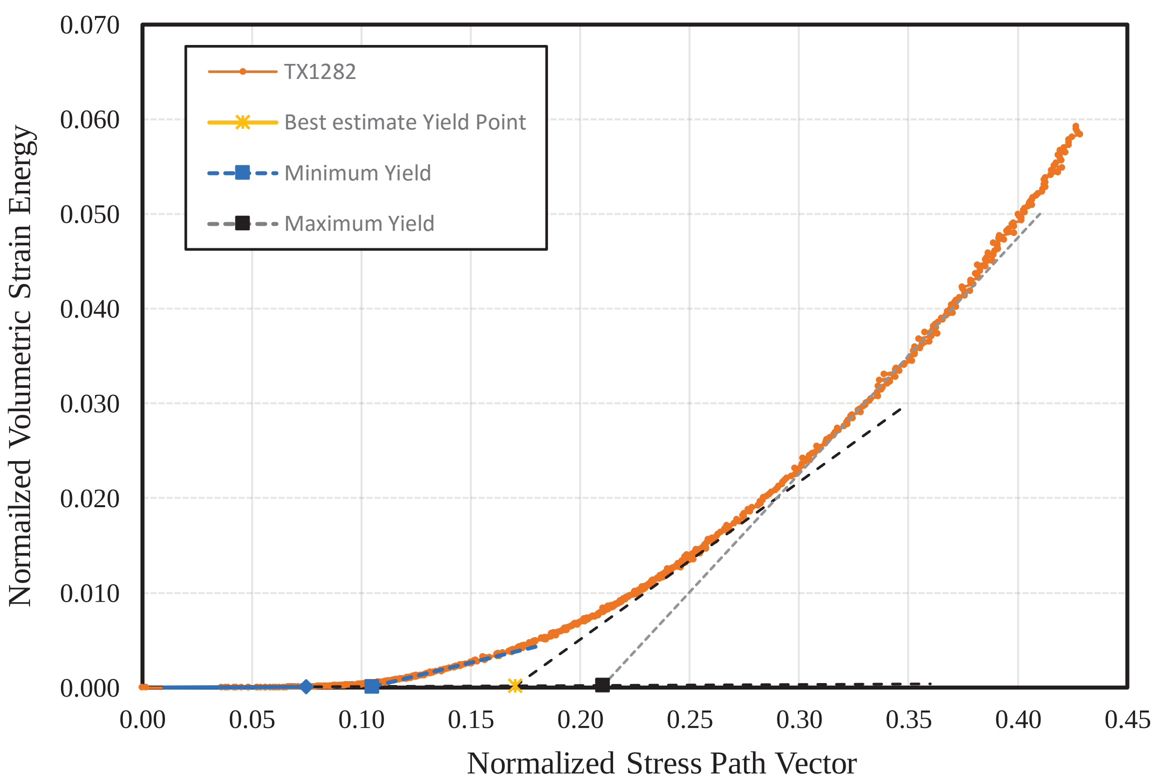

Figure 0-11: Interpreted yield transition zone for test no. TX1282

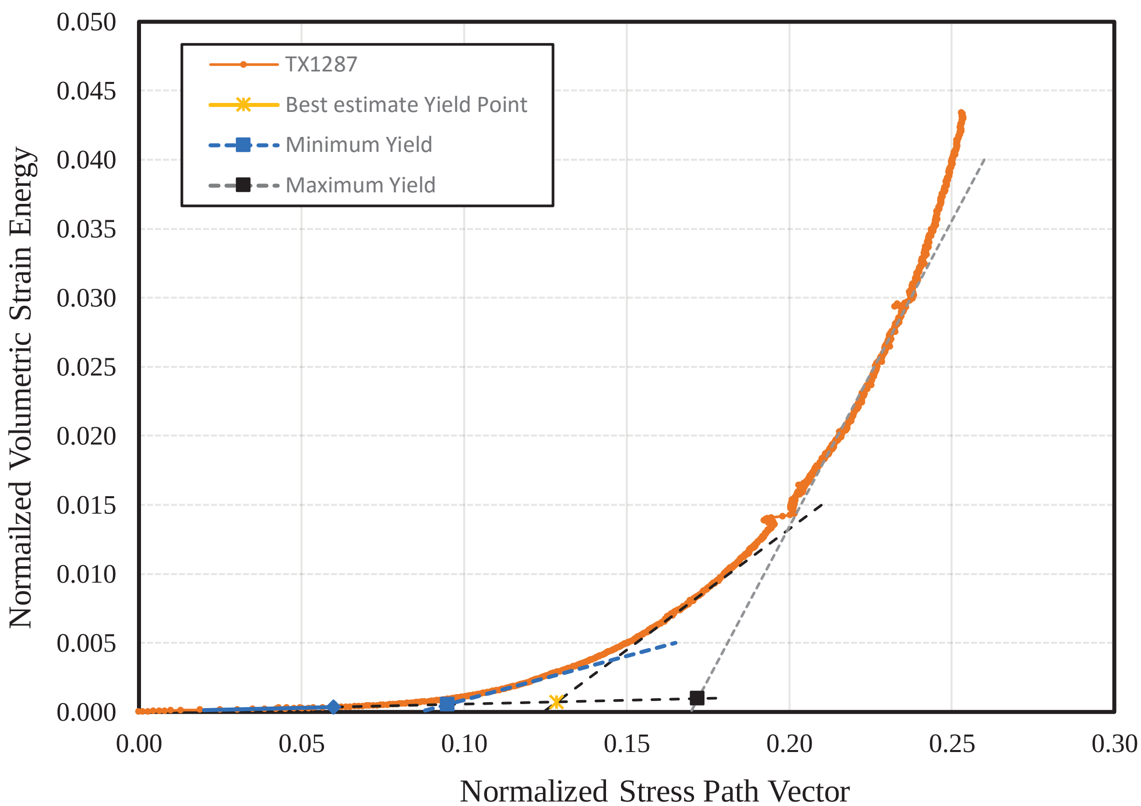

Figure 0-12: Interpreted yield transition zone for test no. TX1287

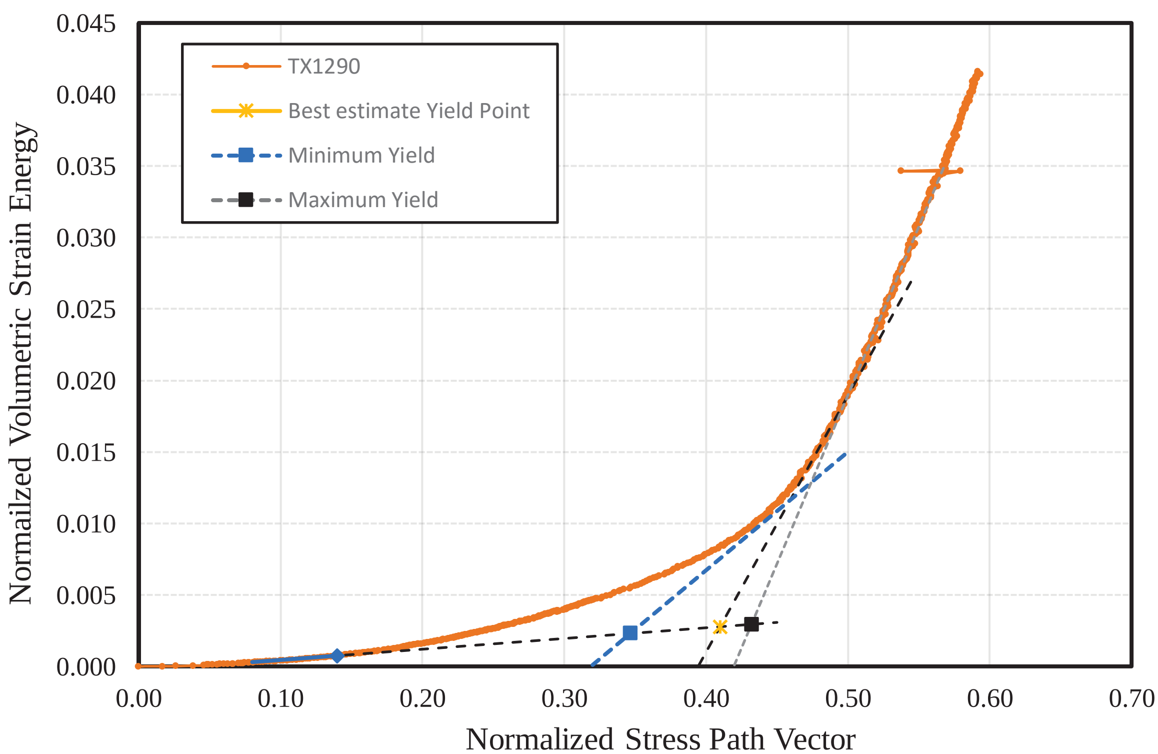

Figure 0-13: Interpreted yield transition zone for test no. TX1290

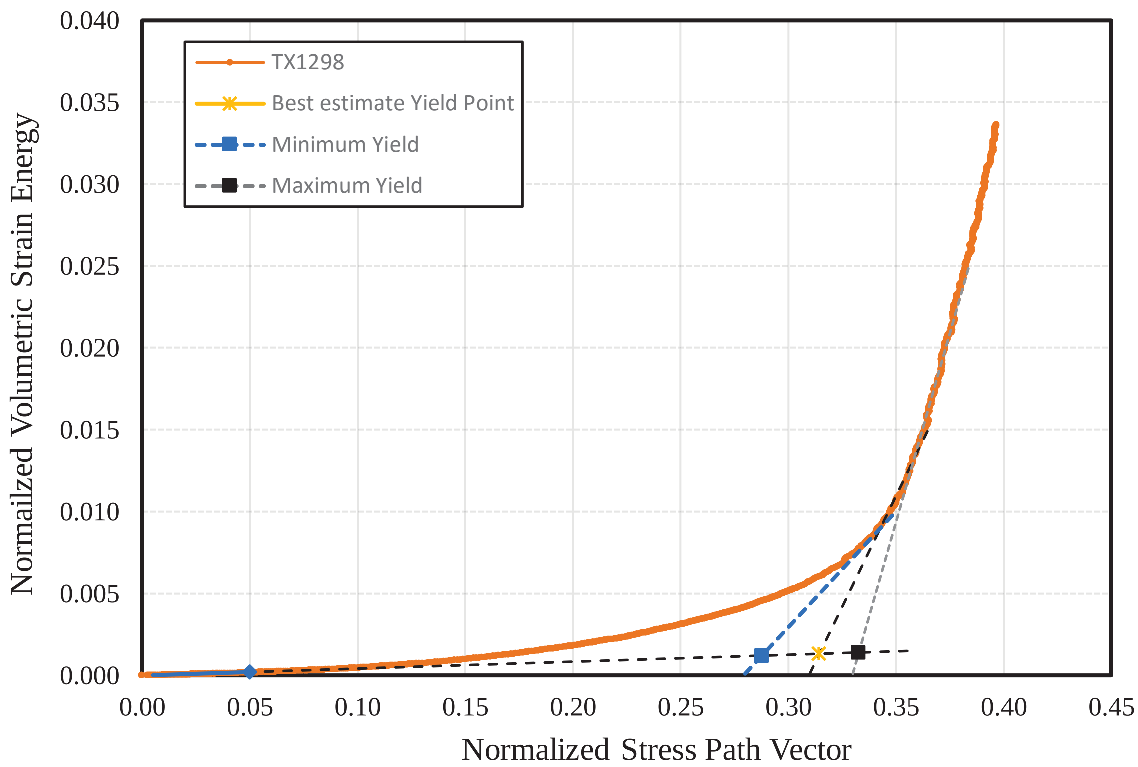

Figure 0-14: Interpreted yield transition zone for test no. TX1298

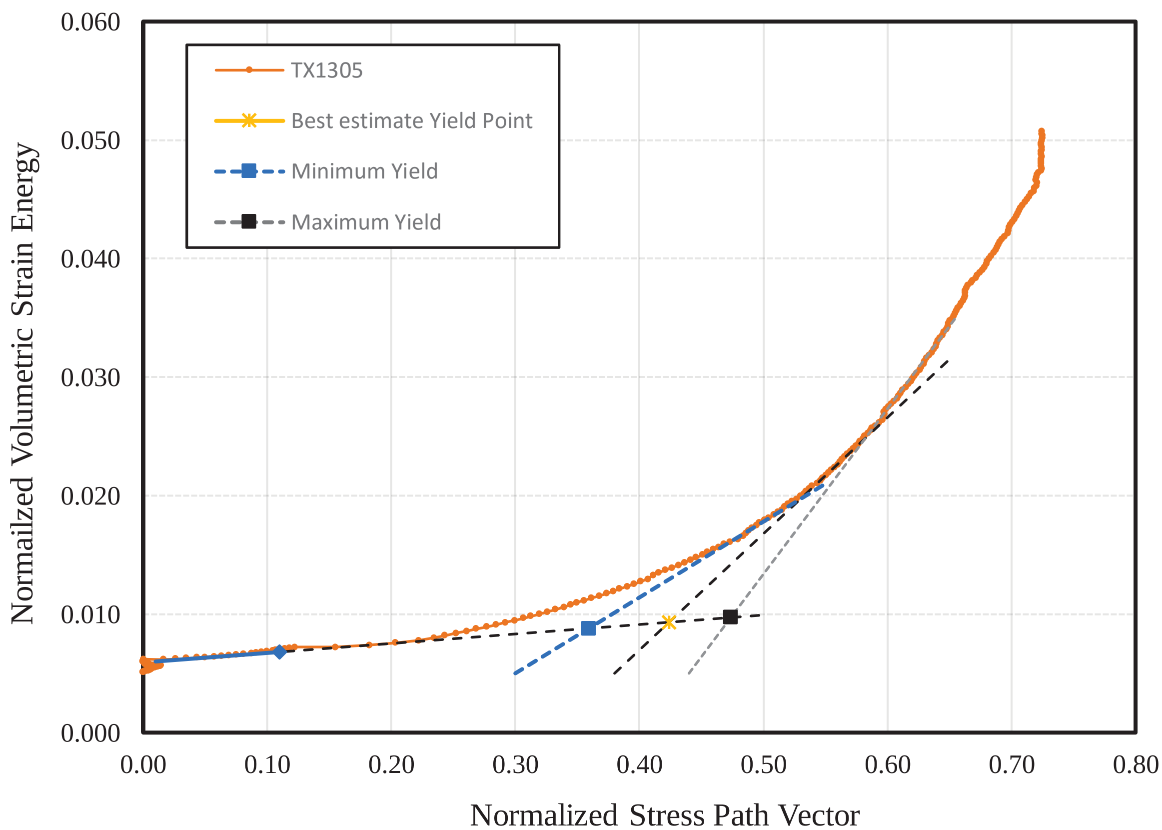

Figure 0-15: Interpreted yield transition zone for test no. TX1305

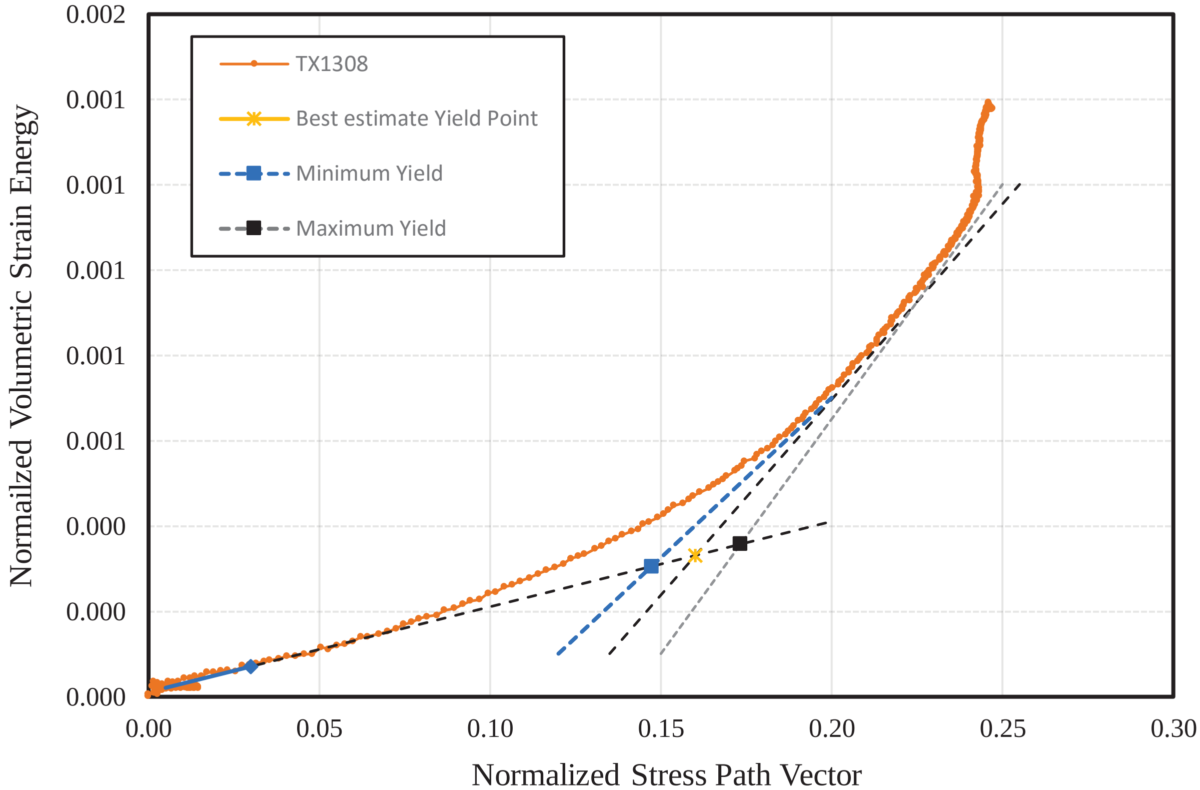

Figure 0-16: Interpreted yield transition zone for test no. TX1308

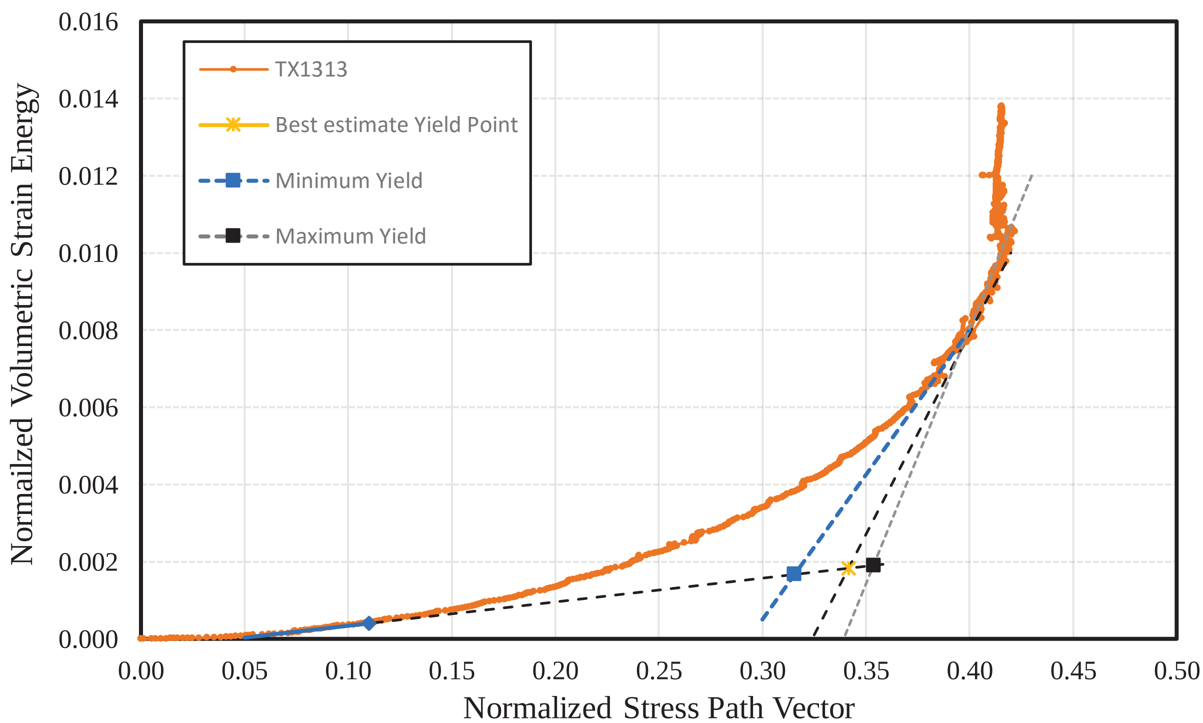

Figure 0-17: Interpreted yield transition zone for test no. TX1313

INTACT BOSTON BLUE CLAY PLOTS

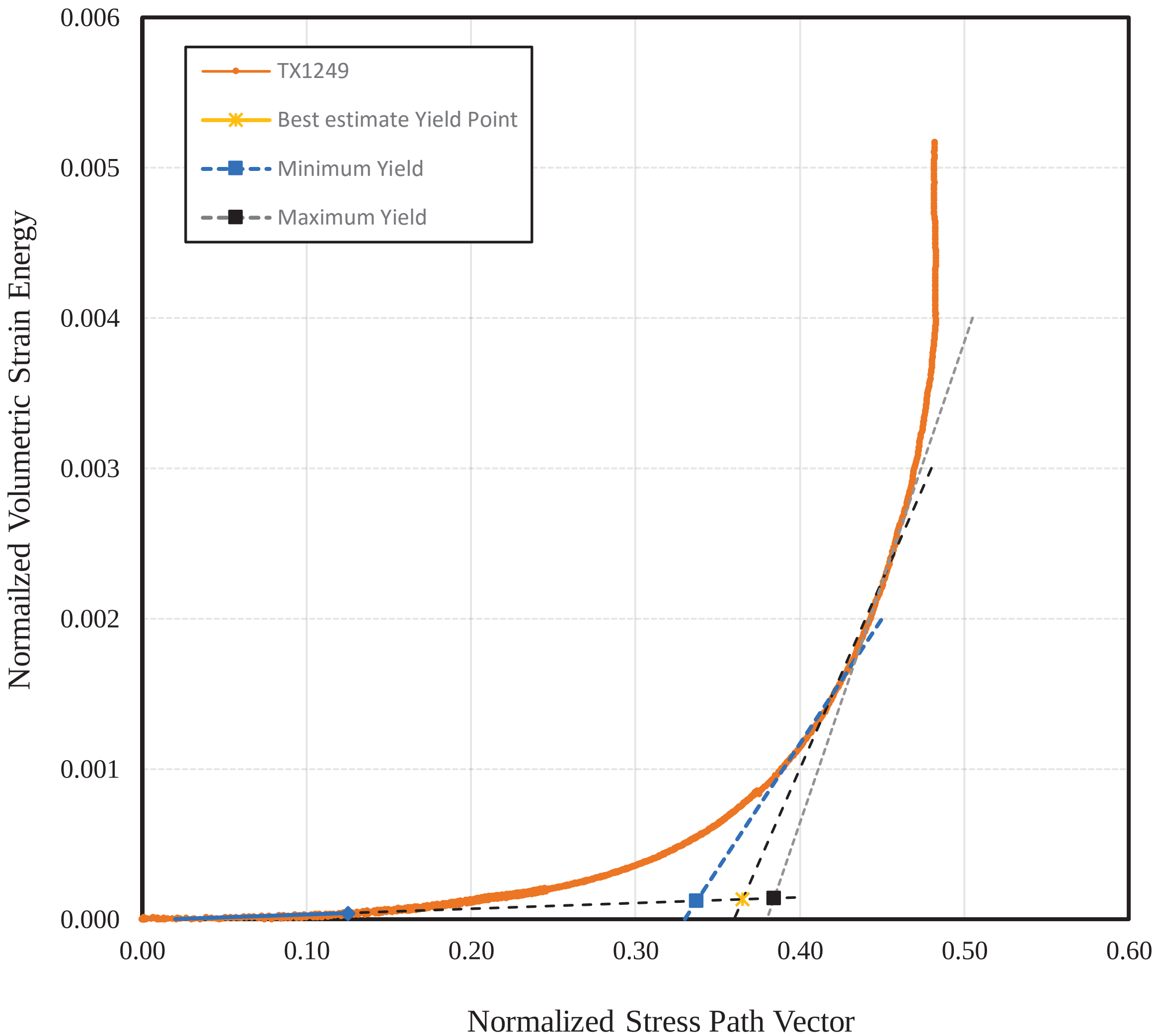

Figure 0-18: Interpreted yield transition zone for test no. TX1249

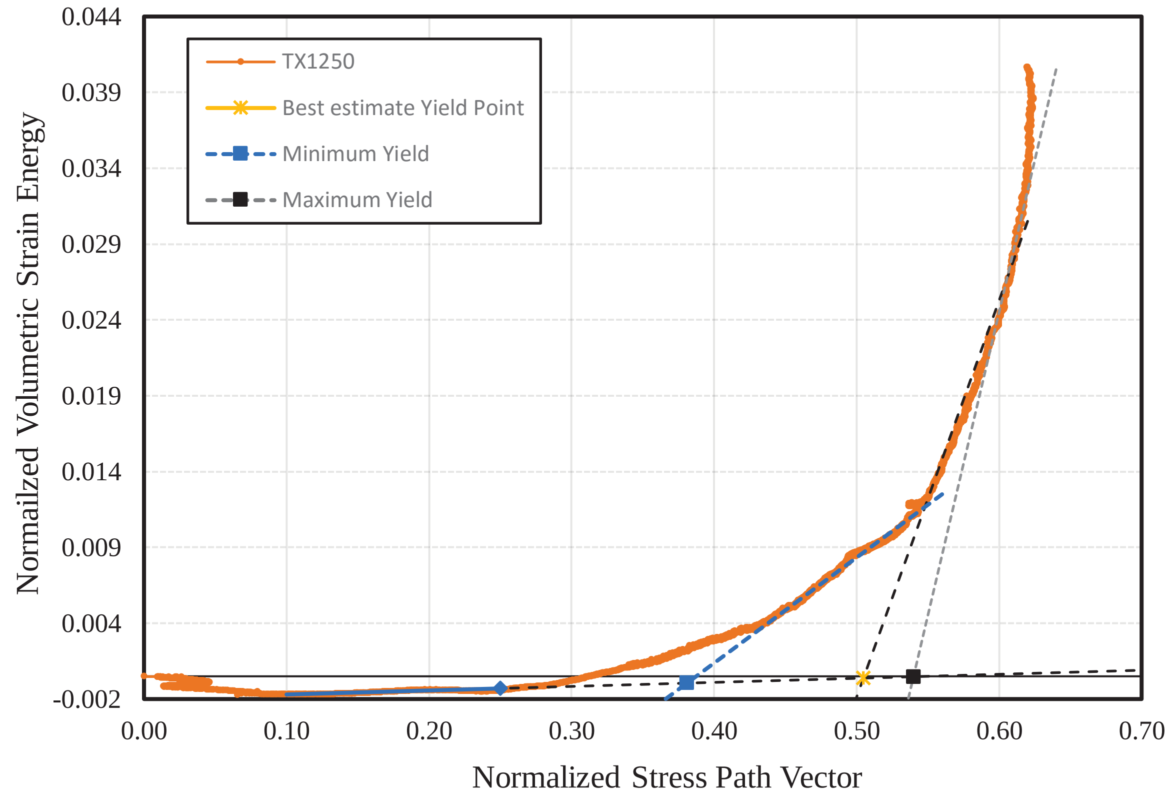

Figure 0-19: Interpreted yield transition zone for test no. TX1250

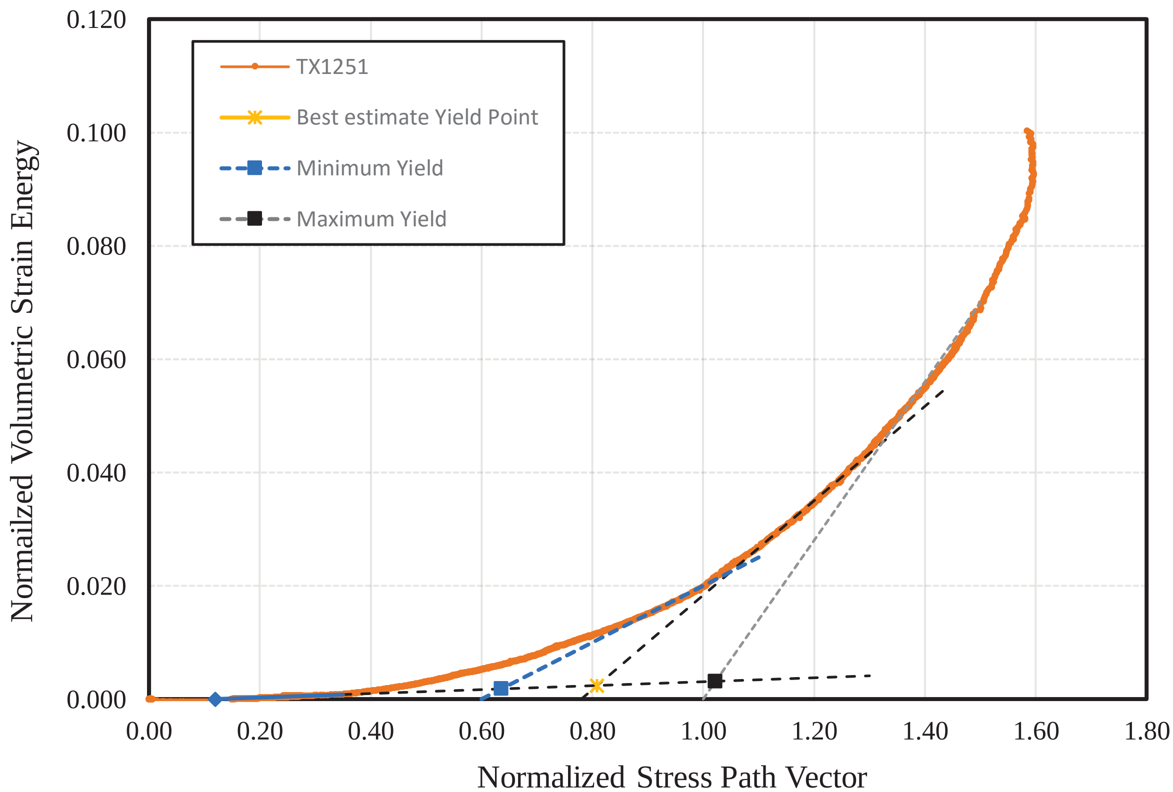

Figure 0-20: Interpreted yield transition zone for test no. TX1251

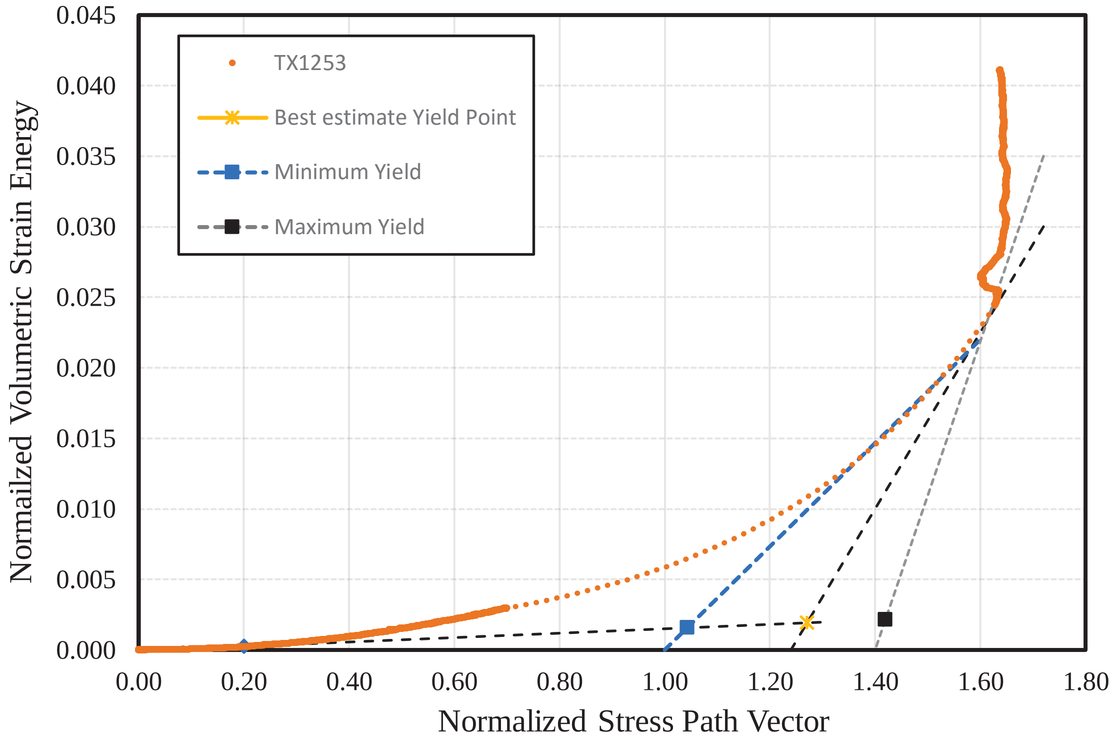

Figure 0-21: Interpreted yield transition zone for test no. TX1253

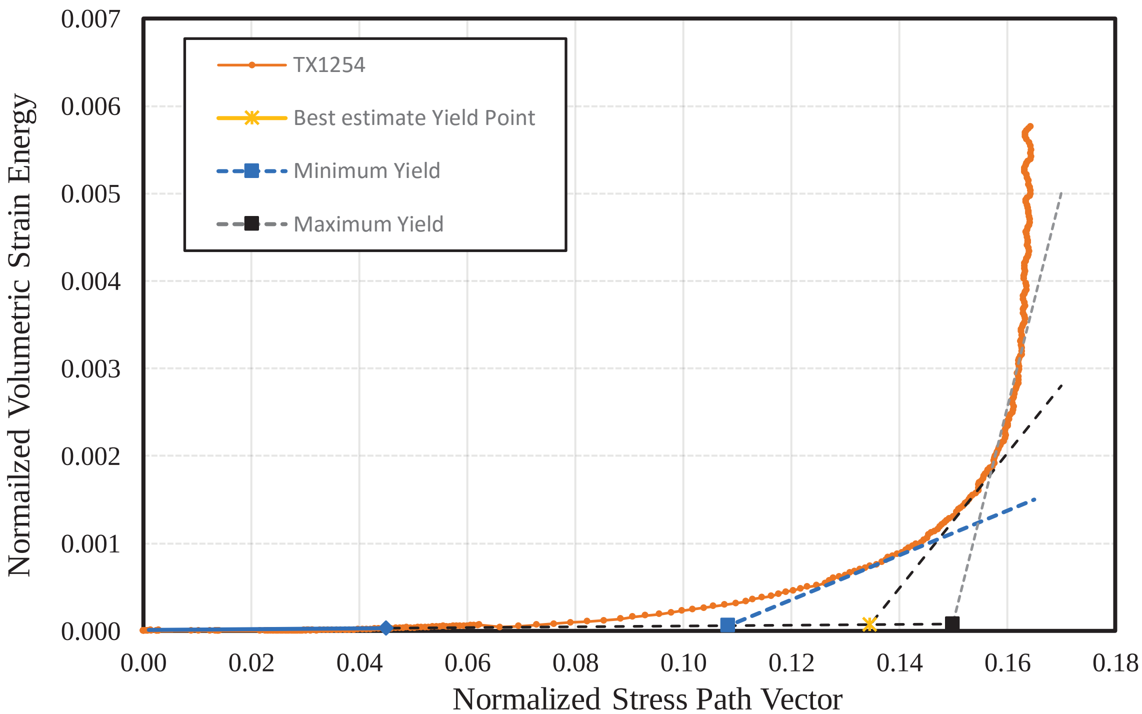

Figure 0-22: Interpreted yield transition zone for test no. TX1254

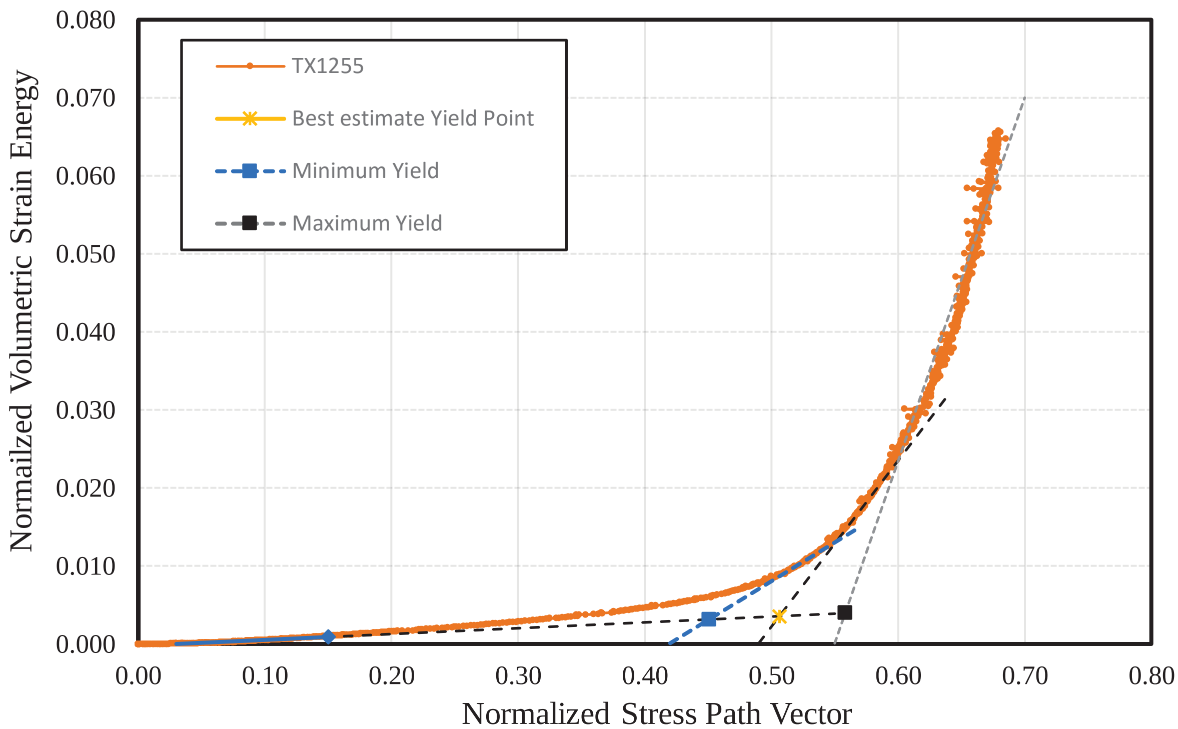

Figure 0-23: Interpreted yield transition zone for test no. TX1255

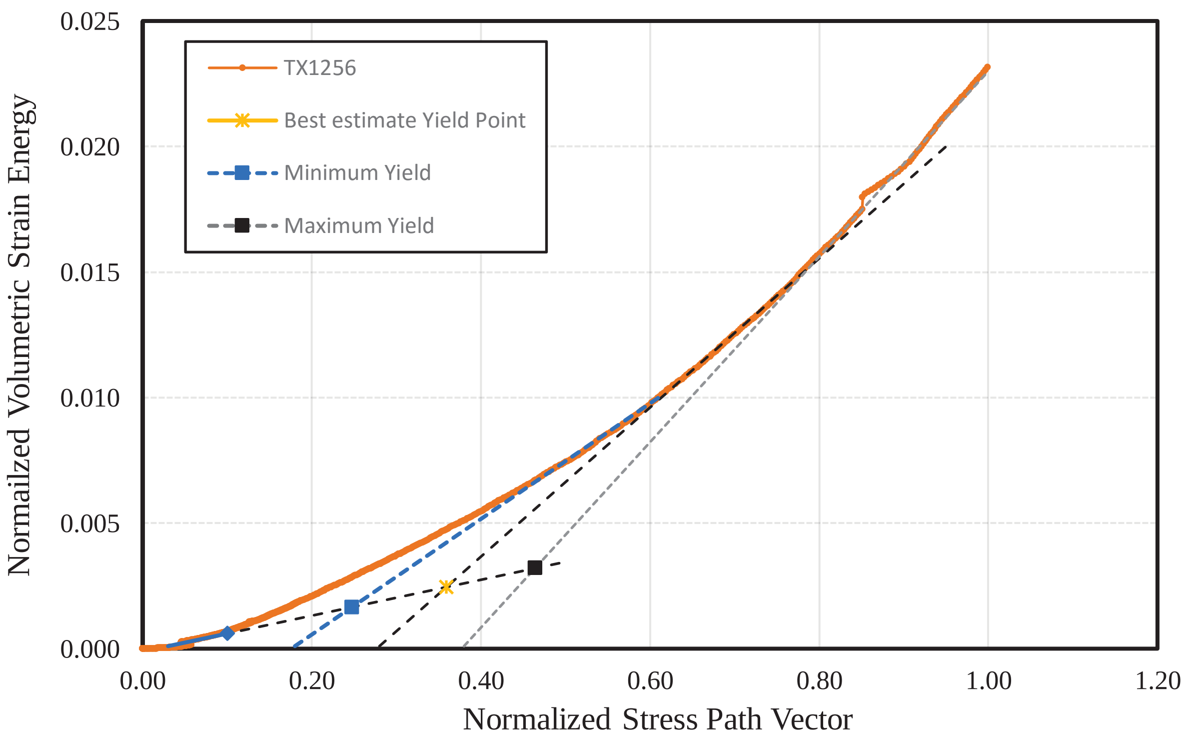

Figure 0-24: Interpreted yield transition zone for test no. TX1256

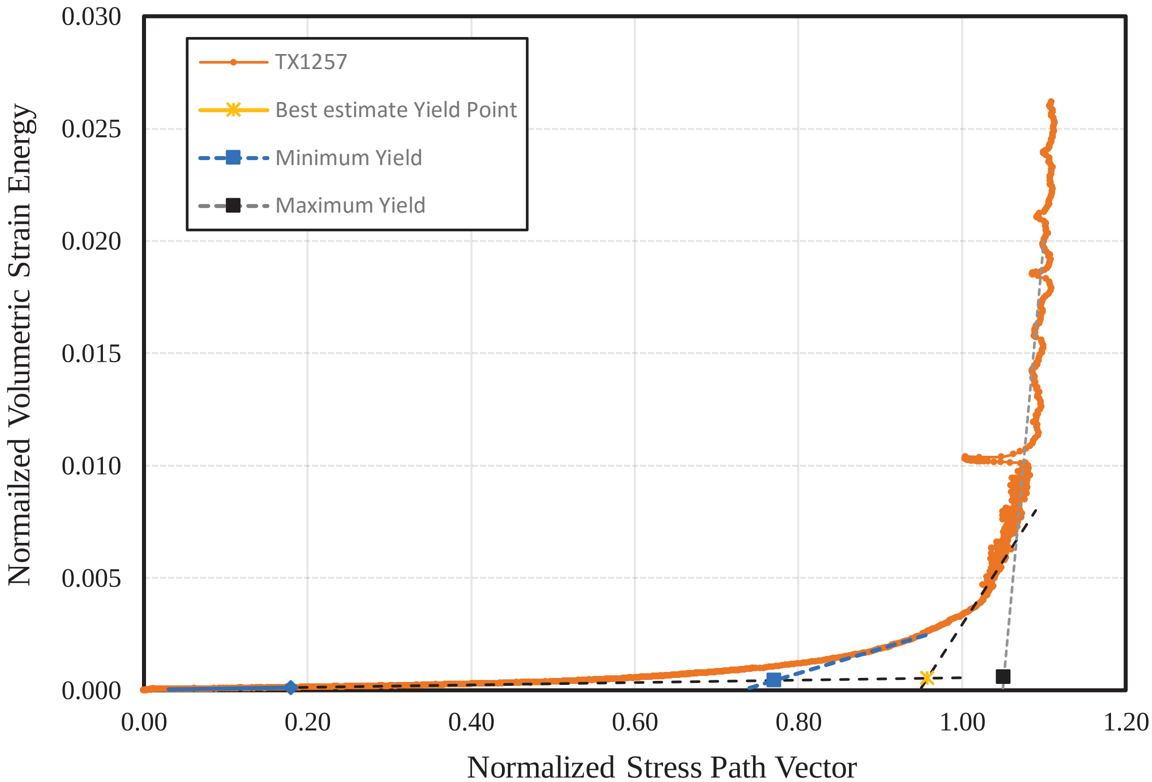

Figure 0-25: Interpreted yield transition zone for test no. TX1257

RESEDIMENTED BOSTON BLUE CLAY PLOT

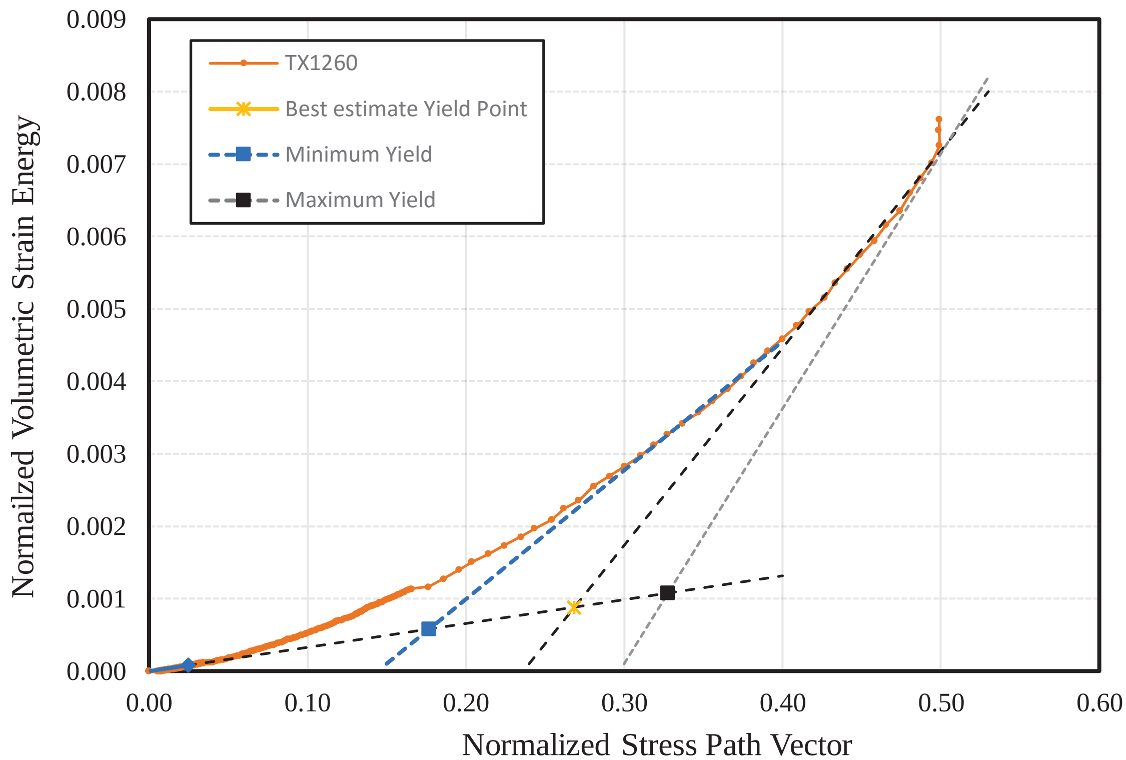

Figure 0-26: Interpreted yield transition zone for test no. TX1260

REFRENCES

Abdulhadi, N.O. (2009). “An Experimental Investigation into the Stress-Dependent Mechanical Behavior of Cohesive Soil with Application to Wellbore Instability”, Ph.D. Thesis, Massachusetts Institute of Technology

Anderson, G.R. (1991). “Physical Mechanisms Controlling the Strength and Deformation Behavior of Frozen Sand”, Sc.D. Thesis, Massachusetts Institute of Technology

ASTM D422 Standard Test Method for Particle-size Analysis of Soils, in ASTM 04.08 Soil and Rock (1), 2007

ASTM D2487 Standard Practice for Classification of Soils for Engineering Purposes (Unified Soil Classification System), in ASTM 04.08 Soil and Rock (1), Revision 11

ASTM D2974 Standard Test Methods for Moisture, Ash, and Organic Matter of Peat and Other Organic Soils, in ASTM 04.08 Soil and Rock (1), Revision 13

ASTM D4186 Standard Test Method for One-Dimensional Consolidation Properties of Saturated Cohesive Soils using Controlled-Strain Loading, in ASTM 04.08 Soil and Rock (1), Revision 12

ASTM D4318 Standard Test Methods for Liquid Limit, Plastic Limit, and Plasticity Index of Soils, in ASTM 04.08 Soil and Rock (1), Revision 12

Bailey, W.A. (1961). “Effects of Salt on the Shear Strength of Boston Blue Clay”, SB Thesis, Massachusetts Institute of Technology

Becker, D. E., J.H.A. Crooks, K. Been, and M. G. Jefferies. 1987. “Work as a Criterion for Determining In Situ and Yield Stresses in Clays.” Canadian Geotechnical Journal, 24 (4), November.

Bellwald, P. (1990). “A Contribution to the Design of Tunnels in Argillaceous Rock”, Ph.D. Thesis, Massachusetts Institute of Technology

Belviso, R., Federico, A. & Popescu, M. (2001). “KO-Undrained Shear Strength Ratio of Normally Consolidated Clays from CIUC tests”, Soft Soil Engineering, Zwets & Zeitlinger, pp. 575-579

Bensari, J.E. (1981). "Stress-Strain Characteristics From Undrained and Drained Triaxial Tests on Resedimented Boston Blue Clay ", S.M. Thesis, Massachusetts Institute of Technology

Berman, D.R. (1993). "Characterization of the Engineering Properties of Boston Blue Clay at the MIT Campus", S.M. Thesis, Massachusetts Institute of Technology

Berre, T. (1985). "Suggested International Code of Soil Engineering Practice for Triaxial Compression Tests", Report No. 56103-30. Norwegian Geotechnical Institute

Betts, W.S. (2014) "Compression and Permeability Behavior of Gulf of Mexico Mudrocks, Resedimented and In-situ", M.S. Thesis, University of Texas at Austin

Bishop, A.W. (1976). "The Influence of System Compressibility on the Observed Pore-Pressure Response to an Undrained Change in Stress in Saturated Rock" (Technical Note), Géotechnique 26, (2), pp. 435-442

Burland, J.B. (1990). "On the Compressibility and Shear Strength of Natural Soils", Géotechnique 40 (3), pp. 329-378

Butterfield, R. (1979). "A Natural Compression Law for Soils (an Advance on e-logp')", Technical Note, Géotechnique 29, (4), pp. 469 – 480

Casey, B. (2014). "The Consolidation and Strength Behavior of Mechanically Compressed Fine-Grained Sediments", Ph.D. Thesis, Massachusetts Institute of Technology

Casagrande, A. & Carillo, N. (1944) "Shear Failure of Anisotropic Materials," Journal of Boston Society of Civil Engineers, 31 (2), 74-87.

Casagrande, A. (1936) "The Determination of the Pre-consolidation Load and its Practical Significance," Proc. 1st ICSMFE, Cambridge, Mass. Vol. 3, pp. 60-67.

Cauble, D.F. (1996). "An Experimental Investigation of the Behavior of a Model Suction Caisson in a Cohesive Soil", Ph.D. Thesis, Massachusetts Institute of Technology

Fahy, B.P. (2014). "The Influence of Salinity on the Mechanical Behavior of High Plasticity Soils", S.M. Thesis, Massachusetts Institute of Technology

Germaine, J.T. (1982). "Development of the Directional Shear Cell for Measuring Cross-Anisotropic Clay Properties", Sc.D. Thesis, Massachusetts Institute of Technology

Germaine, J.T. & Germaine, A.V. (2009). Geotechnical Laboratory Measurements for Engineers, John Wiley and Sons

Grennan, J.T. (2010). “Characterization of a Low Plasticity Silt”, S.M. Thesis, Massachusetts Institute of Technology

Gutierrez, M., Nygard, R., Hoeg, K. & Berre, T. (2008). “Normalized Undrained Shear Strength of Clay Shales”, Engineering Geology 99, pp. 31-39

Hansen, J.B. & Gibson, R.E. (1949) “Undrained Shear Strength of Anisotropically Consolidated Clays,” Géotechnique, 1 (3), 189-204.

Hillier, S. (1999). “Use of an Air Brush to Spray Dry Samples for X-ray Powder Diffraction”, Clay Minerals 34, pp. 127-135

Hillier, S. (2003). “Quantitative Analysis of Clay and Other Minerals in Sandstones by X-ray Powder Diffraction (XRPD)”, International Association of Sedimentologists Special Publication 34: Clays and Clay Cements in Sandstones. Blackwell, Oxford, pp. 213-251

Horan, A.J. (2012). “The Mechanical Behavior of Normally Consolidated Soils as a Function of Pore Fluid Salinity”, S.M. Thesis, Massachusetts Institute of Technology

Hueckel, T., and Nova, R. (1979). "Some hysteresis effects of the behavior of geological media." Int. J. of Solids and Structures, 15, 625-642.

Jambu, N. (1969), “The Resistance Concept Applies to Deformation of Soils, “ Proc. 7th ICSMFE, Mexico, Vol. 1, pp. 191-196

Jamiolkowski, M., Ladd, C.C., Lancellotta, R., & Germaine, J.T. (1985) “New Developments in Field and Laboratory testing of Soils,” Proceedings of 11th International Conference on Soil Mechanics and Foundation Engineering, San Francisco, 57-153.

Jâky, J. (1944). “A nyugalmi nyomâs tényezöje (The coefficient of earth pressure at rest)”, Magyar Mérnok és Epitész Egylet Közlönye (Journal for Society of Hungarian Architects and Engineers), October, pp. 355–358.

Jones, C.A. (2010). “Engineering Properties of Resedimented Ugnu Clay from the Alaskan North Slope”, S.M. Thesis, Massachusetts Institute of Technology

Kavvadas, M. J. (1982). "Non-linear consolidation around driven piles in clays," ScD thesis, Massachusetts Inst. of Tech., Cambridge, Mass.

Kavvadas, M. and Baligh, M, M. (1982). "Non-linear consolidation analysis around pile shafts, " Massachusetts Inst. of Tech, pp. 338-347

Kenney, T.C. (1964). “Sea-Level Movements and the Geologic Histories of the Postglacial Marine Soils at Boston, Nicolet, Ottawa and Oslo”, Géotechnique 14 (3), pp. 203-230

Kontopoulos N.S. (2012). “The Effect of Sample Disturbance on Preconsolidation Pressure for Normally Consolidated and Overconsolidated Clays”, Ph.D. Thesis, Massachusetts Institute of Technology

Ladd, C.C. & Foott, R. (1974). “New Design Procedure for Stability of Soft Clay”, Journal of the Geotechnical Engineering Division, ASCE, 100 (7), pp. 763-786

Ladd, C.C. (1985). “Overview of Clay Behaviour”, MIT Special Summer Course 1.605

Ladd, C.C. (1991). “Stability Evaluation during Staged Construction”, 22nd Karl Terzahgi Lecture, Journal of Geotechnical Engineering 117 (4), pp. 540-615

Lade, P.V. & de Boer, R. (1997). “The Concept of Effective Stress for Soil, Concrete and Rock”, Géotechnique 47 (1), pp. 61-78

Ladd, C.C. & Varallyay, J. (1965). “The Influence of Stress System on the Behavior of Saturated Clays during Undrained Shear”, Research Report R65-11, Soils Publication No. 177, Department of Civil Engineering, Massachusetts Institute of Technology

Lo, K, Y. and Morin, J. P. (1972), “Strength Anisotropy and Time Effects of Two Sensitive Clays,” Canadian Geotech. Journal, 9, pp. 261-277.

Marjanovic, J. (2015). “Stiffness Characterization of Mechanically Compressed Cohesive Soils Using Wave Propagation”, PhD. Thesis, Massachusetts Institute of Technology

Mitchell, J. R. (1970), “The Yielding and Mechanical Strength of Leda Clays,” Canadian Geotechnical Journal, Vol. 7, pp. 297-312.

Norquist, T, J. (2013). “Permeability Anisotropy of Resedimented Mudrocks”, S.M. Thesis, Massachusetts Institute of Technology

O'Niell, D. (1985) "Undrained Strength Anisotropy of an Overconsolidated Thixotropic Clay," SM Thesis, MIT, Cambridge, MA.

Roscoe, K.H. & Burland, J.B. (1968). "On the Generalized Stress-Strain Behaviour of 'Wet' Clay", in Engineering Plasticity, Cambridge University Press, pp. 535 – 609

Santagata, M.C. (1994). "Investigation of Sample Disturbance in Soft Clays Using Triaxial Element Tests", S.M. Thesis, Massachusetts Institute of Technology

Santagata, M.C. (1998). "Factors Affecting the Initial Stiffness and Stiffness Degradation of Cohesive Soils", Ph.D. Thesis, Massachusetts Institute of Technology

Schmertmann, J.H (1955), "The Undisturbed Consolidation of Clays," Trans. ASCE. Vol. 120, pp.535-609.

Seah, T.H. (1990). "Anisotropy of Resedimented Boston Blue Clay", Sc.D. Thesis, Massachusetts Institute of Technology

Sheahan, T.C. (1991). "An Experimental Study of the Time-Dependent Undrained Shear Behaviour of Resedimented Clay Using Automated Stress-Path Triaxial Equipment", Sc.D. Thesis, Massachusetts Institute of Technology

Stokes, W.L. & Varnes, D.J. (1955). Glossary of Selected Geologic Terms, Colorado Scientific Society Proceedings 16, Denver, Colorado

Tavenas, F. and Leroueil, S. (1977), "Effect of Stresses and Time on Yielding of Clays," Proc. 9th Int. Conf. of soil Mec. And Fdn. Eng., Tokyo, 1, pp. 319-326

Terzaghi, K., Peck, R.B. & Mesri, G. (1996). Soil Mechanics in Engineering Practice, 3rd Edition, John Wiley and Sons Inc., New York

Whittle, A.J. & Kavvadas, M. (1994). "Formulation of the MIT-E3 Constitutive Model for Overconsolidated Clays", Journal of the Geotechnical Engineering Division, ASCE, 120 (1), pp. 173-198

William, E. (2007). "Engineering Performance of Bringelly Shale", Ph.D. Thesis, University of Sydney

Wissa, A.E.Z. (1969). “Pore Pressure Measurement in Saturated Stiff Soils”, Journal of Soil Mechanics and Foundations Division, ASCE 95 (S.M.4), pp. 1063-1073

Wissa, A.E.Z., Christian, J.T., Davis, E.H. & Heiberg, S. (1971). “Consolidation at Constant Rate of Strain”, Journal of the Soil Mechanics and Foundations Division, ASCE 97 (SM10), pp. 1393-1493